Aerosol carbon nanotube production via scalable microplasma synthesis of catalyst nanoparticles

by

William J. Sawyer

B.A., Earth and Environmental Science
Wesleyan University, 2016

B.E., Engineering Sciences
Dartmouth College, 2017

S.M., Mechanical Engineering
Massachusetts Institute of Technology, 2020

Submitted to the Department of Mechanical Engineering
in partial fulfillment of the requirements for the degree of

Doctor of Philosophy

at the

MASSACHUSETTS INSTITUTE OF TECHNOLOGY

September 2023

Authored by:	William J. Sawyer Department of Mechanical Engineering August 11, 2023
Certified by:	A. John Hart Thesis Supervisor, Professor of Mechanical Engineering
Accepted by:	Nicolas Hadjiconstantinou Chair, Department Committee on Graduate Theses

Aerosol carbon nanotube production via scalable microplasma synthesis of catalyst nanoparticles

by

William J. Sawyer

Submitted to the Department of Mechanical Engineering
on August 11, 2023 in partial fulfillment of the
requirements for the degree of
Doctor of Philosophy

Abstract

The exceptional properties of individual carbon nanotubes (CNTs) have long indicated their potential for a range of practical applications. Yet, the challenge of synthesizing ordered assemblies of high quality CNTs limits the ability to fully translate those properties into macroscale structures. Floating catalyst chemical vapor deposition (FC-CVD) has emerged as the most promising process for large-scale production with an increasing number of commercial uses. Yet, FC-CVD still requires improvements in control (i.e., reliability and CNT size) and quality (i.e., defects and impurities) to overcome the current trade-off between CNT quality and process intensity and enable the full potential of CNT-based materials.

This thesis describes the design, construction, and implementation of a lab-scale system that achieves end-to-end control of catalyst generation and aerosol CNT growth for the purpose of understanding these processes and assessing potential scalability. First, a stand-alone microplasma reactor is designed and fabricated, and used for synthesis of iron-carbon aerosols from a ferrocene vapor precursor. The microplasma approach achieves precise particle diameter control in the 1–5 nm range and aerosol concentrations an order of magnitude higher than previously published approaches; this is explained by a charge-mediated formation mechanism enabled by the μs-scale residence time. The influence of operating conditions on process stability and run-time is investigated, and a dielectric gradient focusing technique is developed to reduce variability and extend the lifetime of operation. Second, a FC-CVD system is built and integrated with the microplasma reactor and used to explore CNT synthesis on iron-carbon catalyst aerosols. Controlling temperature, gas chemistry, and flow conditions at which the catalyst aerosol and carbon precursor streams mix is shown to be critical for enabling CNT nucleation, controlling CNT diameter, and limiting iron and amorphous carbon impurities. Synthesis of highly-graphitized single-wall CNTs is demonstrated over a range of operating conditions by a Pareto front analysis with production rates of ~1 mg/hr. Based on these findings, an outlook is presented on the limiting factors and criteria for the scale-up of high quality CNT production.

Thesis Supervisor: A. John Hart
Title: Professor of Mechanical Engineering

Acknowledgements

First and foremost, thank you to my advisor Professor John Hart, without whom I would not be here, or who I am, today. Thank you for the mentoring, inquiring, enthusiasm, and confidence that this would all work out. It must be rare to have an advisor who is both so helpful when you need him, and so willing to let you wander off and stumble around when you want to – whether it was a new research idea, a philosophy class, or literally wandering off on a motorcycle for a summer. It was the bumps and bruises, side tracks, and dead ends along the way that made me the person I am today. John has a unique way of looking at the world – I'm convinced that manufacturing is as much a philosophy (one could spend a lifetime unravelling "value at scale") as an engineering discipline, and I am grateful for all of the times he has shared his vision as I find my own.

Thank you to my other committee members, Professors Desiree Plata and Asegun Henry, for helping ensure this journey took enough right turns along the way. Every professor at MIT knows their nuts and bolts. But there are some who, when you talk to them, make you want to learn how to think like they do. I knew Ase was one of those for me when he introduced the concept of entropy to our heat transfer class with a long analogy about wealth inequality. For better or worse, neither of these topics ended up being central to this thesis, but evidence of his work is here in a dozen other ways. Desiree's influence on me extends far beyond her expertise in all things nanotube synthesis. From the exotic locales of Bandera, Texas and Lake Norden, South Dakota, she has inspired me with her passion, conviction, rigor, and wit. Desiree has been a role model of how to be an engineer from the heart.

Thank you also to Professor Alex Slocum for tipping the scales on my decision to apply to graduate school and providing me an academic home when I first arrived.

Without Alex, I might have ended up spending the past six years in California, having fun but missing the fundamentals. I am also indebted to him for his repeated insistence that I talk with John about a research project, which eventually wore through my visceral distrust of all things 3D printing.

This work was initially supported by the National Aeronautics and Space Administration (NASA) Space Technology Research Institute (STRI) for Ultra-Strong Composites by Computational Design (US-COMP), grant number NNX17AJ32G. Thank you to Greg Odegard and the entire US-COMP team for the support and freedom to get this project off the ground. This work was also supported by ExxonMobil, and the MIT Mechanical Engineering MathWorks Seed Fund. Thank you to Ned Corcoran at ExxonMobil for taking an interest in this work, as well as to Mohsen Yeganeh for the continued opportunity to learn from and share with the ExxonMobil research community. This work made use of the MRSEC Shared Experimental Facilities at MIT, supported by the National Science Foundation under award number DMR-1419807 as well as in part through the use of MIT.nano's facilities. Thank you to Tim McClure, Charles Settens, Yong Zhang, Libby Shaw, Paul Tierney, and James Daley for your help learning the ropes on the instruments in these facilities, without which none of the data presented here would be possible. And, without whom this thesis would have been much abbreviated: a photo of a black smudge captioned "take my word for it."

Contents

1 Motivation and scope **31**

1.1 Motivation 31

1.2 Scope 33

References 36

2 Background **38**

2.1 Carbon nanotubes 38

2.2 Macroscopic assemblies 39

2.3 Synthesis 42

2.3.1 Catalyst generation 43

2.3.2 Carbon precursor 45

2.3.3 CNT Nucleation 47

2.3.4 CNT Growth 52

2.3.5 Growth termination 54

2.4 Quality 56

2.5 Applications 57

2.6 Production at scale 59
2.6.1 production for bulk additive applications 63
2.6.2 Production for advanced materials applications 65
2.6.3 Production for ultimate applications 67
References 69

3 Perspective on FC-CVD limitations 78

3.1 Equilibrium defect concentration 78
3.1.1 Molecular model for Stone-Wales defect 80
3.1.2 Defect energy estimation methods 84
3.1.3 Results 85
3.1.4 Summary 86
3.2 Productivity 87
3.2.1 CNT mass concentration and its factors 87
3.2.2 Bundling timescale via aerosol dynamics 91
3.2.3 Bundle-limited maximum CNT number and mass concentration . 95
3.3 Conclusion 99
References 102

4 Microplasma synthesis of aerosol catalyst nanoparticles 104

4.1 Background on nanoparticle synthesis techniques 105
4.2 Prototype microplasma reactor design, operation, and characterization . 108
4.3 Experimental results 111

4.3.1 Orifice reactor . . . 115
4.4 Particle formation analysis . . . 119
4.4.1 Classical nucleation theory . . . 120
4.4.2 Collision theory . . . 122
4.4.3 Charge-mediated formation mechanism . . . 127
4.5 Numerical model . . . 129
4.5.1 Plasma domain . . . 131
4.5.2 Downstream domain . . . 132
4.6 Process performance and scaling . . . 138
4.6.1 Concentration and diameter Pareto performance . . . 138
4.6.2 Discussion . . . 142
4.7 Conclusion . . . 145
References . . . 146

5 Microplasma reactor process intensification 150

5.1 Introduction . . . 152
5.2 Methods . . . 153
5.2.1 Microplasma reactor system . . . 153
5.2.2 Aerosol characterization . . . 156
5.2.3 Flow simulations . . . 158
5.3 Results and discussion . . . 159
5.3.1 Plasma alignment and precursor conversion . . . 159

5.3.2 Stability of aerosol production . . . 165
5.3.3 Control of aerosol size distribution . . . 170
5.3.4 Physical characterization . . . 175
5.3.5 Improved C vs D Pareto performance . . . 182
5.4 Conclusion . . . 183
5.5 Additional information . . . 185
5.5.1 Particle diffusivity in argon and helium . . . 185
5.5.2 Particle coagulation rate in argon and helium . . . 186
References . . . 188

6 Aerosol carbon nanotube production 191

6.1 Introduction . . . 191
6.2 Experimental methods . . . 194
6.2.1 FC-CVD System design . . . 194
6.2.2 CNT collection . . . 195
6.2.3 Characterization . . . 197
6.3 Studies of CNT growth . . . 203
6.3.1 Injector position and temperature . . . 203
6.3.2 Flow rates and fields . . . 218
6.3.3 Moisture . . . 233
6.3.4 Catalyst Composition . . . 241
6.3.5 Summary of CNT synthesis progress . . . 244

6.4 Additional Information 247

6.4.1 Experimental conditions 247

References 253

7 Summary and outlook **255**

7.1 Summary of Contributions 255

7.2 Outlook 256

References 259

List of Figures

2.1 (A) Structure of single wall carbon nanotube of different chiralities. (B) A graphene lattice, representing an unrolled CNT, showing the lattice basis vectors a_1 and a_2, and (n, m) combinations that define chirality. Copyright 2011 RSC, [7] 39

2.2 Ashby Charts comparing nanostructures and nanostructured materials to traditional engineering materials. Reproduced from [18] 41

2.3 Schematic ball-and-stick model of the SWNT growth stages on a substrate. (A) A graphene cap forms on a catalyst particle. (B) The cap is lifted off and forms a CNT nucleus. (C) The CNT continues to grow.Reproduced from [52]. 48

2.4 Radar charts showing, for various physical properties, the present state of SWCNT synthesis as well as the future requirements for various applications. Copyright 2018 ACS, [5] 60

2.5 Applications map of current and potential CNT applications. The x axis corresponds to the concept of assembly organization, illustrated using scales of purity (presence of catalyst or amorphous carbon) and alignment (incorporating both the multi-scale organization and packing density). The y axis corresponds to the concept of CNT control, illustrated using scales of CNT quality (control of defects) and specificity of characteristics (in approximately increasing order of difficulty and utility). Red annotations indicate the regions of bulk additives, advanced materials, and ultimate applications. These regions roughly correspond to the required portion of ideal CNT properties. 61

2.6 Map of manufacturing methods for research and commercial CNT production methods. Axes are identical to, and described in, Figure 2.5. Production rate, in g/yr, is also provided. Black text indicates a commercial industry-wide production rate, while white text indicates an estimated production rate from a lab-scale process (i.e., continuous operation of lab-scale system). End notes detail the estimation methods. [4]: Commercial MWCNT powder, reported industry-wide capacity. [102]: Commercial SWCNT powder, reported industry-wide capacity. [103]: Commercial high quality SWCNT powders, estimated. [104]: Lab-scale SWCNT forest, estimated. [105]: Lab-scale direct-spinning, estimated. [106]: Commercial wet-spun fibers, estimated. [107]: Lab-scale chiral-specific synthesis, estimated. [108]: Lab-scale SWCNT thin film deposition, estimated. 62

3.1 A) A Stone-Wales (SW) defect in a graphene lattice. B) A 5-8-5 divacancy in a graphene lattice. Reproduced from [4] 80

3.2 A) Diagram of molecular model showing use of C-C bonds in a single orientation as the description for the microstate. B) An example SW defect. 81

3.3 Estimated E_{sw} (A) and E_{di} (B) for each orientation for all chiralities (n, m) below $(25, 25)$. 85

3.4 Estimated total L_{sw} (A) and L_{di} (B) for all chiralities (n, m) below $(25, 25)$. 86

3.5 Calculated mass concentration of CNTs and iron weight percent as a function of CNT diameter and length for a catalyst particle concentration of $N_{cat} = 10^9$ #/cm^3 and a nucleation efficiency of $\eta_{nuc} = 0.1$ Note that SWCNTs typically do not grow with diameter greater than 4-5 nm. To account for multiple walls, the CNT mass concentration can be multiplied by the average number of walls, and the iron weight percent divided by the same. 90

3.6 Calculated effective shortening of CNTs in the aerosol phase due to thermal fluctuations using the worm-like chain model. 93

3.7 Calculated effective collision diameter for CNT diameters of 1, 4, and 10 nm at 1000 °C using the spherical and projected area approximations. . . 94

3.8 The collision kernel β for CNT diameters of 1, 4, and 10 nm at 1000 °C in helium using the spherical and projected area approximations. 95

3.9 The minimum τ_B required for a given L_{CNT} using a growth rate of 100 μm/s or 500 μm/s. 96

3.10 The maximum CNT number concentration, N_{CNT}, can be found as a function of τ_B using β values shown in Figure 3.8 and Equation 3.19. N_{CNT} as a function of τ_B is mapped to L_{CNT} using the relation in Figure 3.9. Solid lines correspond to a growth rate of 100 μm/s, while dashed lines correspond to 500 μm/s. 96

3.11 The maximum CNT mass concentration, ρ_{CNT}, based on N_{CNT} using using β values shown in Figure 3.8. Solid lines were calculated using values of N_{CNT} corresponding to a growth rate of 100 μm/s, while dashed lines correspond to 500 μm/s. 98

3.12 The minimum iron catalyst weight percent assuming a nucleation efficiency of $\eta_{nuc} = \sim 0.1$ and a ratio of catalyst diameter to CNT diameter of $\gamma = 2$. Because the concentration of CNTs does not factor in to this calculation, a single curve is valid for both CNT growth rates and different models for the collision area. 98

4.1 Atmospheric pressure microplasma reactors. (a) Cross-section diagram of the electrode configuration for the orifice-mesh reactor (not to scale). The plasma (purple) is ignited between the stainless steel mesh and tungsten-coated ceramic orifice plate. (b) Diagram of the orifice reactor where the plasma is ignited between tungsten coatings on both sides of the plate and exists within the orifice. Gas flow (He + ferrocene) is from left to right in both (a) and (b). (c) Cross section view of the complete orifice-mesh reactor. The blue housing securely holds the orifice plate and mesh between two stainless steel cylindrical sections. (d) Image looking upstream into the orifice-mesh reactor, showing plasma glow. (e) Schematic of the experimental setup including the ferrocene sublimation chamber, microplasma reactor, and aerosol measurement instrument (SMPS). . . . 109

4.2 (a) Representative particle size distribution measurements from the orifice-mesh reactor operating at 400 sccm He with 23 ppb ferrocene. A lognormal distribution (solid line) is fit to measurements (points) to extract D_g and σ_g. (b, c, d) Temporal performance of the orifice-mesh reactor in terms of (b) particle diameter, (c) concentration, and (d) plasma voltage, operated at 350 sccm He with 85 ppb ferrocene, illustrating the start up transience and stable operation. 112

4.3 (a) Measurements of mean diameter D_g and concentration C of aerosols produced at 400 and 600 sccm He in the orifice-mesh reactor with $d_o = 180\mu$m. Plasma residence times are 9.5 and 6.4 μs, respectively. Labels indicate the ferrocene concentration in ppb. (b) Geometric standard deviation σ_g and (c) yield of particle formation Y_{Fe} for the same experimental conditions. 114

4.4 (a) TEM image of as-collected Fe nanoparticles from the microplasma reactor. (b) Close-up of a single particle showing lattice spacing of 0.19 nm from FFT analysis. (c) Histogram of particle diameters assessed from (a). 116

4.5 (a) An example particle size distribution for the orifice reactor overlaid on a reproduction of Figure 4.2a. All three measurements collected at a flow of 400 sccm He with 25 ppb ferrocene. (a,b,c) Temporal performance of the orifice reactor in terms of (b) particle diameter, (c) concentration, and (d) plasma voltage, operated at 370 sccm He with 31 ppb ferrocene illustrating the start up transience, stable operation, and unstable operation. 117

4.6 (a) Measurements of mean diameter (D_g) and concentration (C) of aerosols produced at flow rates of 225-534 sccm He in the orifice reactor with $d_o = 180\mu$m. Labels indicate the ferrocene concentration in ppb. (b) Geometric standard deviation (σ_g) and (c) yield of particle formation (Y_{Fe}) for the same experimental conditions. 118

4.7 a) Cross section of orifice plate after use showing inner surface of orifice. (b) EDS measurement of inner surface showing elevated Fe compared to interior of the ceramic plate and the tungsten-coated face. 119

4.8 Experimental particle size distribution from [28] (points are measurements, dashed line is lognormal distribution fit) compared to collision model results at same conditions. The difference in total concentrations is likely due to particle losses which are not accounted for in the model. . 125

4.9 Calculated enhancement factors for collision rates as a function of the diameters of the interaction particles (D_j and D_k) with charges j and k at T = 293K. (a) Charge-neutral enhancement factor reaches 11 for a collision between a single charged atom and a 0.6–1.3 nm neutral particle. (b) Same-charge enhancement factor is essentially zero for particles smaller than 100 nm. 128

4.10 Proposed mechanism for iron nanoparticle formation in the microplasma reactor. Ferrocene dissociation creates a vapor of neutral and ionized Fe which collide to form particles. Electrostatic interactions are key for enhancing the formation and growth of small particles while limiting aggregation of large particles. Thus, the majority of growth (of large particles) occurs downstream of the plasma due to the short residence time. Cp is cyclopentadienyl formed during ferrocene dissociation. 130

4.11 Collision model simulation of the plasma domain of the orifice-mesh reactor showing the effect of electrostatic enhancement. (a) Cluster size distribution for representative operating conditions: $\tau_p = 6.4\mu$s, 80 Pa ferrocene ($FeCp_2$), and estimated $\chi_{iz} = 0.001$. Less than 1% of Fe vapor has undergone a collision to form a larger cluster by the end of the plasma domain. (b) Cluster size distribution at the end of the plasma domain can be controlled with τ_p, yet in all cases the concentration of clusters n > 1 is small, and no clusters are larger than n = 10. (c) The Choice of χ_{iz} similarly has negligible effect on the cluster size distribution. 133

4.12 (a) Modeled particle size distribution in the downstream domain of the orifice mesh reactor operating at steady state with 80 ppb ferrocene ($FeCp_2$) and $\chi_{iz} = 0.001$. The time axis is equivalent to the distance downstream of the plasma scaled by the flow velocity. (b) and (c) show only the charged and neutral particles, respectively. (d) Geometric mean diameter, D_g as a function of time in the downstream domain for simulations over a range of χ_{iz} values for 80 ppb ferrocene. The initial growth rate is similar in all cases, and fast relative to unenhanced growth. (e,f) Steady state particle size distributions which use the plasma domain results shown in Figure 4.11b,c as the initial condition to highlight the strong influence of χ_{iz} and lack of sensitivity to τ_p. 135

4.13 Particle size distributions comparing experimental measurements to enhanced and unenhanced model results for ferrocene concentrations of 20, 40, and 80 ppb. χ_{iz} values in each case were calculated based on a total Fe ion concentration of 3.57×10^{15} #/m^3, which was found to minimize the error between experimental and modeled D_g (<3% in all cases). Model particle size distributions are scaled by the experimental yield for visual clarity. 137

4.14 Comparison of the orifice-mesh and orifice reactors developed herein to existing aerosol processes for producing iron nanoparticle catalysts for CNT synthesis, in terms of aerosol concentration and particle diameter produced. See text for complete details and references on literature values. 139

5.1 (a) Schematic of the nanoparticle aerosol synthesis system showing the microplasma reactor and aerosol transfer tube. (b) Image of the complete system. (c) Close-up of the microplasma reactor, looking upstream. . . . 154

5.2 Schematic of the two stage dilution system for SMPS measurement. The inlet flow to the SMPS is regulated by an internal air flow controller. . . 156

5.3 (a) PSD when operating with a sheath flow of 0, 60, and 300 sccm (baseline case). (b-d) Fluid dynamics simulations of the three cases showing streamlines of the flow field and colormap of the N_2 mole fraction. The two horizontal lines on the left side of the domain are the walls of the capillary tube and the white dashed line is the mesh electrode. (e) Representative photos of the microplasma reactor showing a misaligned plasma (left, 0 sccm sheath flow) and aligned plasma (right, 60 sccm sheath flow). Note plasma color changes from red in pure He without sheath flow to purple with addition of N_2 in the sheath flow. 161

5.4 (a) PSDs for $Fe(Cp)_2$ vapor added via the inner flow or sheath flow. CFD simulations of the $Fe(Cp)_2$ mass concentration for the cases of injection via the inner flow (b) and the sheath flow (c). The two horizontal lines on the left side of the domain are the walls of the capillary tube and the white dashed line is the mesh electrode. When $Fe(Cp)_2$ is added to the inner flow it forms a narrow highly concentrated stream within the plasma volume (between the electrodes), coincident with the location of the observed tall deposit on the mesh discussed in Section 5.3.2. When $Fe(Cp)_2$ is added to the sheath flow, the concentration in area directly between the electrodes is significantly reduced. 164

5.5 Changes in aerosol PSD statistics and V_p over time for the five long duration experiments. Values for each experiment are normalized to their initial value to enable visual comparison of the variability. 166

5.6 Non-normalized version of Figure 5.5 including the entire 20 hour run of the $Fe(Cp)_2$ in sheath flow case. 167

5.7 SEM images of mesh electrodes after long duration microplasma runs. (a) Mesh after a 10 hour run of the 60 sccm sheath flow case, in which $Fe(Cp)_2$ was added via the inner flow. (b) Mesh after a 20 hour run in which $Fe(Cp)_2$ is added via the sheath flow. In the first case, the base of the tall deposit is where the microplasma initially contacted the mesh. The structure grew via deposition inside the plasma volume and toward the capillary tube. Material is also conformally deposited on a larger area of the mesh. In the second case, the only deposit is a thin conformal coating on the mesh. 168

5.8 Summary aerosol statistics for a series of experiments varying (a) $Fe(Cp)_2$ flow, (b) microplasma current (I_p) and polarity (+/− HV), (c) transfer tube length (L_{tt}), and (d) He:Ar ratio in the transfer flow. The latter experiments were conducted with cases at three $Fe(Cp)_2$ concentrations, with colors corresponding to those values in (a). The red star indicates the same baseline case in each experiment. All experiments were done with $Fe(Cp)_2$ in the inner flow with the exception of the L_{tt} experiments, which were conducted separately, where $Fe(Cp)_2$ was added via the sheath flow. 171

5.9 Simulated spatial aerosol concentration distribution in the transfer tube (L_{tt} = 100 mm) accounting for particle diffusion for (a) the baseline case with 2600 sccm He transfer flow and (b) 2600 sccm Ar transfer flow. Streamlines indicate flow field. Colormap shows the simulated concentration of an aerosol of 4 nm particles input at unit concentration to the plasma flow and subject to diffusion but not aggregation. The higher diffusivity of particles in He allows greater dispersion of the particles, reducing concentration along the centerline of the reactor. 175

5.10 Aerosol PSDs for the deposition experiments in table 5.1. $Fe(Cp)_2$ was added via the sheath flow rather than inner flow in all experiments to ensure stable operation over the 2 hour deposition period. 176

5.11 (a) χ_B for the transfer tube length experiments. The values at L_{tt} = 100 and 260 mm are calculated using Y_{vol} measured from deposits made at those conditions. For L_{tt} = 140, 180, and 220 mm, a range of χ_B is shown bounded by Y_{vol} in the end cases as no deposits were made at these conditions. (b) Estimated χ_B ranges for all transfer tube length experiments at all values of $Fe(Cp)_2$ flow. The increasing trend of χ_B with D_g is typical of fractal aggregation. 181

5.12 Comparison of the aerosol PSD results discussed in this chapter with those of Chapter 4 and other existing processes. See Chapter 4 for complete details and references on literature values. 183

5.13 Coagulation kernel for like-sized iron particles at standard conditions. . . 187

6.1 Examples of typical FC-CVD product at different periods in the system development. (a) A highly-defective isolated tuft on a smooth silicon wafer collected in July 2019. (b) An early P-series sample from July 2021 showing a thin cobweb of CNTs, covered in small iron and carbon particles, collected on a cellulose filter (the lobed micron-scale structure). (c) A recent sample from July 2023 showing thick and cohesive layers of CNTs as evidenced by the peeling and tearing of the top layer. The mottled appearance is from the structure of the sintered microparticle membrane filter below. (d) Close-up image of the corner of the tear shown in (c) to highlight the cohesive and mat-like nature of the CNT deposit. 193

6.2 Photo of the complete FC-CVD reactor system. The furnace in the foreground on the right contains the main CVD process tube, with the microplasma reactor to its left. In the left background is the gas distribution system and mass flow controllers (MFCs). In the right background is the scanning mobility particle sizer (SMPS). 196

6.3 Schematic of the microplasma reactor and FC-CVD reactor inlet. The microplasma is identical to that described in Chapter 5, with the transfer tube now referred to as the injector. Typical values for the inner, sheath, injector, and furnace flows are reported in the text, with total flows in the range 4000–8000 sccm. 197

6.4 (a) Modified 1-inch ball valve used as load lock chamber for small filters. An additional large port with KF-25 stub was attached to the front side side and a custom port on the back side was connected to a gas line with two-way valve to either a roughing pump or the upstream side of the ball valve. When the main ball valve is closed (and process flow directed through the bypass line below), the cylindrical volume within the ball is accessible through the front port and can be pumped down or purges via the rear line. (b, c) The 6 mm version of the cylindrical filter holder. Subsequent versions of the filter holder include an o-ring recessed into the outer diameter to ensure a seal with the ball valve's ball. (d) the filter holder can be inserted into the ball of the ball valve through the front port. 198

6.5 (a) The outlet side of the CVD furnace showing the gate valve and KF-50 load lock chamber. The operation and capability of this system is identical to the ball valve load lock chamber. (b) The custom KF-50 filter holder, designed to take the place of a centering ring in a normal KF-50 connection. The filter holder shown here contains a 16 mm insert, with 21 and 33 mm inserts available as well. (c) Example CNT deposits on sintered silver filters. The two upper left deposits were made using the 9 mm filter holder, the upper right was made using the 11 mm filter holder, The upper row were all made using the ball valve load lock chamber with 9, 9, and 11 mm filter holders, respectively. The lower right deposit was made using the 16 mm filter holder for the KF-50 load lock chamber. . . 199

6.6 Raman characterization of samples P96-P116 showing the influence of injector position and furnace temperature. Legend values specify the injector position. 208

6.7 Characterization of samples P286–298 showing the influence of injector position at 950 and 1000 °C surface set points. A negative injector position is deeper into the furnace. At each temperature, the experiment was run from -20 to -50 mm positions, with a second sample taken at -20 mm at the end (the unconnected points). 210

6.8 Characterization of samples P287, P294, P321–323 showing the influence of furnace set point temperature at an injector position of -30 mm. . . . 211

6.9 Characterization for Samples P427-441 showing CNT growth for injector positions -25 to -80 mm and ferrocene flow rate of 37.5, 75, and 150 sccm. All cases are at 1000 °C and the plasma housing at -15 mm, with injector positions. 214

6.10 SEM images of deposits made at -80 mm injector position and three levels of ferrocene concentration. 216

6.11 RBM portion of the Raman spectra of the three ferrocene flow rate cases overlaid at each injector position. Each spectra has been normalized to its respective G peak intensity. While all show a strong set of peaks in the 200–250 cm^{-1} range (~0.93–1.17 nm diameter), only the 75 and 150 sccm ferrocene cases show RBM peaks in the 125–175 cm^{-1} range, indicating larger CNTs with diameter ~1.35–1.98 nm. The intensity of these peaks is highest for the 150 sccm ferrocene case, indicating an upward shift in the diameter distribution of the CNTs as would be expected for a larger catalyst particle size distribution. 216

6.12 RBM portion of the Raman spectra of the five injector position cases overlaid for each ferrocene flow rate. Each spectra has been normalized to its respective G peak intensity. While it is expected that the mean catalyst particle size will increase with injector length, due to increased aggregation, the effect of this on the CNT diameter distribution, as indicated by Raman RBM intensities, is insignificant. 217

6.13 Characterization of Samples P369–373 and P375 showing the influence of injector flow rate of CNT production. Not shown, the 780 sccm case has a production rate of 2000 μg/hr. 219

6.14 CFD simulations of the microplasma housing, injector, and furnace entry for injector flows of 780–1530 sccm, corresponding to Samples P369–373 and P375. X flow velocity is left to right, with negative value indicating back flow. Stagnant flow being to develop just inside the injector tip at 1080 sccm, with negative flow occurring at 930 sccm and even moreso at 780 sccm. Plots of ethylene molar concentration (equal to 0.017 in the incoming furnace flow) show the back diffusion of ethylene into the injector, exacerbated by the low or negative flow velocity at lower injector flow rates. 221

6.15 Characterization of Samples P399-410, parameter sweeps of injector flow rate at injector length of 0, 10, and 20 mm. 223

6.16 CFD simulations of the microplasma housing, injector, and furnace entry for injector flows of 780–1530 sccm, corresponding to Samples P369–373 and P375. X flow velocity is left to right, with negative value indicating back flow. Stagnant flow being to develop just inside the injector tip at 1080 sccm, with negative flow occurring at 930 sccm and even moreso at 780 sccm. Plots of ethylene molar concentration (equal to 0.017 in the incoming furnace flow) show the back diffusion of ethylene into the injector, exacerbated by the low or negative flow velocity at lower injector flow rates. 224

6.17 Characterization of Samples P414-419 showing the influence of furnace flow rate on CNT growth. A high injector flow, 2028 sccm, was used to ensure an optimal fow field at the injector outlet. 226

6.18 CFD simulations of the microplasma housing, injector, and furnace entry for furnace flows of 1007–29500 sccm. X flow velocity is left to right, with negative value indicating back flow. 228

6.19 Direct aerosol mean diameter and concentration measurements for conditions analogous to the high plasma flow rate experiments. 230

6.20 Characterization of Samples P420–426 showing growth results for the high plasma flow recipes. Injector and furnace flow rates increase in concert with the plasma flow rate to qualitatively maintain the flow field. 232

6.21 RBM portion of the Raman spectra for different total plasma flow rates. The left plot shows those with constant 150 sccm ferrocene flow rate. The right plot shows those with proportionally increasing ferrocene flow rate (150, 200, 250, 300 sccm for 900, 1200, 1500, 1800 sccm total plasma flows). In the former case, increasing the total plasma flow reduces the intensity of large-diameter RBM peaks in the 125–175 cm^{-1} range, while increasing the intensity of small diameter peaks in the 200–250 cm^{-1} range. There is some variation but no similar trend in the latter case. . . 234

6.22 TEM images of sample P43 from March 2022 indicating small diameter SWCNTs as well as significant amorphous carbon and carbon-coated iron particles. 235

6.23 Characterization of samples P117-P130 showing the influence of moisture added to the furnace flow. Moisture is added by bubbling helium through water at 20 °C. In the left column the abscissa is the flow rate of moist helium in sccm. The right column abscissa is the measure moisture level at the system outlet. 237

6.24 Characterization of samples P355-368 and P376-398 showing the influence of moisture added to all four gas flows. Moisture is added by bubbling helium through water at 20 °C. In the left column the abscissa is the flow rate of moist helium in sccm. The right column abscissa is the measure moisture level at the system outlet. 239

6.25 SEM images of sample P394, a baseline case with no moisture addition (average moisture level of 60 ppmv), and P398 with 150 sccm wet helium via the inner flow (average moisture level of 560 ppmv). P398 has a 50% lower mass production rate and is visibly more covered in inactive catalyst and non-CNT carbon. 240

6.26 Characterization of samples P280-P284 synthesized with varying hydrogen flow to the plasma and high voltage polarity. 242

6.27 Overview of all P series experiments. Those experiments mentioned in earlier sections of Chapter 6 are indicated in color. Missing data points indicates an inability to characterize those samples, e.g., insufficient mass to measure a production rate. 245

6.28 Multi-metric scatter plots for all P series experiments. Those experiments mentioned in earlier sections of Chapter 6 are indicated in color. Missing data points indicates an inability to characterize those samples, e.g., insufficient mass to measure a production rate. Tracing along the boundary of points defines the range of Pareto-optimal performance for those two metrics. 246

1. Motivation and scope

1.1 Motivation

The field of carbon nanotube (CNT) synthesis has advanced steadily since seminal work in Japan in the late 1980's and early 1990's [1, 2, 3, 4], driven by an interest in discovering and exploiting the remarkable thermal, electrical, and mechanical properties of CNTs. CNTs are hollow cylindrical molecules with diameters of 1—10 nm and lengths typically from 1—1000 um. The specific strength and electrical conductivity of an individual CNT can be an order of magnitude higher than steel and copper, respectively, yet common crystallographic defects limit their real-world performance, and translating these properties to the macro-scale requires highly ordered assemblies [5]. After three decades of intense research activity, attention is shifting to mass production to meet an increasing range of commercial applications, lead by the production of thousands of tons of multi-wall CNT powders for rechargeable batteries, coatings, rubbers, and plastics [6]. The broad range of structural morphologies (and resulting material properties) that defines the space of CNT materials, as well as a variety of synthesis techniques predisposed to access different areas of this space, indicates potential suitability to a wide range of applications. Additional technically proven applications such as thin film electronics and interlaminar composite reinforcement are only limited by cost, while the promise of high performance structural composites, conductors, and microelectronics dependent on

improved synthesis capabilities continues to drive fundamental research [7].

Floating catalyst chemical vapor deposition (FC-CVD) is an especially flexible production technique, with different implementations able to create high and low quality CNT powders, thin films, and directly spun fibers. FC-CVD utilizes a high temperature continuous flow gas reactor in which an aerosol of nm-scale catalyst particles reacts with a gaseous carbon precursor (e.g., acetylene, ethanol or methane) to grow CNTs [8]. The catalyst particles are typically forming in situ by the thermal decomposition of a gaseous catalyst precursor (e.g., ferrocene to form iron particles) [9]. Lab-scale reactors which operate at relatively low CNT concentration can produce high quality CNTs which remain as isolated aerosols throughout the growth process. The highest quality processes tend to use highly stable carbon precursors such as carbon monoxide to prevent non-catalytic decomposition [10] or add oxygen (in the form of moisture or an alcohol precursor) to etch away amorphous carbon [11]. This CNT aerosol can be collected as a bulk powder, or carefully deposited to form thin film coating [10, 12]. Production rates can be increased by several orders of magnitude by using a higher concentration of catalyst particles and a more reactive carbon precursor. Yet these changes result in a higher content of catalyst material (because not all catalyst precursor forms particles, and not all particles are catalytically active), larger and more defective multi-wall CNTs and amorphous or graphitic carbon overcoating. The aerosol bundling of CNTs in high concentration processes is also double-edged as it limits the ability to precisely control CNT organization yet enables the direct winding of CNT fibers (direct spinning) which can simplify manufacturing and handling [13, 14, 15]. Similar trade-offs between scale and quality occur for other production methods.

1.2 Scope

Ultimately, while FC-CVD is at present the process with the best balance of CNT production rate and quality, a processes which significantly improves upon both of these metrics is needed in order to realize the ultimate potential of CNT applications. Given the incomplete understanding of CNT nucleation and growth in general, and FC-CVD in particular, it is not obvious how to define a fundamental performance ceiling for FC-CVD, yet it is clear that current systems experience a trade-off between productivity and the quality or control of CNT properties. Understanding the physical basis for these relationships and the influence of reactor conditions on them is key for the development of improved synthesis systems which can improve upon, or sidestep entirely, these trade-offs.

To this end, this thesis describes work to advance our understanding of two key challenges:

1. Given the critical role of the catalyst particle, the aerosol dynamics of catalyst particle formation and particle properties set an upper limit in CNT production rate and strongly influence CNT properties. What physical processes govern aerosol particle formation, can these processes be influenced to increase particle concentration and reduce size, and how can this be accomplished in a scalable and reliable system?

2. The dual use of the CVD reactor for catalyst formation and CNT growth results in a tight coupling of these processes which prevents independent optimization and limits reactor design and scale. How do the reactor conditions influence each stage of the CNT synthesis process, to what extent is it possible to decouple each stage such that these conditions can be independently controlled and optimized?

In order to interrogate these questions, a novel FC-CVD reactor system, utilizing a microplasma reactor for aerosol catalyst particle synthesis, was developed. Experimental use of this system was combined with theory and simple models to produce general insights into the governing processes, as well as to iteratively improve the design and performance of the microplasma and FC-CVD reactors. The results of this effort are organized into the following chapters:

Chapter 2, Background, describes the structure and promising nanoscale properties of CNTs, the difficulty associated with realizing these properties in macroscopic assemblies, and the current state of understanding the CNT synthesis process, with specific attention to SWCNTs and aerosol CVD synthesis. It also describes a framework for thinking about various applications of CNTs and their associated requirements in terms of CNT characteristics and production.

Chapter 3, Perspective on FC-CVD limitations, presents a simple macroscale model of CNT production rate for a FC-CVD system to support a perspective on the most important process metrics and considerations for assessing its productivity and performance. Expanding on the preceding motivation, this perspective is used to develop the specific research questions and goals of the subsequent thesis chapters.

Chapter 4, Microplasma synthesis of aerosol catalyst nanoparticles, presents an analysis of the driving forces behind typical particle formation processes to motivate the use of a microplasma to enhance this process, and reports on the design, development, and performance of a microplasma reactor. A charge-mediated formation mechanism is proposed to explain the enhanced formation of small particles, and a numerical simulation of this mechanism is shown to have good agreement with experimental measurements.

Chapter 5, Microplasma reactor process intensification, reports on a series of studies undertaken with a subsequent version of the microplasma reactor which demonstrate the benefits and limitations of the process for high-throughput and scalable particle synthesis.

Chapter 6, Aerosol carbon nanotube production, describes the development of a carbon nanotube synthesis system via the integration of the microplasma reactor for catalyst particle synthesis with a FC-CVD reactor. It also describes the process insights and iterative system development informed by a large set of experimental and theoretical work using the system.

Chapter 7, Summary and outlook, summarizes the main contributions of this thesis and the author's outlook on key remaining questions around CNT synthesis and potential avenues for future process development.

References

[1] Morinobu Endo. "Grow carbon fibers in the vapor phase". In: *Chemtech* 18.9 (1988), pp. 568–576.

[2] Gary G Tibbetts. "Vapor-grown carbon fibers: status and prospects". In: *Carbon* 27.5 (1989), pp. 745–747.

[3] Sumio Iijima. "Helical microtubules of graphitic carbon". In: *nature* 354.6348 (1991), p. 56.

[4] Sumio Iijima and Toshinari Ichihashi. "Single-shell carbon nanotubes of 1-nm diameter". In: *nature* 363.6430 (1993), pp. 603–605.

[5] Agnieszka Lekawa-Raus et al. "Electrical properties of carbon nanotube based fibers and their future use in electrical wiring". In: *Advanced Functional Materials* 24.24 (2014), pp. 3661–3682.

[6] Rahul Rao et al. "Carbon nanotubes and related nanomaterials: critical advances and challenges for synthesis toward mainstream commercial applications". In: *ACS nano* 12.12 (2018), pp. 11756–11784.

[7] M F Volder et al. "Carbon nanotubes: present and future commercial applications". In: *Science* 339.February (2013), pp. 535–540. DOI: 10.1126/science.1222453. URL: https://doi.org/10.1126/science.1222453.

[8] Vincent Jourdain and Christophe Bichara. "Current understanding of the growth of carbon nanotubes in catalytic chemical vapour deposition". In: *Carbon* 58 (2013), pp. 2–39.

[9] Anna Moisala et al. "Single-walled carbon nanotube synthesis using ferrocene and iron pentacarbonyl in a laminar flow reactor". In: *Chemical Engineering Science* 61.13 (2006), pp. 4393–4402.

[10] Antti Kaskela et al. "Highly individual SWCNTs for high performance thin film electronics". In: *Carbon* 103 (2016), pp. 228–234.

[11] Albert G Nasibulin et al. "Carbon nanotube synthesis from alcohols by a novel aerosol method". In: *Journal of Nanoparticle Research* 8.3-4 (2006), pp. 465–475.

[12] Yongping Liao et al. "Direct Synthesis of Colorful Single-Walled Carbon Nanotube Thin Films". In: *Journal of the American Chemical Society* 140.31 (2018), pp. 9797–9800.

[13] Ya-Li Li, Ian A Kinloch, and Alan H Windle. "Direct spinning of carbon nanotube fibers from chemical vapor deposition synthesis". In: *Science* 304.5668 (2004), pp. 276–278.

[14] TS Gspann, FR Smail, and AH Windle. "Spinning of carbon nanotube fibres using the floating catalyst high temperature route: purity issues and the critical role of sulphur". In: *Faraday discussions* 173 (2014), pp. 47–65.

[15] Fiona Smail, Adam Boies, and Alan Windle. “Direct spinning of CNT fibres: Past, present and future scale up”. In: *Carbon* 152 (2019), pp. 218–232.

2. Background

This chapter provides the necessary background on the material properties and synthesis of carbon nanotubes to understand the motivation and work developed here. It uses text adapted and abridged from Chapters 2 and 3 of the author's S.M. thesis [1], which the reader is referred to for additional background information:

Sawyer, W. J., Toward improved manufacturing of carbon nanotubes by microplasma synthesis of catalyst nanoparticles, S.M. Thesis, Massachusetts Institute of Technology, Department of Mechanical Engineering, 2020

2.1 Carbon nanotubes

The carbon nanotube (CNT) is an allotrope of carbon which possesses remarkable properties as a result of its molecular structure. A CNT can be conceptually envisioned as a strip of graphene (a two-dimensional hexagonal lattice of sp^2 hybridized carbon atoms) that has been rolled to form a seamless cylindrical shell (Figure 2.1.A). Single-walled CNTs (SWCNTs), comprised of a single cylindrical shell, have been synthesized with diameter ranging from 0.4 nm [2] to 7 nm [3], although more typically in the range of 1 to 4 nm [4]. Double-walled, few-walled, or multi-walled CNTs (MWCNTs) have multiple concentric shells, with inner diameters typical of SWCNT and outer diameter typically up to 20 nm [4]. CNT length is typically on the order of 100 nm to 100 μm,

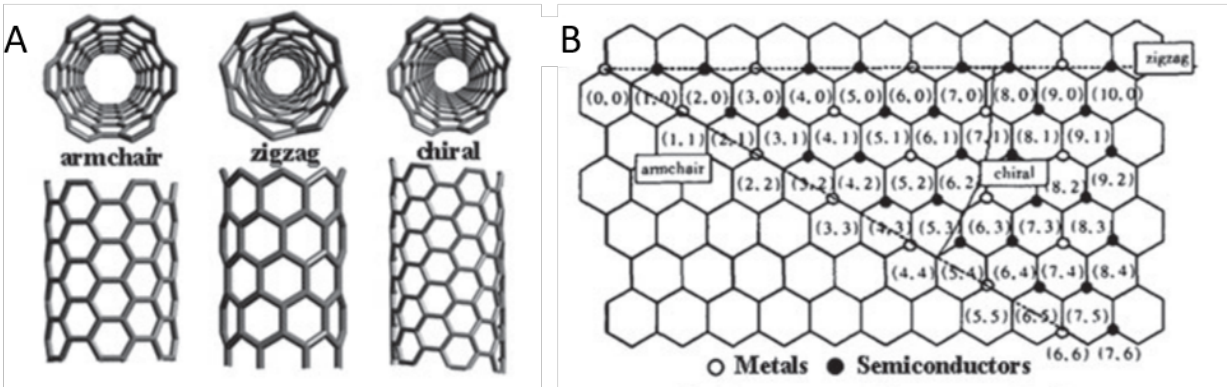

Figure 2.1: (A) Structure of single wall carbon nanotube of different chiralities. (B) A graphene lattice, representing an unrolled CNT, showing the lattice basis vectors a_1 and a_2, and (n, m) combinations that define chirality. Copyright 2011 RSC, [7]

with synthesis of centimeter-long CNTs possible under special conditions [4].

The structure of a CNT is also defined by the chirality - the orientation of the hexagonal lattice relative to the axis of the cylinder. Chirality can be described by the chiral angle, which, due to hexagonal lattice symmetry, varies from 0 to 30 degrees. It is often described by a lattice vector, in terms of the (n, m) combination of lattice basis vectors a_1 and a_2, that define the circumference, thus specifying both chirality and diameter (Fig. 2.1.B). The special cases of chiral angle of 0° $(n, m = 0)$ and 30° $(n, m = n)$ are called "zigzag" and "armchair" while intermediate angles are simply referred to as chiral (Figure 2.1.A) [5]. The dominant effect of chirality is in determining the band gap, and thus electronic properties. Those with $n - m = 3k$ (for integer k, including 0) are metallic (zero band gap) while all others are semiconducting (band gap of 0 to 1 eV) [6].

2.2 Macroscopic assemblies

A carbon nanotube, like other single crystals or nanomaterials, derives its remarkable properties from a low defect concentration and atomic-level order. This level of order

	CNT	CNT assembly	Highest current material
Thermal cond. (W/mK)	3500 [8]	380 [9]	398 (Copper) [10])
Ampacity (A/cm^2)	10^9 [11]	10^8 [12]	10^6 (Copper) [12]
Young's Modulus (GPa)	1000 [13]	120-200 [9]	350 (Carbon fiber) [14]
UTS (GPa)	100 [13]	1-3 [9]	5.5 (Carbon fiber) [14]
Electrical cond. (MS/m)	Quantum [15]	5 [9]	60 (Copper) [16]

Table 2.1: A comparison of the material properties of ideal CNTs, the highest attained properties for macroscale assemblies, and those of common engineering materials.

must be maintained throughout an assembly in order to extend these properties to longer length scales. Inevitably, bulk properties are significantly reduced through the introduction of interfaces, voids, misalignment, and impurities during assembly. CNTs are uniquely poised to overcome this scaling challenge as their individual properties already extend to the macro-scale along one dimension, due to their high aspect ratio and length. However, challenges of entanglement, alignment, anisotropy, chemical bonding, packing, and impurities limit the bulk properties of current CNT assemblies.

A CNT assembly, here defined as a macroscopic, cohesive collection of CNTs which can be considered as a single object or mass, may be a final product, or further processed or combined with other materials. Actual assemblies must be characterized not only in terms of the properties of the individual CNTs (length, wall number, quality, diameter, chirality) but also in their nano- to macro-scale morphology and the presence of impurities - typically amorphous carbon and excess catalyst material from the synthesis process. Even at low packing density, the high aspect ratio of CNTs limits the ability to change nano-scale alignment and morphology, and renders sorting or selecting CNTs based on length, diameter, or chirality impractical. Post-processing to increase alignment, densify, and remove impurities are more effective, yet still limited by high tortuosity and closed voids as packing density increases. High alignment at the individual scale requires self-assembly or controlled growth methods. Thus, in addition to controlling the individual CNT properties, the synthesis method is coupled to the

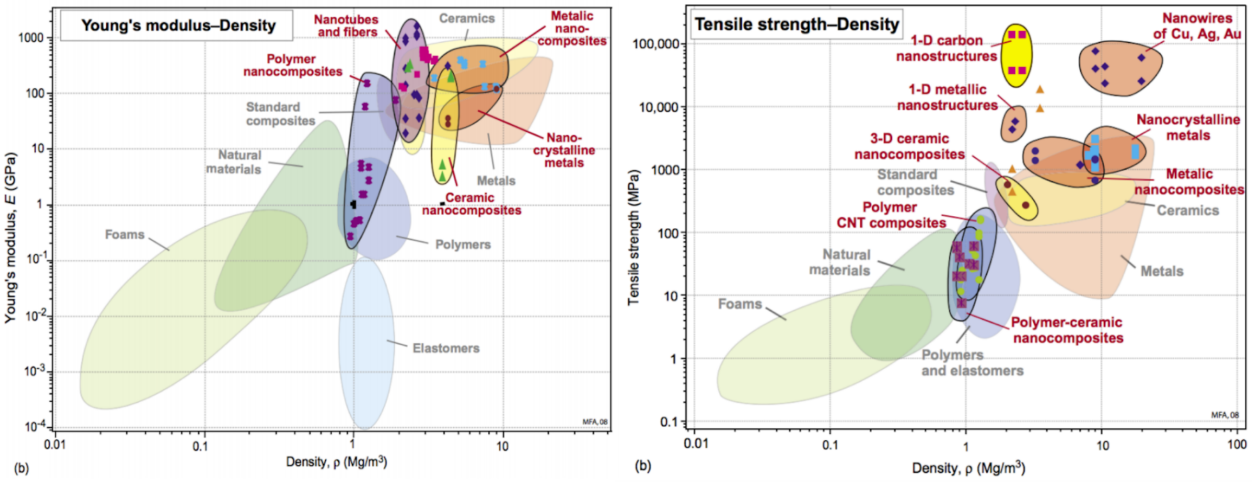

Figure 2.2: Ashby Charts comparing nanostructures and nanostructured materials to traditional engineering materials. Reproduced from [18]

assembly morphology and ultimate assembly performance [17].

A high level view suggests that macroscopic properties are bounded by the individual properties, while the properties of the assembly determine the extent to which these are realized. Additionally, secondary effects of the individual CNTs, such as the dependence of packing density on the diameter distribution, or that of stress transfer on length, may also be important. Comparing the best reported properties for CNTs and assemblies (2.1), a significant opportunity for improvement is apparent.

CNT fibers, a common type of assembly, are macroscopic bundles with a morphology similar to yarn. Fibers are most commonly formed in a single step 'direct spinning' process where a fiber is drawn directly out of a dense aerosol of growing CNTs. Alternatively, CNTs from any synthesis technique can be made into solution and a more traditional wet-spinning process utilized [19]. Theoretically, for a fiber to have ultimate properties, the individual CNTs must be long, defect free, narrow, and of correct chirality [19], and the assembly must be dense, well aligned, and free of impurities [20]. Practically, it is impossible to create such an assembly with current methods and knowledge. The best examples were formed in processes which optimize the trade-offs between

individual properties and assembly morphology with current synthesis and processing methods for the desired properties.

2.3 Synthesis

The earliest CNTs were discovered during the synthesis of fullerenes in arc-discharge experiments [21]. Here, an electrical arc is ignited between two graphite electrodes in a low pressure inert atmosphere. The arc vaporizes carbon, which subsequently condenses into a range of carbon species. MWCNTs were found deposited on the carbon electrode [21]. The first single-wall CNTs were formed similarly using an electrode composed of a mix of cobalt and graphite powders. The SWCNTs were observed to terminate at a cobalt nanoparticle, and it was shown that the nanoparticle served to catalyze their growth [22]. Over the intervening decades, a number of synthesis techniques have been developed with a wide variation in terms of the energy source, material inputs, reactor design, and product characteristics. Yet, almost all share the same fundamental process steps at the atomic scale. A nano-scale metal catalyst particle is formed which interacts which reacts with gas-phase carbon (whether pure carbon which has been vaporized at high temperature, or carbon-containing compounds with sufficiently high vapor pressure at more reasonable temperatures) at elevated temperature. The carbon is deposited onto or into the particle and migrates to the growing nanotube, the dimensions of which are templated (with varying precision) by the catalyst particle. For each individual CNT, this process can be broken down into four stages: catalyst formation, CNT nucleation, CNT growth, and growth termination. The diversity of synthesis processes is evidence of the many macroscopic systems which can produce the appropriate nano-scale conditions for each of these stages.

2.3.1 Catalyst generation

The earliest CNTs were discovered during the synthesis of fullerenes in arc-discharge experiments [21]. Here, an electrical arc is ignited between two graphite electrodes in a low pressure inert atmosphere. The arc vaporizes carbon, which subsequently condenses into a range of carbon species. MWCNTs were found deposited on the carbon electrode [21]. The first single-wall CNTs were formed similarly using an electrode composed of a mix of cobalt and graphite powders. The SWCNTs were observed to terminate at a cobalt nanoparticle, and it was shown that the nanoparticle served to catalyze their growth [22]. An alternative and less energy intensive method is chemical vapor deposition (CVD), in which the carbon is sourced from the decomposition of a gaseous carbon precursor and is again catalyzed by metal nanoparticles. This process is inherently more scalable than synthesis by arc discharge, occurs at lower temperatures, and allows for more control in morphology and structure. Various implementations of CVD quickly became the most common methods in research settings, and continue to dominate academic and commercial activity [23, 24].

A wide range of materials have been found to catalyze CNT growth. Typical processes use transition metal nanoparticles of 1 to 10 nm, most often iron. While the melting point of bulk iron, $T_m = 1538°C$ [25], is above most synthesis temperatures (typically 600–1300°C) [26], the melting point of nanoparticles, due to diameter-dependent melting point depression, may be within this range. For example, an unsupported iron particle has $T_m = 620°C$ at 1.6 nm, and $T_m = 500°C$ at 1.1 nm [27], thus a population of catalyst particles may be solid, liquid, or a combination. The potential dependence of CNT nucleation and growth rate on catalyst phase, the typically wide size dispersion of nanoparticles, and strong dependence of T_m on diameter suggests a complex interaction, and a complete understanding of the process remains elusive [27]. Other catalyst

materials may be used to tailor the process for specific goals, although typically have lower catalytic activity. Alkali metals can be used to lower the synthesis temperature requirement[26], high-temperature tungsten-cobalt alloys can control chirality by lattice matching with their crystal structure [28], and nanodiamonds can produce a pure carbon product with no metal impurities [29].

Classes of CVD systems can be delineated by their method for introducing the catalyst particles to the reactor. The catalyst may be prepared on a support material, called substrate growth, by casting a colloidal suspension of pre-made particles [30], from the dewetting of a thin film of catalyst material [31], or the decomposition of a metal-containing compound [32]. These methods can result in the formation of a vertically aligned nanotube array (VANTA) called a forest, as the direction of growth is constrained by the substrate and neighboring nanotubes.

Alternatively, the catalyst particles may be in the form of an aerosol — called floating catalyst or aerosol CVD. The catalyst particles may be generated inside the reactor, called coupled catalyst generation, through vapor-phase chemical reactions. Most commonly, an organometallic vapor (e.g. ferrocene) is introduced to the reactor. Upon heating, its thermal decomposition results in a supersaturated metal vapor which condenses into an aerosol of metal nanoparticles via homogeneous nucleation [33]. An aerosol of catalyst particles may also be generated outside the reactor, called decoupled catalyst generation, and the aerosol subsequently introduced into the CVD reactor. These processes also rely on condensation of metal vapor, which can be created through methods such as arc discharge [34], spark discharge [35], or hot wire generation [36].

At low catalyst concentration, aerosol CVD allows for synthesis of isolated CNTs without influence from a substrate or neighbors. At higher concentrations, the high aspect ratio of CNTs induces the in-flight assembly of a loosely connected network called an aerogel. This interaction effects the growth process of individual CNTs as well as

the morphology of the final product. While aerogel formation is a critical step in the direct spinning process, and so far unavoidable at high production rates, the additional interactions during synthesis can limit the growth process of individual CNTs and lock in undesirable nanoscale alignment and impurities. Aerogel formation (and direct spinning) often relies on the addition of a promoter, typically S and less often Se, to achieve the needed CNT density. The promoter is thought to increase the nucleation efficiency of coupled catalyst generation [37], resulting in an increased concentration of catalyst particles thus improving yield. It may also play a role in controlling CNT nucleation, although this effect is poorly understood [38].

Fluidized bed reactors, a third form of CVD process, uses a fluidized bed of μm- to mm-scale support particles which are coated in catalyst nanoparticles [39, 15]. While theoretically a more scalable implementation of substrate growth, it appears most suitable for high production rate of low quality MWCNTs as it has proven difficult to maintain the highly controlled environment needed for SWCNT synthesis [39, 5].

2.3.2 Carbon precursor

A wide range of carbon precursors have been used for CNT growth, including acetylene, methane, carbon monoxide, ethylene, benzene, camphor and ethanol [40]. Typically the carbon precursor is introduced to the reactor as a low concentration gas, with carbon concentration at or below 3 at% for high production rate aerosol CVD processes [37]. Most reactors operate at atmospheric pressure, although promising results have been shown for aerosol CVD at high [41] and on substrate CVD at low pressures[42]). The balance of the atmosphere is typically hydrogen, an inert gas (helium, nitrogen, or argon), or a mixture of the two [37]. The specific ratios or flow rates of gases, as well as the temperature and other conditions, is referred to as a growth recipe.

Process temperature typically ranges from 600–1300°C. The reactivity of the precursor must be balanced with the process temperature and other parameters to increase the conversion efficiency of carbon into CNTs and limit formation of soot or other byproducts [43, 26]. Carbon may be directly incorporated into the CNT by catalytically decomposing the carbon precursor on the catalyst particle, as in low-temperature processes with highly reactive precursors, e.g. acetylene. In higher temperature processes, typical of most aerosol CVD, thermal pyrolysis of the carbon precursor may form intermediaries which are then incorporated [37]. These reactions are complex and produce a range of intermediaries, not all of which are catalytically active. Hydrogen may play a role in buffering or biasing these reactions, although understanding of this effect is limited as most basic studies of thermal pyrolysis are done under vacuum or an inert atmosphere [44, 45]. Experiments applying a thermal pretreatment to a range of common precursors and measuring the resulting intermediaries found that the presence of alkynes had the strongest influence on CNT growth rate, suggesting a universal growth mechanism based on the formation of alkyne intermediaries [46, 47].

The carbon conversion efficiency, from carbon precursor to solid carbon or carbon nanotubes, is often quite low (0.1 to 1%) for most carbon precursors, indicating that the majority of the precursor is either unreacted, or forms unreactive intermediaries that leave the system as a gas. The high carbon conversion of some synthesis methods can be attributed to the control of this process. A carbon conversion efficiency of up to 61% has been shown for forest growth using a simple alkyne, acetylene, as the initial carbon precursor. A low pressure, cold-wall system was employed to limit thermal pyrolysis [42]. Increases in conversion efficiency with other carbon precursors can often be traced to biasing the pyrolysis reaction towards production of alkynes. A study of the decomposition of ethanol using CHEMKIN, a chemical kinetics model [48], informed changes in the flow conditions to maximize pyrolysis and the partial pressure of acetylene,

resulting in an increased CNT forest growth rate [49]. High carbon conversion and purity is also seen in high temperature aerosol CVD processes with methane, and is highly dependent on the partial pressure of hydrogen. Industrial production of acetylene is done by 'cracking' methane at high temperature (>1100°C) in a hydrogen-rich atmosphere, thus it reasons that hydrogen plays a similar role in biasing the decomposition of methane in the CVD process [50].

As with the selection of a catalyst material and form, there is no clear best carbon precursor. Good and bad examples can be found for any precursor, and the ultimate capability of a synthesis process is determined by the correct matching of these factors, not optimizing any individual one.

2.3.3 CNT Nucleation

In just the right conditions, the deposition of carbon on a catalyst particle begins to form a graphitic cap (Figure 2.3). While sp^2-bonded carbon typically forms a planar sheet, bonds between the edge of the cap and atoms of the particle bend the sheet. Defects in the form of pentagons and heptagons can form which minimize the energy of this curved surface and lock in a hemispherical shape. Once this hemisphere has formed, the lowest curvature, and thus most favorable, growth configuration is cylindrical, not spherical. As the edge of the cap continues to grow, its center, which only weakly interacts with the particle, is pushed away and a hollow cylinder begins to form [51]. The growth front remains on the catalyst particle, and the diameter of the tube is generally fixed once growth begins.

The initial cap dimensions are related to the curvature of the catalyst particle, thus the diameter of the resulting CNT is generally related to the diameter of the catalyst particle. On iron catalyst particles less than 2 nm in diameter, the CNT diameter is

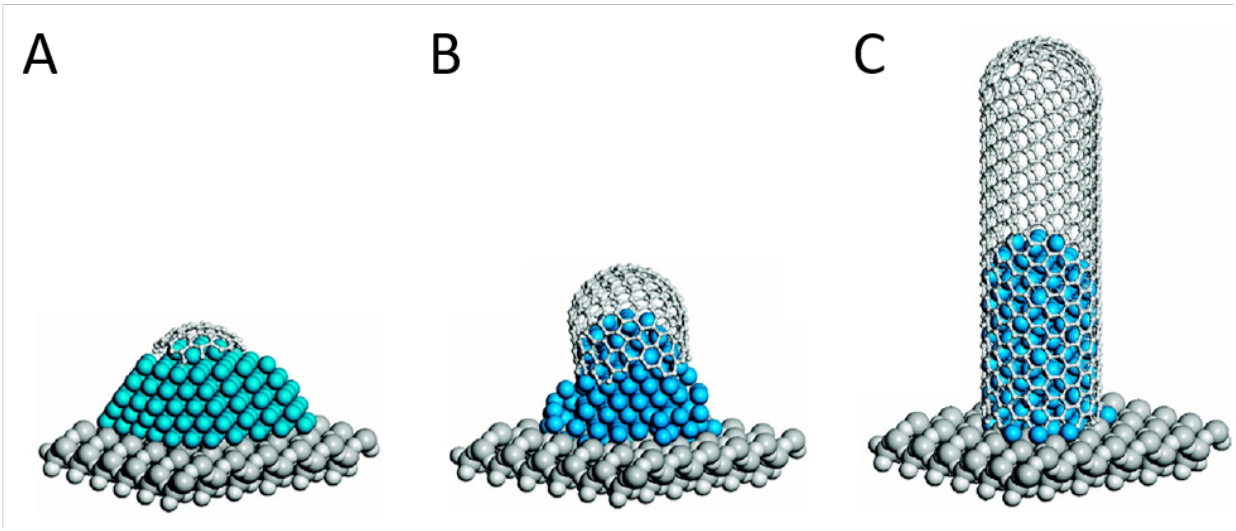

Figure 2.3: Schematic ball-and-stick model of the SWNT growth stages on a substrate. (A) A graphene cap forms on a catalyst particle. (B) The cap is lifted off and forms a CNT nucleus. (C) The CNT continues to grow.Reproduced from [52].

equal to, or slightly larger than that of the particle. This is called tangent growth, as the surface of the CNT is tangent to the equator of the particle [53]. For particles greater than 2 nm, a second growth mode, perpendicular growth, is also seen. In this case, the cap and hemisphere are of smaller diameter than the particle, and during growth the edge of the nanotube extends from the particle at a high or perpendicular angle (no longer tangent). In these cases, the diameter of the tube is controlled less strongly by the particle diameter [54]. The growth mode may be controlled by the carbon content of the particle: a higher carbon fraction decreases the wettability between the catalyst and nanotube, biasing towards perpendicular growth (i.e. a high contact angle) [55]. The contact area between catalyst and CNT is larger for tangent growth, which results in a more stable configuration and may provide increased opportunities for annealing of defects during growth [56]. As the synthesis conditions determine the growth mode, the ratio of CNT diameter to catalyst particle diameter is generally fixed, ranging from 1:1 [57] up to 1:1.6 [58] for FC-CVD in which the catalyst particles are formed in situ, thus the catalyst diameter is considered an important mechanism for controlling, but

not specifying, the CNT diameter [30].

However, an increasing body of work using FC-CVD systems in which the catalyst particles are synthesized externally – and thus the size of the particle is partially decoupled from the CNT nucleation and growth conditions – has shown ratios of 2:1 [59], 2.7:1 [60], and up to 3:1 to 4:1 [35]. Notably, Mustonen et al. found that the mean CNT diameter could be controlled, albeit over a small range from 1.04 to 1.10 nm, with the reactor temperature while using a constant size distribution of catalyst nanoparticles produced ex situ via a spark discharge reactor [35].

Taken as a whole, the wide range of catalyst particle to CNT diameter suggests that, in these systems, other conditions more strongly determine the CNT diameter, while there is a relatively wider window of catalyst particle diameters which can support a CNT of that diameter. In the case of in situ generated catalyst particles which are growing in diameter while in the CNT nucleation zone, one would expect that a CNT will nucleate on the particle at the lower bound of this window – as soon as the particle has grown sufficiently large it will nucleate a CNT and likely stop growth.

Chirality

Controlling the diameter also controls the chirality, however, given the small difference in diameter of adjacent chiralities, the usual inhomogeneity makes it difficult to specify chirality via synthesis. The distribution of chiralities is typically random, resulting in 33% metallic and 67% semiconducting.

Reducing the range of synthesized diameters can bias the chiral distribution. Fewer chiral options exist at smaller diameters, and the difference in activation energy may become more pronounced. Using this approach, samples containing only six chiralities, with up to 54% of a single chirality, (6,5), have been produced at small <0.8 nm diameter

[61]. This capability falls off quickly as diameter increases. At only slightly higher diameter, the best example of diameter control, with 98% between 1.2 and 1.5 nm, still contains at least two dozen different chiralities [62].

A promising alternative route is chemically selecting for chirality through the use of a catalyst that only permits growth of a single chirality. The use of a solid catalyst may constrain growth to only those chiralities which match its lattice spacing. This approach has shown over 90% selectivity of a single chirality, (12,6), using W-Co alloy catalyst, and may be more amenable to selecting specific chirality though tuning of the alloy structure [28].

Nucleation efficiency

Not all particles are catalytically active. Nucleation efficiency, the portion of catalyst particles that grow a CNT, is often low. Direct measurements of the nucleation efficiency show typical values of 1 to 10%. When direct measurement is not possible, it is often estimated at less than 1% by comparing the mass of catalyst to that of the CNTs [63, 64]. Catalyst particles can be characterized as a population with a distribution of sizes, compositions and phases. Additionally, temperature and gas composition can vary locally. The low observed nucleation efficiencies indicate that the variability of particles and these conditions is large relative to the range within which a CNT nucleates. Decreasing variability of catalyst particles and increasing the uniformity of conditions in the reactor is necessary, but not sufficient, for high nucleation efficiency.

ETEM observations of early growth show a critical CNT nucleus length of ~5 nm [54]. Below this, growth is slow and highly defective. Too high a carbon supply rate in this stage can cause the growth front to advance around the particle and fully enclose it in a graphitic shell, preventing further catalytic activity and deactivating the particle [32]. Too low a carbon supply during this critical period and the nuclei may neck

off, as if trying to maintain a linear growth rate with fewer carbon atoms, and form fullerenes or elongated fullerene structures [32]. In this case, the particle is still active, and another nuclei may begin to form. Once a nucleus reaches ~5 nm, it appears that its diameter and growth front have found a stable configuration with the catalyst particle, and growth rate increases significantly [52].This process, when observed on iron catalysts at relatively low temperature with a highly stable carbon precursor (i.e. at 700 °C with carbon monoxide), takes 10 - 40 s, although it may occur orders of magnitude faster at higher temperatures [32].

A catalyst particle may undergo many cycles of attempted nucleation while in the reactor, and the measured nucleation efficiency only captures the final state of this process. Ideally, nucleation would succeed on the first attempt, maximizing the growth time, however a late nucleation is preferable to none. Preventing the deactivation of particles, or providing a mechanism for reactivation, can increase the final nucleation efficiency by allowing for more attempts. The presence of hydrogen, hydroxyl radicals, and other species plays a crucial role in modulating this process through etching of solid carbon. Etching can preserve the activity of a particle by removing or reducing non-nucleus carbon deposits (i.e. defective caps or amorphous carbon), and also reactivate a particle that has been encapsulated by an over-grown nuclei [54]. However, excessive etching may limit the formation of graphitic caps and prevent the formation of, or destroy, CNT nuclei. Once nucleated, the more stable, less defective structure of a CNT appears less susceptible to etching [31, 54]. Improving the uniformity of catalyst particles by controlling their formation environment [31], or fine-tuning the concentration of etchants [64], has been shown to increase nucleation efficiency to over 80%.

2.3.4 CNT Growth

Lengthening

Once a CNT has nucleated, its growth rate may be limited by the kinetics of incorporating additional carbon atoms at the growth front, by the diffusion of carbon on and within the catalyst to the growth front, or by the availability of carbon to the catalyst particle. The kinetically limited growth rate, assuming an ample carbon supply, is generally inversely proportional to diameter [59], and may be influenced by the chirality, which determines the specific structure of the growth front, according to the dislocation growth model developed by Ding et al. [65].

The ratio of particle surface area for catalyzing carbon to the linear carbon density of the CNT scales with diameter. Thus, under carbon supply-limited conditions, the growth rate may also scale with diameter. This ratio increases further in the case of perpendicular growth. CNT length, as an indicator of growth rate, correlates with a larger particle:tube diameter ratio under these conditions [55]. A strong temperature dependence of growth rate for growth at low temperature with acetylene can be explained by an Arrhenius model, and attributed to the growth reaction as growth was not carbon-limited under these conditions [66]. The growth temperature may also influences growth rate by controlling the supply of carbon through thermal pyrolysis of the carbon precursor, whether the catalyst is solid or liquid, and the diffusion rate of carbon in the catalyst.

The growth rate of SWCNTs for high temperature aerosol CVD (i.e. >1200°C) with methane or ethanol is of the order 100 μm/s, 10^2 to 10^3 times faster than typical substrate growth at lower temperatures (~800°C). However, an Arrhenius relationship with activation energy from lower temperature growth would predict an increase in rate

by ~10^9, revealing that at higher temperatures the rate is likely limited by the supply of carbon [67].

Wall number

The factors that control the wall number should also be considered. TEM observations of few-walled CNTs indicate that a small number of walls may grow linearly at once, with staggered growth fronts each intersecting the catalyst particle [52]. In this case, wall number, CNT diameter, and catalyst diameter are related, and found to scale linearly from ~2 nm SWCNTs up to ~8 nm MWCNTs with 6 walls [68, 69]. Growth can also occur laterally, with additional layers growing via direct deposition of carbon onto the sidewalls. This appears to be the dominant method for large MWCNTs with ten or more walls [15]. The relationship between the inner wall diameter and the catalyst diameter for large MWCNTs follows the same trends discussed for SWCNT diameter, suggesting the growth of the inner wall is similar to that of a SWCNT and independent of lateral growth process [53].

Tn general, increasing the carbon supply such that CNT growth is kinetically limited will result in the deposition of additional solid carbon, which may be in the form of additional walls or amorphous carbon on the catalyst or CNT [70]. This can be reduced by trying to limit non-catalytic decomposition of either the carbon precursor or intermediaries, but carbon limited growth in SWCNTs may be a prerequisite for their morphology. Beyond controlling the catalyst and carbon source, the use of etchants can widen the window for SWCNT growth by preventing the formation of multiple walls. It is not clear if the main role of these etchants is to remove carbon from the catalyst - essentially creating carbon limited growth and reducing the linear growth of multiple walls, or to directly etch away carbon deposits on the CNT that would otherwise form additional walls [47].

2.3.5 Growth termination

The termination of CNT growth is the final event in the life cycle of a catalyst. Most directly, termination influences the length of the CNT as well as the yield of the process and purity of the final product. A catalyst with terminated growth is often observed to be over-coated with carbon, although it is not clear whether this is the sole cause or a result of termination. In conditions of carbon oversupply, an excess of carbon may naturally accumulate and eventually encapsulate the particle. Yet, this is also observed for growth in carbon limited conditions, indicating an additional mechanism that either increases the supply of carbon, or decreases the kinetic growth rate for an individual CNT.

The growth of a catalyst particle can increase the flux of carbon into the particle through increased active surface area. This growth is almost an inevitability in substrate growth due to Ostwald ripening, and in aerosol growth due to particle clustering (and, potentially, the continued condensation of iron from coupled particle generation). As this is analogous to catalyst deactivation during nucleation, the same conditions that lead to exceptional nucleation efficiency also result in increased growth by delaying termination [71]. Further, at very large diameter, the compound curvature of the particle surface may decrease below the single curvature of the CNT, and it will become more energetically favorable for the growth front to advance and overcoat the particle [72].

Mechanical forces may also play a role in growth termination. The growth kinetics of a CNT forest under compression have been measured directly and show that even small compressive forces reduce the growth rate, thus creating a local condition of carbon oversupply, and in the extreme may cause termination [73]. Typically, particles are strongly adhered or embedded in the substrate and remain essentially in place during growth. As a CNT extends out from the particle, it initially forms an entangled mat

with adjacent CNTs. Continued growth is only possible by forcing this mat away from the substrate and results in the formation of a forest [57]. As each CNT is constrained between the substrate and the mat that defines the top of the forest, differences in growth rate result in tensile or compressive forces on each CNT. On a local level, this differential may be dominantly controlled by the inverse proportionality of linear growth rate with diameter [74]. As the fastest growing CNTs terminate due to compression, an ever-increasing load of slow and deactivated CNTs is borne by a shrinking population of growing CNTs. This feedback loop may be the limiting factor for forest height and density [74].

In aerosol synthesis, bundling, the aggregation of small groups of CNTs into parallel clusters held together by Van der Waals forces, plays a similar role. Given the long length of a CNT relative to a catalyst particle, it is most likely that the base of a CNT will stick to the middle of another. This essentially anchors the catalyst to its CNT, and any additional growth will have to overcome the shear force provided by this compression. As the propensity for bundling increases with length and concentration, a similar positive feedback exists as in forest growth. Changing growth conditions to produce a lower concentration of CNTs results in less bundling and longer individual CNTs [75].

Kite growth, a specialized substrate growth technique, provides insight into circumventing these termination-inducing conditions and achieving ultra-long growth [32]. The catalyst-support interface is designed to be weak, allowing the potential for the catalyst particle to lift off the substrate during CNT growth, with the other end of the CNT stuck to the substrate [76]. The gas flow and thermal gradients in the reactor are tuned to create an updraft over the substrate which lifts the catalyst particle and gently guides it during growth [77]. The suspended catalyst particle is isolated from mechanical forces and cut off from particle growth mechanisms. With careful balancing of the carbon

supply, CNTs up to 55 cm long have been reported [32].

2.4 Quality

It is possible to characterize individual defects, i.e, at the atomic scale. Observations of typical high quality SWCNTs of 1–2 nm diameter show a mean defect density of one in every 4 μm length, and no evidence of multiple adjacent defects, giving a defect density of 1 in 10^6 sites [78]. It has been observed that larger diameter SWCNTs have higher defect density, and MWCNTs higher still, as there are many more sites available per unit length for defects to occur. The impact of a defect on the CNT properties is dependent by their relative sizes, and observed scaling of strength with diameter, D_{cnt}, of the form $1/\sqrt{D_{cnt}}$ suggests that smaller CNTs also have relatively smaller defects [79, 80]. Molecular dynamics simulations indicate that a single defect can reduce ultimate tensile strength to only 10–50% of the theoretical limit [81].

Given this observed defect density, the average CNT in a typical fiber will have multiple defects, and the strength of the CNT will be limited by the weakest defect, conservatively to 10% of its defect-free performance. Thus, the maximum achievable strength of a fiber, assuming perfect assembly, is also only 10% of theoretical, i.e, 10 GPa instead of 100 GPa. Further developments in fiber spinning may improve strength from the current limit of 3 GPa to approach 10 GPa, but improving quality such that the majority of CNTs have no defects will be necessary for reaching ultimate properties, and may be an easier route for achieving intermediate property values. It is possible to synthesize a CNT with lower defect density - tensile tests of mm-scale bundles have indicated defect density below 1 in 10^9, using highly specific individual growth methods, but the route for translating that capability to bulk synthesis methods and production is unclear [82].

For characterizing larger samples, where measurement of individual defects is prohibitive, Raman spectroscopy is typically employed [83]. The G band at 1580 cm^{-1} is indicative of sp^2 bonded graphitic carbon, and is typically the strongest signal. The D band at 1350 cm^{-1} is a result of disorder in the structure and is indicative of defects. The dynamic range of spectroscopy instruments, higher energy of the G band signal, and confounding D band signal from CNT ends limit the ability to detect defects at low density or the presence of individual defects [84]. Quantifying the relationship between Raman spectra and defect density is difficult. A CNT sample at the limit of detection, a G band to D band peak intensity ratio (I_G/I_G) of 100 or 200, is often referred to as 'defect-free', although this may roughly correspond to a defect density of below 1 in 10^6, thus may be far from defect-free [78, 82]. Raman spectroscopy of any mass produced CNTs suggests a defect density significant higher [78, 19]. This further reinforces the concept that further performance improvements in CNT applications will depend on developments in the synthesis of higher quality CNTs.

While daunting, we can draw inspiration from the modern semiconductor industry which produces and uses 1000s of tons of monocrystalline silicon with a defect density on the order of 1 in 10^{12} [85, 86]. Key to both this technical capacity and its commercial viability is the continued development of the Czochralski process, which enables direct synthesis of meter-scale silicon crystals. Similarly, the development of synthesis techniques which reduce the defect density of individual CNTs and maintain this quality at large production volumes is key to unlocking the real world potential of CNTs.

2.5 Applications

CNTs are potentially useful for a wide variety of applications, with each enabled by a different combination of individual CNT properties and assembly characteristics. Thus

far, commercial applications have depended on matching the specific needs of the application to a synthesis process capable of producing the desired CNT properties at a competitive production rate and cost. Many promising but unrealized applications are limited by some combination, often both, of CNT properties vs production cost. Considering just the first, Figure 2.4 shows the synthesis requirements for several promising applications and compares present synthesis capability with that needed for competitive performance. While some synthesis requirements can be met for each applications, improvement is needed in all cases to equal the performance of current alternatives.

In some applications, a multifunctional material is needed; thus, CNTs may be useful even if their primary property does not improve on current materials. While the electrical conductivity of current CNT fibers is below that of copper, they may be preferable in use cases where toughness or fatigue life is the dominant design constraint. However, in other applications, such as transistors and membranes, very specific properties or functionality must be attained to improve upon exiting materials.

The five metrics of Figure 2.4, already a simplification of these complex materials, can be condensed further into two axes, CNT control and assembly organization, to allow comparison of a wider range of applications. Figure 2.5 presents a map of CNT applications against these two axes, building off a similar framework in [5]. These terms are necessarily vague and qualitative in order to compare the wide range of forms. Here, CNT control refers to both the level of defects within CNTs, and the ability to control specific properties across the collection of CNTs, such as wall number, length, diameter, and chirality. Assembly organization refers to the degree and length scales of controlled assembly. The level of impurities tends to decrease with increasing organization, and the weight fraction or packing density of CNTs tends to increase with organization.

In general, the use of CNTs for each application is in the development of a novel material (either pure CNT or a composite) with the desired material properties. Thus,

the map shown in Figure 2.5 can be divided into several regions based on the required material properties of the application. Applications in the bulk additives region typically seek to improve the performance of a base material through the addition of a small wt% CNTs. Here, the performance criteria is usually defined as an improvement over the properties of the base material (or the base with a different additive), thus the relationship between CNT properties and application properties is indirect. Applications in the 'advanced materials' region seek to replace, rather than improve, existing engineering materials with higher-performance CNT materials or composites. Here, the performance criteria is again an improvement over existing materials, but, the properties are derived primarily from those of the CNTs. Thus, the performance of the material is related to the corresponding properties of the CNT, but the required property values are only 5 to 10% of the those of the CNTs. Applications in the ultimate applications region require material properties unable to be met with traditional materials, necessitating essentially scaling up the properties of an ideal CNT to the macroscale material. Here, the performance criteria is the fraction of the properties of an ideal CNT that can be realized, and may be 50% or more.

2.6 Production at scale

The production of CNTs ranges from the specific synthesis of low numbers of CNTs in research settings to that of kilotons of MWCNTs commercially each year. This is a range of production capacities of 10^{12} or more. Figure 2.6 maps these methods based on assembly organization and CNT control, allowing direct comparison to the applications in Figure 2.5. When available, a cost or production rate is included with the process. In other cases, this has been estimated from other cited information. From Figure 2.5, we see that most current applications are in the bulk additives region. Comparing Figures

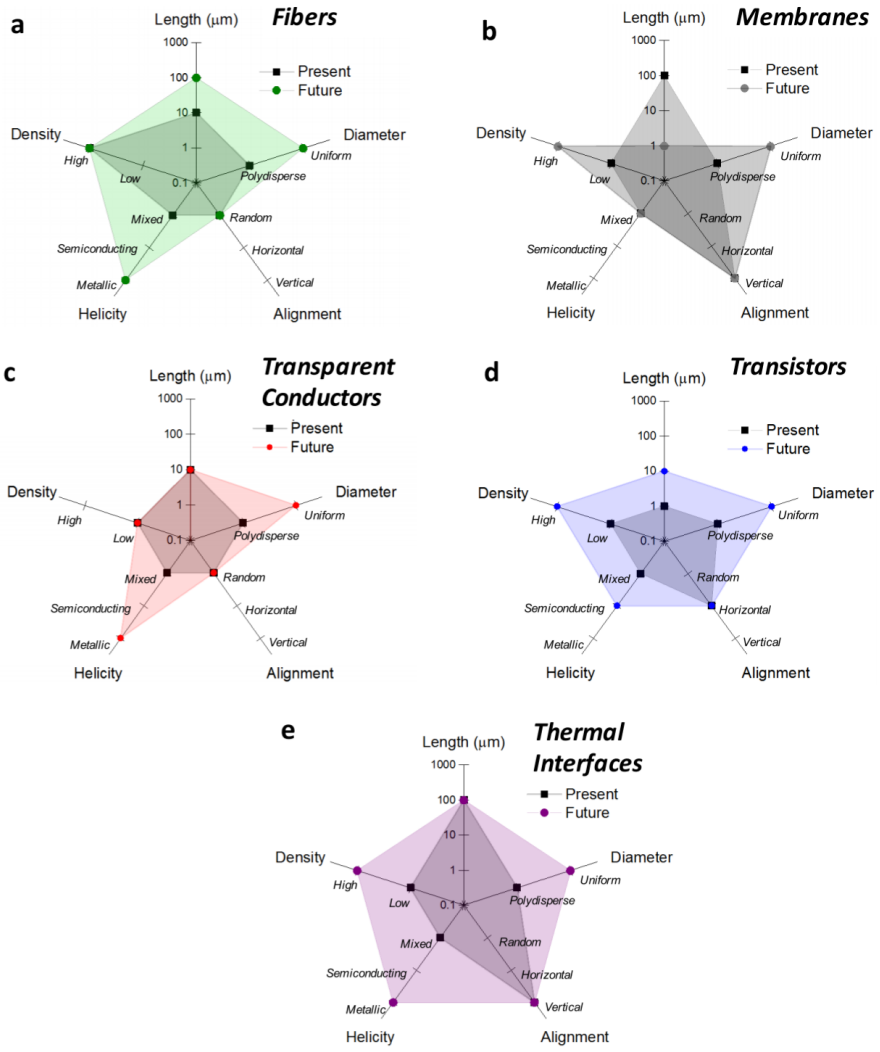

Figure 2.4: Radar charts showing, for various physical properties, the present state of SWCNT synthesis as well as the future requirements for various applications. Copyright 2018 ACS, [5]

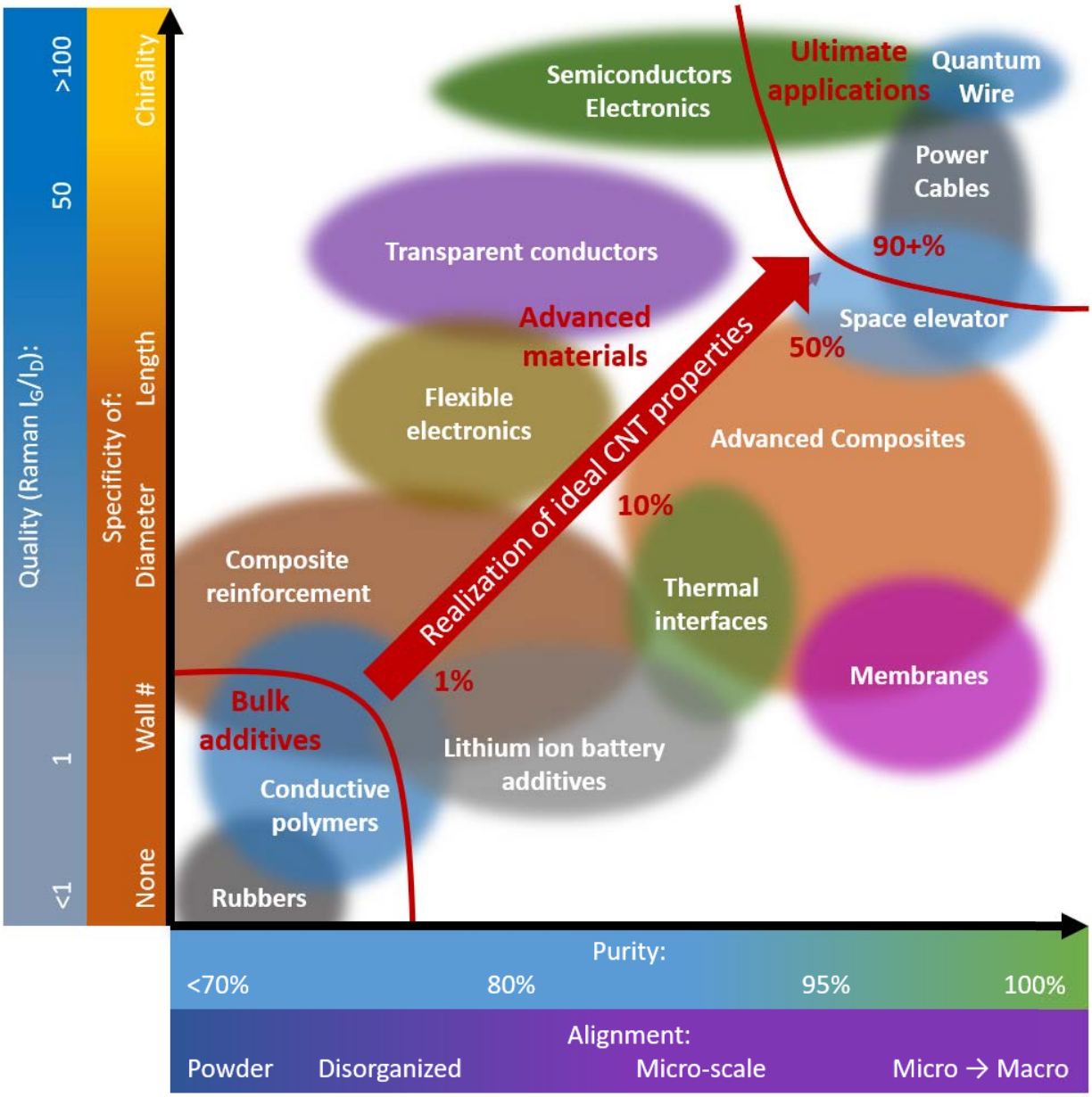

Figure 2.5: Applications map of current and potential CNT applications. The x axis corresponds to the concept of assembly organization, illustrated using scales of purity (presence of catalyst or amorphous carbon) and alignment (incorporating both the multi-scale organization and packing density). The y axis corresponds to the concept of CNT control, illustrated using scales of CNT quality (control of defects) and specificity of characteristics (in approximately increasing order of difficulty and utility). Red annotations indicate the regions of bulk additives, advanced materials, and ultimate applications. These regions roughly correspond to the required portion of ideal CNT properties.

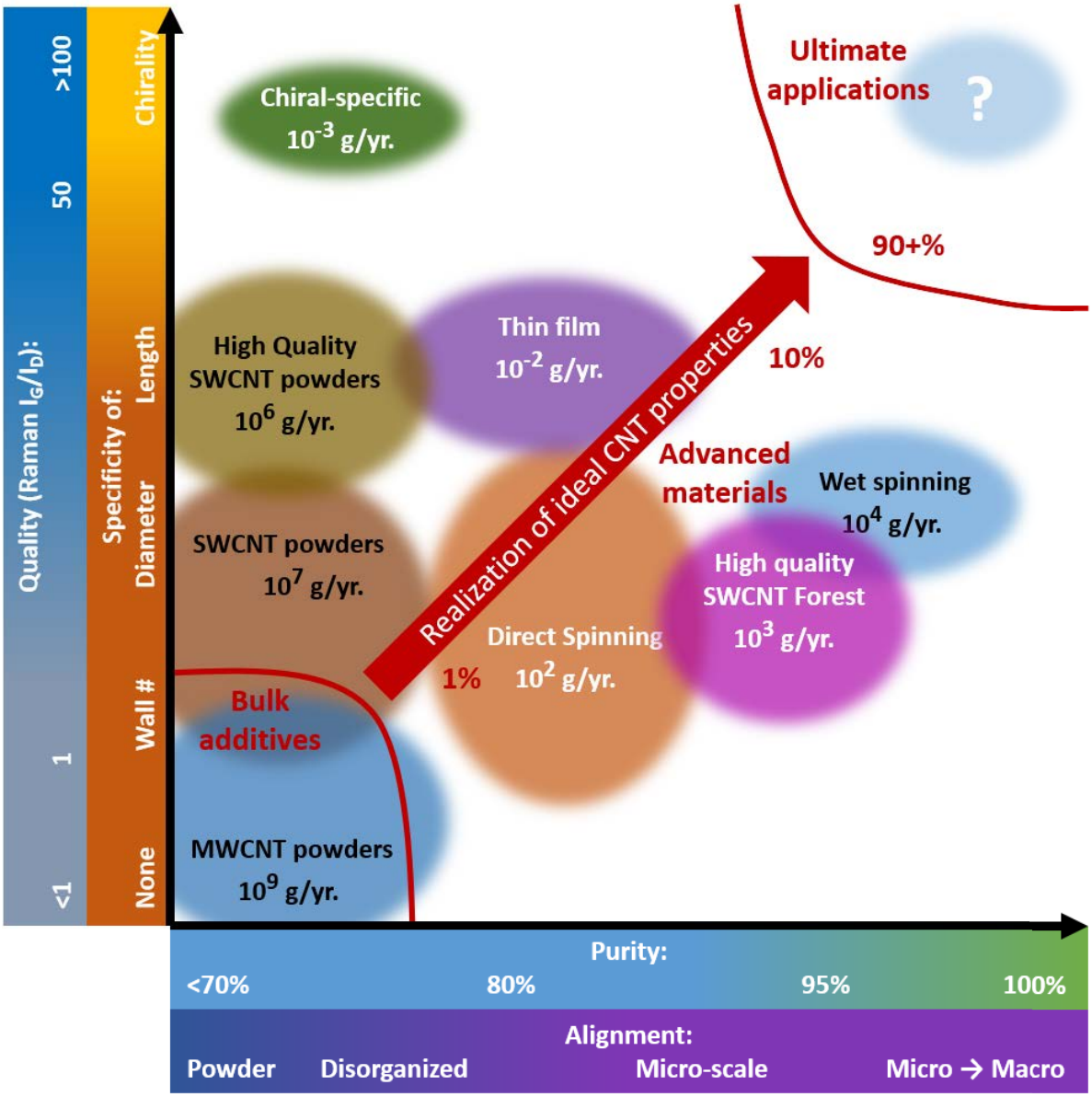

Figure 2.6: Map of manufacturing methods for research and commercial CNT production methods. Axes are identical to, and described in, Figure 2.5. Production rate, in g/yr, is also provided. Black text indicates a commercial industry-wide production rate, while white text indicates an estimated production rate from a lab-scale process (i.e., continuous operation of lab-scale system). End notes detail the estimation methods. [4]: Commercial MWCNT powder, reported industry-wide capacity. [102]: Commercial SWCNT powder, reported industry-wide capacity. [103]: Commercial high quality SWCNT powders, estimated. [104]: Lab-scale SWCNT forest, estimated. [105]: Lab-scale direct-spinning, estimated. [106]: Commercial wet-spun fibers, estimated. [107]: Lab-scale chiral-specific synthesis, estimated. [108]: Lab-scale SWCNT thin film deposition, estimated.

Material	Cost ($/kg)	
Aluminum	2-3	[87]
Copper	6	[88]
Carbon fiber prepreg (auto grade)	15	[89]
Si Wafer (unprocessed)	1000	[90]
Si wafer (7nm transistors)	122,000	[91]
Si transistor (16nm to 7nm)	2–4/bn.	[91]
launch to low earth orbit	5,000	[92]
highest current carbon emission tax	0.13	[93]
highest IPCC recommended tax	5.50	[94]
Ethanol (industrial grade)	1	[95]
Natural gas to HP methane	0.15–32	[96] [97]
Hydrogen (industrial to UHP)	1–140	[98] [97]
carbon black	1	[99]
bulk MWCNT	<100	[4]
bulk SWCNT	50,000-100,000	[100]
high quality SWCNT	100,000-500,000	[101]

Table 2.2: Relevant materials and material costs for CNT applications and synthesis. IPCC is the Intergovernmental Panel on Climate Change, HP is high purity, UHP is ultra high purity.

2.5 and 2.6, we see that many potential applications in the bulk additives and advanced materials regions overlap with current synthesis capabilities. In many of these cases, including transparent conductors [75], membranes [109], and transistors [110], functional devices have been prototyped, but the production capacity and cost is prohibitive.

In the following sections, a deeper analysis of production methods for each region outlined in Figure 2.5 is provided. This analysis highlights current synthesis knowledge needs and the most effective future research directions.

2.6.1 production for bulk additive applications

In most bulk additive applications, CNTs are used as a lower concentration alternative to carbon black or other particulate materials. The ability of CNTs to alter bulk material properties at low wt% is due to a higher aspect ratio and specific surface area than other

additives. These properties are inherent even in low quality or MWCNTs, although are enhanced for SWCNT or at higher quality. A common use of additives is to increase the conductivity of polymers, e.g. epoxy flooring to improve anti-static properties and plastic components in the automotive industry to enable electrostatic-assisted painting [4, 100]. In these cases, the required conductivity can be accomplished with carbon black, MWCNTs, or SWCNTs, and cost is the primary deciding factor. Carbon black is ~$1/kg [99], and requires a loading of 1-10 w% to adequately increase conductivity [111], while a loading of 0.01 wt% MWCNTs is sufficient [4]. At the current bulk cost of ~$100/kg [4], the use of MWCNT is cheaper than carbon black. MWCNTs can also replace carbon black in rubber used for automotive tires. However, the performance of a typical loading of 10 wt% carbon black requires closer to 1 wt% MWCNT, thus this market is not cost effective at current MWCNT prices [112]. Commercial MWCNT powders at this price are synthesized in large fluidized bed or aerosol CVD reactors with global production of 1000-5000 tons/year [102, 4].

Even lower wt% can be realized with SWCNTs or longer, higher quality MWCNTs due to their increased aspect ratio, length, and specific surface area. For example, SWCNTs require only 0.01 wt% loading in rubber to perform equivalent to 10 wt% carbon black, and typically have a similar additive effect as MWCNTs at 1/10 to 1/100 the concentration [100]. However, the production rate of a large scale SWCNT reactor is also orders of magnitude lower than a similar MWCNT reactor. The smaller mass of a SWCNT (the cross sectional area, and thus linear density, of a SWCNT may be 100 to 1000x smaller than a MWCNT) and could for much of this difference, potentially indicating that both processes have approximately similar number production rates. Additionally, in aerosol CVD, the requirement for smaller catalyst diameter and carbon-limited growth further reduces the production rate. As a result, lowest-grade SWCNTs cost ~$50-$100/g, and are not economically competitive [100].

2.6.2 Production for advanced materials applications

Advanced materials applications have more stringent requirements on both the individual CNT properties and the assembly in order to realize a portion of the ideal CNT properties. For example, a CNT composite with 10 GPa UTS would vastly outperform current carbon fiber composites (~5 GPa), yet still be only 10% the UTS of an ideal CNT. Theoretically a range of strategies can meet this performance limit, ranging from a poorly organized assembly of defect-free long, uniform diameter SWCNTs, to a perfectly aligned assembly of mixed diameter, low quality CNTs. The key to developing these materials is balancing the trade-offs in cost and feasibility of these aspects. Commercial production of SWCNTs is closest to meeting the balance of cost and quality needed. MWCNTs are already cost-competitive, but are inherently limited in their material properties, and lab techniques for synthesizing individual CNTs would need to be scaled by many orders of magnitude. However, for nearly all applications, SWCNT-based materials are both vastly more expensive than the traditional material and underperform in key properties; thus, current applications in this region are limited. CNTs do find use in cases of multifunctional, weight-critical, or highly specialized applications, especially when the amount of material is small.

SWCNTs are produced in large quantities by 10 to 20 companies and research labs, totaling ~10 ton/yr [102, 19]. The majority of these are available as an unpurified powder with typical composition 70-75 wt% SWCNT, 5-15 wt% catalyst, and the remainder amorphous carbon. Typical SWCNTs are 1-2 nm diameter and 1-15 um long, with Raman $I_G/I_D > 50$ [113, 114, 100, 19].

In this section, a first order cost model of a SWCNT factory is presented. The difference between this model and commercial activity reveals shortcomings in commercial processes. Table 2.3 shows the reported capital cost and production rate for recently

built SWCNT factories. Based on this information, constructing a 1 ton/yr plant would cost ~$5M, or $1M/yr assuming a five year payback period. A large research-scale reactor may produce up to 10 g/hr, thus ten reactors would be required assuming continuous operation [115, 37]. For a typical high temperature growth recipe, material costs are ~$1000/kg ($2/kg ferrocene and methane, $50/kg electricity for heat, $1000/kg hydrogen) [67], thus $1M/yr. Assuming an additional $1M/yr for staffing and operations ($114/hour, 24/7/365), the total production cost is ~$3M/yr, or $3/g. Current cost- or manufacturing-oriented research aims to reduce this through reducing and recycling hydrogen, and further scaling up reactors (assuming that production rate increases faster than capital and staffing costs). Taking these efforts into account, a cost of $30–50/kg, may be possible using current synthesis technology in a larger, ~100 ton/yr plant [67]. This cost is significantly higher than the $1–10/kg of typical structural materials, but competitive with other advanced composites.

	Capital ($M)	Production (ton/yr)	M $/ton/year	
SWeNT (2007)	$4.96	0.36	13.8	[116]
Supergrowth (2015)	$3.58	10	0.36	[117, 71]
OCSiAl (2015)	$21.7	5	4.4	[118]

Table 2.3: Capital cost (in 2019 USD) and estimated production capacity of SWCNT factories. SWeNT and OCSiAl are aerosol CVD processes, Supergrowth is a continuous forest growth process.

The current market cost for true SWCNTs with minimal processing is ~$100 to $500/g [101]. Considering the above $3/g estimate as an ideal minimum, a factor of 20–150 higher cost indicates significant inefficiencies in real world production. Identifying and improving on these inefficiencies has significantly greater potential for cost reduction. Personal experience with CVD reactor construction and operation, as well as evidence from commercial production, suggests (at least) three potential issues:

1. **Quality.** Maintaining high quality or high purity synthesis over long duration is difficult. Minute changes in ambient conditions, build-up in the reactor, or

other factors may reduce growth rates and affect catalyst formation and nucleation efficiency. Additionally, process monitoring is difficult as the entirety of the process occurs at high temperature in a harsh atmosphere. Thus, additional purification steps may be needed to ensure high and consistent purity.

2. **Production rate.** Similarly, the highest production rate SWCNT conditions are also the most sensitive to disturbances. The carbon precursor concentration will have been increased to just below the limit of amorphous carbon or multi-wall formation, and the catalyst particle concentration maximized, resulting in larger particles more likely to nucleate MWCNTs. While this may be acceptable for hours-long experiments with highly trained operators, the typical growth conditions for continuous operation are likely more conservative and result in lower production rate.

3. **Reliability and down time.** This is a complex process, and issues are difficult and time consuming to troubleshoot. Diagnosing an issue may take a scientist weeks and require expensive characterization, while rectifying the issue may require modification of this custom hardware or re-tuning the growth conditions. At minimum, a high fraction of down time will proportionally reduce the average production rate.

2.6.3 Production for ultimate applications

Ultimate applications require near-perfect assembly of defect-free CNTs to realize a significant portion of the ideal CNT properties at the macroscale. Macroscopic quantum wires, composed of continuous, defect-free metallic SWCNTs, and structural composites with strength sufficient for a space elevator (~50 GPa), are two examples.

Current large scale synthesis techniques, such as aerosol CVD, do not have the needed

quality or specificity for these applications. Small numbers of defect-free [13], or near-uniform chirality [28], or long [32] CNTs can be synthesized, but achieving all three with *a-priori* specificity [119] remains a challenge. Additionally, the production rate for these methods will need to be scaled by ~10^{12} or more for macroscopic applications.

Large scale synthesis techniques are also incapable of sufficiently controlling the organization. Bundles of few CNTs in aerosol CVD are typically parallel and without impurities, promoting nano-scale alignment. However, this alignment is not maintained at larger length scales as entanglement and aerogel formation occur. This entanglement also serves to capture and hold impurities from the synthesis process. Wet-spinning of fibers from solution may be the most promising assembly technique and has produced fibers with the highest strength and conductivity. Solution processing enables purification between synthesis and assembly, and the resultant fibers have higher packing density and alignment than direct-spinning produces [9].

References

[1] William James Sawyer. "Toward improved manufacturing of carbon nanotubes by microplasma synthesis of catalyst nanoparticles". Massachusetts Institute of Technology, 2020.

[2] Ning Wang et al. "Single-walled 4 A carbon nanotube arrays." In: *Nature* 408.6808 (2000), pp. 50–51.

[3] Maoshuai He et al. "Precise determination of the threshold diameter for a single-walled carbon nanotube to collapse". In: *ACS nano* 8.9 (2014), pp. 9657–9663.

[4] M F Volder et al. "Carbon nanotubes: present and future commercial applications". In: *Science* 339.February (2013), pp. 535–540. DOI: 10.1126/science.1222453. URL: https://doi.org/10.1126/science.1222453.

[5] Rahul Rao et al. "Carbon nanotubes and related nanomaterials: critical advances and challenges for synthesis toward mainstream commercial applications". In: *ACS nano* 12.12 (2018), pp. 11756–11784.

[6] Ray H Baughman, Anvar A Zakhidov, and Walt A De Heer. "Carbon nanotubes–the route toward applications". In: *science* 297.5582 (2002), pp. 787–792.

[7] Hongliang Zhang et al. "Separation and/or selective enrichment of single-walled carbon nanotubes based on their electronic properties". In: *Chemical Society Reviews* 40.3 (2011), pp. 1324–1336.

[8] Eric Pop et al. "Thermal conductance of an individual single-wall carbon nanotube above room temperature". In: *Nano letters* 6.1 (2006), pp. 96–100.

[9] Natnael Behabtu et al. "Strong, light, multifunctional fibers of carbon nanotubes with ultrahigh conductivity". In: *science* 339.6116 (2013), pp. 182–186.

[10] John H Lienhard IV. *JH Lienhard V: A Heat Transfer Book*. 2008.

[11] BQ Wei, R Vajtai, and PM Ajayan. "Reliability and current carrying capacity of carbon nanotubes". In: *Applied Physics Letters* 79.8 (2001), pp. 1172–1174.

[12] Chandramouli Subramaniam et al. "One hundred fold increase in current carrying capacity in a carbon nanotube–copper composite". In: *Nature communications* 4 (2013), p. 2202.

[13] Bei Peng et al. "Measurements of near-ultimate strength for multiwalled carbon nanotubes and irradiation-induced crosslinking improvements". In: *Nature nanotechnology* 3.10 (2008), p. 626.

[14] Han Gi Chae et al. "High strength and high modulus carbon fibers". In: *Carbon* 93 (2015), pp. 81–87.

[15] Ado Jorio, Gene Dresselhaus, and Mildred S Dresselhaus. *Carbon nanotubes: advanced topics in the synthesis, structure, properties and applications*. Vol. 111. Springer Science & Business Media, 2007.

[16] EA Brandes, GB Brook, and P Paufler. "Smithells Metals Reference Book. Butterworth-Heinemann Ltd., Oxford, 1992. 1746 Seiten, Preis 150£, ISBN 0-7506-1020-4". In: *Crystal Research and Technology* 28.4 (1993), pp. 530–530.

[17] Natnael Behabtu, Micah J Green, and Matteo Pasquali. "Carbon nanotube-based neat fibers". In: *Nano today* 3.5-6 (2008), pp. 24–34.

[18] M. F. Ashby, P. J. Ferreira, and D. L. Schodek. "Nanomaterials, Nanotechnologies and Design". In: vol. 1. Boston: Butterworth-Heinemann, 2009. Chap. 7 - Nanomaterials: Properties, pp. 199–225.

[19] Dmitri E Tsentalovich et al. "Influence of carbon nanotube characteristics on macroscopic fiber properties". In: *ACS applied materials & interfaces* 9.41 (2017), pp. 36189–36198.

[20] Agnieszka Lekawa-Raus et al. "Electrical properties of carbon nanotube based fibers and their future use in electrical wiring". In: *Advanced Functional Materials* 24.24 (2014), pp. 3661–3682.

[21] Sumio Iijima. "Helical microtubules of graphitic carbon". In: *nature* 354.6348 (1991), p. 56.

[22] DS Bethune et al. "Cobalt-catalysed growth of carbon nanotubes with single-atomic-layer walls". In: *Nature* 363.6430 (1993), p. 605.

[23] Hongjie Dai. "Carbon nanotubes: synthesis, integration, and properties". In: *Accounts of chemical research* 35.12 (2002), pp. 1035–1044.

[24] Hongjie Dai et al. *Controlled chemical routes to nanotube architectures, physics, and devices*. 1999.

[25] William Smith and Javad Hashemi. "Foundations of Materials Science and Engineering". In: McGraw-Hill Higher Education, 2009.

[26] Mukul Kumar. "Carbon nanotube synthesis and growth mechanism". In: *Carbon Nanotubes-Synthesis, Characterization, Applications* (2011), pp. 147–170.

[27] Aiqin Jiang et al. "Theoretical study of the thermal behavior of free and alumina-supported Fe-C nanoparticles". In: *Physical Review B* 75.20 (2007), p. 205426.

[28] Feng Yang et al. "Chirality-specific growth of single-walled carbon nanotubes on solid alloy catalysts". In: *Nature* 510.7506 (2014), p. 522.

[29] Daisuke Takagi, Yoshihiro Kobayashi, and Yoshikazu Homma. "Carbon nanotube growth from diamond". In: *Journal of the American Chemical Society* 131.20 (2009), pp. 6922–6923.

[30] Chin Li Cheung et al. "Diameter-controlled synthesis of carbon nanotubes". In: *The Journal of Physical Chemistry B* 106.10 (2002), pp. 2429–2433.

[31] Nicholas T Dee et al. "Carbon-assisted catalyst pretreatment enables straightforward synthesis of high-density carbon nanotube forests". In: *Carbon* (2019).

[32] Rufan Zhang et al. "Growth of half-meter long carbon nanotubes based on Schulz–Flory distribution". In: *Acs Nano* 7.7 (2013), pp. 6156–6161.

[33] Keita Kobayashi et al. “Wall-Number Selectivity in Single/Double-Wall Carbon Nanotube Production by Enhanced Direct Injection Pyrolytic Synthesis”. In: *Japanese Journal of Applied Physics* 52.10R (2013), p. 105102.

[34] Mikhail Rudolfovich Predtechensky, Oleg Mikhailovich Tukhto, and Ilya Yurievich Koval. “System and method for producing carbon nanotubes”. US8137653B1. 2012.

[35] Kimmo Mustonen et al. “Gas phase synthesis of non-bundled, small diameter single-walled carbon nanotubes with near-armchair chiralities”. In: *Applied Physics Letters* 107.1 (2015).

[36] Albert G Nasibulin et al. “Carbon nanotube synthesis from alcohols by a novel aerosol method”. In: *Journal of Nanoparticle Research* 8.3-4 (2006), pp. 465–475.

[37] Lee Weller et al. “Mapping the parameter space for direct-spun carbon nanotube aerogels”. In: *Carbon* 146 (2019), pp. 789–812.

[38] TS Gspann, FR Smail, and AH Windle. “Spinning of carbon nanotube fibres using the floating catalyst high temperature route: purity issues and the critical role of sulphur”. In: *Faraday discussions* 173 (2014), pp. 47–65.

[39] Kieran J MacKenzie, Oscar M Dunens, and Andrew T Harris. “An updated review of synthesis parameters and growth mechanisms for carbon nanotubes in fluidized beds”. In: *Industrial & Engineering Chemistry Research* 49.11 (2010), pp. 5323–5338.

[40] Mukul Kumar and Yoshinori Ando. “Chemical vapor deposition of carbon nanotubes: a review on growth mechanism and mass production”. In: *Journal of nanoscience and nanotechnology* 10.6 (2010), pp. 3739–3758.

[41] Michael J Bronikowski et al. “Gas-phase production of carbon single-walled nanotubes from carbon monoxide via the HiPco process: A parametric study”. In: *Journal of Vacuum Science & Technology A: Vacuum, Surfaces, and Films* 19.4 (2001), pp. 1800–1805.

[42] Eric R Meshot et al. “High-yield growth kinetics and spatial mapping of single-walled carbon nanotube forests at wafer scale”. In: *Carbon* (2019).

[43] Vincent Jourdain and Christophe Bichara. “Current understanding of the growth of carbon nanotubes in catalytic chemical vapour deposition”. In: *Carbon* 58 (2013), pp. 2–39.

[44] G Ingram and SMH Rizvi. “The pyrolytic identification of organic molecules: III. A mechanistic approach”. In: *Microchemical Journal* 19.3 (1974), pp. 253–271.

[45] Yu-Ran Luo. *Comprehensive handbook of chemical bond energies*. CRC press, 2007.

[46] Desirée L Plata et al. “Multiple alkynes react with ethylene to enhance carbon nanotube synthesis, suggesting a polymerization-like formation mechanism”. In: *Acs Nano* 4.12 (2010), pp. 7185–7192.

[47] G Zhong et al. “Acetylene: a key growth precursor for single-walled carbon nanotube forests”. In: *The Journal of Physical Chemistry C* 113.40 (2009), pp. 17321–17325.

[48] R.J. Kee, F.M. Rupley, and J.A. Miller. “Chemkin-II: A Fortran chemical kinetics package for the analysis of gas-phase chemical kinetics”. In: (Sept. 1989).

[49] Hisashi Sugime and Suguru Noda. “Millimeter-tall single-walled carbon nanotube forests grown from ethanol”. In: *Carbon* 48.8 (2010), pp. 2203–2211.

[50] Heinz Gräfje et al. “Butanediols, butenediol, and butynediol”. In: *Ullmann’s Encyclopedia of Industrial Chemistry* (2000).

[51] Jean-Yves Raty, Francois Gygi, and Giulia Galli. “Growth of Carbon Nanotubes on Metal Nanoparticles: A Microscopic Mechanism from Ab Initio Molecular Dynamics Simulations”. In: *Phys. Rev. Lett.* 95 (9 Aug. 2005), p. 096103. DOI: 10.1103/PhysRevLett.95.096103. URL: https://link.aps.org/doi/10.1103/PhysRevLett.95.096103.

[52] Stephan Hofmann et al. “In situ observations of catalyst dynamics during surface-bound carbon nanotube nucleation”. In: *Nano letters* 7.3 (2007), pp. 602–608.

[53] Mauricio C Diaz et al. “Can Single-Walled Carbon Nanotube Diameter Be Defined by Catalyst Particle Diameter?” In: *The Journal of Physical Chemistry C* (2019).

[54] M-FC Fiawoo et al. “Evidence of correlation between catalyst particles and the single-wall carbon nanotube diameter: a first step towards chirality control”. In: *Physical Review Letters* 108.19 (2012), p. 195503.

[55] Maoshuai He et al. “Linking growth mode to lengths of single-walled carbon nanotubes”. In: *Carbon* 113 (2017), pp. 231–236.

[56] Maoshuai He et al. “Designing Catalysts for Chirality-Selective Synthesis of Single-Walled Carbon Nanotubes: Past Success and Future Opportunity”. In: *Advanced Materials* 31.9 (2019), p. 1800805.

[57] Yiming Li et al. “Growth of single-walled carbon nanotubes from discrete catalytic nanoparticles of various sizes”. In: *The Journal of Physical Chemistry B* 105.46 (2001), pp. 11424–11431.

[58] Albert G Nasibulin et al. “Correlation between catalyst particle and single-walled carbon nanotube diameters”. In: *Carbon* 43.11 (2005), pp. 2251–2257.

[59] Wei-Hung Chiang. “Engineering nanocatalysts for selective growth of carbon nanotubes”. PhD thesis. Case Western Reserve University, 2009.

[60] Guohai Chen et al. “Multi-step chemical vapor synthesis reactor based on a microplasma for structure-controlled synthesis of single-walled carbon nanotubes”. In: *Chemical Engineering Journal* 444 (2022), p. 136634.

[61] Giulio Lolli et al. “Tailoring (n, m) structure of single-walled carbon nanotubes by modifying reaction conditions and the nature of the support of CoMo catalysts”. In: *The Journal of Physical Chemistry B* 110.5 (2006), pp. 2108–2115.

[62] Yongping Liao et al. “Direct Synthesis of Colorful Single-Walled Carbon Nanotube Thin Films”. In: *Journal of the American Chemical Society* 140.31 (2018), pp. 9797–9800.

[63] Z Liu et al. “Pulsed laser CVD investigations of single-wall carbon nanotube growth dynamics”. In: *Applied Physics A* 93.4 (2008), pp. 987–993.

[64] Don N Futaba et al. “Kinetics of water-assisted single-walled carbon nanotube synthesis revealed by a time-evolution analysis”. In: *Physical review letters* 95.5 (2005), p. 056104.

[65] Feng Ding, Avetik R Harutyunyan, and Boris I Yakobson. “Dislocation theory of chirality-controlled nanotube growth”. In: *Proceedings of the National Academy of Sciences* 106.8 (2009), pp. 2506–2509.

[66] Wei-Hung Chiang and R Mohan Sankaran. “Microplasma synthesis of metal nanoparticles for gas-phase studies of catalyzed carbon nanotube growth”. In: *Applied Physics Letters* 91.12 (2007), p. 121503.

[67] Fiona Smail, Adam Boies, and Alan Windle. “Direct spinning of CNT fibres: Past, present and future scale up”. In: *Carbon* 152 (2019), pp. 218–232.

[68] Wei-Hung Chiang and R Mohan Sankaran. “In-flight dimensional tuning of metal nanoparticles by microplasma synthesis for selective production of diameter-controlled carbon nanotubes”. In: *The Journal of Physical Chemistry C* 112.46 (2008), pp. 17920–17925.

[69] Wei-Hung Chiang et al. “Direct wall number control of carbon nanotube forests from engineered iron catalysts”. In: *Journal of nanoscience and nanotechnology* 13.4 (2013), pp. 2745–2751.

[70] Richard F Wood et al. “Simple model of the interrelation between single-and multiwall carbon nanotube growth rates for the CVD process”. In: *Physical Review B* 75.23 (2007), p. 235446.

[71] Kenji HATA. “A super-growth method for single-walled carbon nanotube synthesis”. In: *Synthesiology English edition* 9.3 (2016), pp. 167–179.

[72] Jason H Hafner et al. “Catalytic growth of single-wall carbon nanotubes from metal particles”. In: *Chemical Physics Letters* 296.1-2 (1998), pp. 195–202.

[73] Nicholas T Dee et al. “In Situ Mechanochemical Modulation of Carbon Nanotube Forest Growth”. In: *Chemistry of Materials* 31.2 (2018), pp. 407–418.

[74] Mostafa Bedewy, Eric R Meshot, and A John Hart. “Diameter-dependent kinetics of activation and deactivation in carbon nanotube population growth”. In: *Carbon* 50.14 (2012), pp. 5106–5116.

[75] Aqeel Hussain et al. “Floating catalyst CVD synthesis of single walled carbon nanotubes from ethylene for high performance transparent electrodes”. In: *Nanoscale* 10.20 (2018), pp. 9752–9759.

[76] Maoshuai He et al. “Insights into chirality distributions of single-walled carbon nanotubes grown on different Co x Mg 1- x O solid solutions”. In: *Journal of Materials Chemistry A* 2.16 (2014), pp. 5883–5889.

[77] Shaoming Huang, Xinyu Cai, and Jie Liu. “Growth of millimeter-long and horizontally aligned single-walled carbon nanotubes on flat substrates”. In: *Journal of the American Chemical Society* 125.19 (2003), pp. 5636–5637.

[78] Yuwei Fan, Brett R Goldsmith, and Philip G Collins. “Identifying and counting point defects in carbon nanotubes”. In: *Nature materials* 4.12 (2005), p. 906.

[79] Lin Yang, Israel Greenfeld, and H Daniel Wagner. “Toughness of carbon nanotubes conforms to classic fracture mechanics”. In: *Science advances* 2.2 (2016), e1500969.

[80] Akira Takakura et al. “Strength of carbon nanotubes depends on their chemical structures”. In: *Nature communications* 10.1 (2019), pp. 1–7.

[81] Liyan Zhu, Jinlan Wang, and Feng Ding. “The great reduction of a carbon nanotube’s mechanical performance by a few topological defects”. In: *ACS nano* 10.6 (2016), pp. 6410–6415.

[82] Yunxiang Bai et al. “Carbon nanotube bundles with tensile strength over 80 GPa”. In: *Nature nanotechnology* 13.7 (2018), p. 589.

[83] Mildred S Dresselhaus et al. “Raman spectroscopy of carbon nanotubes”. In: *Physics reports* 409.2 (2005), pp. 47–99.

[84] David Mann et al. “Ballistic transport in metallic nanotubes with reliable Pd ohmic contacts”. In: *Nano Letters* 3.11 (2003), pp. 1541–1544.

[85] Babu Chalamala. *Si Photovoltaics: Materials and Manufacturing*. 2015. URL: https://www.osti.gov/servlets/purl/1340220 (visited on 01/06/2020).

[86] Shengdong Li et al. “Electrical properties of 0.4 cm long single-walled carbon nanotubes”. In: *Nano Letters* 4.10 (2004), pp. 2003–2007.

[87] *Current Aluminum Price*. 2020. URL: http://www.infomine.com/investment/metal-prices/aluminum/ (visited on 01/06/2020).

[88] *Current Copper Price*. 2020. URL: http://www.infomine.com/investment/metal-prices/copper/ (visited on 01/06/2020).

[89] *Autocomposites and the myth of 5 Dollar/lb carbon fiber*. 2017. URL: https://www.compositesworld.com/columns/autocomposites-and-the-myth-of-5lb-carbon-fiber (visited on 01/06/2020).

[90] *Expect Silicon Wafer Tags to Rise Through 2019*. 2018. URL: https://www.sourcetoday.com/supply-chain/article/21867044/expect-silicon-wafer-tags-to-rise-through-2019 (visited on 01/06/2020).

[91] Ramish Zafar. *Apple A13 & Beyond: How Transistor Count And Costs Will Go Up*. 2019. URL: https://wccftech.com/apple-5nm-3nm-cost-transistors/ (visited on 01/06/2020).

[92] National Aeronautics Marshall Space Flight Center and Space Administration. *Advanced Space Transportation Program: Paving the Highway to Space*. URL: https://www.nasa.gov/centers/marshall/news/background/facts/astp.html (visited on 01/06/2020).

[93] *Where Carbon is Taxed*. 2019. URL: https://www.carbontax.org/where-carbon-is-taxed/ (visited on 01/06/2020).

[94] IPCC (Intergovernmental Panel on Climate Change). "Special Report, Global Warming of 1.5°C (SR15)". In: (2018).

[95] *Ethanol market and Pricing Data*. 2018. URL: https://grains.org/ethanol_report/ethanol-market-and-pricing-data-february-20-2018/ (visited on 01/06/2020).

[96] U.S. Energy Information Administration. *Natural Gas Prices*. 2019. URL: https://www.eia.gov/dnav/ng/ng_pri_sum_dcu_nus_m.htm (visited on 01/06/2020).

[97] *Compressed Gas Pricing*. 2019. URL: https://generalstores.psu.edu/pricing-and-lead-time (visited on 01/06/2020).

[98] U.S. Office of Energy Efficiency and Renewable Energy. *Hydrogen Fuel Fact Sheet*. 2019. URL: http://www1.eere.energy.gov/vehiclesandfuels/facts/favorites/fcvt_fotw205.html (visited on 01/06/2020).

[99] Alibaba. *Carbon Black Per Kg Price*. 2020. URL: https://www.alibaba.com/showroom/carbon-black-per-kg-price.html (visited on 01/06/2020).

[100] Michael Enotiades. *Tuball single wall carbon nanotubes, MPG Seminar*. 2017. URL: http://www.iom3.org/sites/default/files/P5%5C%20M%5C%20Enotiades%5C%20-%5C%20OCSiAl%5C%20MPG%5C%20Presentation%5C%2015.05.2017.pdf (visited on 01/06/2020).

[101] Sigma Aldrich. *Carbon nanotube, single-walled, Arc Discharge.* 2020. URL: https://www.sigmaaldrich.com/catalog/product/aldrich/698695?lang=en&region=US (visited on 01/06/2020).

[102] OCSiAl. *OCSiAl Santa Clare Presentation*. 2014. URL: https://ocsial.com/assets/documents/xvsx_ocsial_santaclare_full-public.pdf (visited on 01/06/2020).

[103] An industry report indicated ~360 kg/yr capacity in 2007. It is assumed that this may have growth to order 1000 kg/yr [116].

[104] A high production rate lab-scale method performs growth in 6 inch diameter wafer with a carbon conversion efficiency of 61% [42]. During the growth stage of their recipe, the carbon precursor flow is 4 sccm acetylene, corresponding to 4.1 mg/min carbon percursor, thus a CNT production rate of 2.5 mg/min. Assuming 24/7/365 operation results in an production rate of 1.3×10^3 g/yr, rounded to 10^3.

[105] [67] report a production of single fiber from reactor of 0.08 g/km at a rate of 10 m/min, thus a production rate of 0.8 mg/min. Assuming continuous operation, this results in 4.2×10^2 g/yr, rounded to 10^2.

[106] [120] reports a process 'scale' of 10–50 g. Taking this to mean a production capability of 10–50 g/day, and assuming continuous operation results in a production rate of 3.65×10^3 to 1.5×10^4 g/yr, rounded to 10^4. Note that this is a post-processing method, so requires a synthesis method capable of adequate CNT control.

[107] [28] report 90% single chirality growth on substrate. Details on the synthesis conditions are sparse, however supplemental information estimates an areal density of 50 cnts/ 5 um diameter circle, or 6×10^8 $\#/cm^2$. [. 42] reported an areal density of 2×10^12 $\#/cm^2$, for an estimated production rate of 1.3×10^3 g/yr [104]. The production rate is estimated from the ratio of the areal densities as 3.9×10^{-1} g/yr, for a similar 6 inch substrate. A more typical substrate of 1 cm square gives 2.1×10^-3, rounded to 10^{-3} g/yr.

[108] [121] report aerosol measurements from aerosol CVD synthesis of SWCNTs for thin film production. They report CNTs of 1 nm diameter, 500 nm length, at a concentration of 2×10^6 $\#/cm^3$, with a flow rate of 6000 sccm. Assuming a single wall with areal density equal to that of graphene (38.18 $atoms/cm^2$), these dimensions indicate a mass of 1.2×10^{-18} g per CNT. Multiplying by The concentration and flow rate, a production rate of 1.4×10^-8 g/min is calculated. Assuming continuous operation, this is 7.53×10^{-3} g/yr, rounded to 10^{-2}.

[109] Ngoc Bui et al. "Ultrabreathable and Protective Membranes with Sub-5 nm Carbon Nanotube Pores". In: *Advanced Materials* 28.28 (2016), pp. 5871–5877.

[110] Aaron D Franklin. "Nanomaterials in transistors: From high-performance to thin-film applications". In: *Science* 349.6249 (2015), aab2750.

[111] R Tchoudakov et al. "Conductive polymer blends with low carbon black loading: polypropylene/polyamide". In: *Polymer Engineering & Science* 36.10 (1996), pp. 1336–1346.

[112] Liliane Bokobza et al. "Blends of carbon blacks and multiwall carbon nanotubes as reinforcing fillers for hydrocarbon rubbers". In: *Journal of Polymer Science Part B: Polymer Physics* 46.18 (2008), pp. 1939–1951.

[113] Sigma Aldrich. *Carbon nanotube, single-walled, Nanocyl, Inc.* 2020. URL: `https://www.sigmaaldrich.com/catalog/product/aldrich/755710?lang=en&region=US` (visited on 01/06/2020).

[114] Sigma Aldrich. *Carbon nanotube, single-walled, Zeonano.* 2020. URL: `https://www.sigmaaldrich.com/catalog/product/aldrich/900711?lang=en&region=US` (visited on 01/06/2020).

[115] M. Schauer, Principle Scientist, and E. Zeira, VP Product Development, at Nanocomp Technologies, Inc., personal communication. Oct. 2018.

[116] Ann Thayer. *Carbon Nanotubes By The Metric Ton*. 2020. URL: https://pubsapp.acs.org/cen/business/85/8546bus1.html (visited on 01/06/2020).

[117] Shahrzad Pourriahi. *Zeon opens carbon nanotubes plant in Japan*. 2015. URL: https://www.european-rubber-journal.com/2015/11/26/zeon-opens-carbon-nanotube-manufacturing-plant-japan (visited on 01/06/2020).

[118] OCSiAl. *Fire, Water and Nanotubes*. 2016. URL: https://ocsial.com/en/news/242/ (visited on 01/06/2020).

[119] Ramesh Jasti and Carolyn R Bertozzi. "Progress and challenges for the bottom-up synthesis of carbon nanotubes with discrete chirality". In: *Chemical physics letters* 494.1-3 (2010), pp. 1–7.

[120] Matteo Pasquali. *Carbon conductors for lightweight motors and generators*. 2019. URL: https://www.energy.gov/sites/prod/files/2019/07/f65/Projects19%20-%20Carbon%20Conductors%20for%20Lightweight%20Motors%20and%20Generators_Rice.pdf (visited on 01/06/2020).

[121] Dmitry V Krasnikov et al. "A spark discharge generator for scalable aerosol CVD synthesis of single-walled carbon nanotubes with tailored characteristics". In: *Chemical Engineering Journal* 372 (2019), pp. 462–470.

3. Perspective on FC-CVD limitations

Having established that FC-CVD is the leading process for the production of high quality SWCNTs at scale, this chapter seeks to understand the first-order limitations with respect to the quality of CNTs that can be produced (CNT properties, defect concentration, and assembly characteristics) and the capability of the process (production rate, input requirements).

3.1 Equilibrium defect concentration

The macroscopic properties in CNT assemblies, or the extent to which the nanoscale properties of the constituent CNTs are realized at the macro scale, are limited by the interfaces between CNTs. For example, strength is limited by the shear strength of overlapping CNTs, and electrical conductivity by the contact resistance between the end of each CNT and its neighbor, as the strength and conductivity within each CNT is significantly higher. Reducing the number of these interfaces through the use of longer CNTs should allow macroscopic properties to approach those of an individual CNT. Indeed, an experiment producing highly aligned fibers from a range of CNT types shows scaling of both fiber electrical conductivity and strength with constituent CNT length up to about 10 um [1]. Yet, as CNTs get longer, their individual properties also diminish due to the increased likelihood or frequency of lattice defects. The one dimensional nature

of nanotubes means that a single defect can drastically change or limit the properties. For example, simulations have shown certain types of defects can reduce mechanical properties by a factor of 2 to 10 [2]. While the type and density of defects varies widely depending on the exact experimental conditions, pioneering measurements shows that small diameter high-quality CNTs average one defect every 1 to 10 um [3].

Combining these observations, one could predict that, as fibers and other assemblies are made with individual CNTs longer than 10 um, this defect spacing, not the total CNT length, will become the critical length scale which controls the macroscopic properties of the fiber. While there is no theoretical limit on the length of CNTs that can be synthesized, there is a thermodynamic limit on the maximum lattice defect spacing (the inverse of defect concentration) in a pristine CNT.

CNTs can have many of the same topological defects as graphene or graphite, yet the energy of these defects may be influenced by the curvature of the lattice (and the orientation of the defect with respect to the tube, if not symmetric) and the likelihood of their formation also influenced by the unique environmental condition of a 1D structure and the CNT synthesis environment. Here we will focus on two examples of theoretically common defects to illustrate our analysis and highlight overarching trends. Defects with lowest energy will occur at the highest frequency, and because this is an exponential relationship, the contribution of high energy defects can be considered negligible. Thus, the essence of determining the equilibrium defect spacing is accurately estimating the defect energy. While some studies have estimated defect energy for some defects in graphene and specific (n, m) CNTs, a larger study to understand the role of (n, m) and curvature on the defect energy has not been done, and is the goal of this analysis.

Stone-Wales (SW): Composed of two pentagons and two heptagons, a SW defect can be conceptualized as the rotation of a C-C pair by 90 degrees (Figure 3.1b). While a single pentagon, heptagon, or pair of the two have slightly lower defect energies, the SW

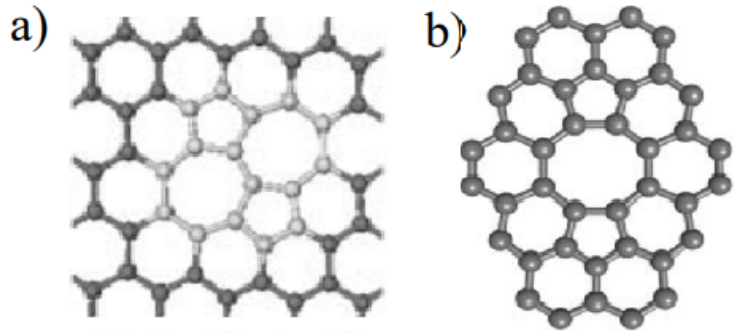

Figure 3.1: A) A Stone-Wales (SW) defect in a graphene lattice. B) A 5-8-5 divacancy in a graphene lattice. Reproduced from [4]

defect is otherwise the lowest energy lattice defect, with estimated defect energy ranging from 3 [5] to 5.5 eV [6] in various (n, m) CNTs up to 5 [7] to 6.3 eV [8] in graphene. The SW defect was also chosen because it is not symmetric with respect to the basis vectors as a pentagon or heptagon are, and does not cause a discontinuity in the lattice as a single pentagon-heptagon pair does.

Divacancy: It is hypothesized that vacancies, especially monovacanies with dangling bonds, are unlikely to persist in the CNT synthesis environment given the excess of free C in the environment that is readily accessible to the exposed 1D surface [4]. An exception here might be larger vacancies which allow a local re-organization of the lattice to prevent dangling bonds. The most simple example is a divacancy which has been ordered into two pentagons and an octagon (Figure 3.1c).

3.1.1 Molecular model for Stone-Wales defect

A Stone-Wales (SW) defect can be conceptualized as rotating a C-C bond by 90 degrees. For a lattice of M atomic sites there are a total of $\frac{3}{2}M$ bonds, ignoring end effects. In a CNT, these bonds can be divided into three groups, each with it's own orientation relative to the axis of the CNT. Because the energy of the SW defect, E_{sw}, may depend on this angle, we will consider these three groups as independent types of defects. It is

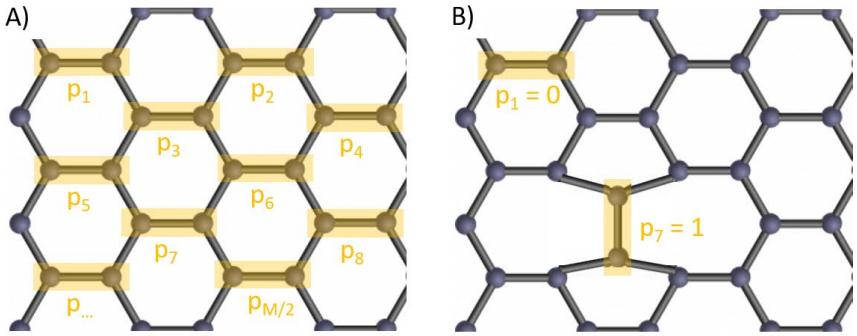

Figure 3.2: A) Diagram of molecular model showing use of C-C bonds in a single orientation as the description for the microstate. B) An example SW defect.

hypothesized that defect spacing is a function of the curvature of the CNT, as described by the chirality (n, m), but this is accounted for in the estimation of E_{sw}, not the molecular model.

Here we derive an equation for the equilibrium defect concentration for one of these orientations, noting that the equation will have the same form for all three, requiring just a substitution for the correct value of E_{sw}. In each orientation there are $M/2$ bonds, and we can define the microstate (Figure 3.2) of the system as:

$$v = \{p_i\} \qquad \text{for } i = 1 \text{ to } M/2 \tag{3.1}$$

where p_i indicates whether or not a pair has undergone a rotation (thus forming a SW defect), and P_v is the total number of defects:

$$p_i = \begin{cases} 0, & \text{if no bond rotation} \\ 1, & \text{if bond rotation} \end{cases} \tag{3.2}$$

$$P_v = \sum_{i=1}^{M/2} p_i \tag{3.3}$$

Thus, the energy of a microstate is $E_v = E_{sw}P_v$, assuming $E_v = 0$ for an ideal CNT and each SW defect has an energy of E_{sw}. Because the SW defect does not introduce a vacancy, we can assume fixed N, V, and T, and use the canonical ensemble to derive the partition function:

$$Q = \sum_v exp(-\beta E_v) = \sum_v exp\Big(\sum_{i=1}^{M/2}(-\beta E_{sw}p_i)\Big) \tag{3.4}$$

$$Q = \Big(1 + exp(-\beta E_{sw})\Big)^{M/2} \tag{3.5}$$

Noting that the average number of defects is proportional to the expectation value of the energy, it is computed as follows:

$$\langle P\rangle = \frac{1}{E_{sw}}\langle E\rangle = -\frac{1}{E_{sw}}\frac{\partial lnQ}{\partial \beta} \tag{3.6}$$

$$\langle P\rangle = -\frac{1}{E_{sw}}\frac{\partial}{\partial \beta} ln\Big[\Big(1 + exp(-\beta E_{sw})\Big)^{M/2}\Big] \tag{3.7}$$

$$\langle P\rangle = \frac{M}{2\Big(exp(\beta E_{sw}) + 1\Big)} \tag{3.8}$$

Finally, taking $\rho = f(n, m)$ as the atomic linear density of an (n, m) CNT, the characteristic defect spacing, L_{sw} is:

$$L_{sw} = \frac{2\Big(exp(\beta E_{sw}) + 1\Big)}{\rho} \tag{3.9}$$

Note that L_{sw} describes only the characteristic spacing of the orientation that cor-

responds to the value of E_{sw} that was used. For a given (n, m), three values of L_{sw} will be found, and the total spacing is the inverse of the sum of the inverses. The ability to superimpose these models relies on the assumption of low defect concentration, such that the probability of adjacent or overlapping defects is negligible.

Modification for divacancy defect

A similar molecular model for the case of a divacancy can be derived by substituting the removal of a pair of adjacent atoms for the rotation or the pair. And the energy of the microstate is similarly $E_v = E_{di}P_v$, where E_{di} is the energy of a divacancy defect. Because N is no longer constant, we find the partition function in the Grand Canonical ensemble:

$$\theta = \sum_v exp(-\beta E_v + \beta \mu_p P_v) \tag{3.10}$$

where $\mu_p = 2\mu_C$ is the chemical potential of a pair of carbon atoms. And following similar manipulations we arrive at a simplified version of the partition function and an expression for L_{di}, the defect spacing for a particular orientation of divacancy defects:

$$\theta = \Big[exp(-\beta E_{di}) + exp(\beta \mu_p)\Big]^{M/2} \tag{3.11}$$

$$L_{di} = \frac{2\Big[exp\Big(\beta(E_{di} + \mu_p)\Big) + 1\Big]}{\rho} \tag{3.12}$$

3.1.2 Defect energy estimation methods

In order to apply the equations for L_{sw} and L_{di} we need to estimate E_{sw} and E_{di} for defects on all (n, m) CNTs in each of 3 orientations. Density Functional Theory (DFT) models are often employed to estimate these values as experimental measurement is difficult. A range of published studies have used DFT to look at specific types of defects in specific chirality CNTs or graphene [9, 10], but none have systematically investigated the influence of (n, m) on the energy for a specific defect as needed here. DFT studies are computationally intensive and require great expertise to ensure accurate results. Lacking these resources, here we employ molecular dynamics simulations as a first-pass analysis.

A custom Matlab program is used to define the geometry of a CNT segment with arbitrary (n, m) and create a SW defect or divacancy at any of three orientations. This geometry is input to LAMMPS [11], a classical molecular dynamics code, and allowed to relax using the Airebo potential, which has been widely used for simulations of hydrocarbons [12], until the forces on all atoms are below 0.02 eV/A. Periodic boundary conditions are used, and the minimum length of the CNT segment is 10 nm. Longer is used when required as the periodicity of the CNT structure varies with chirality. Comparison of the total energies of systems with and without a defect is used to calculate the defect energy as follows:

$$E_{sw} = E_{sw}^{MD} - E_{ideal}^{MD} \tag{3.13}$$

$$E_{di} = E_{di}^{MD} - E_{ideal}^{MD} + 2\frac{E_{ideal}^{MD}}{M} \tag{3.14}$$

Where the $2\frac{E_{ideal}^{MD}}{M}$ term accounts for the different number of atoms in the divacancy simulation.

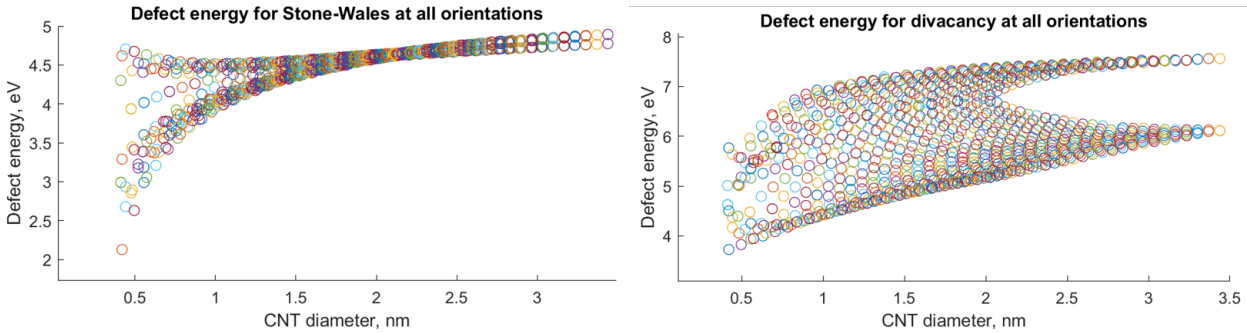

Figure 3.3: Estimated E_{sw} (A) and E_{di} (B) for each orientation for all chiralities (n, m) below $(25, 25)$.

3.1.3 Results

A custom program was written to automate the running of the 7 needed simulations for all chiralities below $(25, 25)$. A temperature of 3000K is used for the equilibrium calculation as representative of conditions in laser or plasma synthesis processes.

Figure 3.3 shows estimated values for E_{sw} ranging from 2 to 3 eV for narrow CNTs up to 4.5 to 5 eV for larger diameter CNTs. This is in general agreement with the range of literature values cited earlier, and shows the expected asymptotic behavior towards the value for graphene as diameter increases. At smaller diameters the curvature is greatest, and the effect of this anisotropy is most pronounced, resulting in a large range in E_{sw} depending upon orientation. We observe similar trends for E_{di}. The apparent bifurcation of E_{di} is an artifact of the range of chiral values simulated. There are many possible (n, m) choices to give approximately the same CNT diameter, and for small diameters there were all simulated. However at the larger diameter range of our study, many of these were above the $(25, 25)$ threshold. For example, at diameter of 3.4 nm, the only simulated CNT is the $(25, 25)$, yet a $(26, 24)$, $(27, 23)$, etc. all have similar diameter and would result in different E_{di} - presumably filling in the envelope between the two asymptotes as occurs at smaller diameters.

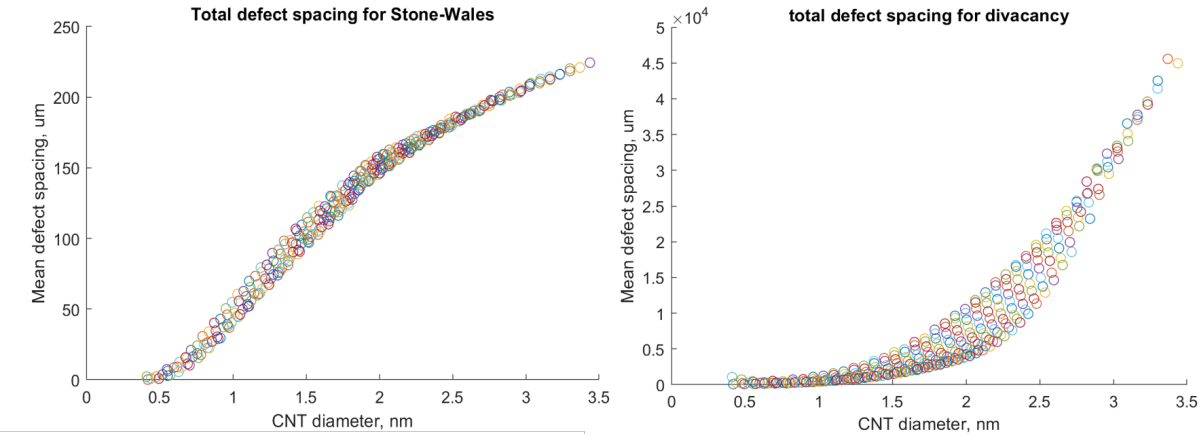

Figure 3.4: Estimated total L_{sw} (A) and L_{di} (B) for all chiralities (n, m) below $(25, 25)$.

Figure 3.4 shows total defect spacing for SW and divacancies. In both cases these collapse to a tighter range than E, as the total spacing for a given chirality is dominated by the lowest energy defect orientation. For constant E, one would expect L to decrease linearly with diameter due to the scaling of ρ. Yet, the gradual increase of the minimum E_{sw} and E_{di} with diameter overwhelms this effect, and L increases monotonically in this diameter range. Hypothetically, at some large enough diameter E_{sw} and E_{di} will level out as the curvature is negligible and L will peak and then decrease. However the experimental synthesis of single-wall CNTs with diameters above 4 nm is extremely rare.

3.1.4 Summary

Using molecular dynamics approach we have been able to estimate E_{sw} and E_{di} for each defect orientation for all chiralities below $(25, 25)$. While we find general agreement with DFT estimates, further validation, sensitivity analysis to simulation parameters, and possibly the use of a more accurate (but computationally intensive) potential such as ReaxFF, should be undertaken to validate these preliminary conclusions.

These extensive simulations highlight the role of curvature, thus CNT diameter, in reducing E_{sw} and E_{di} from that of planar graphene, and thus increasing the defect

concentration, and decreasing L for small diameters. This highlights a critical gap between DFT models (typically limited to diameters below 1 nm by computational complexity) and actual CNTs with diameter greater than 1 nm. We also find that, given a certain diameter, the ultimate role of chirality is relatively minor.

In all cases, the estimated equilibrium defect spacing is orders of magnitude longer than what has been experimentally observed for the highest quality CNTs. Additional consideration of more defect types will reduce the estimated L, yet is unlikely to account for this discrepancy. This indicates that current synthesis techniques have significant room for improvement and are dominate by non-equilibrium processes. This also suggests that high temperature annealing may be a beneficial post-processing treatment. If synthesis or post-processing can be improved to the extent that this becomes the limiting factor, the observed trend suggests a focus on larger-diameter CNTs to improve L further.

3.2 Productivity

3.2.1 CNT mass concentration and its factors

Given the diversity of FC-CVD systems reported in the literature and used commercially, it can be difficult to directly compare the productivity of different systems or approaches. In part, this is due to the spectrum of CNT quality that may be produced - each system may be best characterized by a quality versus quantity curve over the extent of its operating window, rather than a single point as often reported. Yet, the dimensions of quality and quantity are not clearly and universally defined. Having already discussed aspects of individual CNT quality, this section focuses on characterizing the productivity of FC-CVD systems in a generalizable way.

As described in Section 2.6.2, the primary operating costs for a FC-CVD process are the carrier gas and the energy needed to heat the carrier gas. In contrast, the flows of carbon and catalyst are relatively small, thus their cost is as well. Thus, the number or mass of CNTs per volume of carrier gas (number concentration and mass concentration) are economically useful metrics as they indicate the ratio of value produced in the product to operating cost. The number and mass concentration are also relevant from a process physics perspective, as the number concentration of aerosol particles and their size governs aerosol dynamics which influence the synthesis process. Finally, normalizing the production rate in such a way allows comparison across reactor scales and flow rates.

Theoretically, the mass concentration can be related to the CNT properties and number concentration using a simple relationship:

$$\rho_{CNT} = m_{CNT}\ N_{cat}\ \eta_{nuc} \tag{3.15}$$

where ρ_{CNT} is the mass concentration of CNTs, m_{CNT} is the mass of an individual CNT, N_{cat} is the number concentration of catalyst particles, and η_{nuc} is the nucleation efficiency – the fraction of catalyst particles which nucleate a CNT. The mass of a CNT can be calculated from the diameter (d_{CNT}), length (L_{CNT}), and the areal density of a graphene lattice ($\rho_{graphene} = 7.63E-8 g/cm^2$, assuming only a single wall):

$$m_{CNT} = \pi\ d_{CNT}\ L_{CNT}\ \rho_{graphene} \tag{3.16}$$

For a few-walled MWCNT, the mass will scale roughly in proportion with the wall number. The mass concentration of the catalyst particles can also be calculated as:

$$\rho_{cat} = m_{cat}\ N_{cat} \tag{3.17}$$

where the mass of an individual catalyst particle (m_{cat}) is calculated assuming a sphere with density equal to metallic iron (ρ_{Fe}):

$$m_{cat} = \frac{4}{3}\,\pi\,(\gamma\,d_{CNT}/2)^3\,\rho_{Fe} \tag{3.18}$$

The diameter of the catalyst particle is given by $\gamma\,d_{CNT}$, where γ is a scaling factor to relate the diameter of the catalyst particle to that of the CNT. As discussed in Section 2.3.3, γ values of 1 to 4 have been observed experimentally in FC-CVD systems with d_{CNT} = 1–2 nm.

Figure 3.5 shows the estimated CNT mass concentration, ρ_{CNT}, and weight percent of catalyst particles as a function of CNT diameter and length. A catalyst particle concentration of $N_{cat} = 10^9$ #/cm^3 is taken as a typical value for high catalyst concentration systems (see Chapter 4), and a nucleation efficiency of $\eta_{nuc} = 0.1$ is assumed.

In order to maximize the mass concentration of CNTs and minimize the weight percent of catalyst, longer CNTs and a higher nucleation efficiency are required. Increasing the CNT diameter increases CNT mass concentration linearly, while increasing the catalyst mass concentration to the third power, thus also increasing the iron weight fraction. In this analysis, increasing the concentration of catalyst particles is also seen as increasing the CNT mass concentration while not effecting the iron weight percent. In practice, the dynamics of aerosol nucleation and growth result in a coupling between catalyst particle concentration and diameter, making it difficult to maintain a small catalyst diameter at high concentrations (see Chapter 4 for a more detailed exploration of this connection).

Similarly, the length of the CNT can not be increased without bound. The linear growth rate is estimated to be of order 100 µm/s [13], with residence times ranging from 1–60 s [14] for a survey of high productivity FC-CVD reactors. Yet, if growth

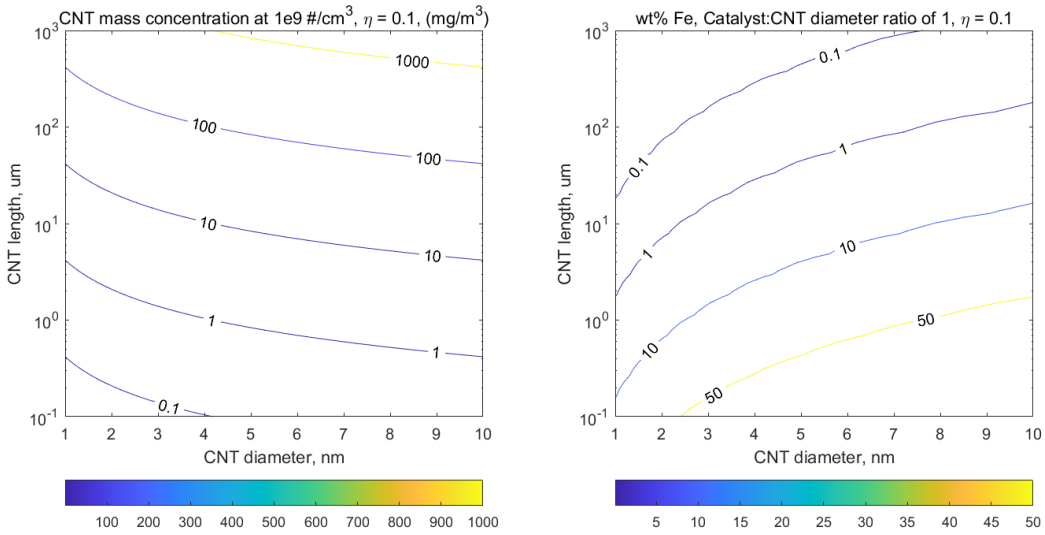

Figure 3.5: Calculated mass concentration of CNTs and iron weight percent as a function of CNT diameter and length for a catalyst particle concentration of $N_{cat} = 10^9$ #/cm^3 and a nucleation efficiency of $\eta_{nuc} = 0.1$ Note that SWCNTs typically do not grow with diameter greater than 4-5 nm. To account for multiple walls, the CNT mass concentration can be multiplied by the average number of walls, and the iron weight percent divided by the same.

termination is caused by, among other mechanisms, the mechanical confinement that is caused by CNT bundling, and bundling is caused by aerosol collisions between individual CNTs, then the upper limit of CNT length may be less than then 100–6000 µm predicted based on residence time alone.

3.2.2 Bundling timescale via aerosol dynamics

The timescale for onset of bundle formation, τ_B, can be defined by the timescale for a halving of aerosol concentration via aggregation. On average, a halving of the number concentration means that each aerosol particle is now a bundle of two CNTs. For a monodisperse aerosol, this is given by:

$$\tau_B = \frac{2}{\beta \ N_{CNT}} \tag{3.19}$$

where N_{CNT} is the initial number concentration of CNTs and β is the CNT collision kernel [15]. β is commonly estimated using the Brownian coagulation coefficient model for spherical aerosol particles. For equally sized particles, the model can be stated as:

$$\beta = 8 \ \pi \ D \ D_p \ \left(\frac{D_p}{D_p + 2^{3/2} g} + \frac{8 \ D}{2^{1/2} \ c \ Dp} \right)^{-1} \tag{3.20}$$

where D_p is the diameter of the particle. D, g, and c are given as follows:

$$D = \frac{k \ T \ C_c}{3 \ \pi \ \mu \ D_p} \tag{3.21}$$

$$g = \frac{1}{3 \ D_p \ l} \left((D_p + l)^3 - ({D_p}^2 + l^2)^{3/2} \right) - D_p l = \frac{8 \ D}{\pi \ c} \tag{3.22}$$

$$c = \left(\frac{8\ k\ T}{\pi\ m_{CNT}} \right)^{1/2} \tag{3.23}$$

where μ is the gas viscosity. The slip correction factor, C_c, and Knudsen number, Kn, are defined as follows based on the mean free path of the gas, λ,

$$C_c = 1 + Kn\ \left(1.257 + 0.40\ exp\left(\frac{-1.10}{Kn} \right) \right) \tag{3.24}$$

$$Kn = \frac{\lambda}{D_p/2} \tag{3.25}$$

An effective D^{eff} is needed for the collision of CNTs due to their high aspect ratio shape. For a particle of any shape, the collision cross section is the projected area of the particle in the plane perpendicular to it's motion relative to it's collision partner.

First, the actual shape of the CNT in the aerosol phase must be determined. As-collected CNTs are rarely straight, often exhibiting significant curvature. Are the thermal fluctuations a CNT experiences as an isolated aerosol particle sufficient to cause its shape, statistically, to deviate from a rigid rod? This can be assessed using the worm-like chain model used to describe the statistical shape of long semi-flexible polymer chains [16]. The root mean square end-to-end distance of the CNT (D_p) is given by:

$${D_p}^2 = 2\ P\ L_{CNT}\ \left(1 - \frac{P}{L_{CNT}} \left(1 - exp\left(\frac{-L_{CNT}}{P} \right) \right) \right) \tag{3.26}$$

where P is the persistence length which is a measure of the bending stiffness of the CNT relative to the strength of thermal fluctuations. For the thin cylindrical shell, P is proportional to the cube of the diameter as follows:

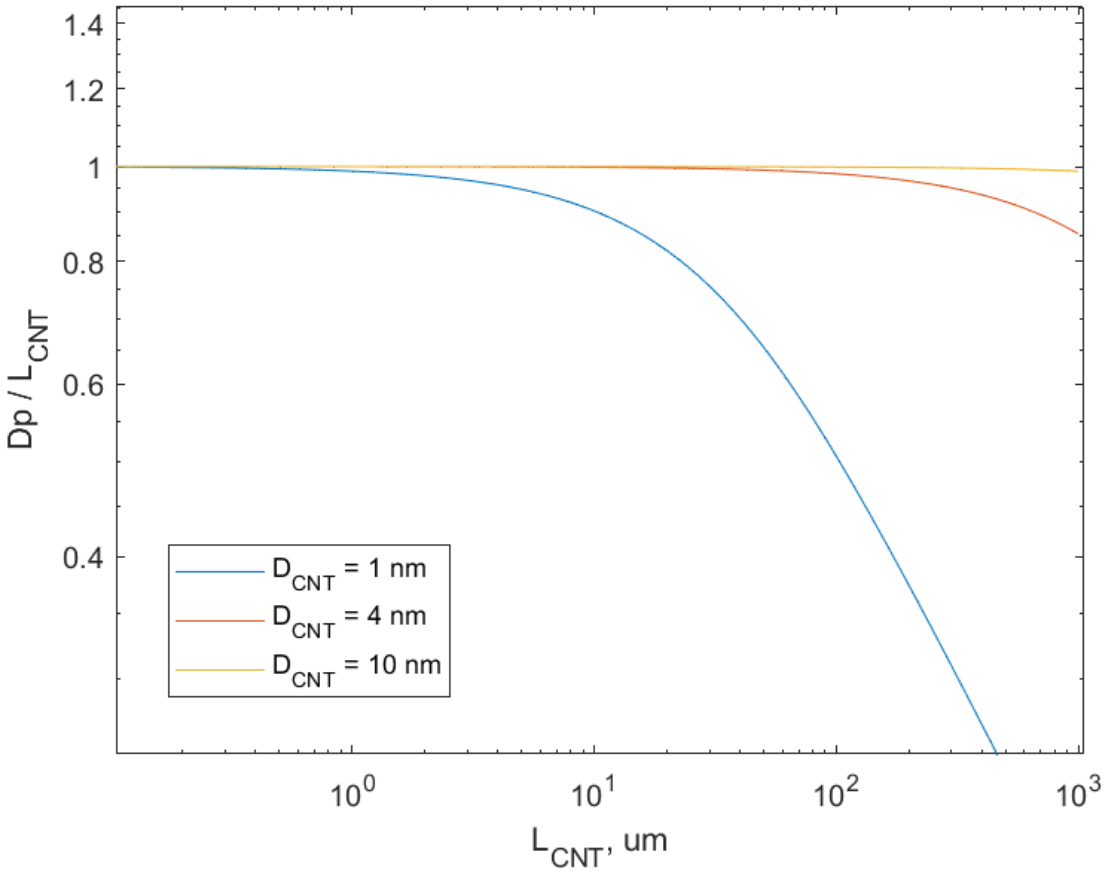

Figure 3.6: Calculated effective shortening of CNTs in the aerosol phase due to thermal fluctuations using the worm-like chain model.

$$P = \frac{C\ \pi\ (d_{CNT}/2)^3}{k_b\ T} \tag{3.27}$$

where $C = 678$ J/m^2 has been determined semi-empirically for SWCNTs [17]. Fakhri et al. report an average persistence length of 60 μm for CNTs with a diameter of 1 nm at 20 °C, which can be extrapolated to a value of ~15 mm for a hypothetical 10 nm diameter SWCNT.

Figure 3.6 shows the ratio of the root-mean-square end-to-end distance of the CNT (D_p) to the actual CNT length (L_{CNT}) as a function of L_{CNT} for CNT diameters of

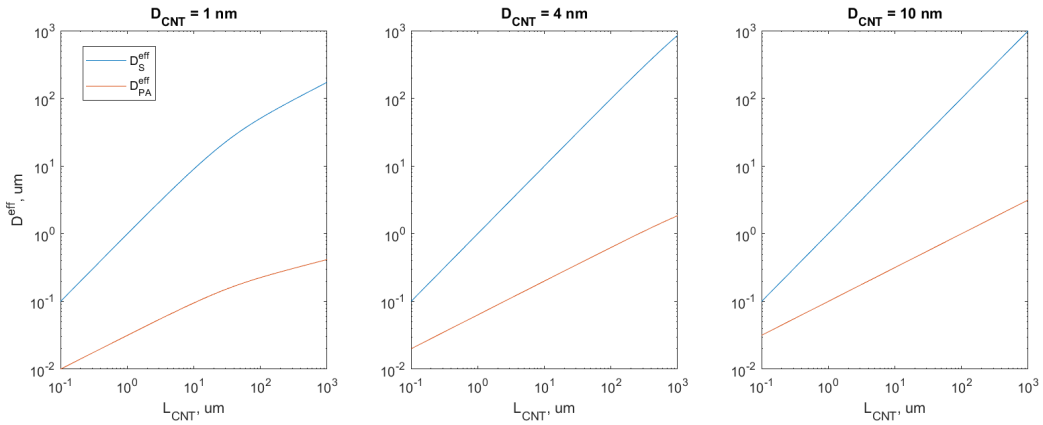

Figure 3.7: Calculated effective collision diameter for CNT diameters of 1, 4, and 10 nm at 1000 °C using the spherical and projected area approximations.

1, 4, and 10 nm at 1000 °C to represent conditions within a FC-CVD reactor. At this temperature, the persistence length of 1, 4, and 10 nm diameter CNTs is 15 μm, 970 μm, and 15 mm.

Second, this effective length must be related to the collision cross sectional area. For a low aspect ratio particle, typically the average projected area is calculated (1/4 the surface area for an arbitrary convex solid shape [18]). Alternatively, for a highly-tortuous high aspect ratio particle, the actual size and shape of the particle, with respect to collisions, would be better approximated by an envelope that encloses it. For the randomly varying shape of a long CNT where $L_{CNT} \gg P$, this envelope can be approximated by a sphere with diameter D_p [16]. Given the range of L_{CNT} considered here, the projected area relationship is likely a more accurate representation. These two definitions are respectively:

$$D^{eff}{}_{pa} = 2 \left(\frac{1}{4\,\pi} A_{CNT}\right)^{1/2} = (d_{CNT}\ D_p)^{1/2} \tag{3.28}$$

$$D^{eff}{}_{wm} = D_p \tag{3.29}$$

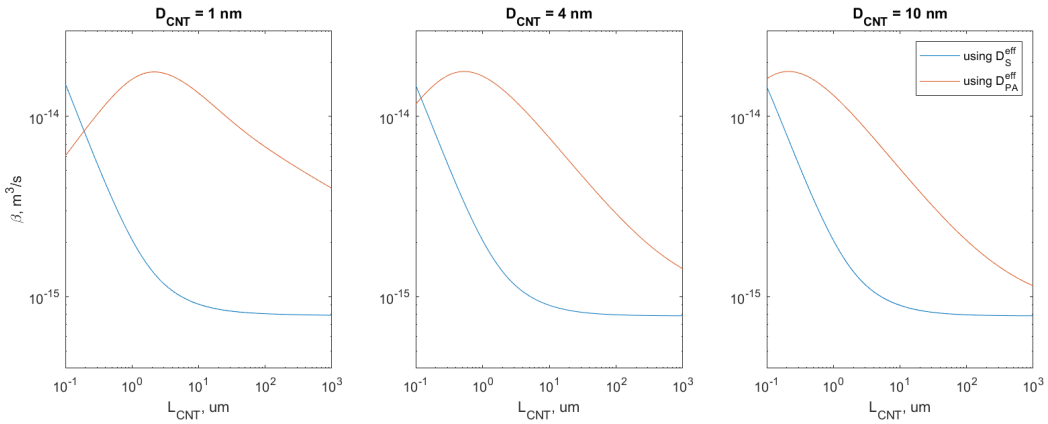

Figure 3.8: The collision kernel β for CNT diameters of 1, 4, and 10 nm at 1000 °C in helium using the spherical and projected area approximations.

While these two approximations diverge significantly, especially for larger values of L_{CNT}, they serve to define a window of possible values. Finally, the collision kernel β is calculated using these six functions for D_p (Figure 3.8). Over the entire range of L_{CNT}, β is approximately in the range of 10^{-15} to 10^{-14} m^3/s as a result of the weak dependence on D_p.

3.2.3 Bundle-limited maximum CNT number and mass concentration

Finally, this bundling analysis can be used to consider the upper limit of CNT number concentration. Taking τ_B as the average time available for a CNT to grow before bundling, Figure 3.9 shows the minimum τ_B required for a given L_{CNT} using the previously stated growth rate of 100 μm/s as well as a hypothetical higher growth rate of 500 μm/s. In other words, in order to have sufficient time for CNTs to grow to a given L_{CNT}, not only must the residence time in the growth region of the furnace be greater than this minimum τ_B, but the aerosol CNT concentration must be sufficiently low that the τ_B calculated from it's bundling is equal to or greater than the minimum τ_B.

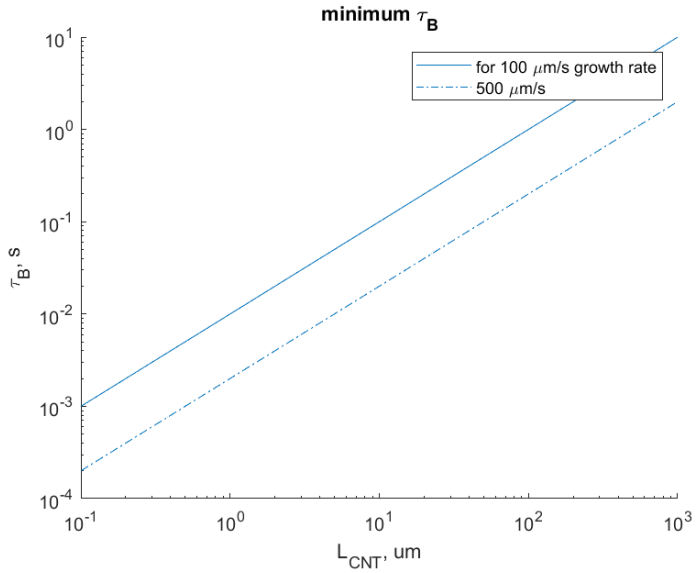

Figure 3.9: The minimum τ_B required for a given L_{CNT} using a growth rate of 100 μm/s or 500 μm/s.

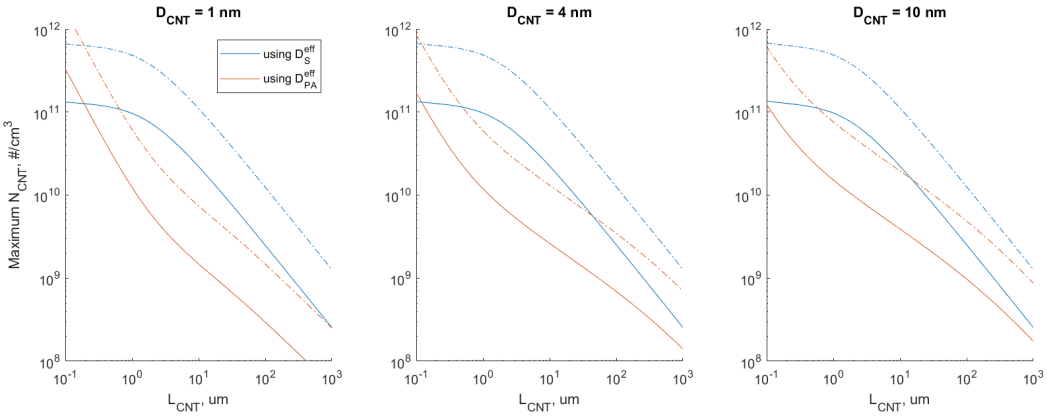

Figure 3.10: The maximum CNT number concentration, N_{CNT}, can be found as a function of τ_B using β values shown in Figure 3.8 and Equation 3.19. N_{CNT} as a function of τ_B is mapped to L_{CNT} using the relation in Figure 3.9. Solid lines correspond to a growth rate of 100 μm/s, while dashed lines correspond to 500 μm/s.

Using the previously found estimates for β (Figure 3.8), the maximum CNT number concentration, N_{CNT}, can be found as a function of τ_B using Equation 3.19 and therefore as a function of L_{CNT} (Figure 3.10. As one point of verification for this analysis, Hoecker et al. observe a catalyst concentration threshold of ~10^9 for the formation of a CNT aerogel in their FC-CVD system, based on in situ aerosol measurements, indicating the onset of significant CNT bundling [19]. They also report a CNT diameter, albeit of MWCNTs, of ~10 nm and length of 100–1000 μm, placing their operation roughly within the window bounded by the two curves at different β_B values in Figure 3.10, assuming a nucleation efficiency of η_{nuc} = ~0.1 [19]. This finding may help explain the difficulty of operating under conditions which enable the formation of an aerogel and direct spinning, and indicates the difficulty of significantly increasing the productivity of direct spinning further. Once the residence time, catalyst concentration (and nucleation efficiency), and CNT growth rate are high enough to hit this bundling threshold, further increases will have diminishing returns towards increasing CNT production. As aerogel formation requires additional bundling and collisions beyond the pair-wise limit explored here, one must either hope that the number or mass concentration at the CNT bundling limit is sufficient to form a cohesive aerogel given enough time, or rely on the decreasing fraction of still-active catalysts to make up the additional difference.

Figure 3.11 shows the maximum CNT mass concentration, ρ_{CNT}, for the same cases. In general, because of the inverse relationship between the maximum N_{CNT} and L_{CNT} (which is proportional to the CNT mass), ρ_{CNT} is not strongly influenced by L_{CNT} for a given CNT diameter. The variation that is seen as a function of L_{CNT} is entirely due to variation in β. Likewise, the mass of an individual CNT increases linearly with diameter, resulting in the increased ρ_{CNT} for the 4 and 10 nm diameter cases.

Figure 3.12 shows the minimum iron catalyst weight percent, assuming a nucleation efficiency of η_{nuc} = ~0.1 and a ratio of catalyst diameter to CNT diameter of $\gamma = 2$.

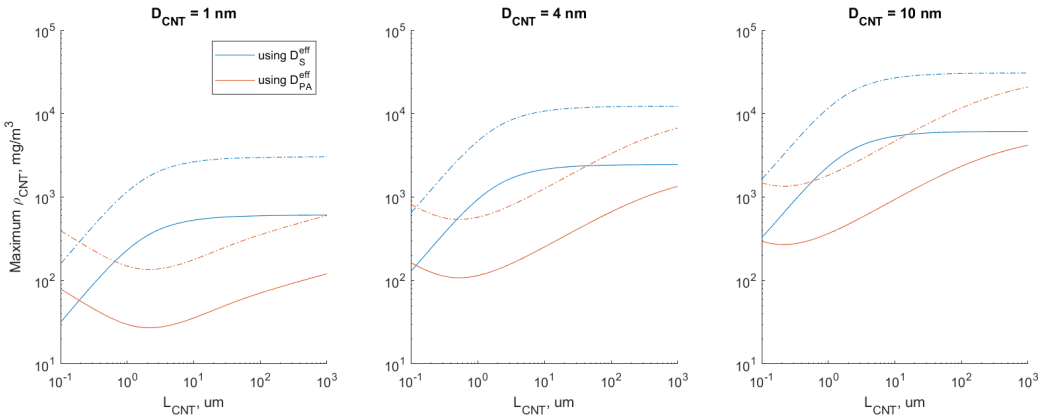

Figure 3.11: The maximum CNT mass concentration, ρ_{CNT}, based on N_{CNT} using using β values shown in Figure 3.8. Solid lines were calculated using values of N_{CNT} corresponding to a growth rate of 100 μm/s, while dashed lines correspond to 500 μm/s.

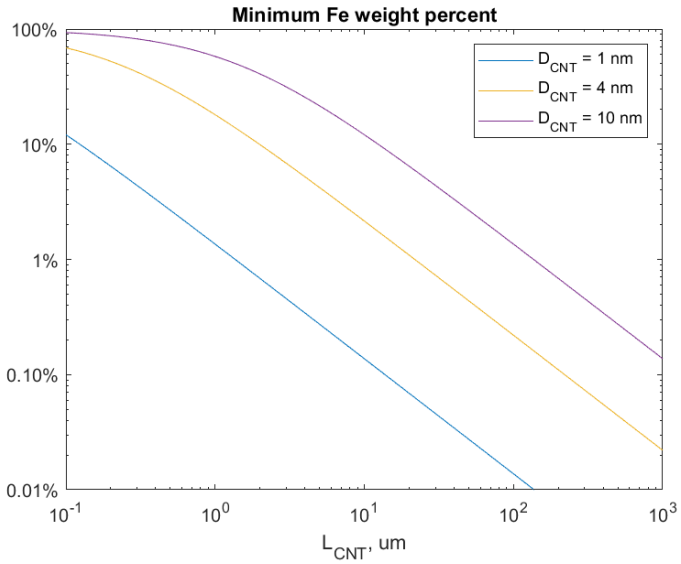

Figure 3.12: The minimum iron catalyst weight percent assuming a nucleation efficiency of $\eta_{nuc} = \sim 0.1$ and a ratio of catalyst diameter to CNT diameter of $\gamma = 2$. Because the concentration of CNTs does not factor in to this calculation, a single curve is valid for both CNT growth rates and different models for the collision area.

Because the concentration of CNTs does not factor in to this calculation, a single curve is valid for both CNT growth rates and different models for the collision area.

3.3 Conclusion

In this chapter the upper bounds for the performance of a FC-CVD system have been investigated with respect to the quality of individual CNTs and the overall production rate. The equilibrium defect concentration is far below that observed in current high quality SWCNTs, indicating that there is no fundamental reason that this cannot be further improved in practice. While lattice defects are only one dimension of the quality of a CNT assembly, they play an outsized role in limiting the material properties of individual CNTs, and therefore the maximum properties that could be achieved in a macroscopic assembly.

The four controls on CNT mass concentration, ρ_{CNT}, in a FC-CVD reactor have been explored: catalyst number concentration, CNT nucleation efficiency, CNT diameter, and CNT length. In isolation, each of these has a linear influence on ρ_{CNT} and all should be considered as potential routes to higher productivity. In practice, second-order interactions between them, the maximum ρ_{CNT} limit due to bundling and additional quality-related objectives, reduce the efficacy of these controls. Notably, the CNT nucleation efficiency in part depends on the catalyst particle size distribution, and the catalyst particle size distribution and concentration are linked via aerosol aggregation dynamics. Among the four, CNT diameter may be the least important control, given the small range of ~1-5 nm in practice, the non-linear increase in minimum catalyst mass fraction with increasing diameter, and the fact that CNT diameter is also a central aspect of quality.

Alternatively, there potential range for CNT length is many orders of magnitude,

and there is a positive correlation between CNT length and macroscopic assembly properties [1]. At low concentration, this can be improved equivalently by either increasing the growth residence time or the growth rate. However, at number concentrations approaching the bundling limit, a high growth rate is preferable because τ_B provides an upper limit of the effective or active residence time.

While ρ_{CNT}, N_{CNT}, and other important values are not typically reported, the author's sense is that most synthesis for small diameter (1–3 nm) SWCNTs is in the range ρ_{CNT} = 1–10 mg/m^3 and thus has at least one to two orders of magnitude of potential improvement. In contrast, synthesis of larger (5–10 nm) SWCNTs and MWCNTs which typically occurs in direct-spinning systems can be up to ρ_{CNT} = 1–10 g/m^3 and is already at the point of diminishing returns. In the latter case, the most effective means for further increases in production rate are to reduce bundling either through a higher growth rate (the reason many operate at unusually high temperature [14]) or through the application of novel forces like electric fields to control the aerosol dynamics and aggregation [20].

In the former case, for small diameter SWCNTs, an 'all of the above' approach is warranted. Empirical catalyst material impurities (or, likewise, precursor flow rates) are typically orders of magnitude higher than the minimum estimated here (1–10 wt% rather than ~0.01 wt% for 100 μm length [14]), indicating very low CNT nucleation efficiency. Further, aerosol measurements show only a small fraction of the input catalyst material forms catalyst particles (As will be discussed further in Chapter 4), indicating that the formation of catalyst particles also has a low efficiency.

Taking all of these factors into account, the author's perspective is that the formation of catalyst particles and their nucleation efficiency once formed are the two weakest links in the synthesis of narrow diameter, high quality SWCNTs in a FC-CVD system. Improvements in these areas have the potential for orders of magnitude improvement

in CNT assembly quality metrics (catalyst mass fraction) and system quantity metrics (number and mass concentration of CNTs). This perspective undergirds the motivation and key research questions outlined in Chapter 1.

References

[1] Dmitri E Tsentalovich et al. "Influence of carbon nanotube characteristics on macroscopic fiber properties". In: *ACS applied materials & interfaces* 9.41 (2017), pp. 36189–36198.

[2] Liyan Zhu, Jinlan Wang, and Feng Ding. "The great reduction of a carbon nanotube's mechanical performance by a few topological defects". In: *ACS nano* 10.6 (2016), pp. 6410–6415.

[3] Yuwei Fan, Brett R Goldsmith, and Philip G Collins. "Identifying and counting point defects in carbon nanotubes". In: *Nature materials* 4.12 (2005), p. 906.

[4] Philip G Collins. "Defects and disorder in carbon nanotubes". In: *Oxford University Press: Oxford* (2010).

[5] Hanqing Jiang et al. "Defect nucleation in carbon nanotubes under tension and torsion: Stone–Wales transformation". In: *Computer Methods in Applied Mechanics and Engineering* 193.30-32 (2004), pp. 3419–3429.

[6] R Conversano et al. In: *Nanotubes and Related Materials, MRS Symposia Proceedings No. 633* MRS Symposia Proceedings No. 633 (2001).

[7] Ge G Samsonidze, GG Samsonidze, and BI Yakobson. "Energetics of Stone–Wales defects in deformations of monoatomic hexagonal layers". In: *Computational materials science* 23.1-4 (2002), pp. 62–72.

[8] Qingzhong Zhao, Marco Buongiorno Nardelli, and Jerry Bernholc. "Ultimate strength of carbon nanotubes: A theoretical study". In: *Physical Review B* 65.14 (2002), p. 144105.

[9] José Eduardo Padilha et al. "Energetics and stability of vacancies in carbon nanotubes". In: *Solid state communications* 151.6 (2011), pp. 482–486.

[10] Wenchao Tian et al. "A review on lattice defects in graphene: types, generation, effects and regulation". In: *Micromachines* 8.5 (2017), p. 163.

[11] Steve Plimpton. "Fast parallel algorithms for short-range molecular dynamics". In: *Journal of computational physics* 117.1 (1995), pp. 1–19.

[12] Steven J Stuart, Alan B Tutein, and Judith A Harrison. "A reactive potential for hydrocarbons with intermolecular interactions". In: *The Journal of chemical physics* 112.14 (2000), pp. 6472–6486.

[13] Fiona Smail, Adam Boies, and Alan Windle. "Direct spinning of CNT fibres: Past, present and future scale up". In: *Carbon* 152 (2019), pp. 218–232.

[14] Lee Weller et al. "Mapping the parameter space for direct-spun carbon nanotube aerogels". In: *Carbon* 146 (2019), pp. 789–812.

[15] Sheldon K Friedlander et al. *Smoke, dust, and haze*. Vol. 198. Oxford university press New York, 2000.

[16] Masao Doi and Samuel Frederick Edwards. *The theory of polymer dynamics*. Vol. 73. oxford university press, 1988.

[17] Nikta Fakhri et al. "Diameter-dependent bending dynamics of single-walled carbon nanotubes in liquids". In: *Proceedings of the National Academy of Sciences* 106.34 (2009), pp. 14219–14223.

[18] Zachary Slepian. "The average projected area theorem-generalization to higher dimensions". In: *arXiv preprint arXiv:1109.0595* (2011).

[19] Christian Hoecker et al. "The Dependence of CNT Aerogel Synthesis on Sulfur-driven Catalyst Nucleation Processes and a Critical Catalyst Particle Mass Concentration". In: *Scientific reports* 7.1 (2017), p. 14519.

[20] Liron Issman et al. "Highly oriented direct-spun carbon nanotube textiles aligned by in situ radio-frequency fields". In: *ACS nano* 16.6 (2022), pp. 9583–9597.

4. Microplasma synthesis of aerosol catalyst nanoparticles

This chapter describes the development of a microplasma-based reactor, with application to iron nanoparticles synthesis for CNT manufacturing. The microplasma is a DC discharge operated in helium or argon at atmospheric pressure with a plasma residence time of 1–10 μs and power of $\sim$ 100 mW. Ferrocene vapor is used as an iron precursor. We characterize the microplasma performance over a range of operating conditions, in terms of particle size distribution and output aerosol concentration. We show that despite significant electrostatic enhancement of the particle growth rate, the growth rate is orders of magnitude too slow to occur entirely within the plasma. Thus, most particle growth occurs downstream of the plasma, enhanced by the residual particle charges from the plasma, and is controlled not only by the plasma conditions (which specify the residual charge distribution) but also the downstream conditions (which controls the dissipation of those charges).

The design and fabrication of the reactors described in Section 4.2 was done as part of the author's S.M. thesis [1]. Additionally, Section 4.3 summarizes the key results obtained with these reactors during the S.M. thesis, and the reader is referred there for additional information:

Sawyer, W. J., Toward improved manufacturing of carbon nanotubes by microplasma

synthesis of catalyst nanoparticles, S.M. Thesis, Massachusetts Institute of Technology, Department of Mechanical Engineering, 2020

The remainder of the chapter communicates work done as part of the PhD, including text adapted and abridged from the following journal article:

Sawyer, W. J., and A. John Hart. High-yield microplasma synthesis of monodisperse sub-3 nm diameter metal nanoparticles explained by a charge-mediated formation mechanism. *Journal of Aerosol Science* 161 (2022): 105915

At the time of development, the performance of these systems, to the author's knowledge, pushed the limits for small diameter, high concentration, and controllable aerosol nanoparticle generation. Many aspects of this performance have since been superceded by a subsequent version of the microplasma reactor, the focus of Chapter 5. Yet, this work remains relevant for developing the understanding and practical knowledge that enabled this subsequent improvement.

4.1 Background on nanoparticle synthesis techniques

Broadly, nanoparticle synthesis processes follow either a wet chemical approach, typically resulting in a colloidal solution, or a physical approach resulting in an aerosol or powder. While chemical approaches have demonstrated excellent size and structure control [2], this is typically a multi-step batch process and the residue from the solvents and surfactants can result in contamination depending on the application [3]. Physical approaches, such as flame pyrolysis, electrospray, and vapor condensation, are better suited for continuous, high throughput synthesis of pristine particles with sizes ranging from $\sim$ 10 nm to microns [4].Yet, due to agglomeration and particle losses via Brownian

and thermophoretic forces, it is difficult to synthesize unagglomerated, < 5 nm particles at high concentration [5]. These mechanisms continue to act after synthesis, thus fine aerosols are not easily stabilized for processing or storage. For applications that utilize nanoparticles below ~ 10 nm in an aerosol, or require their deposition onto a substrate, in situ aerosol generation is attractive if particle size can be controlled with requisite precision and yield.

One such application of metallic nanoparticles is as catalysts for carbon nanotube (CNT) synthesis. Aerosol synthesis of CNTs typically utilizes a continuous flow, high temperature, tubular reactor [6], wherein catalyst nanoparticles are generated thermally from an organometallic precursor. At the entrance of the reactor, the precursor, such as ferrocene vapor, pyrolyzes into a super-saturated iron vapor which condenses into nanoparticles [7, 8]. This aerosol continues to flow into the reactor, where interaction with one or more carbon-containing gases leads to the nucleation and growth of CNTs from the particles. Here, the diameter of the nanoparticle (1-10 nm) is a controlling factor in the CNT diameter and resulting properties. CNT growth has been demonstrated on a wide range of metals and alloys, and iron is commonly used as a catalyst due to its abundance, low toxicity, and facile aerosol synthesis [6].

Atmospheric pressure microplasma techniques have demonstrated a route to accessing these small diameters and have the potential to combine the specificity of chemical approaches with continuous and scalable production [9, 10, 11, 12]. The microplasma reaction volume is determined by the geometry of the electrodes and plasma, and thus is sharply defined, may be arbitrarily small, and is only weakly coupled to the gas flow through the reactor. In contrast, the reaction volume for flame pyrolysis or vapor-condensation, for example, is defined by a temperature gradient, whose sharpness and minimum size is ultimately limited by the thermal properties and flux of the gas flow. The small and sharply defined microplasma volume results in more rapid and uniform

precursor decomposition and a shorter residence time which can be easily tuned. The natural electrostatic charging of particles in a plasma is key to this process as it both increases the initial growth rate and reduces or eliminates agglomeration of larger particles [13]. In the case of CNT synthesis, decoupling the generation of catalyst particles from the CVD reactor in which CNT growth occurs, by use of an upstream microplasma reactor, would potentially allow for more specific tailoring of both reactor conditions to optimize CNT synthesis.

In previous studies, microplasma sources have been used to tailor Fe catalyst particle diameter from $\sim$ 3 to $\sim$ 6 nm by controlling the concentration of the iron precursor, ferrocene [5, 14]; and to synthesize alloy particles via multiple precursors [15], enabling the respective tuning of diameter and chiral selectivity of SWNTs. While these results show promise, the yield of precursor to particles is potentially low and throughput, on a volumetric basis, is also low. For example, [5] report the ability to control particle diameter from 6.4 nm to 2.8 nm by reducing the precursor concentration, yet this also reduces the particle concentration from 10^8 #/cm^3 to 10^6 #/cm^3, where as a concentration of order 10^9 #/cm^3 catalyst particles is needed to enable the formation of a CNT aerogel which in turn can be spun into a fiber [7].

In all, development of microplasma catalyst generation techniques towards industrially relevant production rates and conditions has been hindered by the complexity of the CNT synthesis process and difficulty characterizing the evolution of small nanoparticles at the related timescales. A deeper understanding of microplasma techniques is necessary to achieve high-yield synthesis of < 5 nm diameter particles in a manner amenable to large-scale gas-phase CNT production

4.2 Prototype microplasma reactor design, operation, and characterization

A continuous atmospheric pressure microplasma reactor was constructed to synthesize nanoparticle aerosols over a range of flow rate, concentration, and diameter. The reactor, shown schematically in Figure 4.1a, is operated between a ceramic orifice plate anode and a mesh cathode, which are separated by 2.5 mm. The orifice plate was made by machining a sheet of Macor ceramic to a thickness of 0.03 inches, coating the plasma-facing side with tungsten via sputtering (1 μm), and drilling the orifice to diameter d_o = 180 or 300 μm. The mesh is made of .0012 inch diameter 316 stainless steel wire at 100 wires per inch density (TWP Inc.). We therefore refer to this as the "orifice-mesh" reactor. A second reactor (the "orifice" reactor, Figure 4.1b, replaces the mesh electrode with a second tungsten coating on the upstream face of the orifice plate, shifting the plasma to the volume within the orifice. This reduces the residence time by a factor of $\sim$ 10 (see Supporting Information, section 4.3.1, for more information). The electrodes are sealed within a stainless steel housing.

The full experimental setup is shown schematically in Figure 4.1e. A controlled flow of high purity helium (400 or 600 sccm) is introduced to the plasma through the orifice. A variable fraction of this flow is passed through a temperature-controlled sublimation chamber containing ferrocene powder. The saturation vapor pressure of ferrocene is calculated using the sublimation chamber temperature [16] and scaled by the fraction of total flow to calculate the ferrocene vapor concentration in the reactor. The plasma is ignited and operated at a constant DC current of 0.2 mA using a high voltage supply (Stanford Research PS310) along with a 1.4 MΩ ballast resistance. Under these conditions the plasma voltage is typically $\sim$250–500 V and the total power is 50-100

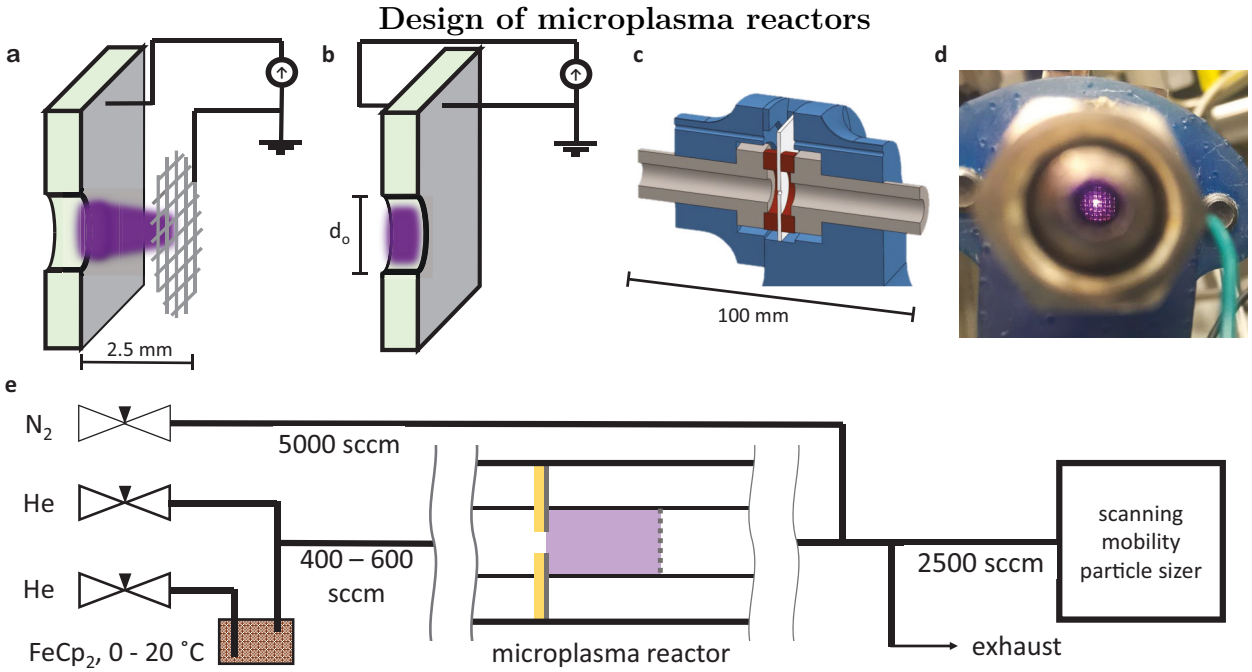

Figure 4.1: Atmospheric pressure microplasma reactors. (a) Cross-section diagram of the electrode configuration for the orifice-mesh reactor (not to scale). The plasma (purple) is ignited between the stainless steel mesh and tungsten-coated ceramic orifice plate. (b) Diagram of the orifice reactor where the plasma is ignited between tungsten coatings on both sides of the plate and exists within the orifice. Gas flow (He + ferrocene) is from left to right in both (a) and (b). (c) Cross section view of the complete orifice-mesh reactor. The blue housing securely holds the orifice plate and mesh between two stainless steel cylindrical sections. (d) Image looking upstream into the orifice-mesh reactor, showing plasma glow. (e) Schematic of the experimental setup including the ferrocene sublimation chamber, microplasma reactor, and aerosol measurement instrument (SMPS).

mW, The low operating current is used to ensure that additional thermo-plasma and thermo-chemical effects are negligible. We estimate that the maximum gas temperature is 17K above ambient by assuming adiabatic heating for the helium flow by the plasma power. Further, [5] used a similar microplasma reactor operated at 2 and 4 mA to show, via OES, that plasma dissociation of the cyclopentadienyl anion of ferrocene does not occur, and, via XPS, that C contamination of the particles occurs only when operated at 4 mA. This suggests that species other than iron should not influence particle formation and composition at our operating conditions.

Nitrogen (5000 sccm) is introduced shortly downstream of the plasma to prevent additional aerosol growth, diluting the concentration for aerosol size classification. Half (2500 sccm) of the flow is sent through a scanning mobility particle sizer (SMPS, TSI model 3938E57) with a measurement range of 1–30 nm. Measurements are recorded once the aerosol reaches steady state which typically occurs within 15 to 60 minutes after the plasma is ignited. Subsequent changes in operating conditions are quickly reflected in the particle size distribution. SMPS measurements of electrical mobility diameter are converted to true diameter by subtraction of 0.3 nm to account for the gas molecule diameter [17, 18]. Propagating this correction through to derived quantities results in a slight increase in σ_g and decrease in mass concentration from those reported with mobility diameters.

For ex-situ characterization, particles were passively collected for 1 hour on a SiNx TEM grid (10 nm membrane thickness, Norcada NT010Z). The TEM grid was located just upstream of the nitrogen flow inlet within the tubing connected to the outlet of the reactor as the most representative location for comparison with SMPS measurements. Particle diameter was estimated from TEM images using an image segmentation algorithm to determine particle area and then calculating the diameter of a circle of the same area.

4.3 Experimental results

Figure 4.2a shows representative size distributions for nanoparticles synthesized in the orifice-mesh reactor with 400 sccm He and 23 ppb ferrocene. The particle size distribution is integrated to find the total concentration and scaled to account for the N_2 dilution upstream of the SMPS (Figure 4.1e), thus reflecting the concentration at the reactor outlet, C. A lognormal distribution was fit to each particle size distribution to yield a geometric mean diameter D_g and geometric standard deviation σ_g. With the small orifice ($d_o = 180\mu$m), these conditions produce an aerosol with $D_g = 1.88$ nm, $\sigma_g = 1.17$, and $C = 8.84 \times 10^7$ #/cm^3. The larger orifice ($d_o = 300\mu$m) results in a slight increase of D_g to 1.97 nm and σ_g to 1.18 and large increase in C to 1.68×10^8 #/cm^3. In these configurations, the plasma residence time is 9.5 and 26 μs, respectively, and the residence time from plasma to nitrogen dilution is 0.12 s.

In order to assess the temporal performance of the orifice-mesh reactor, the plasma was ignited and the reactor was operated at constant conditions with aerosol measurements taken at 90 s intervals. Upon plasma ignition with new electrodes, a break-in period of 15 to 90 minutes was observed, during which the concentration and size of particles asymptotically increases (Figure 4.2b,c) toward a steady value. After this period, D_g, σ_g, and C are remarkably consistent. At a constant plasma current, the required voltage is similarly stable, although the steady voltage can differ by 10–100 V (3–30%) between experiments. This is attributed to small differences in the electrode positioning.

During operation, the plasma flow rate and ferrocene concentration control the resulting aerosol concentration and size. Figure 4.3a plots the values of C and D_g produced by the orifice-mesh reactor with the 180 μm orifice at flow rates of 400 and 600 sccm, and ferrocene concentrations varied stepwise from 10 to 87 ppb. Typically, 1 to 3 min-

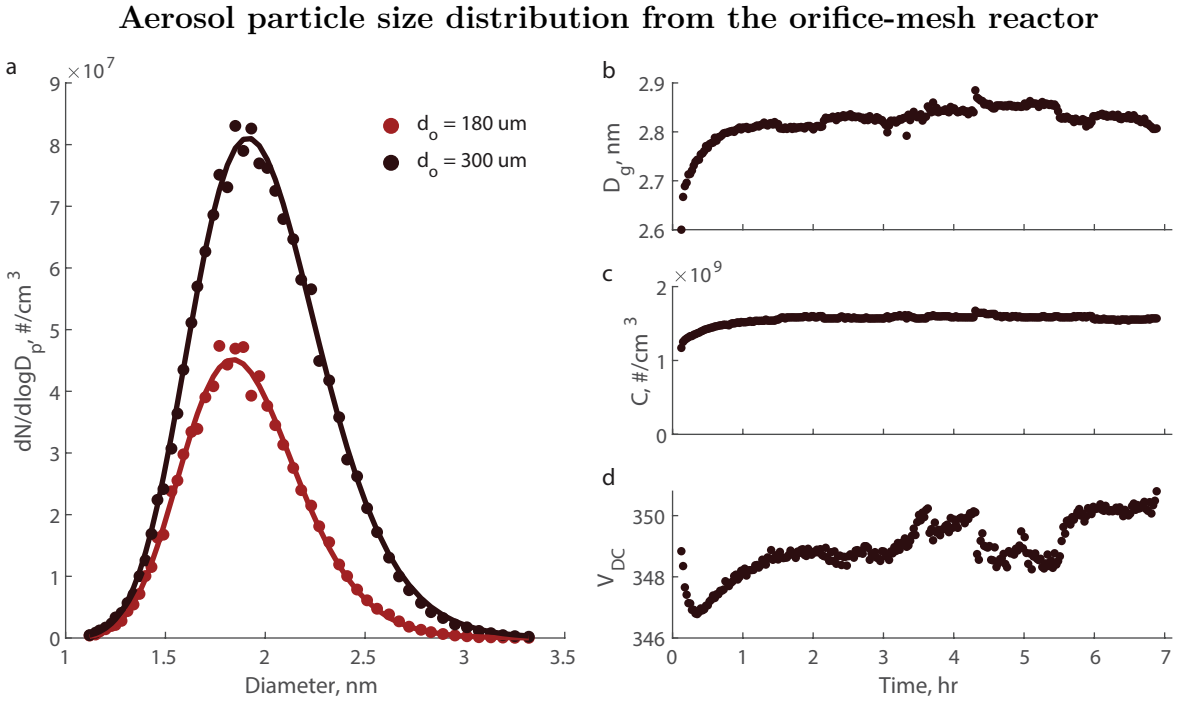

Figure 4.2: (a) Representative particle size distribution measurements from the orifice-mesh reactor operating at 400 sccm He with 23 ppb ferrocene. A lognormal distribution (solid line) is fit to measurements (points) to extract D_g and σ_g. (b, c, d) Temporal performance of the orifice-mesh reactor in terms of (b) particle diameter, (c) concentration, and (d) plasma voltage, operated at 350 sccm He with 85 ppb ferrocene, illustrating the start up transience and stable operation.

utes was required for the aerosol measurement to stabilize after changing the ferrocene concentration. At both flow rates, we find the relationship between D_g and C becomes linear above approximately 20 ppb ferrocene. Note that, for a given D_g, the higher flow rate produces a higher C, but requires a higher ferrocene concentration to do so. At approximately equal ferrocene concentrations, the lower flow rate results in more and larger particles, in terms of C and D_g.

For the same experimental conditions, Figure 4.3b shows that the geometric standard deviation of the particle size distribution is monodisperse, and Figure 4.3c shows the yield of particle formation Y_{Fe}, here defined as the mass flux ratio of iron in nanoparticles to iron in the precursor, for the same experimental conditions. The flux of iron in nanoparticles is estimated using the particle size distribution and total flow rate, assuming spherical iron particles with no porosity.

Transmission electron microscopy (TEM) was used to validate the online size measurements and examine the particle morphology. Figure 4.4a shows particles synthesized using the orifice-mesh reactor ($d_o = 300\mu$m at a flow rate of 800 sccm He with 86 ppb ferrocene). The majority of particles appear round and isolated and are observed in regions of relatively uniform depositions across the TEM grid. We plot a histogram and fit a lognormal distribution with D_g of 2.28 nm and σ_g of 1.22. Comparatively, aerosol measurements taken at 90 s intervals during the 1 hour deposition show an average D_g of 2.33 nm, σ_g of 1.23, and C of 4.32×10^8 #/cm^3.

Despite the close agreement between TEM images and SMPS measurements, the measurements may not represent the exact size distribution as diffusion loss and deposition occurs more readily for small diameter particles, biasing the TEM sample in this direction. Further, while particle collection and aerosol measurement is carried out in a sealed, inert environment, oxidation of metallic particles is likely to have occurred due to exposure to ambient air before TEM imaging. A small number of particles appear

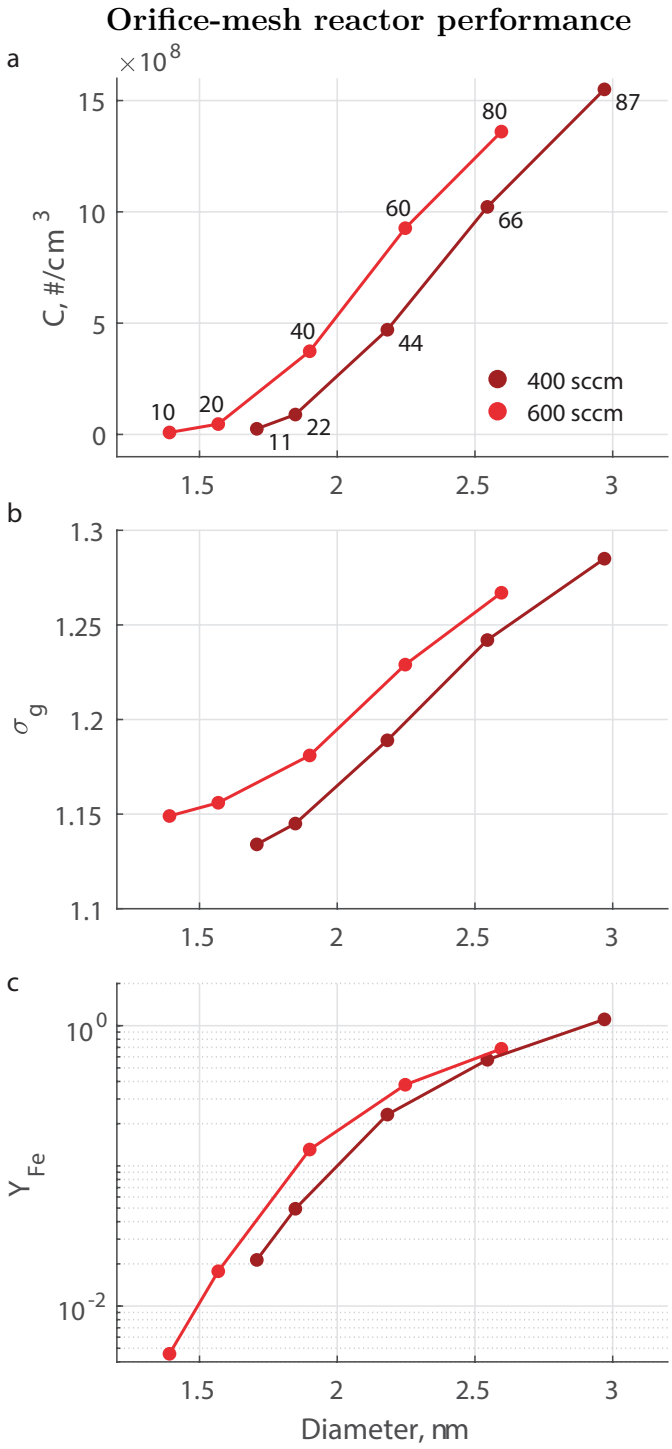

Figure 4.3: (a) Measurements of mean diameter D_g and concentration C of aerosols produced at 400 and 600 sccm He in the orifice-mesh reactor with $d_o = 180\mu$m. Plasma residence times are 9.5 and 6.4 μs, respectively. Labels indicate the ferrocene concentration in ppb. (b) Geometric standard deviation σ_g and (c) yield of particle formation Y_{Fe} for the same experimental conditions.

elongated and may be evidence of agglomeration, either during synthesis or the deposition process. Also, the small size of particles and resolution of the TEM limited our ability to discern lattice fringes for all but the largest particles (Figure 4.4b).

4.3.1 Orifice reactor

The orifice reactor is a modification of the orifice-mesh reactor with reduced plasma volume. The mesh electrode is replaced by an additional tungsten coating applied to the upstream face of the orifice plate (Figure 4.1b. The plasma volume is thus contained within the orifice and the plasma length is equal to the plate thickness (370 μm). This reactor typically produces smaller particles at lower concentration than the orifice-mesh reactor at the same conditions. Figure 4.5a shows an example particle size distribution from the orifice reactor overlaid on orifice-mesh data from Figure 4.2a, all collected while operating at a flow of 400 sccm He with 25 ppb ferrocene. For the orifice reactor these conditions produce an aerosol with $D_g = 1.40$ nm and $\sigma_g = 1.14$. Temporally, the orifice reactor performs similarly during the initial stage of operation, yet becomes increasingly unstable and eventually the plasma de-ignites. When operating in the stable region, performance shows similar trends in terms of C, σ_g, and Y_{Fe} as the orifice-mesh reactor yet at lower D_g and C, as shown in Figure 4.6. Figure 4.5b-d shows a typical performance with instability beginning after approximately 3 hours of use. The duration of stable performance appears inversely related to the ferrocene concentration, and may be attributed to the deposition of iron on the inside surface of the orifice. Figure 4.7 shows a thin film has been deposited inside the orifice after use, and EDS mapping confirms the presence of iron in this layer. It is not clear if the effect is primarily due to changes in the flow geometry or the formation of conductive pathways.

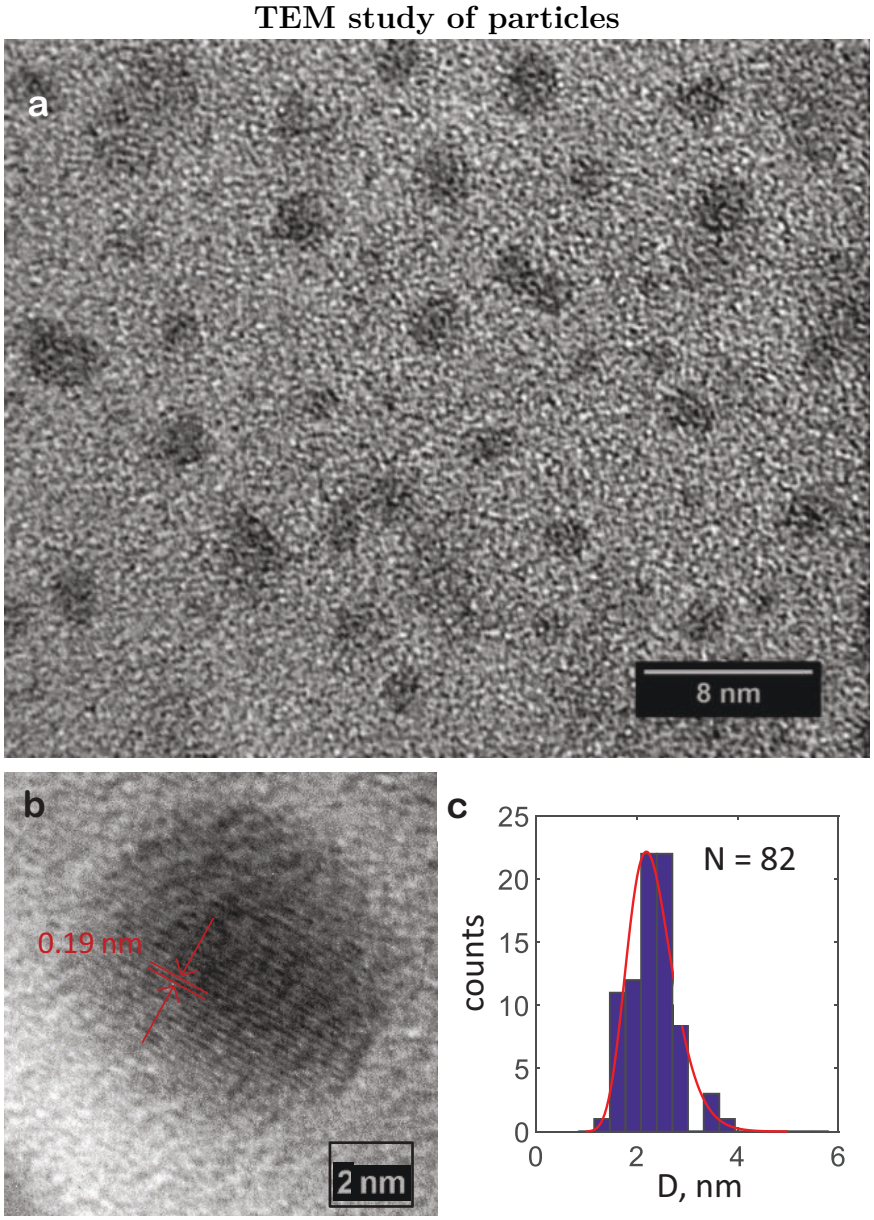

Figure 4.4: (a) TEM image of as-collected Fe nanoparticles from the microplasma reactor. (b) Close-up of a single particle showing lattice spacing of 0.19 nm from FFT analysis. (c) Histogram of particle diameters assessed from (a).

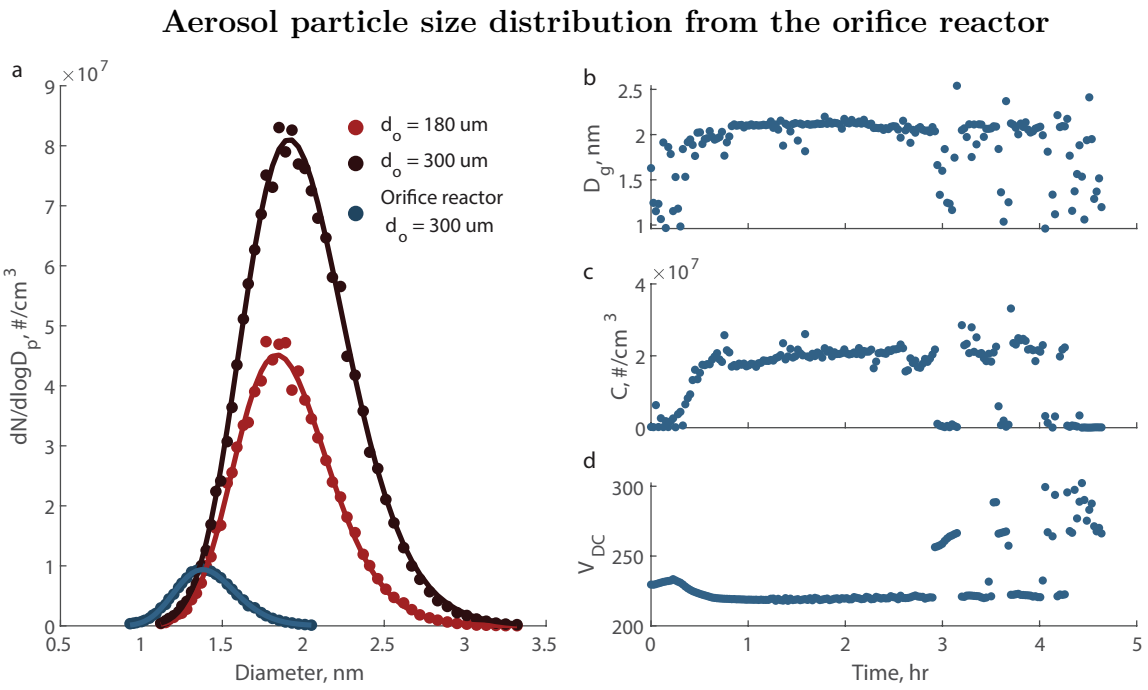

Figure 4.5: (a) An example particle size distribution for the orifice reactor overlaid on a reproduction of Figure 4.2a. All three measurements collected at a flow of 400 sccm He with 25 ppb ferrocene. (a,b,c) Temporal performance of the orifice reactor in terms of (b) particle diameter, (c) concentration, and (d) plasma voltage, operated at 370 sccm He with 31 ppb ferrocene illustrating the start up transience, stable operation, and unstable operation.

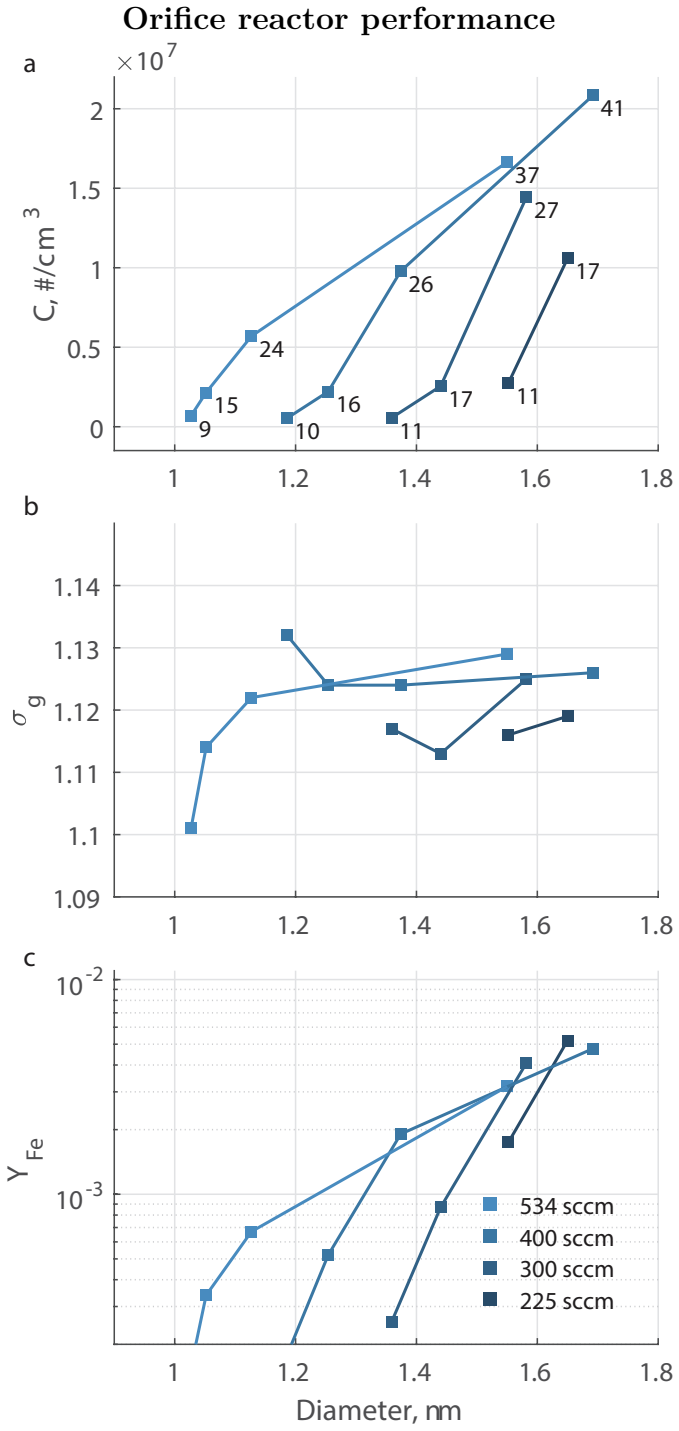

Figure 4.6: (a) Measurements of mean diameter (D_g) and concentration (C) of aerosols produced at flow rates of 225-534 sccm He in the orifice reactor with $d_o = 180\mu$m. Labels indicate the ferrocene concentration in ppb. (b) Geometric standard deviation (σ_g) and (c) yield of particle formation (Y_{Fe}) for the same experimental conditions.

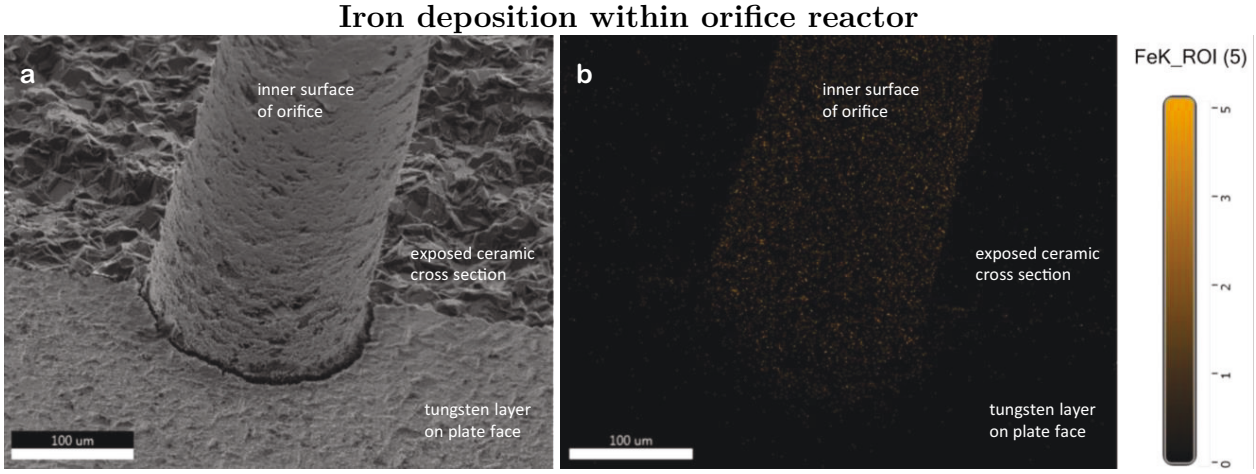

Figure 4.7: a) Cross section of orifice plate after use showing inner surface of orifice. (b) EDS measurement of inner surface showing elevated Fe compared to interior of the ceramic plate and the tungsten-coated face.

4.4 Particle formation analysis

Previous experimental studies have also shown synthesis of nanometer-scale aerosols with narrow size distribution via similar microplasma reactors, yet mechanistic understanding of the formation process is limited [9, 10, 19, 13, 20]. Many aerosol formation processes can be approximated as either nucleation- or growth-dominated. For example, industrial powder manufacturing via large-scale plasma reactors is well-described by the aggregation of large particles (relative to their nucleation size, i.e. $D_g > \sim 100$ nm) in the absence of a vapor phase [21]. Alternately, in cloud formation and other atmospheric processes, understanding the nucleation of droplets from a vapor is critical [22]. For microplasma reactors, the small size and high concentration of aerosols produced imply that both nucleation and growth are important. Here we develop a charge-mediated formation mechanism as a framework for better understanding the present process.

4.4.1 Classical nucleation theory

Studies of manufacturing processes in the chemical engineering literature focus on high concentrations of large ($D_g > \sim 100$ nm) particles. Therein, aggregation or agglomeration are the primary growth mechanisms, a self-similar particle size distribution can be assumed, temperature is often high, and the details of particle nucleation can often be neglected [21]. In contrast, the study of atmospheric aerosols, the other dominant branch of aerosol science, provides rich literature on the nucleation and growth of liquid droplets at near-ambient conditions and relatively low concentrations [22].

Here, particle nucleation is commonly conceptualized as the formation of a critically sized cluster of monomers (in the present study, individual Fe atoms in the gas phase) by the random variations in local vapor density according to classical nucleation theory [23]. The formation of these clusters is a reversible, stepwise process driven by the energy balance between that needed to enlarge the surface of the particle and that gained from condensation. The critical cluster size is determined as the size at which the net of these two effects, the incremental change in Gibbs free energy for monomer addition, becomes negative, indicating the formation of a stable particle. Following the derivation of [24], the nucleation rate, J, is:

$$J = \sqrt{\frac{2\sigma}{\pi m}} v_l N^2 exp(\frac{-\Delta G^*}{k_b T}) \tag{4.1}$$

where σ (J/m^2) is the surface energy of the particle, m (kg) is the monomer mass, v_l (m^3) is the monomer volume, N (#/m^3) is the number density of monomers, k_b (J/K) is the Boltzmann constant, T (K) is the temperature. The change in Gibbs free energy for the critical cluster is given by:

$$\Delta G^* = \frac{16\pi\sigma^3 {v_l}^2}{3(k_b T ln S)^2} \tag{4.2}$$

Here, S is the ratio of actual vapor pressure, p_a, to equilibrium vapor pressure p_e (determined as a function of temperature using the empirical equation of [25]). ΔG^* is dominantly controlled by the σ^3 term and, As σ for iron (2.53 J/m^2 [26]) is relatively high in comparison to common droplet forming species (e.g., water, 0.073 J/m^2 [27]), the barrier for particle nucleation is expected to be relatively high. At conditions representative of both in-situ thermal and microplasma synthesis of iron particles, this model predicts a prohibitively high energy barrier and no particle nucleation, in conflict with experimental observations. For example, in-situ measurements of in-situ thermal synthesis by [28] show the bulk of particle synthesis occurring between 180 and 220 mm into the reactor. Here, conditions are T = 1150 K, p_a = 2.76 Pa, p_s = 2.46 Pa, and $N = 1.73 \times 10^{20}$ #/m^3, resulting in a critical cluster size, N^* of $\sim$1.23 $\times$ 10^7 atoms (D_{crit} = 65 nm), and ΔG^* is 6.77$\times$ 10^6 kJ/mol, indicating that particle nucleation is essentially impossible ($J = 0$). At conditions representative of the orifice-mesh reactor (T = 290 K, p_a = 0.01 Pa, $p_s = 5.8 \times 10^{-22}$ Pa, and $N = 2.50 \times 10^{18}$ #/m^3), the lower temperature results in a drastically lower p_s and significantly higher S of 1.74 $\times$ 10^{19}, leading to a more favorable N^* of 13 atoms, and ΔG^* of 706 kJ/mol, yet the estimated nucleation rate remains zero.

This analysis does not consider the presence of contaminant species who may lower the energy barrier for nucleation. [29] observed that the addition of sulfur to a thermal particle synthesis can increase the final concentration of iron nanoparticles, explained by a reduction in surface energy by the presence of sulfur (σ = 0.01 J/m^2) [26]. However, significant amounts of carbon (σ = 0.02 J/m^2) are also present from the thermal decomposition of ferrocene, indicating that the additional effect of surface energy reduction via S is likely minor. Additionally, the high molar fraction of C or S needed to drastically reduce the surface energy is not observed in compositional analysis of particles, and some processes, i.e. spark discharge, do not have any low σ impurities present.

4.4.2 Collision theory

Instead, we consider a limiting case where it is always energetically favorable for iron vapor to combine to form particles, e.g., supersaturation is infinite, or surface energy is zero. Here, we can consider a single aggregation mechanism as operating not just for large particles, but also small particles down to individual vapor atoms, at a rate determined by collision rates rather than energy considerations. Yet, the particle size distribution is not characteristic of an aggregation-dominated process, where σ_g of 1.44–1.46 would be expected [30]. Recent studies on particle aggregation within dusty plasmas have indicated that electrostatic charging of particles can enhance growth rates [31, 32].

Collision Kernel

Particles are conceptualized as individual gas-phase molecules such that both particles and vapor can be described as belonging to a continuum of Fe_n molecules, where the subscript denotes the number of iron atoms in the molecule. In addition to assuming that all collisions between two Fe_n particles result in the formation of a single new particle, the loss of atoms from a particle, for example due to evaporation, is neglected based on the assumption that at high supersaturation and low temperature this rate is negligible. Thus, the growth of particles is analogous to the step growth model for polymer chains and is described by the following irreversible reaction:

$$Fe_j + Fe_k \rightarrow Fe_{j+k} \tag{4.3}$$

The rate constant for this reaction, $k_{j,k}$, is equal to the frequency of collisions between Fe_j and Fe_k. Following the work of [32], the approximation of particles as gas phase molecules allows their motion to be described using the kinetic molecular theory of gases.

Assuming spherical particles with a unity sticking coefficient in the free molecular regime, and neglecting any attractive or repulsive potentials, the collision rate constant can be written as [33]:

$$k_{j,k} = \sigma_{j,k}\sqrt{\frac{8k_bT}{\pi\mu_{j,k}}} \tag{4.4}$$

where $\sigma_{j,k} = \pi(r_j + r_k)^2$ is the collision area and $\mu_{j,k} = \frac{m_j m_k}{m_j + m_k}$ is the reduced mass of the collision pair. As particles of any size can react with any other, the net rate of formation of Fe_n, r_n ($\#/(\mathrm{m}^3 s)$), is given by the balance of its formation and consumption:

$$r_n = \frac{1}{2}\sum_{j=1}^{n-1} k_{j,n-j}C_jC_{n-j} - \sum_{j=1}^{n_{max}} k_{j,n}C_jC_n \tag{4.5}$$

where C_n is the concentration of Fe_n, and n_{max} is the maximum particle size being considered. Beginning with some initial concentration of Fe_1, this equation can be used to predict the evolution of the particle size distribution with time. To demonstrate the model in a simplified case, it is applied to [28]'s study of the formation of iron particles from thermally decomposed ferrocene in a tube furnace , where all particles are assumed neutrally charged. [28] reports aerosol particle size distribution for their in-situ thermal synthesis at intervals along the centerline of a heated reactor tube as well as temperature and gas velocity distributions. At a setpoint of 1200 °C, essentially no particles are observed at 180 mm into the reactor (lower detection limit of 6 nm), with the bulk of particle formation appearing to occur by 220 mm. The center line temperature and velocity are reported as 880 °C and 0.044 m/s, respectively, at 180 mm, and 1180 °C and 0.060 m/s at 240 mm. By linear interpolation, we estimate values of 1080 °C and 0.055 m/s at 220 mm, thus an average temperature of 980 °C and a residence time of 0.82 s in the region of particle formation.

Using these parameters with an initial concentration $C_1 = 1.593 \times 10^{20}$ #/m^3, the particle size distribution at the end of this region (i.e., at 220 mm) is modeled and compared to the observed distribution in Figure 4.8. The collision theory model predicts $D_g = 11.22$ nm, $\sigma_g = 1.453$, and $C = 1.49 \times 10^9$ #/cm^3; while Hoecker et al. found $D_g = 13.90$ nm, $\sigma_g = 1.55$, and $C = 5.9 \times 10^8$ #/cm^3. The approximately three-fold difference in concentration can be attributed to particle losses in the thermal reactor, as well as the assumption of complete and instant ferrocene decomposition. The difference in D_g and presence of >30 nm particles in the observed distribution may be a result of radial dispersion resulting in a residence time distribution, i.e., mixing with outer streamlines which, being at lower velocity and higher temperature, will have larger particles. The high experimental σ_g further indicates dispersion of particles, while the modeled σ_g falls within the typically observed range of 1.44–1.46 for other self-similar growth processes [30], Overall, the collision model is a satisfactory representation of particle formation in the in-situ thermal process.

Enhancement Factor

When applied to the microplasma reactor an enhancement factor, η is used to account for increased collision rates due to electrostatic interactions. For neutral-neutral collisions this factor accounts for attraction due to the Van der Waals potential, and for charge-neutral collisions it additionally accounts for attraction between the charge and induced dipole in the neutral particle using the complete image potential formula of [34]. More commonly used simplifications of the image potential can not be used as they approximate the charged particle as a point (i.e., collision of a large neutral particle with an ion) which is generally not the case here (we expect charged particles are of similar or larger size to neutral). We do not consider here a potential for oppositely charged particles as this type of collision is not included in the model.

Collision model validation for neutral aerosol (no enhancement)

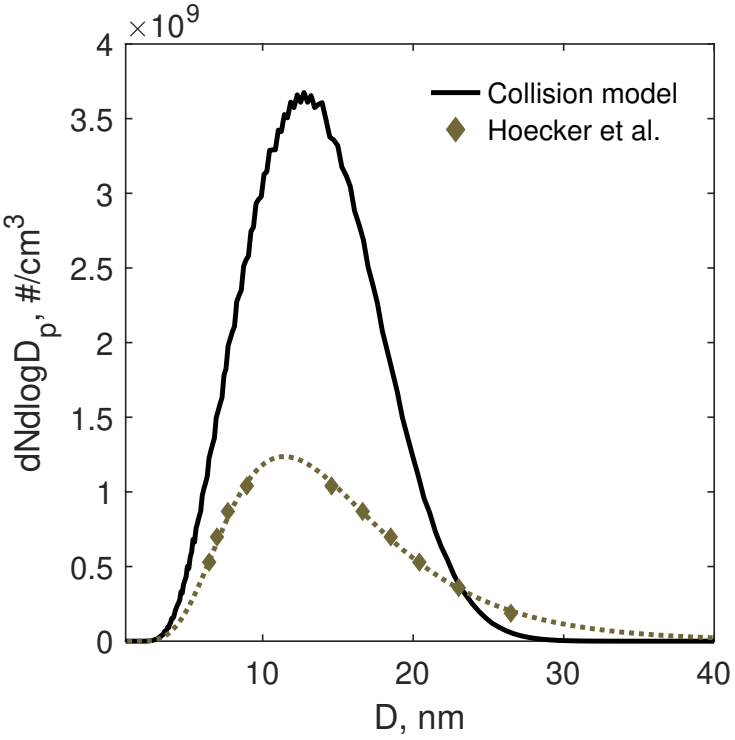

Figure 4.8: Experimental particle size distribution from [28] (points are measurements, dashed line is lognormal distribution fit) compared to collision model results at same conditions. The difference in total concentrations is likely due to particle losses which are not accounted for in the model.

In order to determine η from this potential function we consider how an attractive potential changes the trajectory of two particles. First, we consider a non-enhanced case. Two particles are traveling on straight trajectories which have a closest distance b between them. The kinetic energy of the system is $E_k = \frac{1}{2}\mu_{j,k}{v_{j,k}}^2$ where $v_{j,k}$ is the reduced velocity of the pair. The angular momentum for this system is $L = \mu_{j,k}v_{j,k}b$. We can define an angular momentum potential as:

$$\phi_{ang} = \frac{L^2}{2\mu_{j,k}r^2} \tag{4.6}$$

Where r is the center-center distance between the particles. Note that ϕ_{ang} increases as $r \to 0$. We can define a value r_{min} such that $\phi_{ang}(r_{min}) = E_k$. r_{min} is the smallest distance between the *particles* as they travel: in this case of no additional potentials, $r_{min} = b$ and we see that, trivially, the smallest distance between the *particles* is the same as that of their *initial trajectories*. To consider the influence of additional electrostatic potentials, ϕ_e, they are simply added as additional terms to this equation:

$$\phi_{ang}(r_{min}) + \phi_e(r_{min}) = E_k \tag{4.7}$$

As $\phi_e(r) < 0$ for the image and Van der Waals potentials, when solving this equation for r_{min} we expect $r_{min} < b$, meaning that the particles pass closer than they otherwise would have if they followed their initial trajectories. In order to calculate the enhancement, we define b_{crit} as the value of b at which $r_{min} = r_j + r_k$, indicating the largest value of b at which a collision will still occur. This derivation and definition of b_{crit} is equivalent to that of [35].

Finally, we follow the approach of [36] to calculate η from b_{crit}. A comparison of techniques by [35] found this method in good agreement with their own, yet with more

straightforward computation as it includes the simplification that $v_{j,k}$ is calculated from the average speed of each particle (neglecting the Maxwell–Boltzmann distribution of speeds for particles of a given size). [35] also show that it is more conservative than the approaches of [37] and [34]. The enhancement factor is expressed as:

$$\eta = \sqrt{\frac{3}{2}} b_{crit}^2 \tag{4.8}$$

Figure 4.9 shows calculated enhancement factors as a function of the diameters of the interaction particles (D_j and D_k). $T = 293$ K is representative of a room temperature microplasma process. A Hamaker constant of 460 zJ for iron is used for the calculation of the Van der Waals potential [38]. The charge-neutral enhancement factor, Figure 4.9a, reaches 11 for a collision between a single charged atom and a 0.6–1.3 nm neutral particle. The same-charge enhancement factor, Figure 4.9b, is essentially zero for most collisions below 100 nm, indicating that these collisions do not occur.

4.4.3 Charge-mediated formation mechanism

The findings using the collision theory model with electrostatic enhancement form the basis of the proposed charge-mediated formation mechanism. The complete process by which iron nanoparticles are synthesized from ferrocene vapor in the microplasma reactor is summarized in the following five stages, as illustrated in Figure 4.10:

1. He and ferrocene vapor are introduced to the microplasma at ambient temperature.

2. Ferrocene is dissociated into cyclopentadienyl and other hydrocarbons, which remains stable in the gas phase, and Fe vapor [39]. A small fraction of He and Fe are ionized by the plasma; He has a higher ionization energy than Fe, 2370 kJ/mol to 762 kJ/mol, thus Fe is preferentially ionized [40].

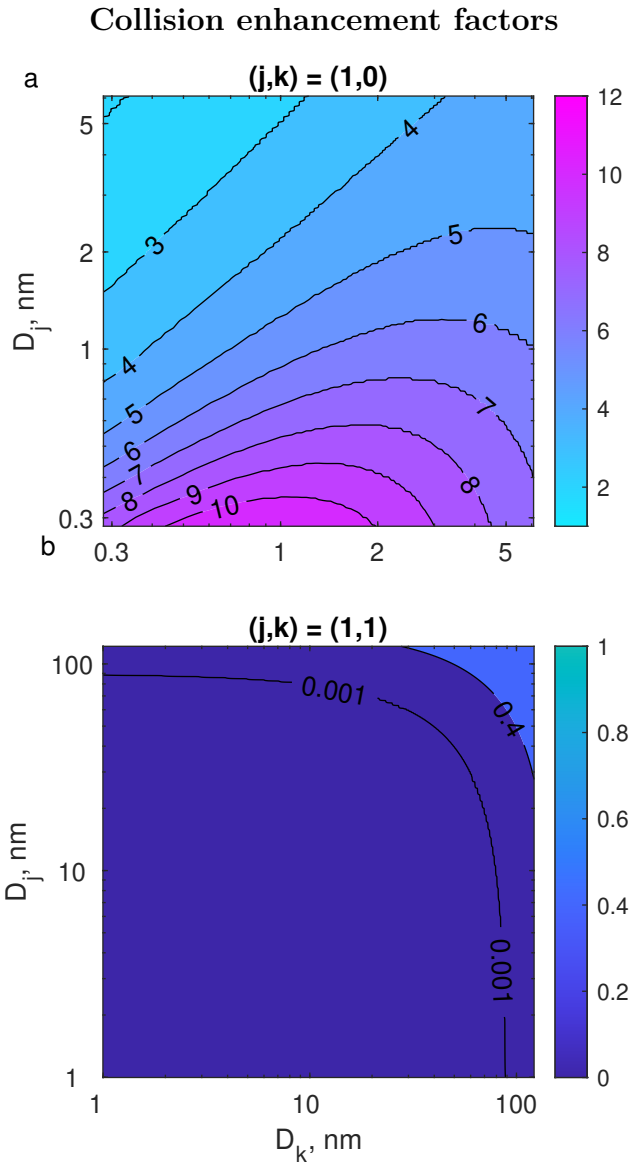

Figure 4.9: Calculated enhancement factors for collision rates as a function of the diameters of the interaction particles (D_j and D_k) with charges j and k at T = 293K. (a) Charge-neutral enhancement factor reaches 11 for a collision between a single charged atom and a 0.6–1.3 nm neutral particle. (b) Same-charge enhancement factor is essentially zero for particles smaller than 100 nm.

3. Within the short residence time of the plasma, few collisions between Fe vapor atoms take place. At the plasma outlet, more than 99% of Fe remains in the vapor phase while less than 1% has formed clusters of n=2 to n=6. The charge distribution of vapor and small clusters is determined by equilibrium with the plasma environment, and assumed either neutral or having a single positive charge.

4. Downstream of the plasma, collisions between vapor atoms and clusters begin to form particles. Outside of the plasma environment, charge is conserved during collisions between particles. Charged particles grow rapidly due to electrostatic enhancement, while neutral particles grow slowly, leading to a bimodal size distribution. The total charge among the Fe particle population is also conserved.

5. In the final stage of particle growth, collisions of large particles are prevented by charge-charge repulsion and the particle size distribution approaches a steady state as small neutral particles are fully consumed.

4.5 Numerical model

Now, we explore the charge-mediated formation mechanism through a numerical model which describes the formation of particles from Fe vapor in the microplasma reactor system. Particles are treated as behaving like individual gas-phase molecules such that both particles and vapor can be described as belonging to a continuum of Fe_n molecules, where the subscript denotes the number of iron atoms in the molecule. Particle growth occurs via collisions, $Fe_j + Fe_k \rightarrow Fe_{j+k}$. The rate constant is derived using the kinetic theory of gases and scaled by an enhancement factor calculated following the approach of [36] due to attractive potentials between particles. This approach was chosen based on its relatively low computational cost, and good agreement with other

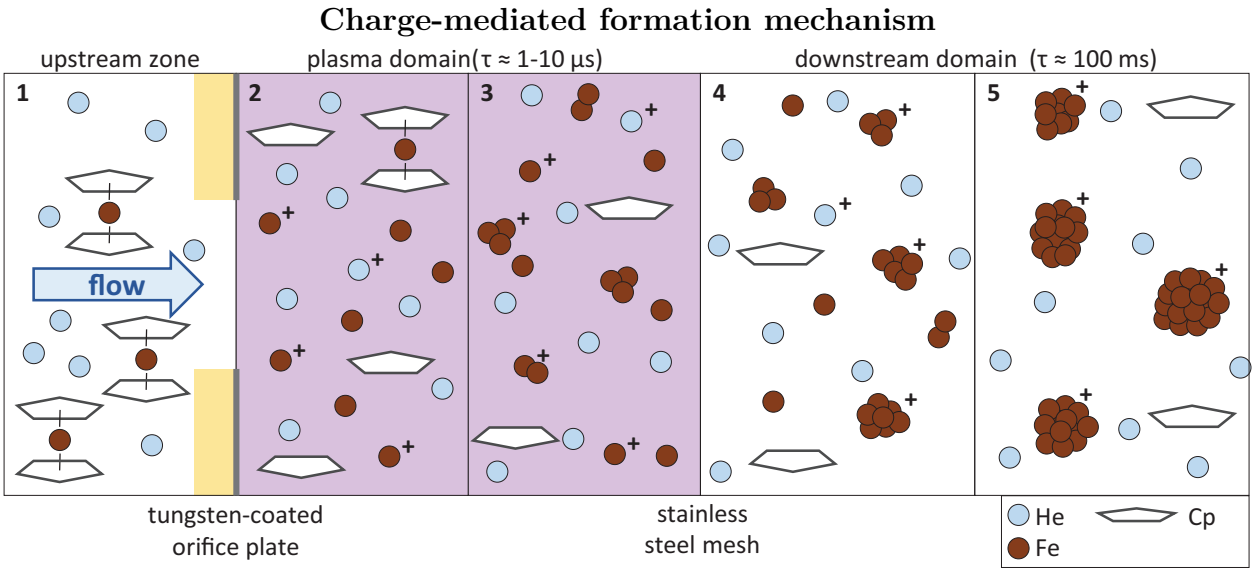

Figure 4.10: Proposed mechanism for iron nanoparticle formation in the microplasma reactor. Ferrocene dissociation creates a vapor of neutral and ionized Fe which collide to form particles. Electrostatic interactions are key for enhancing the formation and growth of small particles while limiting aggregation of large particles. Thus, the majority of growth (of large particles) occurs downstream of the plasma due to the short residence time. Cp is cyclopentadienyl formed during ferrocene dissociation.

approaches based on the comparison of [35]. For neutral-neutral collisions this factor accounts for attraction due to the Van der Waals potential. For charge-neutral collisions it additionally accounts for the electrostatic attraction between the charge of the charged particle and the dipole which this charge induces in the neutral particle using the image potential of [34]. See 4.4.2 for the complete derivation. The collision model can be used to investigate the orifice-mesh reactor and understand the role microplasma-induced charges on the evolution of particle size. The two primary roles of the microplasma are dissociation of ferrocene to generate the initial Fe vapor, as well as partial ionization of that vapor.

4.5.1 Plasma domain

The model is divided into a plasma domain bounded between the two electrodes and a downstream domain extending from the downstream electrode to the point of N_2 dilution (after which particle growth is assumed to be effectively halted until measurement in the SMPS). These spatial boundaries are used to calculate the average residence time for each domain based on the gas flow rate. We will find that the particle growth is relatively insensitive to the precise location of the dividing boundary. It is assumed that ferrocene decomposition is complete and instantaneous upon flow into the plasma domain, thus the initial condition is iron vapor with a concentration equal to the original ferrocene vapor concentration, and particle formation is modeled for a period of time equal to the average residence time of the plasma. The population of vapor and particles is also assumed to be in electrical equilibrium with the plasma resulting in fractional ionization. In a low temperature plasma, including the microplasma reactors discussed here, the fractional ionization χ_{iz} of He and Fe vapor is much less than one [41]. The plasma conditions also enforce an equilibrium charge distribution which is a function of particle size. Small particles may have a single positive or negative charge, with the fraction of particles having a negative charge increasing with particle size [42, 43, 31].

Figure 4.11a shows an example simulation of the plasma domain for τ_p of 6.4 μs (based on an orifice diameter of 180 μm, electrode spacing of 2.5 mm, and He flow rate of 600 sccm), initial Fe_1 concentration of 2×10^{18} #/m^3 (based on complete dissociation of 80 Pa ferrocene), and χ_{iz} of 0.001 for Fe vapor and clusters. From the model, we find that less than 1% of Fe vapor has undergone a collision to form a larger cluster by the end of the plasma domain, and no clusters are larger than n = 10, thus more than 99% of Fe remains in the vapor phase. The portion of Fe that forms clusters, and the size distribution of these clusters, is relatively insensitive to changes in the residence

time, i.e., the determination of a shorter effective residence time to account for gradual ferrocene decomposition is unnecessary (Figure 4.11b). Further, the small size of even the largest of these clusters (n=6, d ∼0.5 nm) indicates that the likelihood of some clusters acquiring a negative charge in the plasma is low (While existing studies of particle charge distribution in dusty plasmas only consider down to d = 1 nm, they show a trend of a decreasing fraction of particles having a negative charge as diameter is reduced [42, 31]). Non-ambient conditions likely persist downstream of the mesh electrode in a spatial afterglow region for a residence of order that of the plasma, although this is not modeled explicitly. Other studies have shown that gas ions persist longer in this region than high mobility electrons and thus can contribute additional positive charge to aerosol particles [44, 45]. For a predominantly negatively charged aerosol of larger particles this has the effect of creating a bipolar charge distribution, yet in this case, given that Fe vapor and clusters are already positive, will just effect the degree of ionization. Further, given the negative electron affinity and high ionization energy of He, relative to Fe, we also assume that change transfers will happen in greater proportion to the Fe vapor. We expect that a majority of the ions in the plasma are Fe, not He, thus the effect of those He ions in the spatial afterglow is likely small. These results, we believe, support the use of a single value for χ_{iz} and the assumption that Fe vapor and clusters can only acquire either a neutral or positive charge while in the plasma domain.

4.5.2 Downstream domain

Upon flowing out of the plasma and entering the downstream domain, the charge of Fe vapor, clusters, and particles is no longer constrained by the equilibrium charging effect, and it is assumed that charge is thus conserved during collisions between charged and neutral particles. It is also assumed that He ions and free electrons have been depleted or neutralized, therefore no sources or sinks of charge exist and the total particle

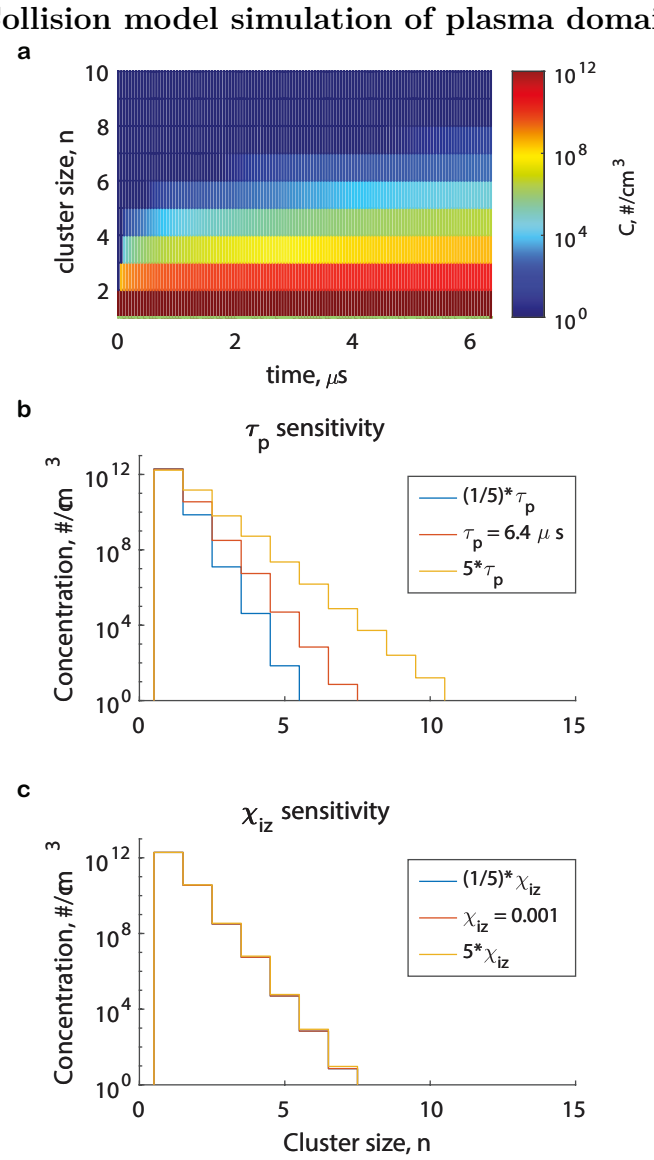

Figure 4.11: Collision model simulation of the plasma domain of the orifice-mesh reactor showing the effect of electrostatic enhancement. (a) Cluster size distribution for representative operating conditions: $\tau_p = 6.4\mu$s, 80 Pa ferrocene ($FeCp_2$), and estimated χ_{iz} = 0.001. Less than 1% of Fe vapor has undergone a collision to form a larger cluster by the end of the plasma domain. (b) Cluster size distribution at the end of the plasma domain can be controlled with τ_p, yet in all cases the concentration of clusters n > 1 is small, and no clusters are larger than n = 10. (c) The Choice of χ_{iz} similarly has negligible effect on the cluster size distribution.

charge is conserved. To model particle growth in this region, the vapor and cluster distribution from the plasma domain is used as the initial condition, and the particle size distribution evolves through charge-conserving collisions until a steady state is reached. Using the results shown in Figure 4.11a as the initial condition, Figure 4.12a-c illustrates the particle size distribution evolution within the downstream domain and highlights the transient bimodal distribution that develops. This distribution is characteristic of a fractionally ionized initial condition: a population of charged particles which do not interact with each other but continue to grow by accreting a second population of neutral iron vapor and clusters. Eventually, the neutral population is entirely consumed resulting in a steady state particle size distribution entirely of charged particles. Both the mean diameter (Figure 4.12d) and the full particle size distribution (Figure 4.12e) are influenced by χ_{iz}. The initial growth rate shown in Figure 4.12d as D_g as a function of time, is relatively insensitive and in all cases significantly faster than the unenhanced case ($\chi_{iz} = 0$).

While the model can result in a range of narrow size distributions similar to that observed experimentally, Figure 4.12e also shows that χ_{iz} is a critical parameter for determining and controlling the size distribution. More precisely constraining this value is critical to understanding the growth process. The range of χ_{iz} values used here, of order 0.001, are consistent with both the ionization of gas molecules in a typical low temperature plasma [41], and with experimental observations of decreasing charging efficiency, i.e., $\chi_{iz} < 1$ for particles in a variety of plasma environments as diameter is decreased below 10 nm [44, 46]. In the case of larger particles existing in the plasma, one can assume that χ_{iz} is not effected by changes in particle concentration, because χ_{iz} is controlled by the charging efficiency, so long as the change in particle concentration is small enough to not influence the plasma environment. Yet, if the main source of charged Fe comes from ionization of Fe vapor, as the modeling results indicate, the total ion

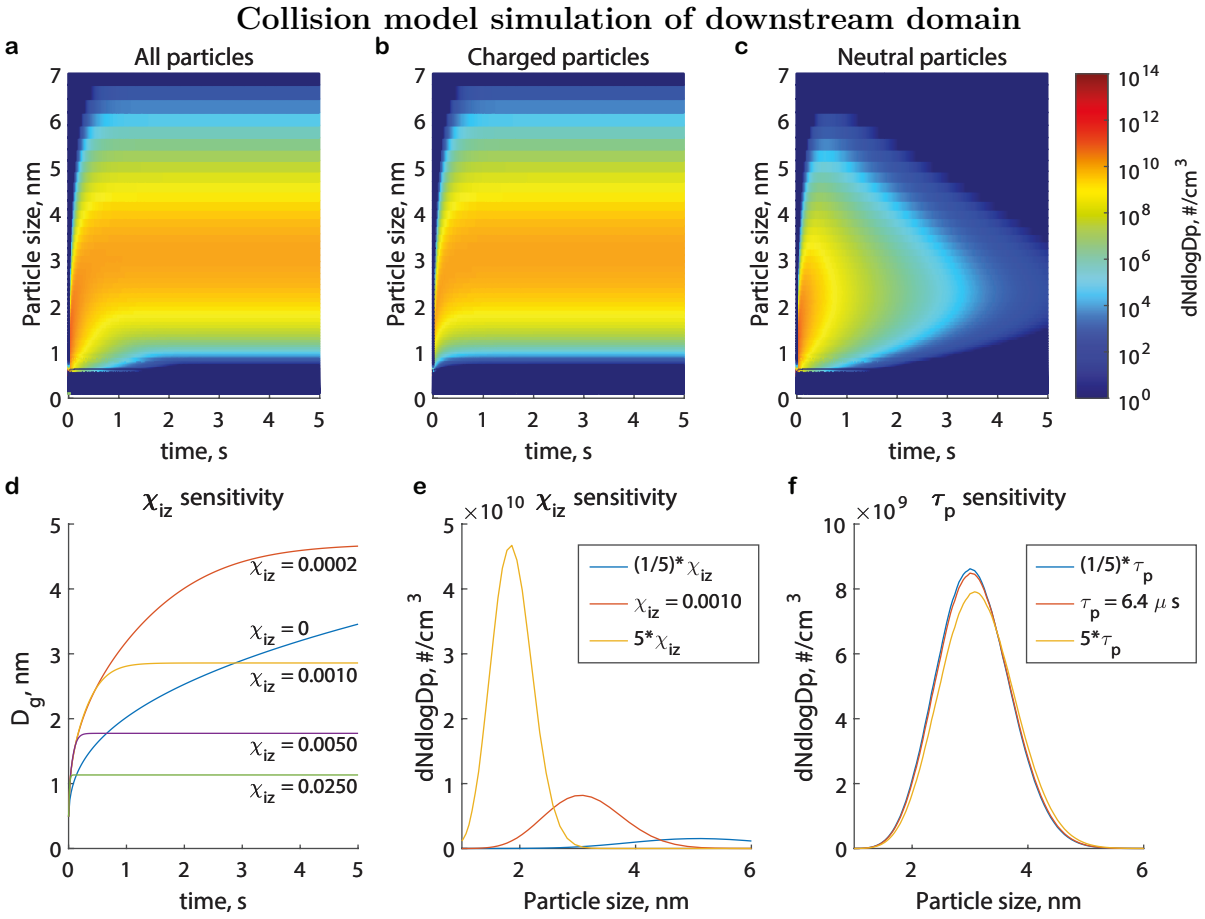

Figure 4.12: (a) Modeled particle size distribution in the downstream domain of the orifice mesh reactor operating at steady state with 80 ppb ferrocene ($FeCp_2$) and $\chi_{iz} = 0.001$. The time axis is equivalent to the distance downstream of the plasma scaled by the flow velocity. (b) and (c) show only the charged and neutral particles, respectively. (d) Geometric mean diameter, D_g as a function of time in the downstream domain for simulations over a range of χ_{iz} values for 80 ppb ferrocene. The initial growth rate is similar in all cases, and fast relative to unenhanced growth. (e,f) Steady state particle size distributions which use the plasma domain results shown in Figure 4.11b,c as the initial condition to highlight the strong influence of χ_{iz} and lack of sensitivity to τ_p.

concentration should remain constant with changes in the Fe vapor concentration, thus χ_{iz} will vary inversely proportional to the Fe vapor concentration. For an experiment where the ferrocene concentration is varied, the former would result in the observation of relatively uniform particle size (controlled by χ_{iz}) and proportional changes in particle concentration. The latter would result in proportional changes in both particle size and concentration which agrees with our experimental results (Figure 4.3 and 4.6). Indeed, Using a microplasma with geometry and operating conditions similar to the orifice-mesh, [20] measured a fixed concentration of charged particles at multiple precursor concentrations using a DMA-electrometer system without the typical neutralizer.

Figure 4.13 compares the particle size distributions from experimental measurements to that of the enhanced and unenhanced model at 20, 40, and 80 ppb ferrocene. Because the operating conditions were otherwise constant, a constant Fe ion concentration is assumed in all three cases, and χ_{iz} calculated by dividing this by the total Fe concentration. An Fe ion concentration of 3.57×10^{15} $\#/\mathrm{m}^3$ was found to minimize the difference in D_g between the enhanced model and experimental results, with less than 3% error in all cases. The formation time, taken as the time to reach $0.99D_g$, are in the range 0.65 to 0.68 s. For the unenhanced case, $\chi_{iz} = 0$ and no steady state is reached. Instead, the formation time is the time at which D_g is equal to the enhanced model value and the size distribution at this time is used. Unenhanced formation times are in the range 1.71 to 1.84 s.

While this enhancement increases the overall growth rate by a factor of about 3 for the examples considered in Figure 4.13, it is not sufficient to entirely explain the rapid growth rate observed experimentally, and indicates that simplifying assumptions may not be accurate or additional factors are at work in this process. The most likely explanation for this discrepancy is the possibility that some negatively charged particles do form and increase the formation rate through enhanced collisions of oppositely charged particles.

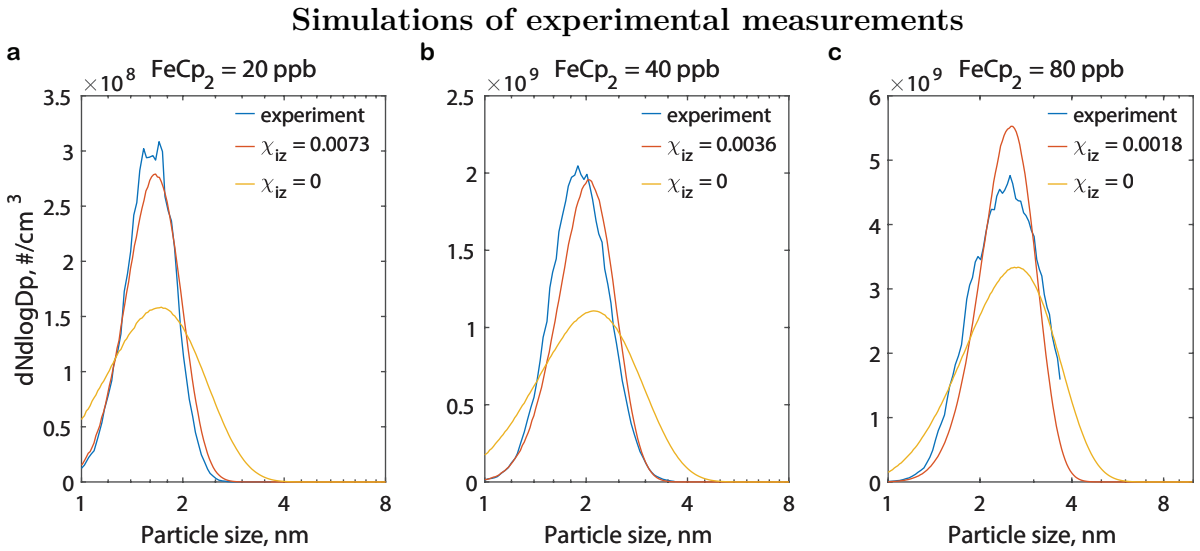

Figure 4.13: Particle size distributions comparing experimental measurements to enhanced and unenhanced model results for ferrocene concentrations of 20, 40, and 80 ppb. χ_{iz} values in each case were calculated based on a total Fe ion concentration of 3.57×10^{15} #/m^3, which was found to minimize the error between experimental and modeled D_g (<3% in all cases). Model particle size distributions are scaled by the experimental yield for visual clarity.

Within the plasma a portion of the larger Fe clusters may acquire a negative charge, although this would still be an very small concentration. Diffusion and turbulence in the plasma may also broaden the residence time distribution and allow the growth of larger Fe clusters as well. It is also possible that free electrons in the spatial afterglow may charge particles, although they are quickly lost to the walls due to high mobility [44].

Additionally, charge is likely not perfectly conserved in the downstream domain, indicating that the assumption of reaching a truly steady state particle size distribution is inaccurate. Experimental observations of particles after a long residence time (i.e., with a formation time of $>$ 1 s) show continued aggregation with larger D_g and σ_g. While the charging theory of aerosols assumes that the charge transfer rate between large aerosol particles and vapor molecules is negligible, charge transfer is experimentally observed to occur in 1-nm-scale particles with rate inversely proportional to size [47]. A more in-

depth model could consider this through incorporation of an empirical size-dependent decay constant for particle charges. Second, the model assumes a conservation of Fe from ferrocene vapor to final particles, which is not true under experimental conditions where $Y_{Fe} < 1$. This may be due to incomplete dissociation of ferrocene, aerosol particles below the 1 nm detection limit of the SMPS, and/or particle deposition on the reactor walls. Future work will focus on understanding the mechanism(s) behind the remaining enhancement and relating these mechanisms to process parameters. Nevertheless, the model accurately replicates the size distribution of the produced aerosols, and offers insights as to the critical role of charge-mediated growth.

4.6 Process performance and scaling

4.6.1 Concentration and diameter Pareto performance

Now, we discuss the performance of the microplasma reactor versus established methods of nanoparticle synthesis for CNT synthesis, and its potential scalability toward high-performance manufacturing. Figure 4.14 compares the concentration-diameter performance of the orifice-mesh and orifice reactors to four benchmark techniques from the literature. These processes were selected for comparison based on their similarity, previous use for CNT synthesis, and availability of aerosol measurements via SMPS to allow a direct comparison. While all report the synthesis of iron nanoparticles, these and related processes have been used for synthesis of other metal nanoparticles including nickel, copper, cobalt through substitution of different electrode materials or organometallic compounds. This comparison highlights a number of promising attributes of the present microplasma approach as well as areas where further development is needed to enable industrial application at scale. Insights drawn from the new model of particle formation

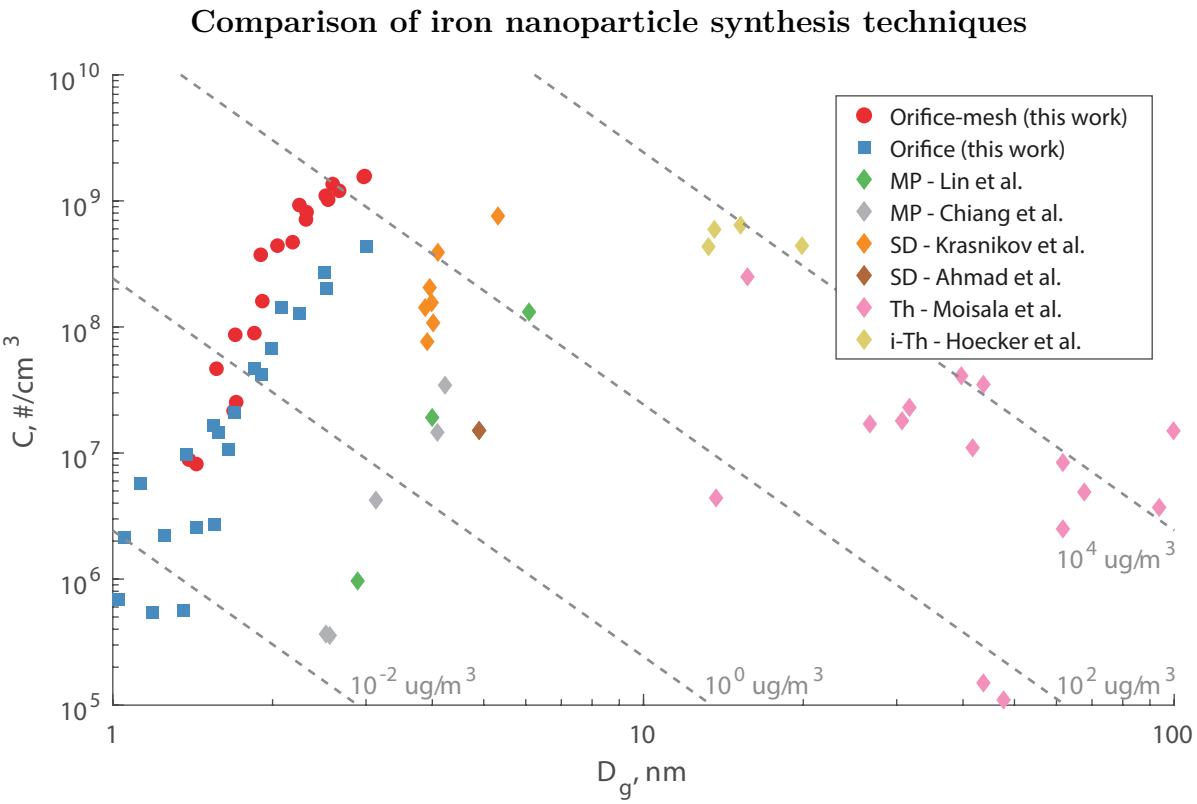

Figure 4.14: Comparison of the orifice-mesh and orifice reactors developed herein to existing aerosol processes for producing iron nanoparticle catalysts for CNT synthesis, in terms of aerosol concentration and particle diameter produced. See text for complete details and references on literature values.

in Section 4.4 offer a mechanistic understanding of these shortcomings and indicate ways for improvement.

The cited microplasma processes, 'MP - [5]' and 'MP - [9]', utilize a design similar to the orifice-mesh reactor with 100 sccm Ar flow and ferrocene vapor. The spark discharge processes, 'SD - [48]' and 'SD - [49]', use a high voltage intermittent discharge between two iron electrodes to generate iron vapor in a nitrogen flow, which condenses to form particles.The thermal process,'Th - [50]', is commonly used to supply catalyst particles for CNT synthesis. Here, ferrocene vapor is thermally decomposed in the CVD reactor to produce iron vapor which condenses into particles. The in-situ thermal process, 'i-Th - [28]', is identical to the thermal process, but the aerosol measurements were taken inside the furnace instead of at the outlet, more closely measuring the aerosol at the location of CNT nucleation and growth. In all cases, as-reported electrical mobility diameter was converted to mass diameter by subtracting 0.3 nm, assuming spherical particles.

Data processing of literature values for Figure 4.14

For some literature values used in Figure 4.14, some assumptions were needed to calculate the actual concentration at the device. These assumptions are noted here and are based off data reported for other operating conditions or instrument and equipment specifications. Given the orders of magnitude variation in C, it is apparent that small errors in these values does not materially effect the interpretation of, or conclusions from, Figure 4.14. In all cases, as-reported electrical mobility diameter was converted to mass diameter by subtracting 0.3 nm, assuming spherical particles.

Data for the two groups of microplasma processes was collected from a series of publications by Chiang: [51, 52, 9] and the work of [5], all of which appear to use same experimental set-up. The reactor is similar to the orifice-mesh reactor however uses a stainless steel capillary tube (178 μm inner diameter) as the upstream electrode and is

operated with a flow of 100 sccm argon. C, D_g, and σ_g were found by fitting log-normal distributions to particle size distributions reported in figures. A dilution flow of 1400 sccm N_2 was assumed in calculating C as the instrumentation used requires a flow rate of 1500 sccm. Ferrocene concentration was estimated assuming that argon exiting the ferrocene sublimation chamber is fully saturated using values from [16].

Data for the spark discharge processes was reported by [48] and [49].In the former, the reactor contains two iron electrodes separated by a small gap oriented perpendicular to a flow of 2000 sccm N_2. Again, C, D_g, and σ_g were found by fitting log-normal distributions to particle size distributions reported in figures. In the latter, the reactor contains concentric iron electrodes which create a cylindrical gap through which the carrier gas flows. C, D_g, and σ_g were reported for a flow rate of 2000 sccm.

Data for the thermal process was reported by [50]. Ferrocene vapor and a carrier gas are injected into a laminar flow tubular reactor (22 mm inner diameter and 400 mm length). C, D_g, and σ_g are reported at the outlet as well as gas flow rates, furnace temperature, and ferrocene concentration for all runs.

Data for the in-situ thermal process was reported by [28]. Again, ferrocene vapor and a carrier gas are injected into a laminar flow tubular reactor (40 mm inner diameter and 700 mm length). A probe is used to measure the particle size distribution along the reactor center line at different axial locations, and particle size distribution is reported as a function of axial position. C, D_g, and σ_g were found by fitting log-normal distributions to the particle size distribution at the position of highest concentration. Gas flow rates, furnace temperature, and ferrocene concentration were reported for all runs. The presence of S in some of their experiments is not considered here as it does not appear to influence the initial nucleation and growth of particles, only the secondary nucleation at the reactor outlet.

4.6.2 Discussion

For many applications, including CNT synthesis, the particle diameter plays a key role in determining its catalytic effect during subsequent reactions and/or the structure of final products. Figure 4.14 shows that microplasma-based processes, and to a lesser degree, spark discharge, are uniquely capable of producing small diameter aerosols in the 1–5 nm range. While the initial particles formed in the thermal processes are of similar 5–10 nm diameter, rapid aggregation leads to growth of fractal aggregates of 10–100 nm size which is recorded by aerosol size classification. TEM images of particles reported by [50] from the thermal process show solid, spherical particles up to 10–20 nm, indicating complete melting and coalescence of primary particles, while larger particles are loose fractal aggregates of the former.

It is also desirable to control D_g independently of C, instead of using the input precursor (e.g., ferrocene) concentration as a means of diameter control. Using the microplasma reactor, the aerosol will ideally reach a steady state particle size distribution which can be tuned through modifying the extent of negative charging, as the magnitude of the net charge is inversely proportional to the average number of atoms per particle in the final distribution. The plasma current, type (DC, AC, RF), geometry, and residence time will influence this. The composition of the carrier gas may also play a role by altering the supply of positive ions at the plasma exit or by facilitating charge transfer and loss downstream of the plasma, and may contribute to the lower concentration of the existing microplasma, which uses Ar. Alternatively, the residence time of the downstream section can be a means of tuning the output size distribution if less than needed to reach the steady state distribution. However, the aerosol will continue to grow and thus must be well integrated with the subsequent processing steps or operations, such as deposition of a coating or, as motivated by the present focus on Fe particles, CNT

growth. As electrostatic enhancement also influences σ_g, increasingly monodisperse particles may be possible by operation below room temperature as η is inversely related to T through the velocity term. As the collision rate without enhancement is proportional to $T^{1/2}$, the penalty is not drastic.

Y_{Fe} determines not only the needed precursor input to meet a production rate, but also indicates potential deposition of iron within the reactor or the presence of unwanted products. Figure 4.3c shows that, for the orifice-mesh reactor, Y_{Fe} ranges from $\sim 10^{-2}$ to 1.1. The calculation of $Y_{Fe} = 1.1$ at a flow of 600 sccm with 87 ppb ferrocene indicates that the simplifying assumptions used in this calculation may not be uniformly valid. This likely indicates a reduced density due to porosity or fractal-aggregate geometry, but may also indicate the incorporation of carbon into the particle, oxidation by trace amounts of oxygen in the system, or measurement error. Whether or not these sources of error apply to all the reported Y_{Fe} values, the trend of decreasing Y_{Fe} with decreasing D_g will remain, and we attribute this to particle loss to the system walls via diffusion. The rate of diffusion loss increases for smaller diameter particles due to increased particle diffusivity [53, 54], explaining the trend of decreasing Y_{Fe} with final diameter. Additionally, intermediate-size particles may be lost during the growth period, in which case conditions of slower growth rate will have lower Y_{Fe}. The difference between the orifice and orifice-mesh results may be explained by diffusion losses related to the geometry of the reactors, with the orifice reactor presenting a larger wall surface area to the microplasma.

The particle production rate could be scaled up by increasing concentration or flow rate, each with distinct trade-offs. The maximum size of a reactor is constrained by the microplasma operating window, limiting maximum flow rate, although multi-reactor arrays can be used (e.g., a plate with an array of orifices). Yet, careful consideration of the flow and mixing downstream of the reactor is needed to maintain the desired

size distribution, and downstream collection or processing devices may need to be scaled accordingly. In contrast, increasing concentration can allow for a decrease in total system size while maintaining a needed residence time and production rate. This presents a more efficient use of the carrier gas, yet may limit the operating window and increase the rate of particle aggregation.

The orifice-mesh reactor has demonstrated a significant concentration improvement over similar systems, and further improvements are likely possible. While the current work only begins to inform which factors limit the performance for microplasma aerosol synthesis, it indicates two areas for future research: reactor geometry and operating conditions. Figure 4.2a shows that a small geometry change (increasing the orifice diameter from 180 to 300 μm) can change concentration by a factor of two. Similarly, Figure 4.5a shows an order of magnitude difference in concentration between the orifice-mesh and orifice reactor designs. The operating conditions used here also differ substantially from the other microplasma processes in Figure 4.14: lower plasma current, higher flow rates, and the use of helium. For example, we demonstrate the sensitivity of particle size and concentration to flow rate in Figure 4.3 and Figure 4.6. The mechanisms by which these changes effect particle formation and concentration are yet to be validated, yet may include changes to the flow field and residence time, particle losses to reactor walls, the extent of precursor decomposition, particle charging and fractional ionization.

If the aerosol is to be used directly, the continuous evolution of the particle size distribution must be considered from the microplasma reactor to the point of use within subsequent equipment. For CNT growth, in order to achieve a concentration of $\sim 10^9$ $\#/\text{cm}^3$ at the point of catalytic activity within the CVD furnace, a concentration of 10^{10} $\#/\text{cm}^3$ or higher at the microplasma reactor may be needed to account for diffusion and thermophoretic losses, evaporation, and aggregation. The integration of these systems must be carefully designed to limit aerosol evolution and ensure the fidelity of aerosol

measurements.

4.7 Conclusion

In this Chapter, a novel atmospheric pressure DC microplasma reactor was developed and used to study the synthesis of Fe nanoparticles from ferrocene vapor. This device is capable of producing high concentration ($> 10^9$ #/cm^3) sub-3 nm iron particles with narrow size distribution ($\sigma_g < 1.3$) during stable operation for multiple hours. The mass yield of particles increases with particle diameter until saturating at near unity at 3 nm, suggesting diffusion losses as the primary loss mechanism. The ability to tune particle diameter and concentration via the carrier gas flow rate and ferrocene concentration is demonstrated. We develop a charge-mediated formation mechanism and show that the ~ 10 μs plasma residence time is insufficient for the growth of clusters beyond 10 atoms, indicating that the equilibrium charging of iron vapor and clusters in the plasma is predominantly neutral or positive. The formation of negatively charged clusters, as is typical in a plasma process with longer residence time, is unlikely to occur. Thus, the bulk of particle growth occurs downstream of the plasma domain through aggregation of neutral and positively charged clusters. The value of fractional ionization for the iron vapor is found to be a critical control on the formation process, and future work will seek to measure and control this parameter. While the charge-mediated formation mechanism is able to closely reproduce the observed size distributions, is not sufficient to entirely explain the rapid growth rate observed experimentally, and future work will focus on understanding the mechanism(s) behind the remaining enhancement and relating these mechanisms to process parameters.

References

[1] William James Sawyer. "Toward improved manufacturing of carbon nanotubes by microplasma synthesis of catalyst nanoparticles". Massachusetts Institute of Technology, 2020.

[2] Yuan Pu et al. "Colloidal synthesis of semiconductor quantum dots toward large-scale production: a review". In: *Industrial & Engineering Chemistry Research* 57.6 (2018), pp. 1790–1802.

[3] J Kimling et al. "Turkevich method for gold nanoparticle synthesis revisited". In: *The Journal of Physical Chemistry B* 110.32 (2006), pp. 15700–15707.

[4] Neel Narayan, Ashokkumar Meiyazhagan, and Robert Vajtai. "Metal Nanoparticles as Green Catalysts". In: *Materials* 12.21 (2019), p. 3602.

[5] Pin Ann Lin, Ajay Kumar, and R Mohan Sankaran. "New insights into plasma-assisted dissociation of organometallic vapors for gas-phase synthesis of metal nanoparticles". In: *Plasma Processes and Polymers* 9.11-12 (2012), pp. 1184–1193.

[6] Yibo Yan et al. "Carbon nanotube catalysts: recent advances in synthesis, characterization and applications". In: *Chemical Society Reviews* 44.10 (2015), pp. 3295–3346.

[7] Fiona Smail, Adam Boies, and Alan Windle. "Direct spinning of CNT fibres: Past, present and future scale up". In: *Carbon* 152 (2019), pp. 218–232.

[8] Lee Weller et al. "Mapping the parameter space for direct-spun carbon nanotube aerogels". In: *Carbon* 146 (2019), pp. 789–812.

[9] Wei-Hung Chiang, Carolyn Richmonds, and R Mohan Sankaran. "Continuous-flow, atmospheric-pressure microplasmas: a versatile source for metal nanoparticle synthesis in the gas or liquid phase". In: *Plasma Sources Science and Technology* 19.3 (2010), p. 034011.

[10] Alborz Izadi and Rebecca J Anthony. "A plasma-based gas-phase method for synthesis of gold nanoparticles". In: *Plasma Processes and Polymers* (), e1800212.

[11] Kostya Ken Ostrikov, Uros Cvelbar, and Anthony B Murphy. "Plasma nanoscience: setting directions, tackling grand challenges". In: *Journal of Physics D: Applied Physics* 44.17 (2011), p. 174001.

[12] Liangliang Lin and Qi Wang. "Microplasma: a new generation of technology for functional nanomaterial synthesis". In: *Plasma Chemistry and Plasma Processing* 35.6 (2015), pp. 925–962.

[13] Davide Mariotti and R Mohan Sankaran. "Microplasmas for nanomaterials synthesis". In: *Journal of Physics D: Applied Physics* 43.32 (2010), p. 323001.

[14] Wei-Hung Chiang and R Mohan Sankaran. “In-flight dimensional tuning of metal nanoparticles by microplasma synthesis for selective production of diameter-controlled carbon nanotubes”. In: *The Journal of Physical Chemistry C* 112.46 (2008), pp. 17920–17925.

[15] Wei-Hung Chiang and R Mohan Sankaran. “Linking catalyst composition to chirality distributions of as-grown single-walled carbon nanotubes by tuning Ni x Fe 1- x nanoparticles”. In: *Nature materials* 8.11 (2009), p. 882.

[16] Michal Fulem et al. “Recommended vapor pressure and thermophysical data for ferrocene”. In: *The Journal of Chemical Thermodynamics* 57 (2013), pp. 530–540.

[17] Bon Ki Ku and Juan Fernandez De La Mora. “Relation between electrical mobility, mass, and size for nanodrops 1–6.5 nm in diameter in air”. In: *Aerosol Science and Technology* 43.3 (2009), pp. 241–249.

[18] Carlos Larriba et al. “The mobility–volume relationship below 3.0 nm examined by tandem mobility–mass measurement”. In: *Aerosol Science and Technology* 45.4 (2011), pp. 453–467.

[19] Souvik Ghosh et al. “Atmospheric-pressure dielectric barrier discharge with capillary injection for gas-phase nanoparticle synthesis”. In: *Journal of Physics D: Applied Physics* 48.31 (2015), p. 314003.

[20] R Mohan Sankaran et al. “Synthesis of blue luminescent Si nanoparticles using atmospheric-pressure microdischarges”. In: *Nano letters* 5.3 (2005), pp. 537–541.

[21] Beat Buesser and Sotiris E Pratsinis. “Design of nanomaterial synthesis by aerosol processes”. In: *Annual review of chemical and biomolecular engineering* 3 (2012), pp. 103–127.

[22] Renyi Zhang et al. “Nucleation and growth of nanoparticles in the atmosphere”. In: *Chemical reviews* 112.3 (2012), pp. 1957–2011.

[23] Richard Becker and Werner Döring. “Kinetische behandlung der keimbildung in übersättigten dämpfen”. In: *Annalen der Physik* 416.8 (1935), pp. 719–752.

[24] Barbara E Wyslouzil and Judith Wölk. “Overview: Homogeneous nucleation from the vapor phase—The experimental science”. In: *The Journal of chemical physics* 145.21 (2016), p. 211702.

[25] CB Alcock, VP Itkin, and MK Horrigan. “Vapour pressure equations for the metallic elements: 298–2500K”. In: *Canadian Metallurgical Quarterly* 23.3 (1984), pp. 309–313.

[26] Richard Tran et al. “Surface energies of elemental crystals”. In: *Scientific data* 3.1 (2016), pp. 1–13.

[27] NB Vargaftik, BN Volkov, and LD Voljak. “International tables of the surface tension of water”. In: *Journal of Physical and Chemical Reference Data* 12.3 (1983), pp. 817–820.

[28] Christian Hoecker et al. “Catalyst nanoparticle growth dynamics and their influence on product morphology in a CVD process for continuous carbon nanotube synthesis”. In: *Carbon* 96 (2016), pp. 116–124.

[29] Christian Hoecker et al. “The Dependence of CNT Aerogel Synthesis on Sulfur-driven Catalyst Nucleation Processes and a Critical Catalyst Particle Mass Concentration”. In: *Scientific reports* 7.1 (2017), p. 14519.

[30] James D Landgrebe and Sotiris E Pratsinis. “Gas-phase manufacture of particulates: interplay of chemical reaction and aerosol coagulation in the free-molecular regime”. In: *Industrial & engineering chemistry research* 28.10 (1989), pp. 1474–1481.

[31] Benjamin Santos et al. “Electrostatic enhancement factor for the coagulation of silicon nanoparticles in low-temperature plasmas”. In: *Plasma Sources Science and Technology* 28.4 (2019), p. 045002.

[32] Steven L Girshick. “Particle nucleation and growth in dusty plasmas: On the importance of charged-neutral interactions”. In: *Journal of Vacuum Science & Technology A: Vacuum, Surfaces, and Films* 38.1 (2020), p. 011001.

[33] Sheldon K Friedlander et al. *Smoke, dust, and haze*. Vol. 198. Oxford university press New York, 2000.

[34] David D Huang, John H Seinfeld, and Kikuo Okuyama. “Image potential between a charged particle and an uncharged particle in aerosol coagulation—enhancement in all size regimes and interplay with van der Waals forces”. In: *Journal of colloid and interface science* 141.1 (1991), pp. 191–198.

[35] Hui Ouyang, Ranganathan Gopalakrishnan, and Christopher J Hogan Jr. “Nanoparticle collisions in the gas phase in the presence of singular contact potentials”. In: *The Journal of chemical physics* 137.6 (2012), p. 064316.

[36] NA Fuchs and AG Sutugin. “Coagulation rate of highly dispersed aerosols”. In: *Journal of Colloid Science* 20.6 (1965), pp. 492–500.

[37] Mark G Sceats. “Brownian coagulation in aerosols—the role of long range forces”. In: *Journal of colloid and interface science* 129.1 (1989), pp. 105–112.

[38] Sara R Gomes de Sousa, Alice Leonel, and Antonio JF Bombard. “On the Hamaker constant of the metallic iron, the retardation effect and their relevance in DLVO theory applied to oil-based magnetorheological fluid with 1-octylamine”. In: *Smart Material Structures* 29.5 (2020), p. 055039.

[39] Liangliang Lin et al. “Synthesis of iron oxide nanoparticles in microplasma under atmospheric pressure”. In: *Chemical Engineering Science* 168 (2017), pp. 360–371.

[40] David R Lide. *CRC handbook of chemistry and physics*. Vol. 85. CRC press, 2004.

[41] Michael A. Lieberman and Allan J. Lichtenberg. “Principles of Plasma Discharges and Materials Processing”. In: Hoboken: John Wiley and Sons, Inc, 2005.

[42] M Mamunuru et al. “The existence of non-negatively charged dust particles in nonthermal plasmas”. In: *Plasma Chemistry and Plasma Processing* 37.3 (2017), pp. 701–715.

[43] Marco Gatti and Uwe Kortshagen. “Analytical model of particle charging in plasmas over a wide range of collisionality”. In: *Physical Review E* 78.4 (2008), p. 046402.

[44] Girish Sharma et al. “Characterization of particle charging in low-temperature, atmospheric-pressure, flow-through plasmas”. In: *Journal of Physics D: Applied Physics* 53.24 (2020), p. 245204.

[45] Xiaoshuang Chen et al. “Size and structural characterization of Si nanocrystal aggregates from a low pressure nonthermal plasma reactor”. In: *Powder Technology* 373 (2020), pp. 164–173.

[46] Francisco J Romay and David YH Pui. “Free electron charging of ultrafine aerosol particles”. In: *Journal of aerosol science* 23.7 (1992), pp. 679–692.

[47] Vinay Premnath, Derek Oberreit, and Christopher J Hogan Jr. “Collision-based ionization: bridging the gap between chemical ionization and aerosol particle diffusion charging”. In: *Aerosol Science and Technology* 45.6 (2011), pp. 712–726.

[48] Dmitry V Krasnikov et al. “A spark discharge generator for scalable aerosol CVD synthesis of single-walled carbon nanotubes with tailored characteristics”. In: *Chemical Engineering Journal* 372 (2019), pp. 462–470.

[49] Saeed Ahmad et al. “Gas phase synthesis of metallic and bimetallic catalyst nanoparticles by rod-to-tube type spark discharge generator”. In: *Journal of Aerosol Science* 123 (2018), pp. 208–218.

[50] Anna Moisala et al. “Single-walled carbon nanotube synthesis using ferrocene and iron pentacarbonyl in a laminar flow reactor”. In: *Chemical Engineering Science* 61.13 (2006), pp. 4393–4402.

[51] Wei-Hung Chiang and R Mohan Sankaran. “Microplasma synthesis of metal nanoparticles for gas-phase studies of catalyzed carbon nanotube growth”. In: *Applied Physics Letters* 91.12 (2007), p. 121503.

[52] Wei-Hung Chiang and R Mohan Sankaran. “Synergistic effects in bimetallic nanoparticles for low temperature carbon nanotube growth”. In: *Advanced Materials* 20.24 (2008), pp. 4857–4861.

[53] David Covert, Alfred Wiedensohler, and Lynn Russell. “Particle charging and transmission efficiencies of aerosol charge neutralizes”. In: *Aerosol Science and Technology* 27.2 (1997), pp. 206–214.

[54] Prashant Kumar et al. “Treatment of losses of ultrafine aerosol particles in long sampling tubes during ambient measurements”. In: *Atmospheric Environment* 42.38 (2008), pp. 8819–8826.

5. Microplasma reactor process intensification

This chapter describes the continued development of microplasma-based nanoparticle synthesis, focusing on the design of a new reactor with a focus on two attributes. First, a physical design which is amenable to integration with the FC-CVD system for CNT synthesis. While the designs outlined in Chapter 4 were used for integrated CNT synthesis experiments, the materials and geometry necessitated a long flow path between the microplasma and the hot zone of the CVD system. Second, a focus on improving the practical performance of the system in terms of productivity and reliability, to better enable its use in an integrated system. To do so, several studies were undertaken to better understand the physical processes which govern performance. This chapter uses text and figures adapted from the following journal article, currently under revision:

Sawyer, W. J., and A. John Hart. Process intensification of microplasma nanoparticle synthesis enabled by gas flow design. *Chemical Engineering Journal*, under review. Available at http://dx.doi.org/10.2139/ssrn.4492561

Notation

$Fe(Cp)_2$	ferrocene
sccm	cm^3/min at 1 atm and 293 K
L_{tt}	transfer tube length
I_p	plasma current
V_p	plasma voltage
SMPS	scanning mobility particle sizer
PSD	particle size distribution
d_m	electrical mobility diameter of particle in N_2
d_p	physical diameter of particle (d_m - 0.3 nm)
d_{ve}	volume-equivalent diameter of particle
C_N	aerosol number concentration
C_V	aerosol volume concentration
D_g	geometric mean diameter of PSD
σ_g	geometric standard deviation of PSD
Y_{Fe}	iron yield
Y_C	carbon yield
Y_{mass}	mass-weighted yield of iron and carbon
Y_{vol}	volume-weighted yield of iron and carbon
w_{Fe}	iron mass fraction
Y^a_{vol}	aerosol volume yield
χ	dynamic shape factor
χ_B	bulk dynamic shape factor

5.1 Introduction

Tailored synthesis of nanoscale (<100 nm) metal particles is important to many applications including catalysis [1, 2, 3], material synthesis [4], drug delivery [5], and photonics [6]. For synthesis of nanoscale metal particles, many aerosol synthesis techniques have been developed including spark discharge [7], flame spray pyrolysis [8], and nonthermal plasma [9], and remain of interest due to the potential for high purity and continuous production when compared to wet chemical techniques. However, the aerosol nature of these processes entails a fundamental trade-off between process control and intensity as the rate of particle aggregation scales with the square of concentration. Thus, aerosol particle synthesis typically result in a wide distribution and poor control of particle size [8], or are done at impractically low concentration [7, 10] for scaled production. This trade-off is especially salient for sub-10 nm particles due to the heightened effect of Brownian and thermophoretic forces, and the strict requirement to limit aggregation to maintain such a small size [11]. The intensification of sub-10 nm aerosol synthesis and the development of these processes for industrial operation therefore is an important manufacturing challenge.

Atmospheric pressure microplasma processes using metallorganic precursors have produced sub-10 nm aerosols [12, 13, 14, 15] at number concentrations (C_N) up to 10^9 #/cm^3 [16], yet are typically operated at low flow rates or the order 100 cm^3/min at standard conditions (sccm). While many authors conceptualize particle formation as a discrete event within the microplasma, we showed that the microplasma residence time is too short for particle growth, thus the bulk of particle growth occurs in the downstream region: as the aerosol flows from the microplasma reactor to the point of collection, sampling, or application [16]. We used this insight to design a system with an improved diameter-concentration pareto front. Thus, the fundamental aerosol synthesis trade-off

between concentration and aggregation is not a ceiling on process performance, but is a challenge that can be overcome by incorporating an awareness of aerosol dynamics into the design of the entire system, from precursor dissociation to the point of particle collection or use (e.g., a catalytic reaction).

In this paper we present the design of a new reactor system for practical use which has been developed and optimized to improve process intensification and reliability. The system utilizes an atmospheric pressure DC microplasma to synthesize iron-carbon particles from a ferrocene ($Fe(Cp)_2$) vapor precursor at a flow rate of 3500 sccm. To improve the yield and long-term stability of aerosol synthesis, the microplasma reactor incorporates a novel plasma focusing technique and indirect injection of $Fe(Cp)_2$. On-line aerosol measurement is used to investigate the relationship between operating conditions, system design, and particle size distribution (PSD), as well as to characterize the stability of operation for a period of 10 hours at various conditions. Ex-situ bulk particle characterization for select operating conditions is used in tandem to assess the improvement in yield, constrain particle shape to gain insight into the growth process, and determine the selectivity of iron with respect to carbon impurities.

5.2 Methods

5.2.1 Microplasma reactor system

The aerosol synthesis system developed here, shown schematically in Figure 5.1(a) is composed of a microplasma reactor placed inside a transfer tube. The outlet of the transfer tube can be connected to either a scanning mobility particle sizer (SMPS) for aerosol measurement or a filter holder for aerosol collection, both described in Section 5.2.2. Figure 5.1(b) and (c) show photos of the complete assembly and a close-up of the

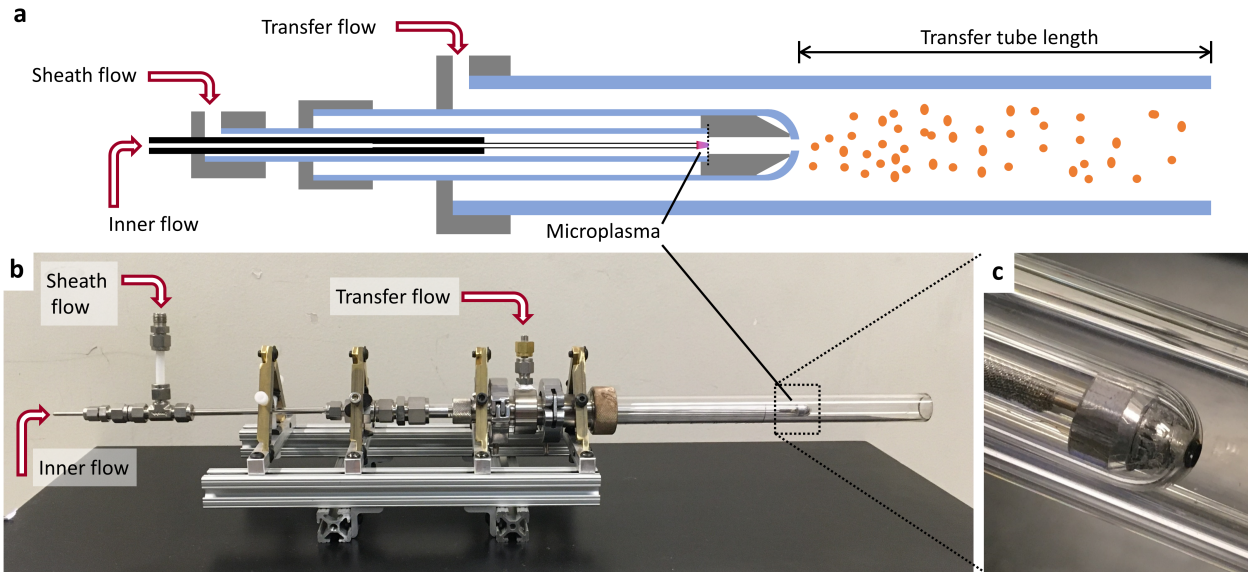

Figure 5.1: (a) Schematic of the nanoparticle aerosol synthesis system showing the microplasma reactor and aerosol transfer tube. (b) Image of the complete system. (c) Close-up of the microplasma reactor, looking upstream.

microplasma reactor.

The microplasma reactor is contained within a quartz tube housing (ID = 10.5 mm, OD = 12.7 mm) with a hemispherical end. The hemisphere has a 2 mm diameter orifice at its apex. Within this housing, the upstream side of the microplasma reactor is composed of a stainless steel capillary tube (ID = 0.87 mm, OD = 1.07 mm), which is centered inside a quartz tube (ID = 4 mm, OD = 6 mm) using a mesh spacer. The capillary tube serves as the high voltage electrode (with either positive or negative polarity) and contains the inner flow. The annular gap between these tubes contains the sheath flow. The downstream side of the microplasma reactor is composed of a hollow aluminum cylinder with a cap which securely holds a piece of 316 stainless steel mesh (TWP Inc., 30 μm wire, 20x20 wire/cm). The stainless steel mesh acts as the downstream electrode and is electrically grounded. The cap geometry is such that it mates precisely with the inner quartz tube to position the mesh electrode flush with the end of the quartz tube. The capillary tube is recessed from the end of the quartz tube

by 2 mm to create the electrode gap. The outer diameters of the cap and cylinder are machined to a slip fit tolerance inside the quartz housing to ensure proper alignment. The inner volume of the aluminum cylinder (ID = 3 mm, L = 10.3 mm) determines the volume of the microplasma reactor downstream of the mesh electrode, while the plasma forms upstream of the mesh electrode with a plasma volume roughly determined by the electrode gap and capillary tube diameter.

The microplasma reactor is contained within a quartz transfer tube (ID = 20 mm, OD = 25 mm), and the transfer tube length (L_{tt}) is defined as the distance from the tip of the microplasma housing to the end of the transfer tube. A third gas flow, the transfer flow, is introduced in the annular gap outside the microplasma housing and inside the transfer tube. The transfer tube is intended to simulate the conditions that would be present if the aerosol is transported and injected into a downstream process, such as the aerosol synthesis of carbon nanotubes. Thus, the aerosol characterized at the outlet of the transfer tube represents that which would be input into an application.

The set of experiments discussed in Section 5.3.1, 5.3.3, and 5.3.4 was performed as a single continuous run, varying parameters and conditions on-line. Each of the long duration experiments in Section 5.3.2 was performed as an independent run. Before each run the microplasma reactor is disassembled and cleaned, the capillary tube is cleaned of deposits by rinsing with 37% hydrochloric acid, and a clean piece of mesh is installed. Once assembled, the system is evacuated to below 20 mtorr using a roughing pump (Varian DS102) to ensure no major leaks and refilled with He (Airgas, UHP, 99.999%). All gas lines are evacuated and purged when gas cylinders are changed to minimize the potential impact of unknown impurities. Slight variations in performance between runs are attributed to small variations in the electrode gap and mesh position on reassembly.

We define the baseline case of operating conditions for the microplasma reactor as follows: inner flow of 600 sccm He, sheath flow of 150 sccm He and 150 sccm N_2 (Airgas,

HP, 99.998%), positive high voltage polarity, and plasma current (I_p) of 1 mA. Ferrocene ($Fe(Cp)_2$) vapor is added to the inner or sheath flow by diverting 30 sccm He through a sublimation chamber containing $Fe(Cp)_2$ powder at room temperature. The vapor pressure of $Fe(Cp)_2$ in the sublimation chamber is calculated using the sublimation chamber temperature, assuming saturation [17]. This is scaled by the ratio of the sublimation chamber flow rate to the total microplasma flow rate to calculate the $Fe(Cp)_2$ vapor concentration in the microplasma reactor (for example, 200 ppb at 21 °C for 30 sccm sublimation chamber flow and 900 sccm total microplasma flow). The transfer tube conditions for the baseline case are: transfer flow of 2600 sccm He and L_{tt} = 100 mm. In section 5.3, a range of other operating conditions based on changing one or more of these parameters is investigated, including the use of H_2 (Airgas, UHP, 99.999%) and Ar (Airgas, UHP, 99.999%).

5.2.2 Aerosol characterization

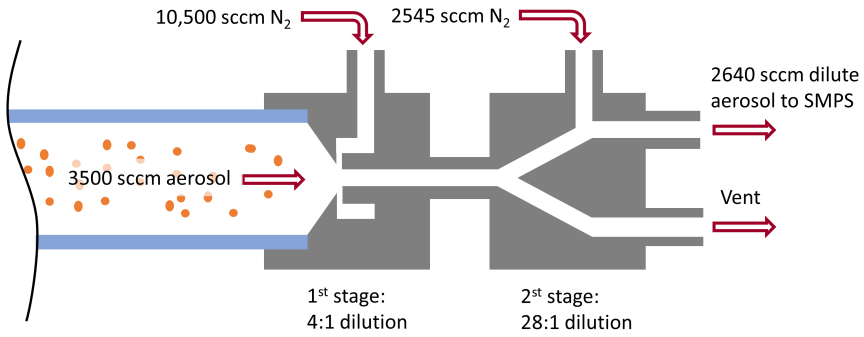

Figure 5.2: Schematic of the two stage dilution system for SMPS measurement. The inlet flow to the SMPS is regulated by an internal air flow controller.

Aerosol PSD was characterized in-line by SMPS (TSI Inc. 3938E57, mobility diameter range 1.4 to 30 nm). The SMPS system is calibrated for, and intended to be used in, air or N_2. We have found that its performance is highly influenced by the gas composition with significant error when greater than 1% He, H_2, or Ar is present. A two-stage

dilution system, shown schematically in Figure 5.2, was designed to ensure the inlet flow composition is >99% N_2. Dilution of the aerosol also limits particle aggregation en route to the SMPS, preserving the PSD as it was at the sampling location, and ensures operation within instrument concentration limits. The first dilution stage uses a ring of radially oriented gas jets to mix 10,500 sccm N_2 into the 3500 sccm aerosol stream at the end of the transfer tube. The second dilution stage splits this flow into a waste stream (open to atmospheric pressure) and a sample stream which is combined with a second N_2 flow before flowing into the SMPS. The flow rate of the sample stream is set by the difference between the SMPS inlet flow, internally regulated to a nominal 2500 sccm, and the second N_2 flow, the entirety of which is directed into the SMPS. The dilution system was calibrated and found to have a dilution ratio of 4 in the first stage and 28 in the second stage (with a secondary N_2 flow rate of 2545 sccm), resulting in a total dilution ratio of 112.

Electrical mobility diameter (d_m) as measured via SMPS is converted to physical diameter (d_p) by subtracting 0.3 nm to account for the diameter of the N_2 carrier gas molecules [18, 19]. PSD and lognormal statistical parameters – geometric mean diameter (D_g) and geometric standard deviation (σ_g) – use the corrected d_p data. For non-porous spherical particles, d_p uniquely indicates the actual size and volume of the particle. For porous or non-spherical particles, d_p overestimates the true volume or mass of the particle [20]. Particle shape is investigated in Section 5.3.4.

Aerosols were collected on a sintered silver filter (Sterlitech; 45328) inserted at the end of the transfer tube. A sealed filter holder was used to ensure the entire aerosol flow passed through the filter. Downstream SMPS measurements show a $10^3 - 10^4$ reduction in particle concentration with the filter inserted, indicating a collection efficiency of $> 99.9\%$. A collection period of two hours was used to ensure the deposit was of sufficient mass and thickness to minimize subsequent measurement errors.

For the purpose of assessing production rate and yield, particle composition was assumed to be solely iron and carbon from $Fe(Cp)_2$, and oxygen from trace impurities in the gases. Iron nanoparticles are highly reactive and easily oxidize in the presence of oxygen or moisture [21]. Oxygen and moisture impurities in the process gases provide a sufficient supply of oxygen to fully oxidize iron in the particles during synthesis. In cases where H_2 is used and may prevent oxidation within the microplasma reactor system, oxidation is likely to proceed once the aerosol is diluted for SMPS measurement. Scanning Electron Microscope Energy Dispersive Spectroscopy (SEM-EDS; Zeiss Gemini 450, Oxford Instruments Ultim Max) was used to characterize the ratio of these elements and confirm the absence of other elemental impurities. As oxygen is difficult to measure accurately via SEM-EDS, we calculate the oxygen fraction by assuming complete oxidation of the iron, thus a 2:3 molar ratio [22].

As both the deposit thickness and SEM-EDS analysis depth are of the order 1–3 μm, the raw measured composition typically contains 5–10 at% silver, which is attributed to the filter material and removed from the analysis. The only other elements that might be expected in the collected samples are H (from $Fe(Cp)_2$ or in cases where H_2 is used), N (from the sheath flow), and impurities from the $Fe(Cp)_2$ or sputtered material from the electrodes. The presence of H can not be assessed via EDS, and would be a small fraction of the total mass if present. N and other elements are not readily observed in the EDS signal, and thus, if present, are negligible.

5.2.3 Flow simulations

Simulation studies of the gas flow and aerosol diffusion within the system were performed using Solidworks Flow Simulation and the Tracer Study feature (Version 2022, Dassault Systèmes). $Fe(Cp)_2$ vapor and representative aerosol particles were modeled as gas tracers with binary diffusion coefficients calculated to first order using the rigid sphere

model described in 5.5.1 and explained in further detail by Hirschfelder, et al. [23]. The following diffusion coefficient values were used: 2.66×10^{-5} m^2/s for $Fe(Cp)_2$ in He, 1.02×10^{-6} m^2/s for 4 nm iron aerosol particles in He, and 3.08×10^{-7} m^2/s for the same particles in Ar. As the gas composition is not uniform within the model domain, the accuracy of the diffusion tracer analysis is necessarily limited and is only intended to highlight qualitative differences in performance between operating conditions.

5.3 Results and discussion

5.3.1 Plasma alignment and precursor conversion

The first objective was to characterize the conversion efficiency of $Fe(Cp)_2$ into particles. The residence time of a gas molecule flowing through the plasma of our reactor is approximately 100 μs. Our previous study of a μs-scale reactor shows that the residence time is not sufficient for appreciable particle growth, rather the primary role of the microplasma is to dissociate the vapor precursor and produce a supersaturated vapor of atoms, here iron and carbon, that will later condense into particles [16]. The fraction of precursor that is dissociated is thus the first limiting factor for the material efficiency of microplasma-based nanoparticle synthesis, and increasing this fraction is key to practical uses of the technique.

During the development of our reactor, we observed order-of-magnitude variation in the yield correlating with the precise location at which the plasma formed between the capillary tube and mesh electrodes, with the highest yield occurring when the plasma is centered over the end of the capillary tube. If the diameter of the capillary tube is small relative to the electrode gap, the plasma reliably forms in this location, with a discharge emanating equally from the entire circumference of the tube. As the tube diameter is

increased to enable a higher gas flow rate, local variations in the electric field become important. If the face of the capillary tube is not parallel with the mesh, the plasma preferentially forms at the closest point. Small features with high surface curvature like burrs or scratches concentrate the electric field and can localize the plasma. The spacing and curvature of wires in the mesh has a similar effect. We observed that increasing the I_p to 5–10 mA can partially compensate for this issue, yet this introduces other operational issues, including a higher gas temperature, melting of the fine wires in the mesh, and erosion of the electrodes.

The reactor hardware was designed for assembly precision and repeatability, and with freshly cut and polished capillary tubes a well-centered plasma was achieved. However, as the surface quality of the electrodes degrades over prolonged use, the well-centered plasma could not be reliably maintained. When the plasma localizes to specific points on the electrodes this degradation is also focused, resulting in a positive feedback loop which locks in the off-center position.

Repeatable and stable plasma positioning was achieved through the use of a second coaxial gas flow, the sheath flow, which has a higher breakdown voltage than the inner flow. Here, a blend of 50:50 N_2 and He is used. Aerosol measurement of cases with a sheath flow of 0, 60, and 300 sccm (baseline case) show an increase in particle concentration and diameter with the sheath flow (Figure 5.3(a)).

Photos in Figure 5.3(e) illustrate how plasma alignment can be observed directly. With 0 sccm sheath flow (left) the plasma is localized to the top edge of the capillary tube and an off-center point on the mesh. The plasma moves to be centered between both electrodes when 60 sccm sheath flow is added (right). The addition of N_2 in the sheath flow results in a gradient of gas composition in the region between the two electrodes. At the center, the high velocity jet emerging from the capillary tube is predominantly He, while the edges have an increased N_2 fraction. This gradient of gas composition

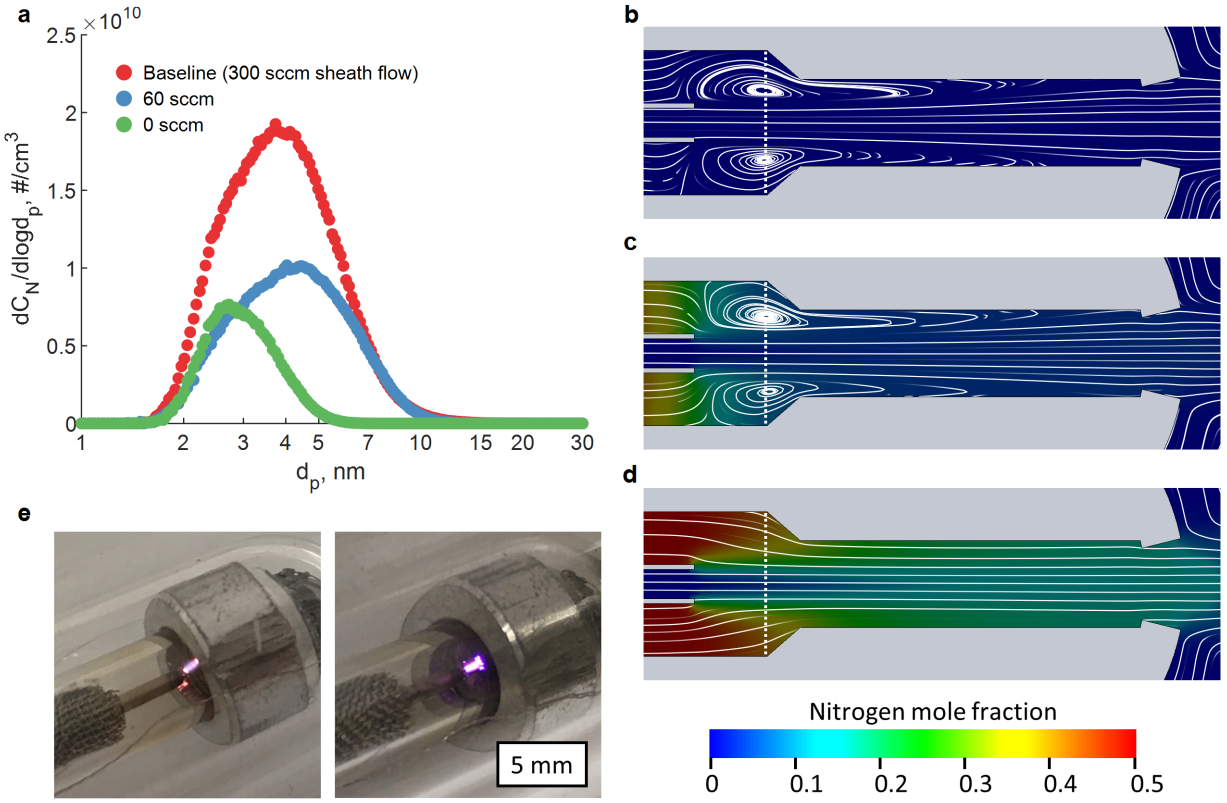

Figure 5.3: (a) PSD when operating with a sheath flow of 0, 60, and 300 sccm (baseline case). (b-d) Fluid dynamics simulations of the three cases showing streamlines of the flow field and colormap of the N_2 mole fraction. The two horizontal lines on the left side of the domain are the walls of the capillary tube and the white dashed line is the mesh electrode. (e) Representative photos of the microplasma reactor showing a misaligned plasma (left, 0 sccm sheath flow) and aligned plasma (right, 60 sccm sheath flow). Note plasma color changes from red in pure He without sheath flow to purple with addition of N_2 in the sheath flow.

creates a gradient in breakdown voltage, resulting in a restoring force that ensures the plasma is aligned with the He jet of the inner flow. A higher N_2 fraction in the sheath flow, or higher sheath flow rate relative to the inner flow, creates a sharper gradient, more effectively centering the plasma. Figure 5.3(b-d) shows this composition gradient for all three cases.

For the baseline case, characterization of aerosol deposits indicates a total mass yield (Y_{mass}) of 0.49, iron yield (Y_{Fe}) of 0.83, and carbon yield (Y_C) of 0.26. These yields are defined as the mass of that element in the deposit (calculated from the total mass and composition) to the mass of that element supplied by $Fe(Cp)_2$ during the deposition. This indicates that the majority of $Fe(Cp)_2$ is dissociated, despite a lower plasma current and shorter residence time than similar DC microplasma systems [24, 25]. These studies do not report yields, yet, using reported C_N and $Fe(Cp)_2$ concentrations we estimate Y_{mass} of the order 0.001 [24] to 0.01 [25].

Yet, Lin et al. [25] also report the ability to limit carbon incorporation by reducing the plasma current below 4 mA, in contrast to the significant carbon fraction in this study, even at 1 mA. This suggests a potential trade-off between the complete dissociation of $Fe(Cp)_2$ and the formation of both iron and carbon species which are available for particle formation. A further investigation of mass yield and particle composition is carried out in Section 5.3.4.

The sheath flow also serves to prevent recirculation within the microplasma reactor. As the gas jet from the capillary tube expands and decelerates into the microplasma reactor it entrains and accelerates the surrounding gas. If the sheath flow is insufficient, recirculation occurs with reversed flow in the outer zone of the microplasma reactor. With no sheath flow, the CFD simulation (Figure 5.3(b)) indicates that the recirculation zone extends nearly to the outlet of the microplasma reactor. We have observed changes in the color of the plasma and plasma voltage (V_p) upon addition of other gases to the

transfer tube, indicating that back flow or back diffusion of gases from the transfer tube occurs with this flow condition. At 60 sccm sheath flow (Figure 5.3(c)) the recirculation zone is reduced in size and the conditions in, and performance of, the microplasma reactor are effectively decoupled from the conditions within the transfer tube. Yet, this recirculation is responsible for a long tail on the residence time distribution within the microplasma, resulting in the continued growth of particles which become trapped in the microplasma and causing a sluggish response to changes in operating conditions. At 300 sccm sheath flow (Figure 5.3(d)), recirculation is entirely suppressed which tightens the residence time distribution and results in highly responsive performance to changes of operating conditions. These changes are evidenced by the higher concentration, smaller diameter, and narrower size distribution of the aerosol formed in the 300 sccm sheath flow case (Figure 5.3(a)).

Further increasing the sheath flow beyond 300 sccm shows diminishing returns on these metrics, and an increased penalty due to dilution reducing the total aerosol concentration. Notably, the effect of the sheath flow on the flow field is primarily determined by the relative mass flow of the sheath flow to the inner flow, as the extent of gas entrainment by the jet is mediated by momentum transfer. Thus, the use of N_2 in the sheath flow, with molecular mass 7× that of He, has the additional benefit of reducing the needed sheath volume flow to prevent recirculation. While performance with different inner flow rates or microplasma reactor geometries are not reported here, these factors would also influence the optimal sheath gas composition and sheath to inner flow ratio.

We now consider why improved plasma alignment increases yield. Centering the plasma on the capillary tube gas jet ensures that all $Fe(Cp)_2$ passes through the plasma, which is hypothesized to be necessary for dissociation, i.e., we assume the conditions needed for $Fe(Cp)_2$ dissociation exist only within the visible plasma volume. To test this hypothesis, $Fe(Cp)_2$ vapor was added to the sheath flow instead of the inner flow,

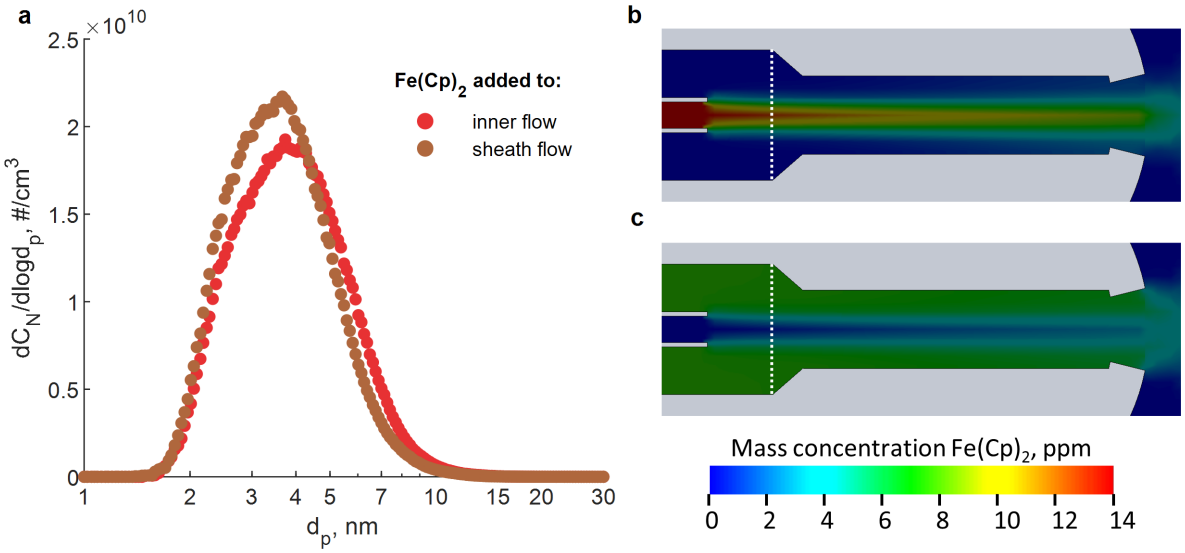

Figure 5.4: (a) PSDs for $Fe(Cp)_2$ vapor added via the inner flow or sheath flow. CFD simulations of the $Fe(Cp)_2$ mass concentration for the cases of injection via the inner flow (b) and the sheath flow (c). The two horizontal lines on the left side of the domain are the walls of the capillary tube and the white dashed line is the mesh electrode. When $Fe(Cp)_2$ is added to the inner flow it forms a narrow highly concentrated stream within the plasma volume (between the electrodes), coincident with the location of the observed tall deposit on the mesh discussed in Section 5.3.2. When $Fe(Cp)_2$ is added to the sheath flow, the concentration in area directly between the electrodes is significantly reduced.

with CFD simulations confirming that the bulk of $Fe(Cp)_2$ flows around the plasma volume (Figure 5.4(b) and (c)). Indeed, in this case the focusing effect of the N_2 should serve to ensure the plasma and $Fe(Cp)_2$ do not intersect. However, both cases result in nearly identical PSDs as shown in Figure 5.4(a) with only a small decrease in total yield.

An alternative hypothesis is that the plasma forms a spatial afterglow in the region downstream of the mesh electrode, maintaining an environment conducive to $Fe(Cp)_2$ dissociation. This afterglow region may encompass a greater portion of the internal cross section of the microplasma reactor as well, interacting with $Fe(Cp)_2$ in the sheath flow. In the case of the misaligned plasma, the afterglow may be similarly off-center or prematurely terminate upon impinging on the inner reactor wall. The addition of a molecular gas like N_2 to a DC plasma discharge has been shown to increase the extent of the spatial afterglow [26], which may be a contributing factor, but does not explain the observed difference in yield between an off-center and aligned plasma in cases without a sheath flow.

5.3.2 Stability of aerosol production

The ability to produce an aerosol with stable concentration and size distribution is critical for practical use, yet long duration experiments are typically not reported for microplasma reactors using a vapor precursor. The more common spark-discharge process, which uses similar hardware and gas flow rates but instead ablates material from the electrodes, typically has poor temporal stability due to the loss of material from the electrodes and subsequent changes in spark energy and frequency. While some designs have minimized this effect through clever electrode geometry and demonstrated run times exceeding 10 hours [10, 27], improving temporal stability is a primary motivation for the use of a vapor precursor and lower power discharge. Previously, we

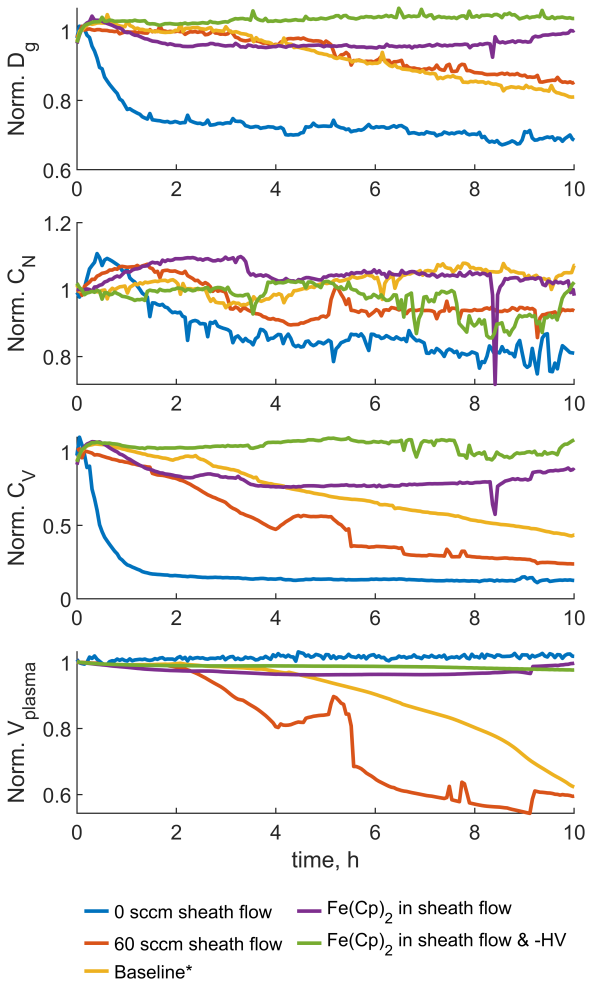

Figure 5.5: Changes in aerosol PSD statistics and V_p over time for the five long duration experiments. Values for each experiment are normalized to their initial value to enable visual comparison of the variability.

reported continuous synthesis for up to 7 hours of sub-3 nm aerosol at $> 10^9$ #/cm^3, using a related reactor [16]. Yet, electrode degradation is not the only source of temporal instability or degradation. In the present reactor, the accumulation of deposits on the electrodes and other reactor surfaces can be significant. As this deposition rate should scale proportionally to the aerosol concentration, the relative significance of deposition in the present reactor, as opposed to other microplasma or spark-discharge reactors, is attributed to the high aerosol concentration (~10× mass concentration of [16], ~40× C_N of [27], and ~100× C_N of [10].

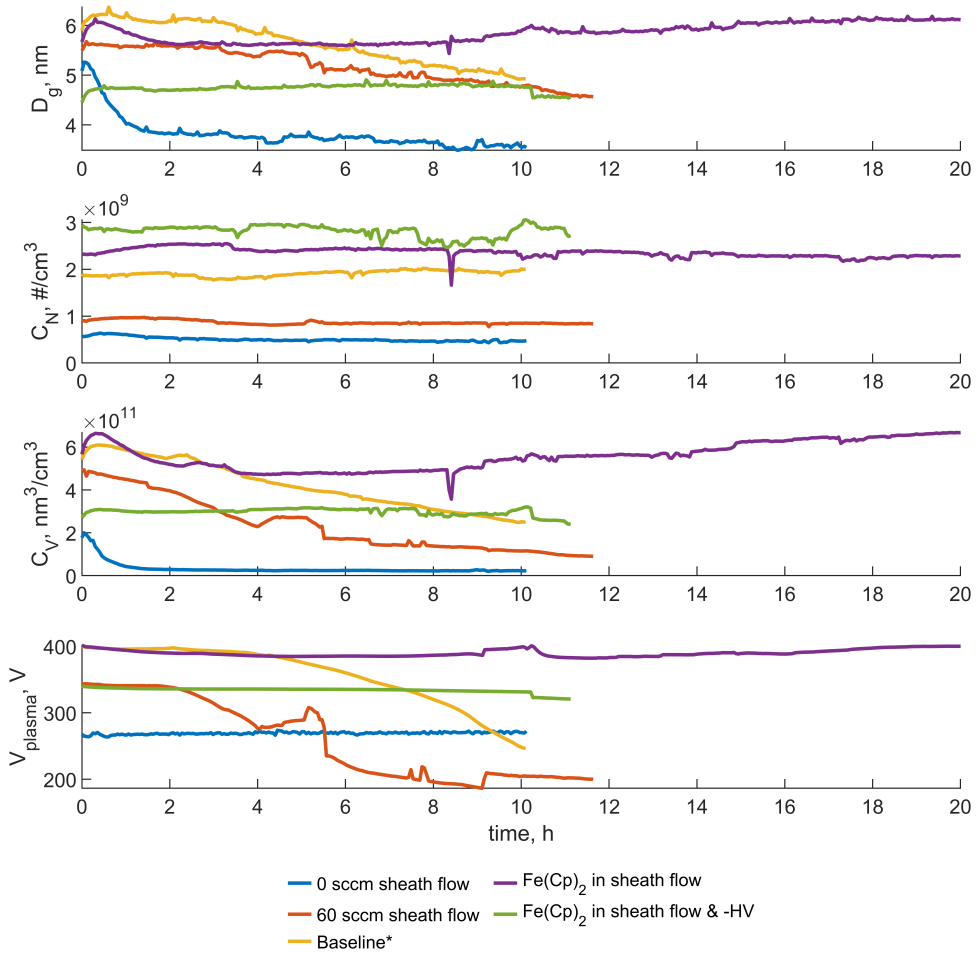

Figure 5.6: Non-normalized version of Figure 5.5 including the entire 20 hour run of the $Fe(Cp)_2$ in sheath flow case.

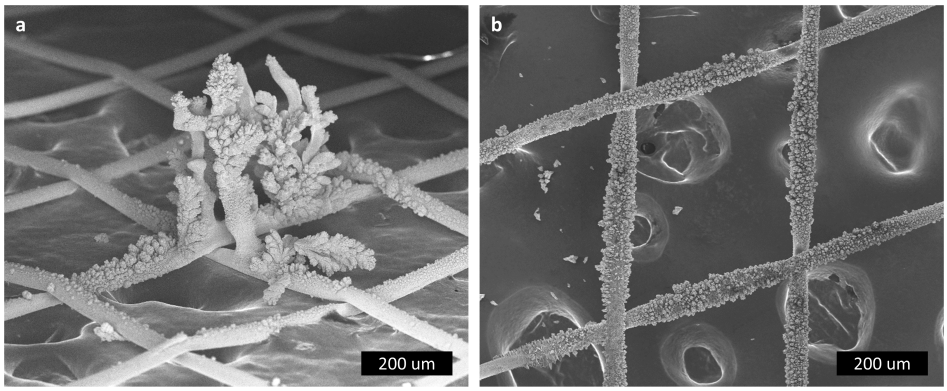

Figure 5.7: SEM images of mesh electrodes after long duration microplasma runs. (a) Mesh after a 10 hour run of the 60 sccm sheath flow case, in which $Fe(Cp)_2$ was added via the inner flow. (b) Mesh after a 20 hour run in which $Fe(Cp)_2$ is added via the sheath flow. In the first case, the base of the tall deposit is where the microplasma initially contacted the mesh. The structure grew via deposition inside the plasma volume and toward the capillary tube. Material is also conformally deposited on a larger area of the mesh. In the second case, the only deposit is a thin conformal coating on the mesh.

To investigate the relationship between operating conditions, deposition rate, and temporal stability, five operating condition cases were each run for 10 hours while continuously monitoring via SMPS at a 2 min scan period. For this set of experiments, two additional changes to the operating conditions were made: $L_{tt} = 120$ mm, and the transfer flow was decreased to 1400 sccm, neither of which should influence temporal stability. Figure 5.5 shows aerosol PSD statistics and V_p for these experiments, normalized to their initial values to enable visual comparison of the relative variability during each experiment. Figure 5.6 shows the non-normalized values for the same experiments. When a sheath flow is not used (0 sccm), the temporal performance is representative of our previous microplasma system [16] and the stable spark-discharge systems: after an initial break-in period (during which the initially centered plasma was observed to drift off-center), the PSD is extremely stable due to a low internal deposition rate – the volume concentration (C_V) of aerosol is ~20× lower than the other four conditions – and negligible electrode erosion at $I_p = 1$ mA (which would be observed as in increase in V_p over time).

For the 60 sccm sheath flow and baseline* cases, C_N remains stable, while D_g and thus C_V (a proxy for yield) decrease gradually. In both cases V_p also decreases, with the higher sheath flow in the baseline* case appearing to prolong the initial stable period. Inspection of the used mesh from the 60 sccm sheath flow case (Figure 5.7(a)) shows the build-up of a 0.5 mm tall deposit of material which reduced V_p by reducing the electrode gap. The mesh wires are also coated with a thin conformal layer of debris, thickest at the base of the large deposit.

For both cases where the supply of $Fe(Cp)_2$ vapor is switched to the sheath flow, we observe fluctuations in D_g and V_p but no decreasing trend. One of these experiments was continued to 20 hours with no decrease in performance (Data for the entire experiment is shown in Figure 5.6). Even after 20 hours, no large deposits are observed, although the mesh wires are also conformally coated (Figure 5.7(b)).

It is clear that the material contributing to the growth of the large deposit results from $Fe(Cp)_2$ dissociation upstream of the mesh electrode. By removing $Fe(Cp)_2$ from the inner flow, the source of this material is greatly reduced. This is analogous to downstream injection of reactive species or particles in larger-scale plasma jets (e.g., [28]), yet miniaturized and without the need for additional gas streams. Further, the more rapid onset of V_p decline in the 60 sccm sheath flow case as opposed to the baseline* implies that recirculation in the microplasma reactor increases the amount of material available to deposit on the mesh, or the rate at which it deposits.

The contrast between cases with $Fe(Cp)_2$ in the inner flow and sheath flow suggests that while the conformal deposit indicates a loss of material and sub-optimal yield, its growth does not effect the temporal performance of the system on these timescales. It also suggests that the decrease in D_g is related to the reduction of the electrode gap via the growth of the large deposit structure. However, the fact that the number concentration remains stable in this case indicates that the change in performance is

not simply an increasing fraction of material being captured on an increasingly large deposit, as a reduction in the effective $Fe(Cp)_2$ concentration should effect both particle size and concentration.

5.3.3 Control of aerosol size distribution

A series of one-dimensional parameter sweeps centered on the baseline case were used to illustrate the influence of the most salient operating parameters on the aerosol PSD (Figure 5.8). The total flow rate is held constant, thus changes in aerosol concentration are synonymous with changes in production rate.

Understanding the mechanistic relationship among these parameters, the initial formation of particles, and the PSD evolution is key for the design of practical microplasma systems. Based on our understanding of particle formation, the majority of the iron and carbon vapor produced from $Fe(Cp)_2$ dissociation quickly form nm-scale particles in the region immediately downstream of the microplasma. While this formation is essentially a homogeneous nucleation process driven by a super-saturated vapor, the supersaturation ratio for both iron and carbon is much higher ($\sim 10^{10}$) than is typical for condensation, and the growth rate is limited by the collision rate of this atomic vapor even in the initial stages of nucleation [16]. Thus, the evolution of the iron and carbon vapor to the final aerosol can be modeled as a single continuous aggregation process. In typical handling of nm-scale aerosols, particle losses via particle-wall collision have a significant influence on PSD evolution. This is due to a high sticking coefficient and exponential increase in diffusion velocity, thus particle-wall collision frequency, as particle size decreases [11]. Yet, at the high aerosol concentration attained in the reactor, PSD is dominantly controlled by aggregation because the particle-particle collision frequency increases as ${C_N}^2$, while losses scale linearly with C_N.

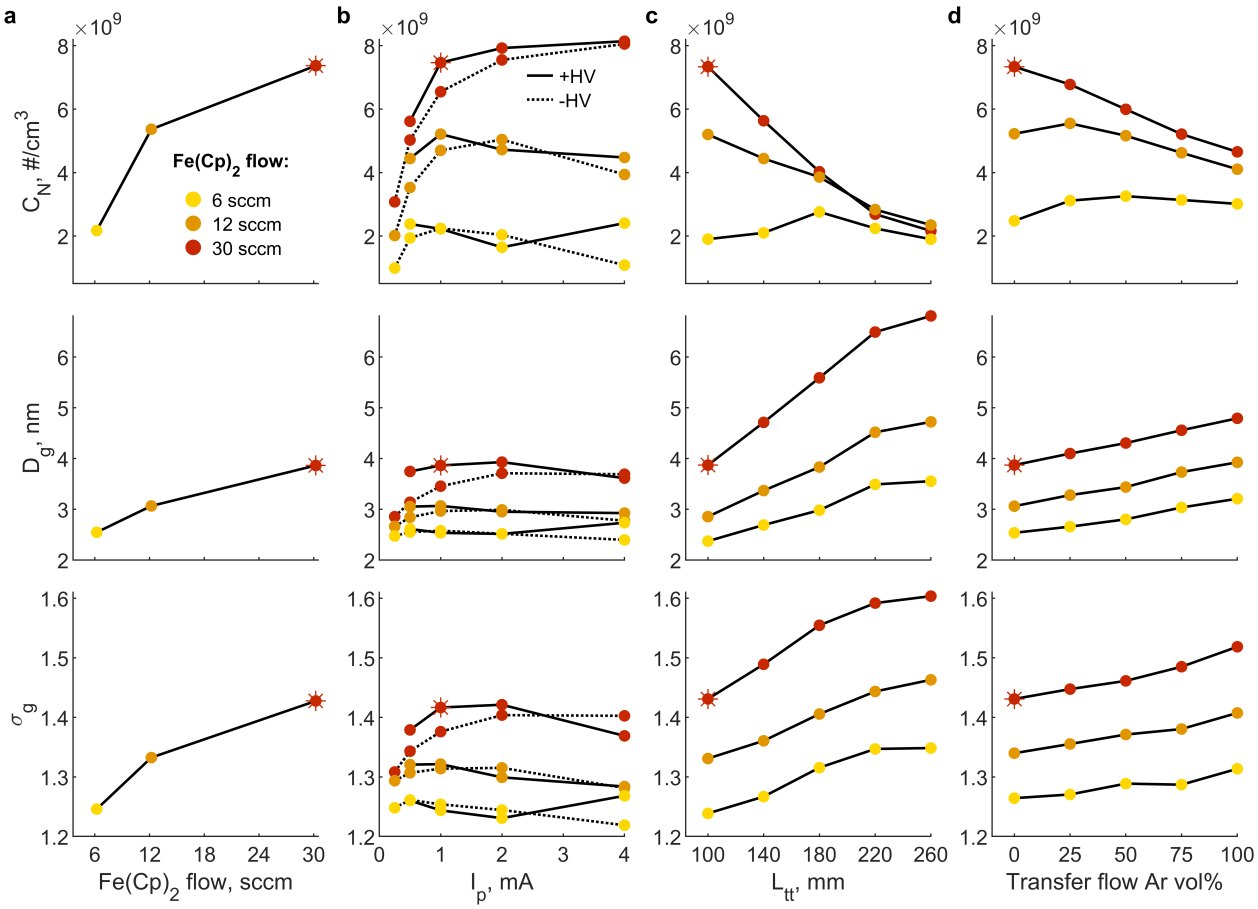

Figure 5.8: Summary aerosol statistics for a series of experiments varying (a) $Fe(Cp)_2$ flow, (b) microplasma current (I_p) and polarity (+/− HV), (c) transfer tube length (L_{tt}), and (d) He:Ar ratio in the transfer flow. The latter experiments were conducted with cases at three $Fe(Cp)_2$ concentrations, with colors corresponding to those values in (a). The red star indicates the same baseline case in each experiment. All experiments were done with $Fe(Cp)_2$ in the inner flow with the exception of the L_{tt} experiments, which were conducted separately, where $Fe(Cp)_2$ was added via the sheath flow.

The concentration of $Fe(Cp)_2$ vapor has limited influence on the aerosol PSD (Figure 5.8(a)). Continuing to increase $Fe(Cp)_2$ concentration shows a diminishing increase in particle concentration. For example, a 2× increase in $Fe(Cp)_2$ vapor from 6 to 12 sccm leads to a 2.47× increase of particle concentration (2.17 to 5.36×10^9 #/cm^3; likely indicating a lower mass yield at 6 sccm as well), while an additional increase of $Fe(Cp)_2$ vapor to 30 sccm leads to only a 1.38× increase in C_N (7.37×10^9 #/cm^3). To a first approximation, the concentration of particles that initially form depends linearly on the initial concentration of iron and carbon vapor, while their aggregation rate depends on the square of initial concentration. Thus, if high $Fe(Cp)_2$ concentration is to be used to increase particle concentration, the residence time must also be reduced drastically to limit aggregation.

In addition to the initial $Fe(Cp)_2$ vapor concentration, the extent of dissociation may influence the availability of iron and carbon vapor, as discussed in Section 5.3.1. The effect of I_p and the polarity of the plasma voltage source on this dissociation is explored in Figure 5.8(b). With positive high voltage polarity, the plasma is stable down to I_p = 0.5 mA, but operating with negative high voltage polarity extends this limit to $I_p = 0.25$ mA. At both of these extremes, the coupled decrease in D_g and C_N appears to indicate a reduced fraction of $Fe(Cp)_2$ dissociating. This fraction appears to saturate around I_p = 1 mA, and further increasing the current does not yield proportionally higher D_g or C_N.

Increasing I_p also increases the total plasma power and the magnitude of any thermal effects. Thermal dissipation of the plasma energy into the gas was estimated using a fine thermocouple (Omega; K-type, 0.003" wire diameter) inserted into the microplasma reactor for I_p = 0.5, 1, and 2 mA. During these three experiments, V_p remained in the range 402–406 V, indicating a total power of 0.2, 0.4, and 0.8 W. If the entirety of this energy were dissipated into the inner and sheath flow gases as heat, the resulting

temperature rise would be 13.6, 27.2, and 54.4 K, respectively. Observed temperature rises of 8.0, 15.6, and 31.0 K indicate that approximately half the energy is dissipated as heat into the gas. In all cases, the maximum temperature is well below that of $Fe(Cp)_2$ decomposition, and it does not appear that these changes in temperature influence particle formation kinetics nor introduce sufficient thermal gradients to cause observable thermophoretic diffusion. The effect of this heating on the flow field or diffusion rates was not included in the CFD simulations. This very low temperature operation is a result of the low plasma power and high gas flow rate and may be unique among similar microplasma systems. For instance, Ghosh et al. [29] report a plasma power of 1.0 W with 100–800 sccm Ar, resulting in a theoretical maximum temperature rise of 80–640 K. Chiang and Sankaran [24, 30] also report a power of 1.0 W with 100 sccm Ar, resulting in a theoretical maximum temperature rise of 640 K.

As we established that the microplasma operating conditions have only limited influence on the final aerosol PSD, and that PSD is primarily driven by particle aggregation, it is clear that the parameters that influence aggregation in the transfer tube are the main controls of PSD evolution. The total extent of aggregation in the transfer tube can be reduced by either reducing the aggregation rate or the residence time. Simply reducing the volume of the transfer tube to reduce the residence time is the most straightforward way to limit aggregation, although this may not always be possible as the design of this flow path may be constrained by other aspects of the system.

In Figure 5.8(c) we show the influence of L_{tt} at constant flow rate as a proxy for transfer tube residence time. For all $Fe(Cp)_2$ concentrations, D_g increases monotonically with L_{tt}, indicating increased particle growth due to aggregation. A broadening of the PSD, indicated by an increase in σ_g, is also observed. However, the effect on concentration is obfuscated by the 1.4 nm d_m lower detection limit of the SMPS. For the cases at 12 and 30 sccm $Fe(Cp)_2$, C_N monotonically decreases with increasing L_{tt},

as expected due to each aggregation event consuming a particle. The faster rate of aggregation (observed as a more rapid decrease in C_N) in the 30 sccm $Fe(Cp)_2$ cases is due to the larger average particle size and the power-law relationship between aerosol collision rate and diameter within this regime (this relationship is described in 5.5.2 and explained in further detail in Fuchs and Sutugin [31]). In the 6 sccm $Fe(Cp)_2$ cases, the growth rate is slow enough that small clusters are still growing through the SMPS detection limit, causing the observed increase in C_N over the range of $L_{tt} = 100$ to 180 mm.

The transfer flow can also be used to change the residence time within the transfer tube, and further limits particle growth by diluting the aerosol to limit the collision rate. It stands to reason that the maximum aerosol concentration will be achieved at some intermediate transfer flow: too low and the concentration is reduced by aggregation; too high and the concentration is reduced by dilution. Yet, because of limited mixing between the aerosol flow emerging from the microplasma reactor and the transfer flow, the effect of the transfer flow on limiting aggregation in the transfer tube is less than predicted. For the baseline transfer flow of 2600 sccm He and total plasma flow of 900 sccm, complete mixing would yield a dilution ratio of 3.9 and a 15× reduction in the collision frequency.

In Figure 5.9(a) we show the simulated concentration distribution in the transfer tube, using a diffusivity corresponding to 4 nm particles and not accounting for aggregation. While the aerosol stream does widen radially outward into the transfer flow due to diffusion, the maximum concentration remains essentially unchanged. A sufficient transfer flow also prevents recirculation (analogous to the role of the sheath flow within the microplasma reactor) and so narrows the residence time distribution of the gas. However, recirculation will only influence the aerosol residence time if it is large enough to entrain the aerosol flow, which is not the case at the baseline condition, despite a

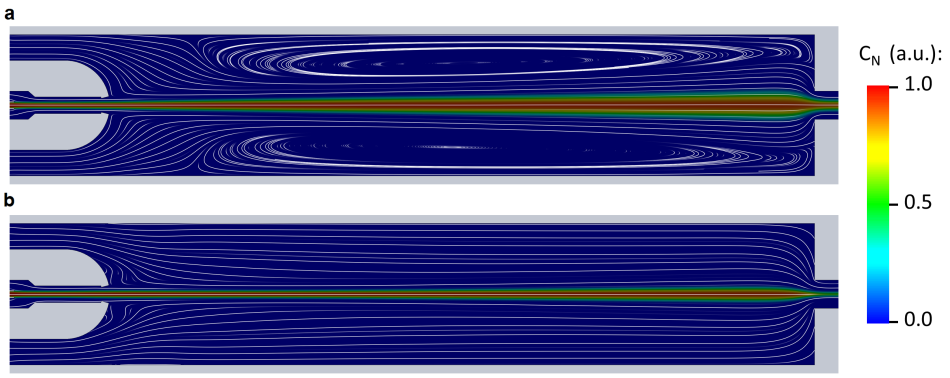

Figure 5.9: Simulated spatial aerosol concentration distribution in the transfer tube (L_{tt} = 100 mm) accounting for particle diffusion for (a) the baseline case with 2600 sccm He transfer flow and (b) 2600 sccm Ar transfer flow. Streamlines indicate flow field. Colormap shows the simulated concentration of an aerosol of 4 nm particles input at unit concentration to the plasma flow and subject to diffusion but not aggregation. The higher diffusivity of particles in He allows greater dispersion of the particles, reducing concentration along the centerline of the reactor.

large recirculation zone (Figure 5.9(a)).

These effects are further illustrated with the use of Ar in the transfer flow, which reduces the diffusivity of the aerosol particles. As with the use of N_2 in the sheath flow, increasing the density of the transfer flow with Ar also prevents recirculation at this flow rate (Figure 5.9(b), 2600 sccm). If the aerosol were well-mixed in the transfer tube, these effects would decrease the aggregation rate and average residence time, yet we find (Figure 5.8(d)) an increase in D_g and decrease in C_N with increasing Ar fraction. Instead, the low diffusivity prevents the aerosol stream from widening, maintaining a high local concentration and high aggregation rate throughout the length of the transfer tube (Figure 5.9(b)).

5.3.4 Physical characterization

To complement the online aerosol characterization described in the previous sections, particles were collected over a range of cases for ex situ measurement of the bulk compo-

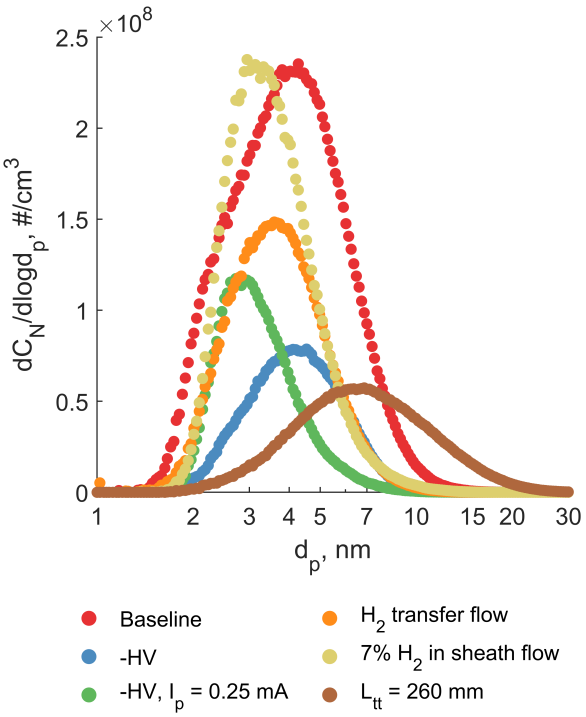

Figure 5.10: Aerosol PSDs for the deposition experiments in table 5.1. $Fe(Cp)_2$ was added via the sheath flow rather than inner flow in all experiments to ensure stable operation over the 2 hour deposition period.

	Aerosol Measurements:			Deposit Characterization:						
Condition:	D_g, nm	C_N, #/cm^3	Y^a_{vol}	w_{Fe}	Y_{Fe}	Y_C	Y_{mass}	Y_{vol}	Y^a_{vol}/Y_{vol}	χ_B
Baseline	3.96	7.51×10^9	2.90	0.47	0.83	0.26	0.49	0.37	7.74	1.98
-HV	4.18	3.09×10^9	1.07	0.59	0.86	0.11	0.41	0.25	4.23	1.62
-HV, $I_p = 0.25$ mA	3.20	3.48×10^9	0.55	0.42	0.35	0.15	0.23	0.19	2.91	1.43
H_2 transfer flow	3.66	5.82×10^9	1.44	0.52	0.75	0.17	0.40	0.28	5.11	1.72
7% H_2 sheath flow	3.52	8.04×10^9	1.81	0.56	0.72	0.12	0.36	0.24	7.67	1.97
$L_{tt} = 260$ mm	6.81	2.16×10^9	5.52	0.48	0.93	0.29	0.54	0.41	13.37	2.37

Table 5.1: Aerosol SMPS measurements and deposit characterization for a range of microplasma operating conditions. Y^a_{vol} is the aerosol volume yield. w_{Fe} is the bulk iron mass fraction of the deposited aerosol. Y_{Fe} and Y_C are the iron and carbon yields in the deposit. Y_{mass} and Y_{vol} are the total mass-weighted and volume-weighted yields. χ_B is bulk dynamic shape factor, as defined in Section 5.3.4.

sition and mass production rate. Aerosol PSDs for these conditions are shown in Figure 5.10, along with aerosol statistics and a summary of the deposit characterization in Table 5.1. These measurements allow the calculation of iron and carbon yields to better understand the flow of materials through the process. In combination with the volume production rate from integrating the volume-weighted aerosol PSD, particle shape can also be constrained. In addition to particle size and size distribution, composition and shape are key for evaluating the utility of this process.

Yield and composition

In Section 5.3.1 the particle yield from $Fe(Cp)_2$ was framed as depending on two processes: first, the dissociation of $Fe(Cp)_2$ into iron and carbon vapor, and second the formation of particles from this vapor. Similarly, the final composition of the particle is due to the differential effect of these two processes on the iron and carbon supplied by $Fe(Cp)_2$. If both are incorporated equally, the 1:10 atomic ratio of iron to carbon would yield a particle with an iron mass fraction (w_{Fe}) of 0.28, assuming iron is in the form of Fe_2O_3. In all experimental cases, w_{Fe} is significantly higher, indicating preferential incorporation of iron, yet a significant portion of carbon is still incorporated into the

particles which may render these particles unsuitable for some applications.

In contrast, the synthesis of carbon-free particles from $Fe(Cp)_2$ and other metallocenes has been reported using similar microplasma reactors [25, 30], although we suspect at significantly lower total yield (Section 5.3.1). Lin et al. [25] attribute the lack of carbon to a partial dissociation of the $Fe(Cp)_2$ molecule within the plasma, liberating the central iron atom while the cyclopentadienyl rings remain intact or are broken into smaller hydrocarbon species. The carbon-containing species are stable vapors and thus do not contribute to particle formation. Lin et al. propose that the extent of molecular dissociation may be related to the plasma current [25].

While the present system does exhibit a decrease in total yield when I_p is reduced from 1 mA to 0.25 mA, w_{Fe} also decreases from 0.59 to 0.42 indicating an increased carbon content. Negative high voltage polarity was used for these cases to more closely match the conditions in Lin et al. [25]. In this system, the change in yield with current is moreso due to its effect on the portion of $Fe(Cp)_2$ that dissociates than the extent of molecular dissociation. We estimate that the Lin et al. [25] system achieves a relatively low Y_{mass} (Section 5.3.1), and suggest that plasma conditions which achieve high Y_{mass} may inherently also result in liberation of carbon for particle growth. There may not be a condition at which all $Fe(Cp)_2$ molecules only partially dissociate, yet further improvement in both metrics is possible. In our findings it is notable that Y_{mass} is similar between the positive and negative polarity cases, 0.83 to 0.86, while Y_C is reduced by more than half from 0.26 to 0.11.

The introduction of H_2 to the sheath flow or transfer flow also decreases Y_C, although the effect on composition is less pronounced due to a concurrent decrease in Y_{Fe}. H_2 in the transfer tube may provide an alternative reaction pathway for any remaining carbon vapor to form hydrocarbons, but is unlikely to react with carbon already incorporated into particles. The addition of a much smaller flow of H_2 via the sheath flow shows an

even stronger effect. This may be due to a greater fraction of carbon still potentially reactive as vapor, or a plasma enhancement of hydrogen-carbon reactions. Additionally, extra H_2 in the plasma may bias against the complete dissociation of $Fe(Cp)_2$, which also produces H_2.

Particle shape

Aerosol measurement via SMPS only characterizes the mobility diameter (d_m) of particles, not their true size and shape. As SMPS measurement is faster and easier than deposition-based characterization, it is tempting to use the aerosol volume concentration based on d_m, flow rate, and an assumed density to calculate the total production rate. However, without understanding the relationship between mobility diameter (d_m) and the true size and shape of particles, this calculation can be a drastic misrepresentation. This issue is illustrated by the discrepancy between process yields calculated from SMPS measurements and from the deposited aerosol, reported in Table 5.1. The aerosol volume yield (Y^a_{vol}) is the ratio of the aerosol volume concentration (the sum of the volume-weighted PSD as measured via SMPS) to the hypothetical volume concentration of the iron oxide and carbon from $Fe(Cp)_2$ and ranges from 0.55 to 5.52. The deposit volume yield (Y_{vol}) is calculated analogously, using the deposit mass and composition to estimate its volume, and ranges from 0.19 to 0.41. The discrepancy between these two measurements, as well as the impossibility of a yield greater than one, indicates that the SMPS systematically overestimates the true volume of particles in this aerosol. The extent of overestimation is given by the ratio of the aerosol volume yield to the true volume yield, and is up to 13.37 in the $L_{tt} = 260$ mm case.

This discrepancy is the result of non-spherical particles and the size-selection technique used in the SMPS instrument. The SMPS uses a differential mobility analyzer (DMA) which sorts particles according to their migration velocity in an electric field.

For non-spherical particles, d_p, calculated as d_m - 0.3 nm, is the diameter of a spherical particle with the same migration velocity in an electric field as the particle of interest [32]. Non-spherical particles can also be described by a volume-equivalent diameter (d_{ve}) defined as the diameter of a spherical particle with the same volume as the non-spherical particle. While $d_p = d_{ve}$ for a spherical particle, d_p is typically greater than d_{ve} for non-spherical particles as the lumpy shape of a particle formed by aggregation has a higher drag force in the DMA than a sphere of the same volume. The dynamic shape factor, χ, is defined as the ratio of the drag force on a particle to that on its volume-equivalent sphere [32]. As these forces are respectively incorporated in the measurement of d_p and definition of d_{ve}, the following approximate definition for χ is used here:

$$\chi = \frac{d_p}{d_{ve}} \tag{5.1}$$

While the distribution of d_p is measured via SMPS, we are not able to measure d_{ve} for individual particles. However, if this equation is reformulated in terms of particle volumes as

$$\chi^3 = \frac{v_p}{v_{ve}} \tag{5.2}$$

a bulk dynamic shape factor (χ_B) can be defined for the entire aerosol, rather than individual particle, in terms of the aerosol and true volume yields

$${\chi_B}^3 = \frac{\sum v_m}{\sum v_{ve}} = \frac{Y^a_{vol}}{Y_{vol}} \tag{5.3}$$

Values for χ_B are reported in Table 5.1 and fall within the range of 1.43 to 2.37. This range is typical of a fractal aggregate particles composed of loosely packed spherical primary particles [33, 20]. To contextualize these values, $\chi = 1$ for a sphere, 1.2 for four

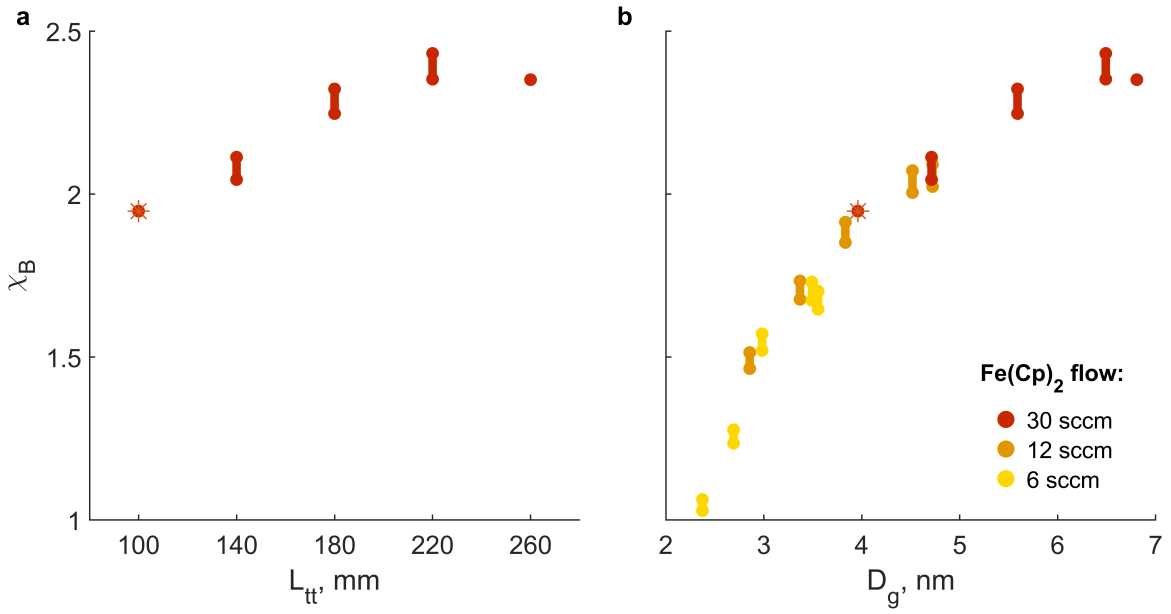

Figure 5.11: (a) χ_B for the transfer tube length experiments. The values at L_{tt} = 100 and 260 mm are calculated using Y_{vol} measured from deposits made at those conditions. For L_{tt} = 140, 180, and 220 mm, a range of χ_B is shown bounded by Y_{vol} in the end cases as no deposits were made at these conditions. (b) Estimated χ_B ranges for all transfer tube length experiments at all values of Fe(Cp)$_2$ flow. The increasing trend of χ_B with D_g is typical of fractal aggregation.

spheres arranged in a tetrahedron, and 1.4 for a cylinder with aspect ratio of ten [32].

As particle aggregation leads to increasingly non-spherical final particles, χ tends to increase with size for particles within the aerosol population. The influence of aggregation is most directly observed across cases varying L_{tt}, as the conditions within the microplasma reactor and transfer tube are held constant, thus the initial aerosols should be similar. This is supported by the similarity of the deposit characterization for the L_{tt} = 100 mm and L_{tt} = 260 mm cases, with a nearly constant iron weight fraction (0.47 to 0.48) and true volume yield only slightly increasing from 0.37 to 0.41. Between these two cases χ_B is observed to increase from 1.98 to 2.37. For the intermediate length cases, χ_B can not be calculated because deposits were not made to measure Y_{vol}, yet an estimate can be made by assuming the volume yield falls within the range of 0.37 to 0.41. Figure 5.11(a) shows these ranges alongside the measured values for each transfer

tube length, supporting the trend of χ_B increasing with the extent of aggregation.

Extending this analysis to include the transfer tube length experiments at 6 and 12 sccm $Fe(Cp)_2$ reported in Figure 5.8(c), this trend can be seen to hold over a wide range of D_g values in Figure 5.11(b). In Section 5.3.3 it was determined that the growth mode for the smallest aerosol we report, corresponding to $L_{tt} = 100$ mm and 6 sccm $Fe(Cp)_2$, includes the accretion of vapor and clusters of size below the SMPS detection limit, rather than only aggregation between equally sized particles. The estimated $\chi_B \sim 1$ corroborates this, as such growth should result in more densely packed or spherical particles. When looking at other cases in Table 5.1 where the conditions in the microplasma reactor and transfer tube are changed, the correlation between D_g and χ_B does not always hold. For example, the positive high voltage polarity case has a smaller D_g yet larger χ_B than the negative polarity case, as does the H_2 sheath flow case compared to the H_2 transfer flow case. These discrepancies suggest physical changes to the particle growth process which may inform system design. In general, these results make clear that a sole reliance on aerosol SMPS measurements will result in an incomplete understanding of the processes governing particle synthesis within microplasma systems. Supplementing this information with physical characterization of the particles, even in bulk as done here, can identify limiting assumptions and improve design and selection of operating conditions.

5.3.5 Improved C vs D Pareto performance

To directly demonstrate the improved performance on the new microplasma reactor relative to the orifice and orifice-mesh reactors described in Chapter 4, The concentration versus mean diameter Pareto plot (Figure 4.14) is reproduced here as Figure 5.12 with the experimental results from the previous sections overlaid. For consistency, the concentration values are scaled based on the total plasma flow rate. In other words, the

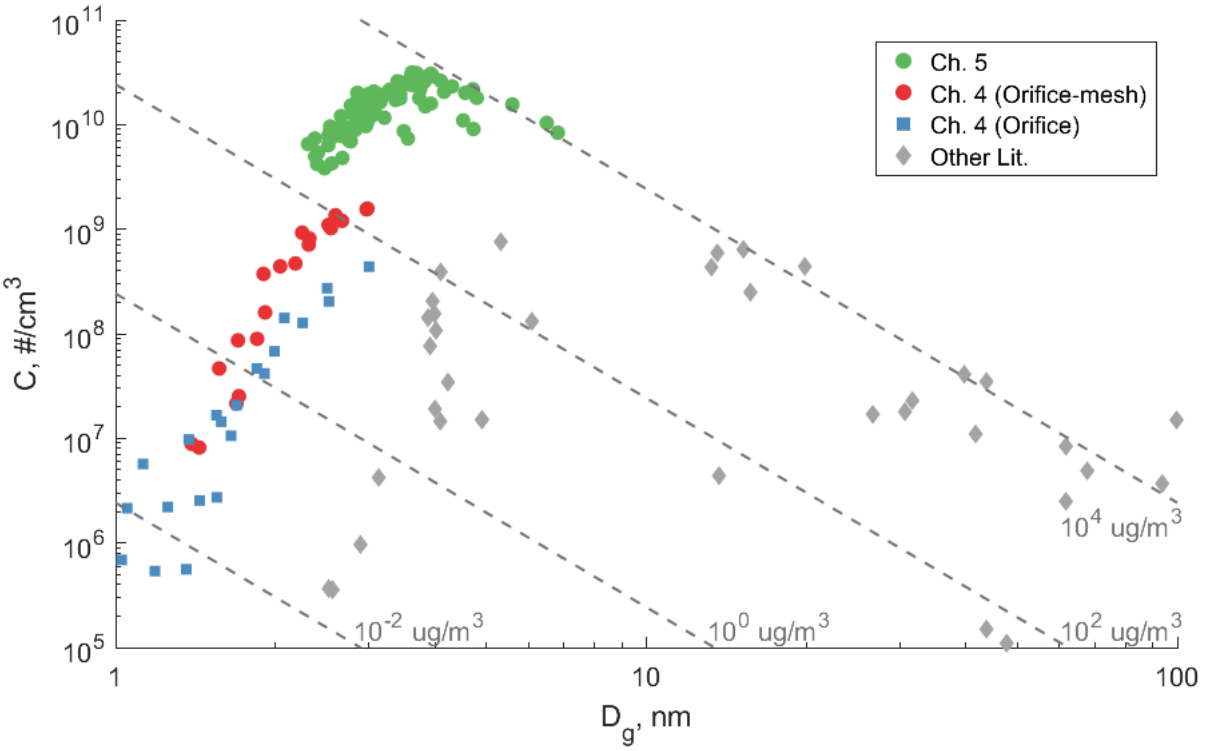

Figure 5.12: Comparison of the aerosol PSD results discussed in this chapter with those of Chapter 4 and other existing processes. See Chapter 4 for complete details and references on literature values.

measured concentration at the transfer tube outlet is multiplied by the ratio of the total flow at the transfer tube outlet (transfer flow, inner flow, and sheath flow) to the total plasma flow (inner flow and sheath flow). Given the longer residence time of the transfer tube compared to the orifice and orifice-mesh reactors from Chapter 4, it is unable to access the 1–2 nm diameter range. However, in the ~3 nm range, the new reactor shows a ~20-fold increase in number concentration.

5.4 Conclusion

We have developed a novel atmospheric pressure DC microplasma reactor and demonstrated its utility as a nanoparticle aerosol source by the synthesis of iron-carbon particles

from $Fe(Cp)_2$ vapor. Through the use of concentric gas flows of different composition, the flow field and location of the plasma within the reactor can be controlled. The addition of N_2 to the sheath flow is used to focus the plasma by producing a spatial gradient of dielectric strength in the gas within the reactor. Ensuing that the plasma discharge is centered in the reactor appears to enable nearly complete dissociation of the $Fe(Cp)_2$ precursor as evidenced by Y_{Fe} up to 0.93. This additionally improves the electrical stability of the plasma circuit, allowing the use of a relatively low $I_p = 1$ mA which limits heating of the outlet gas to 15.6 K. The plasma power is sufficiently low that material loss from the stainless steel electrodes does not occur, in contrast to spark-discharge aerosol generators whose long-term performance is typically limited by electrode erosion. Temporal degradation from the build-up of deposits on the electrodes is also prevented with negligible effect on yield or aerosol PSD by shifting the supply of $Fe(Cp)_2$ vapor from the inner flow to the sheath flow. In this configuration, we demonstrate the generation of an aerosol with stable PSD for 20 hours. Within this operating window, we demonstrate a limited ability to control conversion (Y_{mass} of 0.23 to 0.54) and particle composition (w_{Fe} of 0.42 to 0.59) via plasma high voltage polarity, I_p, and the addition of H_2. The high yield demonstrated here is of particular value for inline applications, such as the use of nanoparticles as a catalyst for carbon nanotube growth, where the unreacted precursor can not be removed from the gas flow and is thus present for subsequent reactions and in the final product. In such cases,the concentration of impurities and their effect in subsequent reactions and the final product is directly linked to the initial particle yield.

We have discussed the need for minimizing the distance between nanoparticle synthesis and application, ideally integrating both within a single system, in order to limit and control PSD evolution due to particle losses and aggregation. In a system comprising the microplasma reactor and a transfer tube with additional gas flow, we show that the res-

idence time and gas composition in the transfer tube (downstream of the microplasma) influence the final PSD to similar extent as the microplasma operating conditions. We estimate $\chi_B = 1$ to 2.37 under different conditions, consistent with a range of particle shapes from spherical to loose fractal aggregate. Particle growth within and immediately after the plasma is dominated by the accretion of vapor and small clusters onto larger particles. As the aerosol is transmitted through the transfer tube, these small species are consumed and growth transitions to dominantly the combination of similarly sized particles resulting in a highly non-spherical shape. The extent of particle growth and thus final aerosol PSD can be thus controlled by both microplasma operating conditions and transfer tube conditions. The system is used to generate a 3500 sccm aerosol stream with D_g of 2 to 7 nm and C_N of 2 to $8{\times}10^9$ #/cm^3 measured at the system outlet. The ability to control particle size in this range is especially important for applications, including carbon nanotube and photonic material synthesis, where only particles within a certain size range are active and the final material properties are highly sensitive to particle size. Our results indicate the potential to improve the productivity and control of applications such as these through the integration of a microplasma reactor based on the techniques and design insights developed here.

5.5 Additional information

5.5.1 Particle diffusivity in argon and helium

Binary diffusion coefficients for iron particles in a helium or argon carrier gas were derived using the rigid sphere model as described by Hirschfelder, et al. [23]. The diffusivity, D, in cm^2/s, is given by:

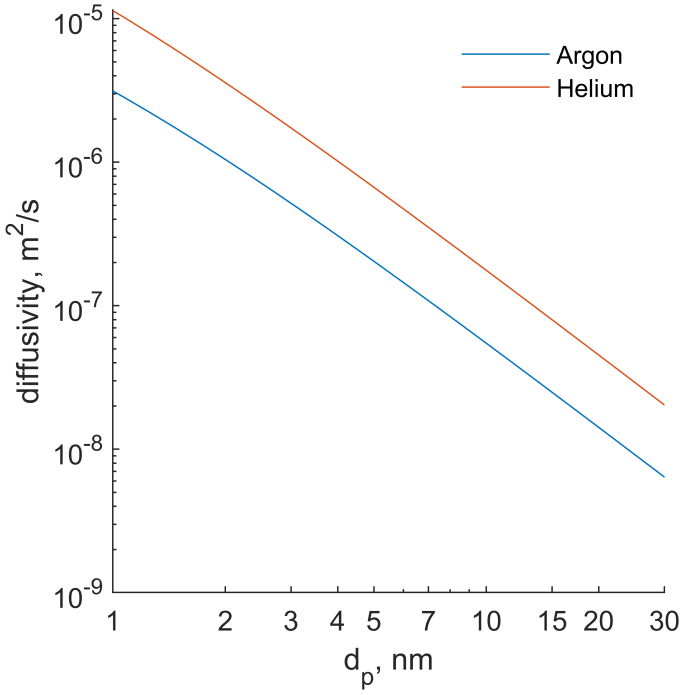

$$D = \frac{C_1}{P\sigma^2}\sqrt{\frac{T^3}{2m_r}} \tag{5.4}$$

$$\sigma = r_p + r_g \tag{5.5}$$

$$m_r = \frac{m_p m_g}{m_p + m_g} \tag{5.6}$$

where P is the pressure, T is the temperature, r is the radius of the gas molecule or particle, and m is the molar mass of the gas molecule or particle. For P in atm, T in K, r in m, and m in g/mole, $C_1 = 2.628{\times}10^{-3}$.

5.5.2 Particle coagulation rate in argon and helium

Aerosol particle growth via aggregation can be described using a coagulation kernel which specifies the collision frequency between two particles of given sizes. Three regimes of particle coagulation are delineated by the dimensionless Knudsen number: $Kn = \lambda/r_p$ where λ is the mean free path and r_p is the particle radius. In the continuum regime

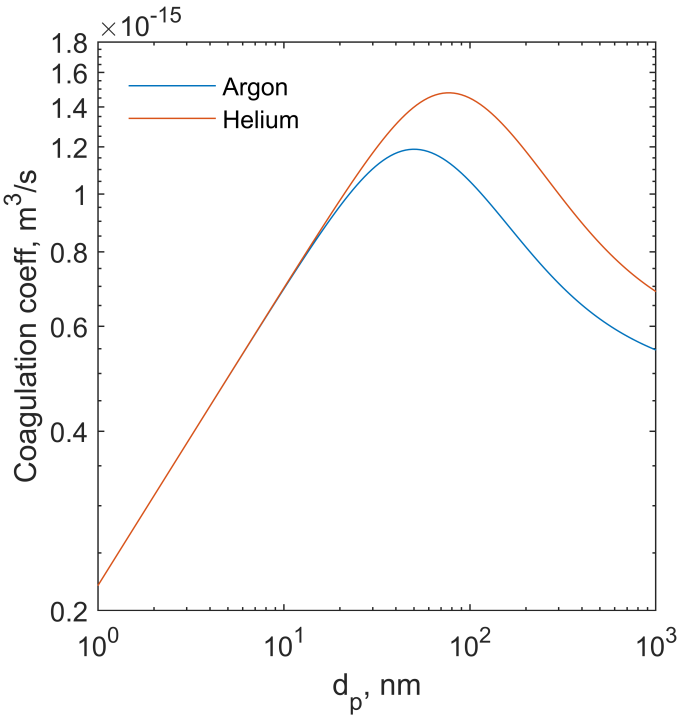

Figure 5.13: Coagulation kernel for like-sized iron particles at standard conditions.

($Kn << 1$), the particle is large relative to the mean free path of the gas and its motion is described by Brownian diffusion in a continuous medium. In the free molecular regime ($Kn >> 1$), the particle's motion is described by the kinetic theory of gases. Fuchs [31] developed a formula to interpolate the coagulation kernel between these two processes for the transition regime ($0.1 < Kn < 10$).

Figure 5.13 shows this coagulation kernel for two iron particles of the same diameter in argon or helium at standard conditions. Under these conditions, particles less than 10 nm are in the free molecular regime, with collision rate increasing with particle diameter following a power-law relationship.

References

[1] Alexis T Bell. "The impact of nanoscience on heterogeneous catalysis". In: *Science* 299.5613 (2003), pp. 1688–1691.

[2] Neel Narayan, Ashokkumar Meiyazhagan, and Robert Vajtai. "Metal Nanoparticles as Green Catalysts". In: *Materials* 12.21 (2019), p. 3602.

[3] Kohsuke Mori and Hiromi Yamashita. "Progress in design and architecture of metal nanoparticles for catalytic applications". In: *Physical Chemistry Chemical Physics* 12.43 (2010), pp. 14420–14432.

[4] Yibo Yan et al. "Carbon nanotube catalysts: recent advances in synthesis, characterization and applications". In: *Chemical Society Reviews* 44.10 (2015), pp. 3295–3346.

[5] Sreekanth Thota and Debbie C Crans. *Metal nanoparticles: synthesis and applications in pharmaceutical sciences*. John Wiley & Sons, 2018.

[6] Weijia Wang et al. "The rich photonic world of plasmonic nanoparticle arrays". In: *Materials today* 21.3 (2018), pp. 303–314.

[7] Bengt O Meuller et al. "Review of spark discharge generators for production of nanoparticle aerosols". In: *Aerosol Science and Technology* 46.11 (2012), pp. 1256–1270.

[8] Wey Yang Teoh, Rose Amal, and Lutz Mädler. "Flame spray pyrolysis: An enabling technology for nanoparticles design and fabrication". In: *Nanoscale* 2.8 (2010), pp. 1324–1347.

[9] Uwe R Kortshagen et al. "Nonthermal plasma synthesis of nanocrystals: fundamental principles, materials, and applications". In: *Chemical reviews* 116.18 (2016), pp. 11061–11127.

[10] Saeed Ahmad et al. "Gas phase synthesis of metallic and bimetallic catalyst nanoparticles by rod-to-tube type spark discharge generator". In: *Journal of Aerosol Science* 123 (2018), pp. 208–218.

[11] Prashant Kumar et al. "Treatment of losses of ultrafine aerosol particles in long sampling tubes during ambient measurements". In: *Atmospheric Environment* 42.38 (2008), pp. 8819–8826.

[12] Wei-Hung Chiang, Carolyn Richmonds, and R Mohan Sankaran. "Continuous-flow, atmospheric-pressure microplasmas: a versatile source for metal nanoparticle synthesis in the gas or liquid phase". In: *Plasma Sources Science and Technology* 19.3 (2010), p. 034011.

[13] Alborz Izadi and Rebecca J Anthony. "A plasma-based gas-phase method for synthesis of gold nanoparticles". In: *Plasma Processes and Polymers* (), e1800212.

[14] Kostya Ken Ostrikov, Uros Cvelbar, and Anthony B Murphy. “Plasma nanoscience: setting directions, tackling grand challenges”. In: *Journal of Physics D: Applied Physics* 44.17 (2011), p. 174001.

[15] Liangliang Lin and Qi Wang. “Microplasma: a new generation of technology for functional nanomaterial synthesis”. In: *Plasma Chemistry and Plasma Processing* 35.6 (2015), pp. 925–962.

[16] William J Sawyer and A John Hart. “High-yield microplasma synthesis of monodisperse sub-3 nm diameter metal nanoparticles explained by a charge-mediated formation mechanism”. In: *Journal of Aerosol Science* 161 (2022), p. 105915.

[17] Michal Fulem et al. “Recommended vapor pressure and thermophysical data for ferrocene”. In: *The Journal of Chemical Thermodynamics* 57 (2013), pp. 530–540.

[18] Bon Ki Ku and Juan Fernandez De La Mora. “Relation between electrical mobility, mass, and size for nanodrops 1–6.5 nm in diameter in air”. In: *Aerosol Science and Technology* 43.3 (2009), pp. 241–249.

[19] Carlos Larriba et al. “The mobility–volume relationship below 3.0 nm examined by tandem mobility–mass measurement”. In: *Aerosol Science and Technology* 45.4 (2011), pp. 453–467.

[20] Peter F DeCarlo et al. “Particle morphology and density characterization by combined mobility and aerodynamic diameter measurements. Part 1: Theory”. In: *Aerosol Science and Technology* 38.12 (2004), pp. 1185–1205.

[21] Attarad Ali et al. “Synthesis, characterization, applications, and challenges of iron oxide nanoparticles”. In: *Nanotechnology, Science and Applications* (2016), pp. 49–67.

[22] John Konopka. “Options for quantitative analysis of light elements by SEM/EDS”. In: *Thermo Fisher Scientific;* Technical Note 52523 (2013).

[23] Joseph Oakland Hirschfelder, Charles F Curtiss, and R Byron Bird. *Molecular theory of gases and liquids*. Structure of Matter Series. Wiley, 1964.

[24] Wei-Hung Chiang and R Mohan Sankaran. “Microplasma synthesis of metal nanoparticles for gas-phase studies of catalyzed carbon nanotube growth”. In: *Applied Physics Letters* 91.12 (2007), p. 121503.

[25] Pin Ann Lin, Ajay Kumar, and R Mohan Sankaran. “New insights into plasma-assisted dissociation of organometallic vapors for gas-phase synthesis of metal nanoparticles”. In: *Plasma Processes and Polymers* 9.11-12 (2012), pp. 1184–1193.

[26] Nikolay A Dyatko, Yury Z Ionikh, and Anatoly P Napartovich. “Influence of nitrogen admixture on plasma characteristics in a DC argon glow discharge and in afterglow”. In: *Atoms* 7.1 (2019), p. 13.

[27] Sukbyung Chae et al. “Wire-in-hole-type spark discharge generator for long-time consistent generation of unagglomerated nanoparticles”. In: *Aerosol Science and Technology* 49.7 (2015), pp. 463–471.

[28] M Vardelle et al. “Controlling particle injection in plasma spraying”. In: *Journal of Thermal Spray Technology* 10 (2001), pp. 267–284.

[29] Souvik Ghosh et al. “Atmospheric-pressure dielectric barrier discharge with capillary injection for gas-phase nanoparticle synthesis”. In: *Journal of Physics D: Applied Physics* 48.31 (2015), p. 314003.

[30] Wei-Hung Chiang and R Mohan Sankaran. “Linking catalyst composition to chirality distributions of as-grown single-walled carbon nanotubes by tuning Ni x Fe 1- x nanoparticles”. In: *Nature materials* 8.11 (2009), p. 882.

[31] NA Fuchs and AG Sutugin. “Coagulation rate of highly dispersed aerosols”. In: *Journal of Colloid Science* 20.6 (1965), pp. 492–500.

[32] William C Hinds and Yifang Zhu. *Aerosol technology: properties, behavior, and measurement of airborne particles*. John Wiley & Sons, 1999.

[33] Zhangfa Wu and I Colbeck. “Studies of the dynamic shape factor of aerosol agglomerates”. In: *Europhysics Letters* 33.9 (1996), p. 719.

6. Aerosol carbon nanotube production

6.1 Introduction

In parallel with the development of the microplasma reactors, a FC-CVD reactor has been developed and undergone several design iterations. The challenge of developing this system can be divided into three coupled aspects: the operation of the microplasma reactor, integration of the microplasma reactor with the CVD furnace, and the typical tuning of the CVD operating conditions for CNT growth. Microplasma integration and CVD tuning are highly coupled, as the optimal growth conditions depend in part on the particle characteristics and multiple dependencies between the two exist. For example, a higher furnace temperature will require the microplasma be located further outside the furnace to remain sufficiently cool. In all cases, stable operation of the microplasma for many hours is a prerequisite for conducting informative experiments. During the initial tuning up of the FC-CVD system one is essentially flying blind until it is able to producing CNT samples which are repeatable and sufficiently large to enable quality and quantity characterization. Once some signal has been established, the process of investigating the system becomes significantly more fruitful.

The first complete FC-CVD system was constructed in July 2018, and has undergone near-continuous revision since them, both incorporating the latest microplasma reactor developments and modifying hardware to test different integration techniques and CVD

conditions. An additional unforeseen challenge was the collection of small amounts of aerosol material, and the collection methodology and hardware has undergone a similar evolution. By April 2019 the system was able to sporadically produce extremely small quantities of carbonaceous material that may have included CNTs, but were predominantly nanofibers of 10s nm diameter, with Raman G/D ratio of 1–1.5. By the end of 2019, it was confirmed that CNTs were being produced with a G/D ratio of 5, yet still unreliably and of negligible amount. Figure 6.1(a) shows a typical "tuft" of large-diameter highly-defective CNT. This early development, up to the end of 2019, was done as part of the author's S.M. thesis [1], and is not discussed in detail here.

In July 2021 the production rate had been increased to the point that it could be relatively compared between experiments based on a qualitative observation of SEM images of the collection filter. The sparse CNTs form a cobweb morphology as seen in Figure 6.1(b), and the productivity can be estimates by the density of this structure. The purity can be qualitatively assessed from the extent of carbon and iron deposits along the CNTs. Having pulled ourselves up by our bootstraps over the previous three years, the system was now in a state where scientific investigation could begin in earnest, and subsequent experiments are referred to as the "P series" ("P" standing for *phew*!). Utilizing this qualitative metric for production rate and measuring quality via Raman and SEM image morphology, system performance was improved to the next major threshold in May 2023 (P276), where the mass of deposited CNTs was sufficient to be measured directly (~10 µg), and the deposit thickness sufficient to characterize the catalyst content via SEM EDS as an additional metric for quality. Figure 6.1(c,d) shows the thick and cohesive mat of CNTs typical of the current work.

The objective of this chapter is two-fold, reflecting the combination of art and science inherent in developing a FC-CVD system. First, to detail a series of more general conclusions or insights about FC-CVD synthesis of CNTs on ex-situ catalyst particles

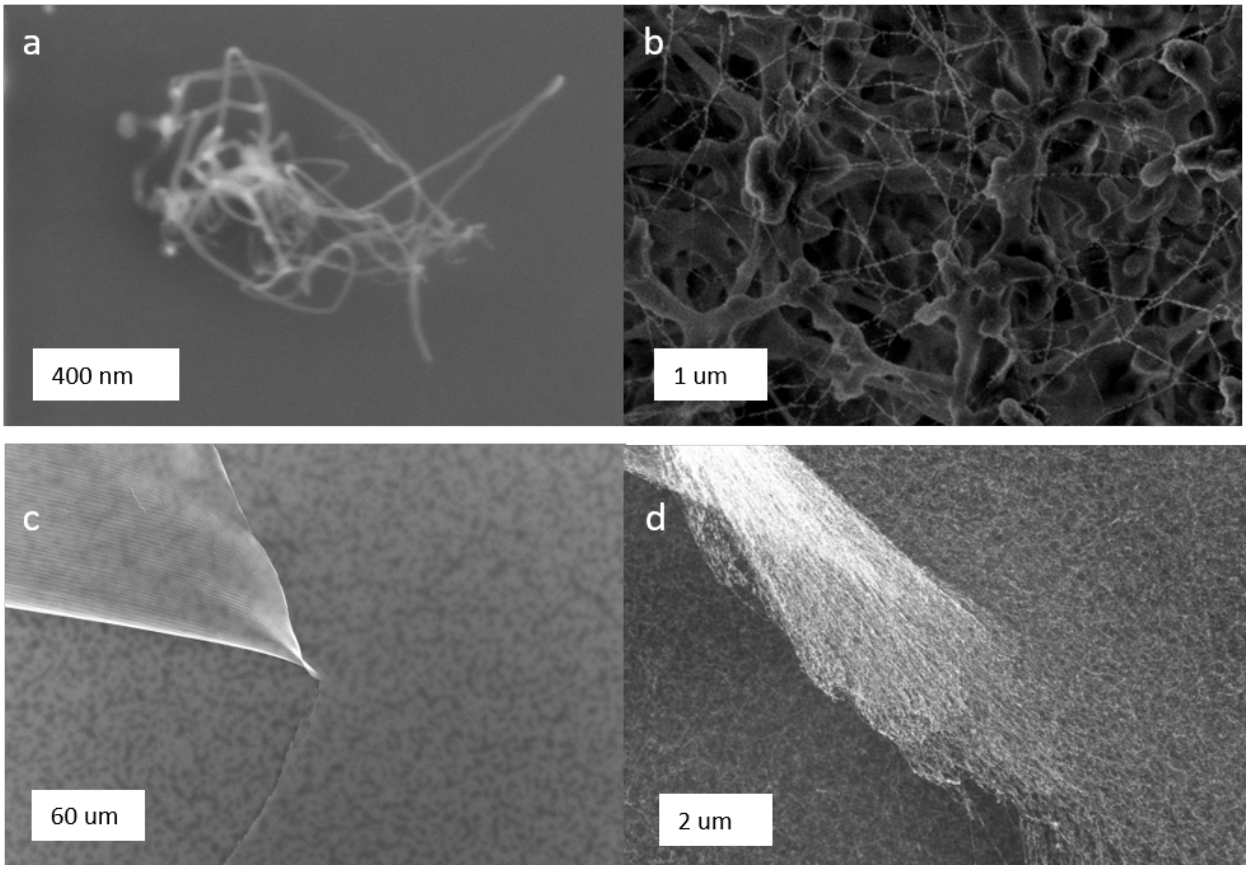

Figure 6.1: Examples of typical FC-CVD product at different periods in the system development. (a) A highly-defective isolated tuft on a smooth silicon wafer collected in July 2019. (b) An early P-series sample from July 2021 showing a thin cobweb of CNTs, covered in small iron and carbon particles, collected on a cellulose filter (the lobed micron-scale structure). (c) A recent sample from July 2023 showing thick and cohesive layers of CNTs as evidenced by the peeling and tearing of the top layer. The mottled appearance is from the structure of the sintered microparticle membrane filter below. (d) Close-up image of the corner of the tear shown in (c) to highlight the cohesive and mat-like nature of the CNT deposit.

based on experiments, CFD modeling, and existing theories for CNT growth. Second, as this knowledge typically conveys trends or relationships but not specifics, the iterative process of experimentally exploring these trends in order to find optimal synthesis conditions for this system. This will primarily focus on post-P276 experiments as these have the most rich characterization, allowing the most robust conclusiosn to be drawn.

6.2 Experimental methods

6.2.1 FC-CVD System design

This section describes the physical design of the FC-CVD system and typical operating conditions, as it has been from May 2023 (Experiment P276) to the present. Figure 6.2 shows a photo of the reactor system, including ancillary hardware like gas flow controllers and the scanning mobility particle sizer (SMPS). Figure 6.3 shows a schematic of the FC-CVD reactor inlet region. The microplasma is identical to that described in Chapter 5, with the transfer tube now referred to as the injector to communicate its role in transporting the aerosol into the furnace region. The injector position is measured from the outer face of the insulation of the furnace, while the injector length is measured from the tip of the plasma housing to the end of the injector.

Flow rates and composition for the inner, sheath, injector, and furnace flows are varied across experiments and full details are reported below. Typically, the inner flow is predominantly helium (Airgas, UHP, 99.999%) with a small fraction of hydrogen (Airgas, UHP, 99.999%) with total flow rate 450–900 sccm. The sheath flow is a mixture of helium and nitrogen (Airgas, HP, 99.998%) with ferrocene ($Fe(Cp)_2$) vapor added by diverting 30 sccm He through a sublimation chamber containing $Fe(Cp)_2$ powder at room temperature totalling 450–900 sccm. The injector flow is a variable mix of hydrogen

and either nitrogen or argon (Airgas, UHP, 99.999%) totalling 700–3200 sccm. Finally, the furnace flow is a mixture of a hydrogen-argon carrier gas with a carbon precursor (ethylene, acetylene, or methane, all Airgas, UHP, 99.999%) totalling 1000–3100 sccm. A flow of up to 150 sccm of helium saturated with water vapor can also be added to any of the four flows. The injector tube (ID = 20 mm, OD = 25 mm or ID = 16 mm, OD = 19 mm) and furnace tube (ID = 35 mm, OD = 38 mm or ID = 47 mm, OD = 50 mm; L = 110 or 120 cm) are both quartz (Technical Glass Products, Inc.). The furnace is a three zone split tube furnace (Carbolite Gero) operated at up to 1200 °C with an external length of 75 cm and heating element length of 60 cm. A full list of the 29 variables which define each experimental case are listed in Table 6.4.1.

6.2.2 CNT collection

CNTs are collected at the furnace outlet on sintered silver membrane filters with nominal 0.8 μm pore size (Sterlitech; 45328). During early experiments with low production rate, filter holders with a circular collection area of 6, 9, or 11 mm diameter were used to ensure a sufficiently thick CNT deposit for characterization. A 1" ball valve was modified to serve as a load lock chamber enabling the removal and replacement of filters while the system is operating (Figure 6.4). Using this device, a filter can be loaded, the load lock chamber pumped down and refilled with gas from the process tube (to prevent atmospheric contamination, especially oxygen, from entering the CVD system), and the filter positioned in-line to the process tube and the full gas flow diverted through the filter. For CNT deposits greater than 50–100 μg, the additional back pressure causes the filter to burst. Thus, as the production rate of the system was increased, a new load lock chamber was built to replace the ball valve chamber to hold filters of larger area. The KF-50 load lock chamber (Figure 6.5) has filter holders to accommodate collection areas of 16, 21, and 33 mm diameter.

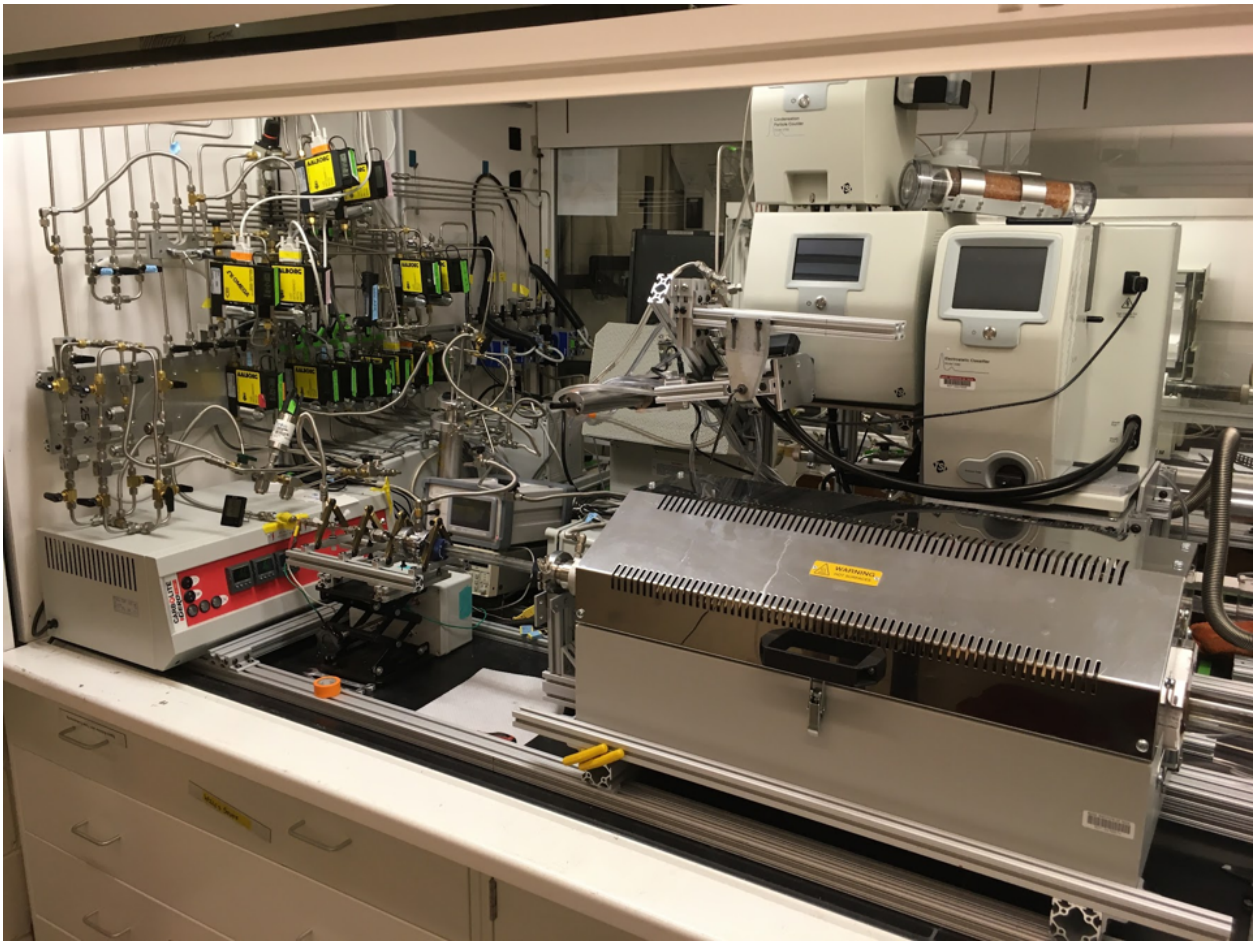

Figure 6.2: Photo of the complete FC-CVD reactor system. The furnace in the foreground on the right contains the main CVD process tube, with the microplasma reactor to its left. In the left background is the gas distribution system and mass flow controllers (MFCs). In the right background is the scanning mobility particle sizer (SMPS).

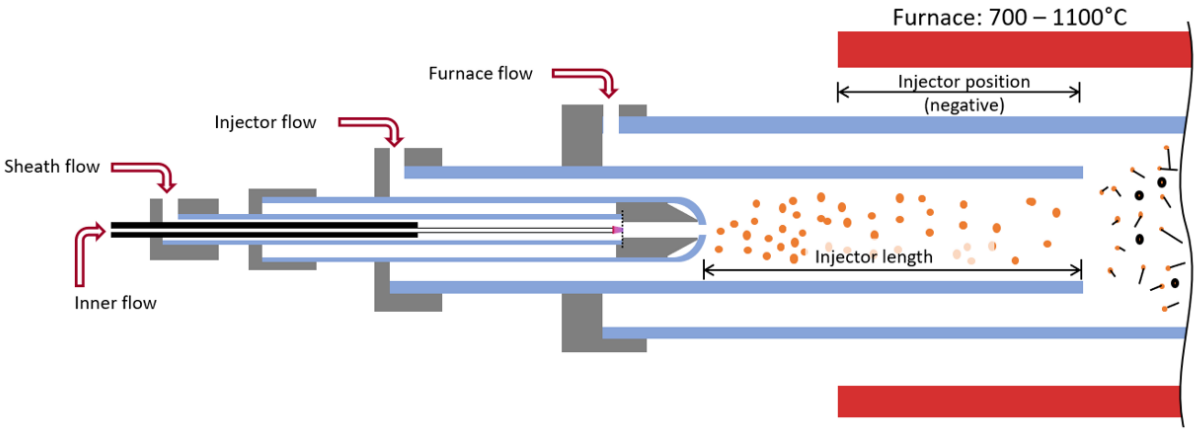

Figure 6.3: Schematic of the microplasma reactor and FC-CVD reactor inlet. The microplasma is identical to that described in Chapter 5, with the transfer tube now referred to as the injector. Typical values for the inner, sheath, injector, and furnace flows are reported in the text, with total flows in the range 4000–8000 sccm.

6.2.3 Characterization

Unless otherwise noted, a uniform set of characterization protocols has been used for all CNT samples discussed in this section to enable the most direct comparison across samples.

Mass

The mass production rate is determined by the difference in measured mass of the filter before and after collection. The neat filters weigh approximately 50 mg for a 13 mm diameter disc or 180 mg for a 25 mm diameter disk. Filter mass is established by the mean of five measurements on a microbalance (Discovery DV215CD, ±0.01 mg), and the product mass is reported as the mean difference and standard deviation of the difference. Given the small mass of the product (<10 to 100s μg) relative to the total filter mass and the resolution of the microbalance, other sources of error such as the amount of absorbed water on the filter due to changes in humidity may be significant yet are not

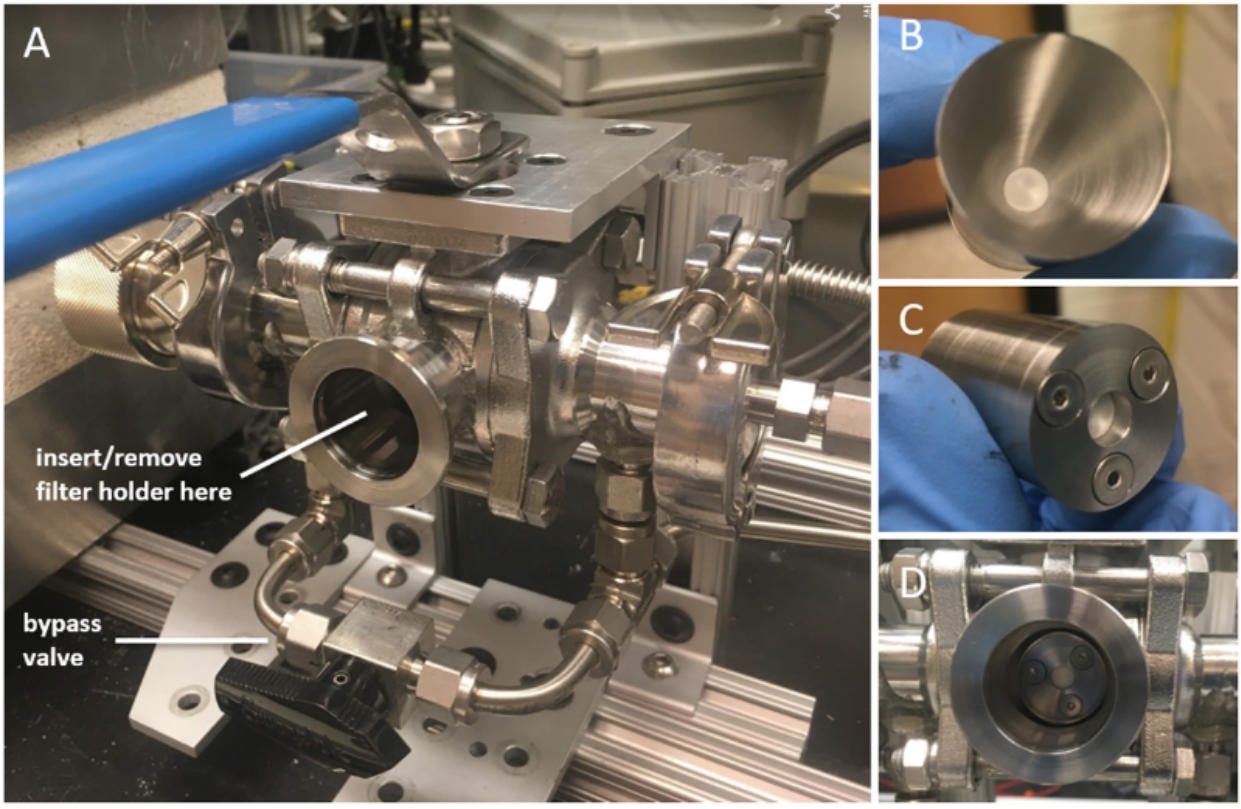

Figure 6.4: (a) Modified 1-inch ball valve used as load lock chamber for small filters. An additional large port with KF-25 stub was attached to the front side side and a custom port on the back side was connected to a gas line with two-way valve to either a roughing pump or the upstream side of the ball valve. When the main ball valve is closed (and process flow directed through the bypass line below), the cylindrical volume within the ball is accessible through the front port and can be pumped down or purges via the rear line. (b, c) The 6 mm version of the cylindrical filter holder. Subsequent versions of the filter holder include an o-ring recessed into the outer diameter to ensure a seal with the ball valve's ball. (d) the filter holder can be inserted into the ball of the ball valve through the front port.

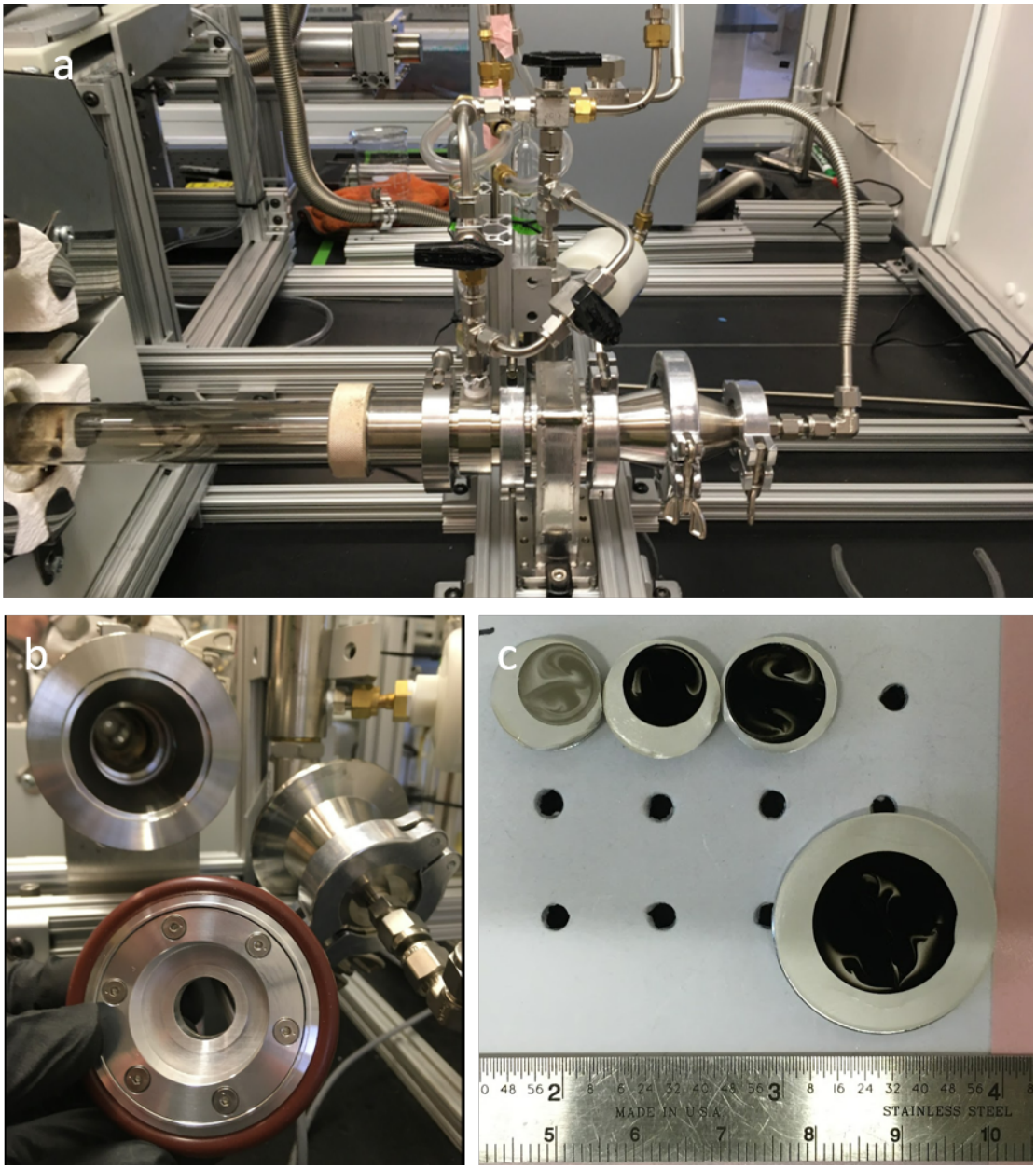

Figure 6.5: (a) The outlet side of the CVD furnace showing the gate valve and KF-50 load lock chamber. The operation and capability of this system is identical to the ball valve load lock chamber. (b) The custom KF-50 filter holder, designed to take the place of a centering ring in a normal KF-50 connection. The filter holder shown here contains a 16 mm insert, with 21 and 33 mm inserts available as well. (c) Example CNT deposits on sintered silver filters. The two upper left deposits were made using the 9 mm filter holder, the upper right was made using the 11 mm filter holder, The upper row were all made using the ball valve load lock chamber with 9, 9, and 11 mm filter holders, respectively. The lower right deposit was made using the 16 mm filter holder for the KF-50 load lock chamber.

accounted for in the error estimate.

Raman spectroscopy

Raman spectroscopy uses the spectrum of scattered light emitted by a surface under illumination by a laser of precise wavelength to characterize the chemical bonds present in the surface [2]. Light is scattered by electrons in the material being excited by the laser into a higher energy state and then re-emitting light upon returning to a lower energy state. Most scattered light is of the same wavelength as the incident light (the electron returns to the same energy state it initially had). A small fraction of electrons instead return to a slightly lower or higher energy state, emitting light with a slightly shifted wavelength in the process. This process is known as Raman scattering. Intensity peaks in the spectrum of scattered light in units of Raman shift (cm$^-$1) can illuminate specific chemical bonds in the material.

Of primary interest for CNTs and other carbon materials are the G peak at ~1580 cm^{-1} indicating graphitic sp^2 carbon (graphite, graphene, or CNT lattice) and the D peak at ~1290 cm^{-1} for a 785 nm incident laser (More commonly referred to as ~1350 cm^{-1} for a 532 nm laser). The ratio of the intensities of the G and D peaks, here referred to as G/D, indicates the quality of a CNT, or CNT assembly. A lower value indicates lattice defects within the CNT or the presence of non-sp^2 carbon elsewhere in the sample (e.g., an amorphous carbon coating on the outside of CNTs) [3, 4, 5]. SWCNTs also exhibit radial breathing mode peaks in the <500 cm^{-1} range which correspond to the radial vibration mode of the CNT. The following empirical relationship is used to relate SWCNT diameter to RBM peak position:

$$\omega = \frac{227}{d}\left(1 + C\ d^2\right)^{1/2} \tag{6.1}$$

where ω is the RBM frequency in cm^{-1}, d is the SWCNT diameter in nm, and C is an environmental effect factor of approximately 0.05–0.07 [6]. The presence of RBM peaks is a strong indicator of SWCNTs, as opposed to MWCNTs or other carbon allotropes. The Raman shift of the RBM peaks can be used to infer the CNT diameter as well as chirality, however the strength or presence of the RBM single from a given CNT is dependant on the bandgap of the CNT being similar to the laser energy. Thus, a specific laser wavelength will only excite a fraction of potential CNT chiralities, thus multiple wavelengths are needed to fully characterize a sample via RBM peaks [7].

As-deposited samples were characterized via Raman spectroscopy (Renishaw Invia Reflex Raman Confocal Microscope) in the ASEF-OTC Lab in the Materials Research laboratory (MRL). Unless otherwise indicated, a 785 nm, 100 mW laser source is used with the following settings: "extended scan" from 125 to 3000 cm^{-1}, 1200 l/mm grating, six scans of 3 s duration at 0.05% laser power, using a 50x objective lens. Given the high quality of the CNT samples, the relevant peaks are sufficiently strong that no background subtract is needed. It was found that the signal is also significantly enhanced by the use of the sintered silver filter as compared to PTFE and cellulose-based filters. The overall strength of the Raman signal appears to scale with the thickness or density of the deposit, which is not spatially uniform as seen in Figure 6.5(c). The signal strength appears to saturate when the deposit is sufficiently thick to look "very black" to the eye. To account for this variability of thickness, and the potential spatial variability of CNT quality, 3–5 measurements were taken present the darkest regions of the filter. Raw Raman spectra are automatically processed to determine the G and D peak heights based on the peak-to-trough distance.

SEM and EDS

Scanning Electron Microscope Energy Dispersive Spectroscopy (SEM-EDS; Zeiss Gemini 450, Oxford Instruments Ultim Max) was used to characterize the ratio of iron to carbon in samples and confirm the absence of other elemental impurities. For each sample, 3–5 EDS maps are taken at 500KX magnification using 15.00 KV EHT and a current of 1 nA, and the average elemental composition is reported. The map area is approximately 3 μm^2. As both the deposit thickness and SEM-EDS analysis depth are of the order 1–10 μm, the raw measured composition typically contains 5–10 at% silver, which is attributed to the filter material and removed from the analysis. A few percent oxygen is also typically observed. While it is hypothesized that this may indicate iron oxide (as any exposed nanoscale iron would rapidly oxidize once removed form the FC-CVD system into ambient air [8]), the signal magnitude does not always correlate with the iron signal. As oxygen is difficult to measure accurately via SEM-EDS, this signal was not analyzed [9]. Having removed the silver and oxygen signals, and not observing any other elemental signals, the atomic percent of iron and carbon are scaled to total 100. The average and standard deviation of the atomic percent iron is reported based on the average of the 3–5 map averages.

The sensitivity of SEM/EDS is not as high as other methods such as TGA and EDX, and thus may give a false negative when iron is less than 0.1 at%, and in general may have a greater degree of noise and error in the range of ~1 at% [10]. For the purposes of this work, where measured iron atomic percent range from <1 up to 20 or higher, this is still a sufficiently informative technique, with a strong signal for process tuning and control over most of this range. Yet, as the process continues to improve and SEM/EDS indicates a consistent <2 at% Fe signal, more precise characterization will be needed.

6.3 Studies of CNT growth

6.3.1 Injector position and temperature

Our understanding of CNT nucleation suggests that there is an optimal window of temperature based on the carbon precursor and catalyst particle properties. As the temperature profile generally increases from the furnace inlet into the interior, this temperature window is also a spatial window. Further, based on the flow velocity of gas into the furnace, and the choice of some reference point in the gas delivery system, this window can be described by the range of gas residence times it encompasses. This thermal, spatial, or temporal window is referred to as the CNT nucleation zone. It is apparent that a central challenge associated with the use of externally-synthesized catalyst particles is the delivery of the particles to the CNT nucleation zone.

In a traditional FC-CVD system where catalyst particles are generated in situ by the thermal decomposition of ferrocene, there are two distinct approaches to creating a CNT nucleation window. The first generally favors lower temperatures (< 1000 °C) and creates a nucleation window in the inlet of the furnace. The temperature of the catalyst precursor decomposition defines the beginning of the CNT nucleation zone with respect to temperature. The temporal duration of the CNT nucleation window is limited by the continued growth and aggregation of these particles, becoming too large for CNT nucleation after a certain period of time. A second set of boundaries is enforced by the carbon precursor. The temperature must be sufficiently high for carbon species to react catalytically with the catalyst particle, but not so high that pyrolysis and soot formation occurs. In practice a range of carbon precursors can be used. More reactive species such as acetylene are available at lower temperatures and thus begin to nucleate CNTs as soon as catalyst particles form, biasing towards small diameter SWCNTs. However, the

maximum temperature of the system must be low enough to limit pyrolysis. On the other hand, more stable carbon species like methane are not available until much higher temperatures (and indeed, it has been shown that it is often the thermal decomposition products, not the stable carbon species itself, which are the actual precursor species [11]), at which time catalyst particles are larger, biasing towards MWCNTs. The second approach uses a high furnace temperature (1000–1300 °C) to create a nucleation window in the second half of the furnace as gases are cooling. Here, the temperature is sufficiently high to fully evaporate the iron input in the middle zone of the furnace. As the gas flows through the second half of the system it begins to cool, driving iron particle condensation [12].

Even in a traditional FC-CVD system, there is a great deal of control in trying to maximize the CNT nucleation zone by spatially aligning the optimal windows for the catalyst particle and carbon precursor. A common technique is the use of an actively cooled injector to release either the carbon precursor, catalyst precursor, or both, at a location inside the furnace [12, 13]. This allows the particles to form at a higher temperature than otherwise and in doing so removes the opportunity for the catalyst particle and carbon to interact at low temperatures where non-CNT solid carbon would be formed. Lee et al. [13] show a large increase in productivity and quality through the use of a deep injector.

Alternatively, the selection of precursor chemistry can also be used to shift the CNT nucleation windows. Moisala et al. [14] compare the use of iron pentacarbonyl and ferrocene as the iron precursor and found that the more thermally stable ferrocene delayed the formation of particles until deeper in the furnace, analogous to the previously discussed injector, and thus resulted in more and smaller catalyst particles and a higher production rate of SWCNTs. The analogous use of a higher reactivity carbon precursor to shift is less advantageous as it will also impact the later stages of CNT growth. How-

ever, one potential avenue is the use of multiple carbon precursors of different reactivity, as is done by the eDIPS process [15]. Tailoring of both carbon precursors has been shown to have a forcing effect on CNT diameter and wall number, and this process is used commercially by Meijo Nano Carbon Co.,Ltd.

By using ex-situ generated catalyst particles, the challenge is to ensure the mixing of the catalyst aerosol and the carbon precursor occurs within the optimal temperature range for the carbon precursor. The optimal temperature is in some respect determined by the choice of carbon precursor, and the location of that temperature determined by the temperature set point and the specific temperature profile of the reactor. The injector tube is positioned such that its outlet is within this window. However, the actual location of this window is not known precisely, and the process is made more complex by a non-uniform flow field, radial temperature variations, and non-instantaneous mixing of the injector and furnace flows.

Additionally, the ex situ catalyst particles still aggregate, thus the residence time of the aerosol within the injector must be considered in order to ensure the appropriate particle size distribution at the point of mixing. Without the ability to characterize the performance of the microplasma reactor at elevated temperature, it is desirable to keep it at as close to ambient temperature as possible. Thus, the deeper the injector position, the longer the injector residence time, and the greater catalyst aggregation occurs.

Given the complexity of these trade-offs, the relationships between injector position, injector length (thus, plasma position), and furnace set point temperature have been investigated in multiple experiments at several points in the FC-CVD system development process. The majority of these experiments use ethylene (C_2H_4) and a total hydrogen molar fraction of 30–50%.

Temperature-position overview

To begin to understand these relationships, an experiment (Samples P96-P116) was performed to look at a matrix of conditions at five different set point temperatures (700, 750, 800, 850, 900 °C) and five injector positions (-50, -100, -150, -200, -250 mm). The plasma was maintained at a position of at minimum 50 mm outside the furnace to prevent any stray influence of temperature upon the plasma operation. This necessitated an injector length of 200–300 mm. These experiments used a previous iteration of the microplasma reactor which uses a stainless steel tube and fittings to serve the same role as the quartz microplasma housing. The following recipe was used in all cases: inner flow of 1025 sccm helium, 25 sccm helium with ferrocene vapor; sheath flow of 100 sccm nitrogen; injector flow of 1100 sccm hydrogen; furnace flow of 120 sccm hydrogen and 30 sccm ethylene. A 47 mm I.D. process tube was used. Samples were collected for 15 minutes on polycarbonate membrane filters.

Figure 6.6 shows Raman characterization for these samples. In general, a higher furnace temperature (900 °C) and shorter injector (-50 mm) appear to give the best conditions. All experiments at -50, -100, -150 mm show RBMs, as do the lower-temperature experiments at -200 mm, confirming SWCNTs are present. Based on the relatively high RBM and G intensities at -50 mm injector position, it appears that, under these conditions, mixing of ethylene and catalyst particles at low temperature in the furnace inlet does not inhibit CNT nucleation. Following this, it reasons that the strong temperature dependence may be predominately due to the effect of temperature on CNT growth in the interior of the system, rather than CNT nucleation at the inlet. Finally, the overall small amount of material deposited (as evidenced by low RBM, G, and D intensities) at the deepest injector positions is interesting, especially because it appears mostly invariant to the set point temperature. One hypothesis could be the evaporation of the

catalyst particles within the injector, with the low G and D intensities indicating the formation of partially-graphitic soot via thermal decomposition. A second hypothesis is that this is due to the excessive thermal pretreatment of the ethylene before mixing. The deep injector increasing the time at which ethylene is at elevated temperature and potentially thermally decomposing. If this decomposition lead to soot, one would expect it to occur independent of the injector position or presence of catalyst particles. Instead, it may lead to the excess formation of more reactive decomposition products which rapidly coat the catalyst particles in a partially-graphitic cap – preventing CNT nucleation but still producing a small amount of carbonaceous product. While the injector length of 200–300 mm provides a long residence time for particle aggregation, this does not appear to have been a significant influence in this case, likely due to the relatively low aerosol concentration (due to both a low ferrocene input and lower yield of this microplasma reactor).

High temperature-position studies

900 °C and -50 mm is the optimal condition from within the range of furnace temperature and injector position investigated previously. Given the positive trend with temperature, additional experiments were conducted up to 1100 °C, the maximum temperature of the furnace, with the intention of finding an optimal value. Because the spatial resolution of the previous set of experiments was low, a more fine-grained study of injector position was also conducted. Additionally, if the mechanistic understanding of injector position is as a proxy for the temperature at the injector tip. then changes to the furnace temperature will result in a re-scaling of the temperature profile of the inlet and shift the position of this optimal temperature.

Figure 6.7 shows the results of a fine grained study of injector position from -20 to -50 mm at 950 °C (Samples P286–290) and 1000 °C (Samples P291–294 and P297). The

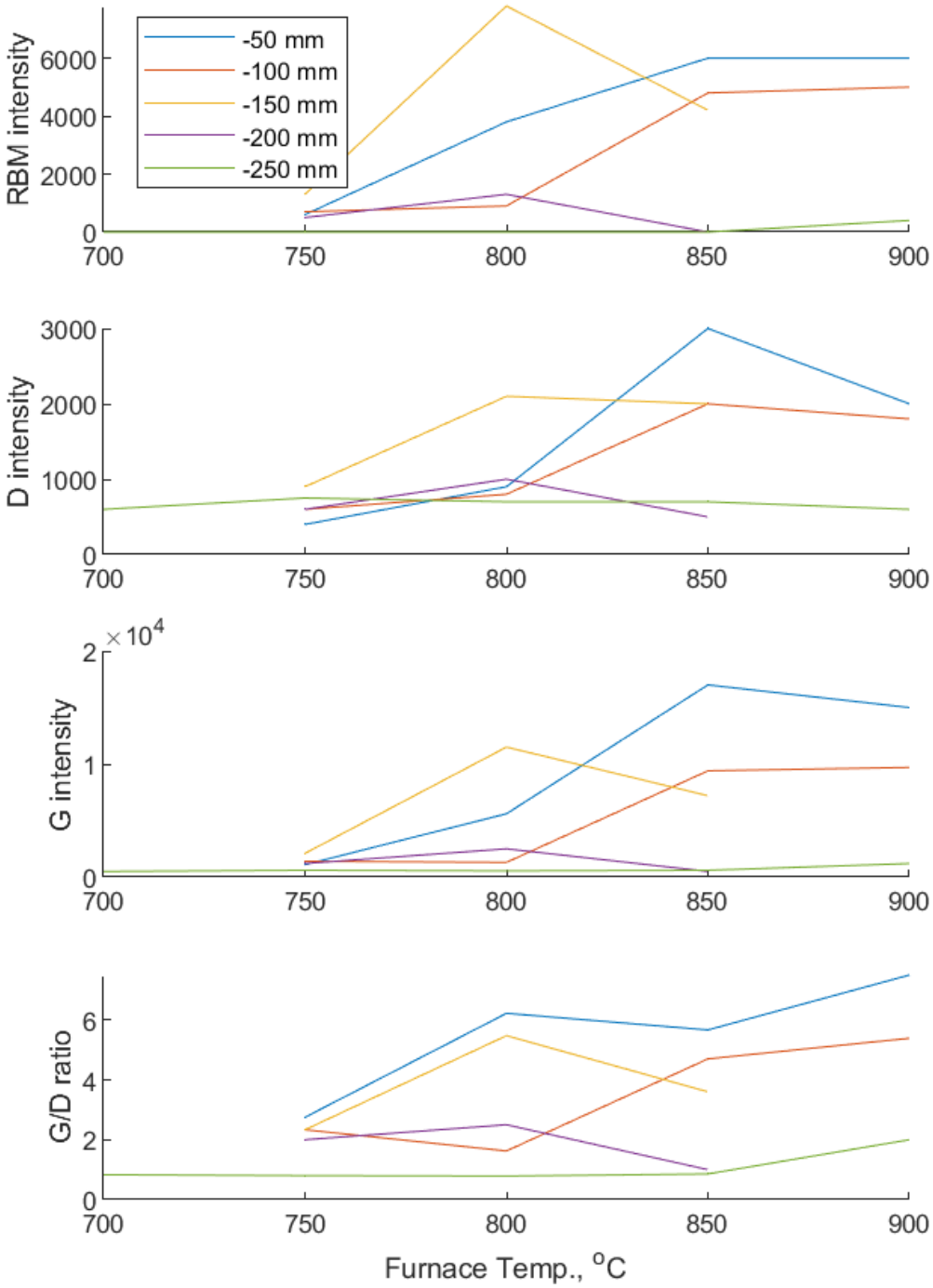

Figure 6.6: Raman characterization of samples P96-P116 showing the influence of injector position and furnace temperature. Legend values specify the injector position.

Raman G/D ratio and Fe at% indicate the best performance in the range -20 to -40 mm at 1000 °C. The lack of sensitivity to injector position within the range indicates a low sensitivity to the temperature at the injector tip, thus the difference in performance of the 950 °C cases and the 1000 °C cases likely indicates an improvement in CNT growth rather than nucleation. Production rate and Fe at% are expected to scale inversely with a fixed ferrocene input, as both a higher production rate and lower Fe at% indicate a greater amount of solid carbon product. The negative production rate for 950 °C at -20 mm indicates a negative change in mass between the initial and post-growth filters, potentially attributable to a small piece of filter material breaking off during handling. Unlike the previous set of experiments in which the injector length was very long, an injector length of only 20 mm was used here. The benefits of such a short injector are two-fold. First, the residence time within the injector is reduced, reducing catalyst aggregation. Second, a relatively smaller injector flow rate is needed to suppress eddy formation in the injector. However, the sharp drop in performance at the -50 mm injector position is attributed to an increase in the temperature of the microplasma housing. The mechanism for this has not yet been determined. The lack of Fe at% data for the 1000 °C -50 mm case is because the production rate was so low that a sufficiently thick deposit for SEM/EDS could not be found.

Concluding that an injector position of -30 mm was optimal under these conditions, and that, so long as the plasma housing does not overheat, the system is relative insensitive to changes in the injector position, a follow up study was conducted to investigate temperatures up to 1100 °C. Figure 6.8 shows characterization for the two previous experiments, P287 and P294, at -30 mm, as well as P321–323 at increasing temperatures. Additionally, the latter set used a higher flow rate of ferrocene. A full description of growth conditions can be found in Table 6.4.1.

At 1000 °C, both ferrocene levels result in similar production rate, while the high

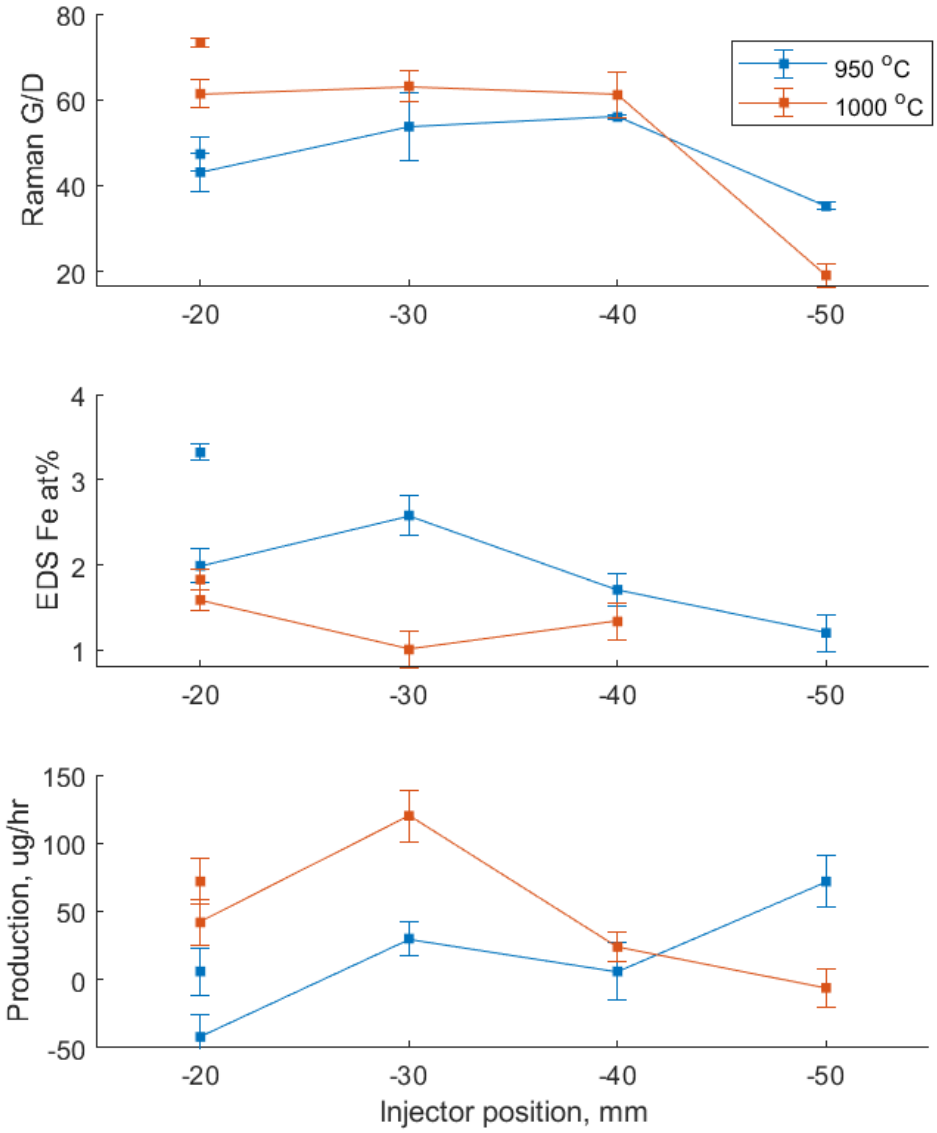

Figure 6.7: Characterization of samples P286–298 showing the influence of injector position at 950 and 1000 °C surface set points. A negative injector position is deeper into the furnace. At each temperature, the experiment was run from -20 to -50 mm positions, with a second sample taken at -20 mm at the end (the unconnected points).

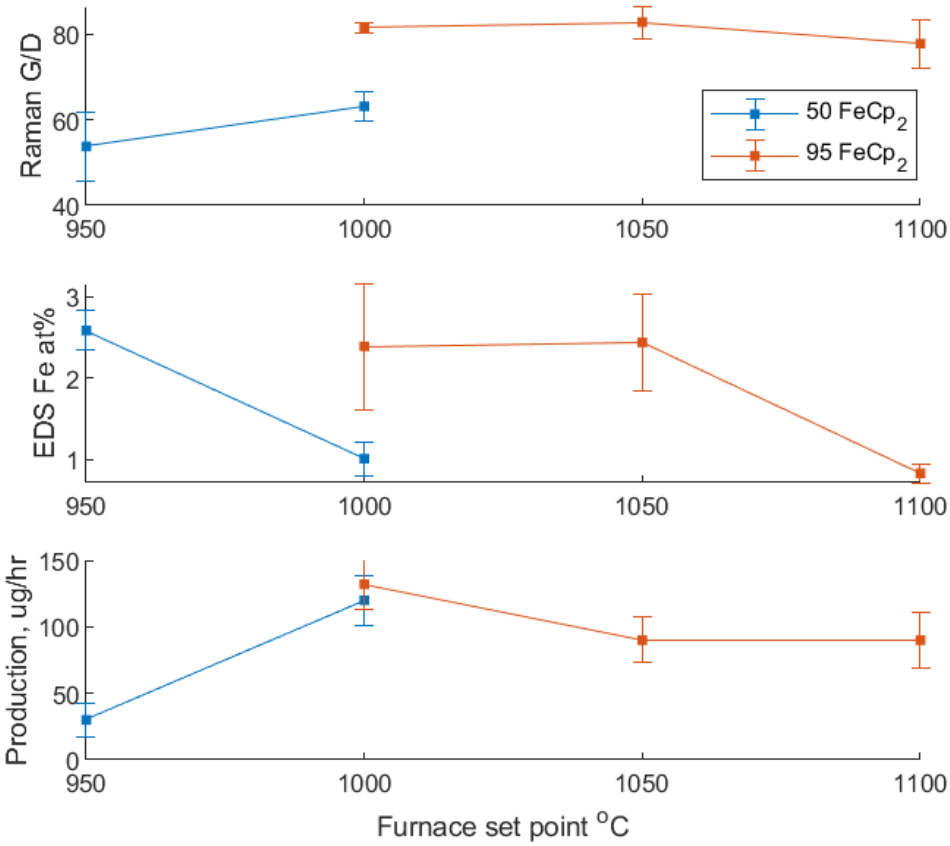

Figure 6.8: Characterization of samples P287, P294, P321–323 showing the influence of furnace set point temperature at an injector position of -30 mm.

ferrocene case has approximately twice the Fe at%, indicating that the conversion of carbon and iron is roughly constant in both cases. Experiments in Chapter 5 show that, all else being equal, increasing the ferrocene concentration does increase the total aerosol production, but mainly by producing more particles on the larger side of the size distribution, while the concentration of small particles remains roughly constant. If iron particles at the lower end of the particle size distribution are primarily responsible for CNT nucleation, this could explain why both cases produce approximately the same CNT product despite the high ferrocene case having significantly more catalyst particles. The cause of the increase in Raman G/D ratio for the high ferrocene cases is less obvious. The most apparent trade-off in the temperature range of 1000 °C to 1100 °C is between the production rate, slightly higher at 1000 °C, and the Fe at%, lowest at 1100 °C. The Raman G/D ratio is relatively constant.

A low Fe at% does not necessarily indicate a greater fraction of CNTs, as other forms of carbon will also contribute to the total amount of carbon. At higher temperature the barrier to non-catalytic carbon formation from the thermal decomposition of ethylene decreases. This should result in an increase in the production rate (potentially offset by changes to the CNT growth rate), decrease in Fe at%, and decrease in Raman G/D. The uniformity of the production rate and Raman G/D ratio indicate that this is not the mechanism behind the low Fe at% at 1100 °C. Alternatively, if the amount and quality of carbon is unchanged, is that the high temperature increases the evaporation rate of iron in the furnace. As the gases cool upon exiting the furnace, this iron vapor will condense onto any available surface, thus having a net effect of driving iron out of the CNT aerosol and onto the reactor walls and other surfaces.

Deep injector study

While the previous two studies found optimal injector positions of -50 and -30 mm, respectively, neither fully investigates this parameter space: the earlier study was only at low temperatures and the second study is hypothesized to be limited by the effect of temperature on the microplasma itself. Additionally, the accumulation of small changes to the reactor design and baseline recipe since the initial experiments may have caused the optimal position to shift, or changed the limiting relationship as other problems were addressed.

Thus, a third study was conducted, at high temperature and with the injector length and position adjusted in concert to keep the absolute position of the plasma housing fixed and isolate the effect of the inject position. Yet, of course, with the new confounding factor of a changing residence time in the injector potentially changing the aerosol size distribution. Figure 6.9 shows characterization for Samples P427-441, all at 1000 °C and the plasma housing at -15 mm. Ferrocene flow rates of 37.5, 75, and 150 sccm were used to assess if the variable injector length used in this study has a discernible effect on the final mean particle size at the injector tip due to changing the residence time for aggregation. Unexpectedly, the ferrocene concentration appears to be the strongest influence, while the injector position, in the range -25 to -80 mm, has only a minor effect. Notably, all five of the experiments with 37.5 sccm ferrocene have a low G/D ratio, low Fe at%, and low production rate. Comparing SEM images of the three ferrocene flow rates at an injector position of -80 mm (visually representative of the samples from other injector positions) in Figure 6.10, the 37.5 sccm case has an entirely different morphology than that with greater ferrocene. Instead of the typical long clean CNTs interspersed with clusters of carbon and catalyst particles, the entire sample is small fractal-like tufts with rare longer CNTs. The very low Fe at% indicates that this material is not the same

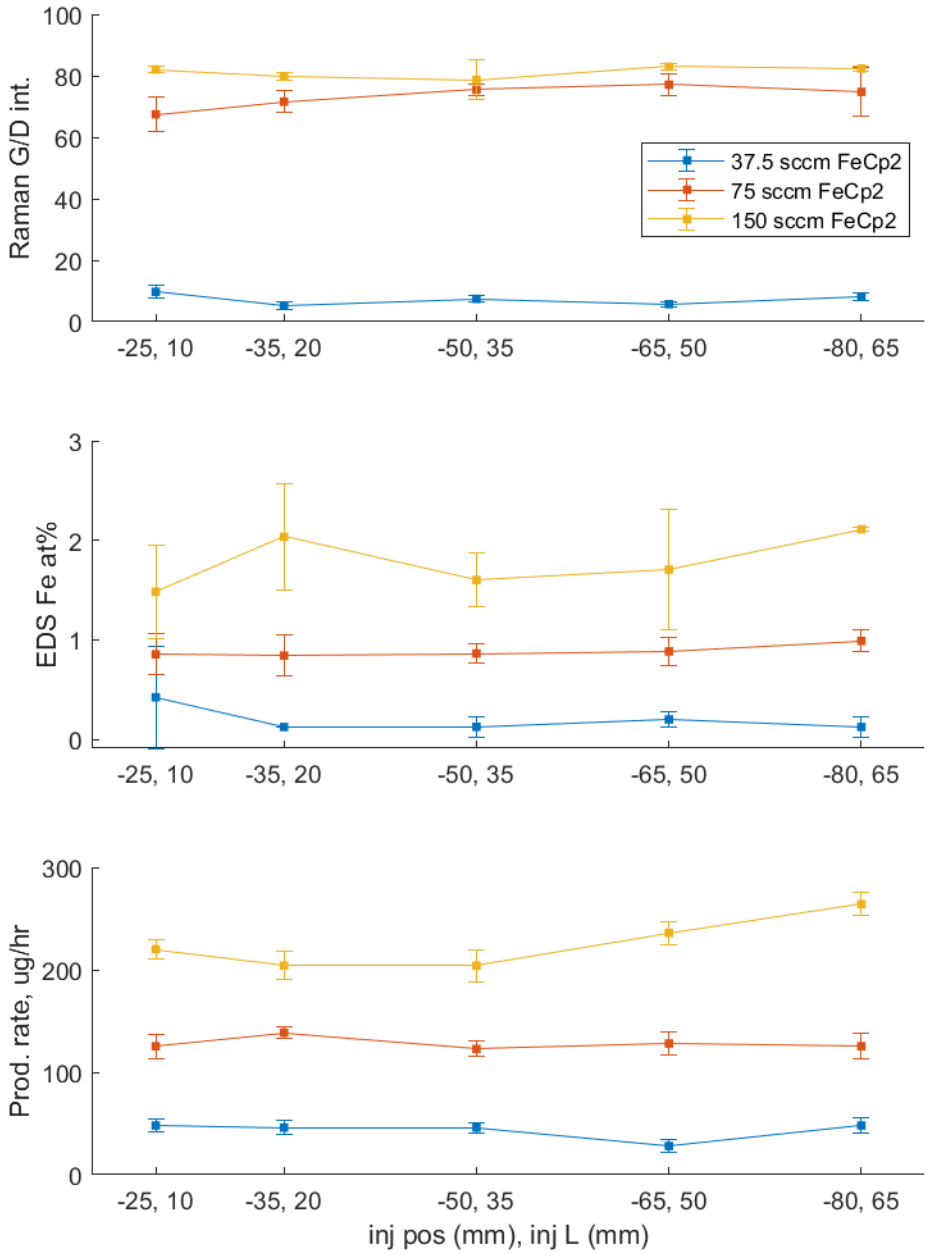

Figure 6.9: Characterization for Samples P427-441 showing CNT growth for injector positions -25 to -80 mm and ferrocene flow rate of 37.5, 75, and 150 sccm. All cases are at 1000 °C and the plasma housing at -15 mm, with injector positions.

as the iron-carbon decoration on the CNTs in other cases.

The presence of a small-diameter Raman RBM peak in Figure 6.11 and 6.12 confirms a small amount of SWCNTs are formed under this condition. The Raman RBM spectra in Figure 6.11 and 6.12 are normalized to the G peak intensity. Despite the 37.5 sccm ferrocene cases having very low G peak intensity (as indicated by the G/D ratios in Figure 6.10), the ratio of the RBM to G peaks is relatively consistent with the other samples, indicating that in all cases that SWCNTs comprise roughly the same fraction of the total graphitic carbon. Thus, the fractal-like tufts of carbon are likely amorphous or highly disordered. All samples show a strong set of peaks in the 200–250 cm^{-1} range (~0.93–1.17 nm diameter) while only the 75 and 150 sccm ferrocene cases show RBM peaks in the 125–175 cm^{-1} range, indicating larger CNTs with diameter ~1.35–1.98 nm. At each injector position, the intensity of these peaks is highest for the 150 sccm ferrocene case, indicating an upward shift in the diameter distribution of the CNTs as would be expected for a larger catalyst particle size distribution. It is possible that the catalyst particle size distribution in the 37.5 sccm ferrocene cases, even with the long injector length, are mostly below ~1 nm and too small for CNT nucleation, instead forming the observed short defective carbon structures. Figure 6.12 shows the same Raman RBM spectra overlaid by ferrocene flow rate in order to visualize the effect of the injector length and position within each group. While it is expected that the mean catalyst particle size will increase with injector length, due to increased aggregation, the effect of this on the CNT diameter distribution, as indicated by Raman RBM intensities, is insignificant. This effect should be most pronounced in the 150 sccm ferrocene cases as the particle aggregation rate in the injector scales with the square of concentration. Indeed, the small spread of RBM intensity in the 125–175 cm^{-1} range does indicate a slight shift to larger diameter at longer injector lengths.

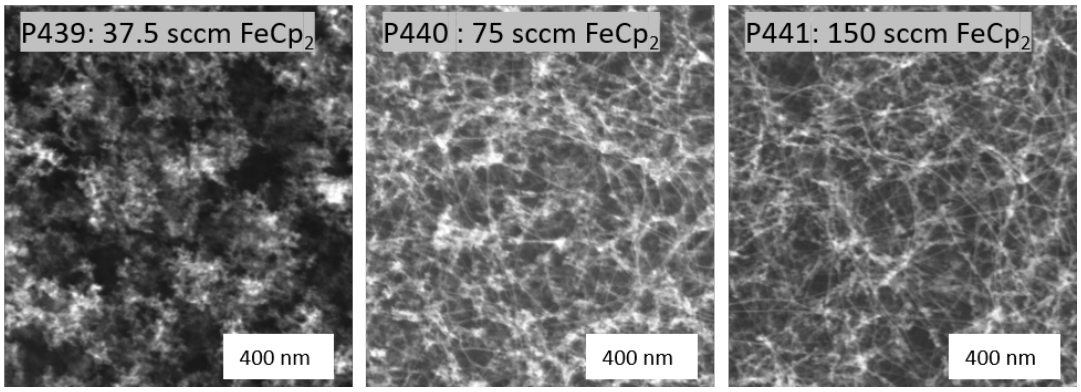

Figure 6.10: SEM images of deposits made at -80 mm injector position and three levels of ferrocene concentration.

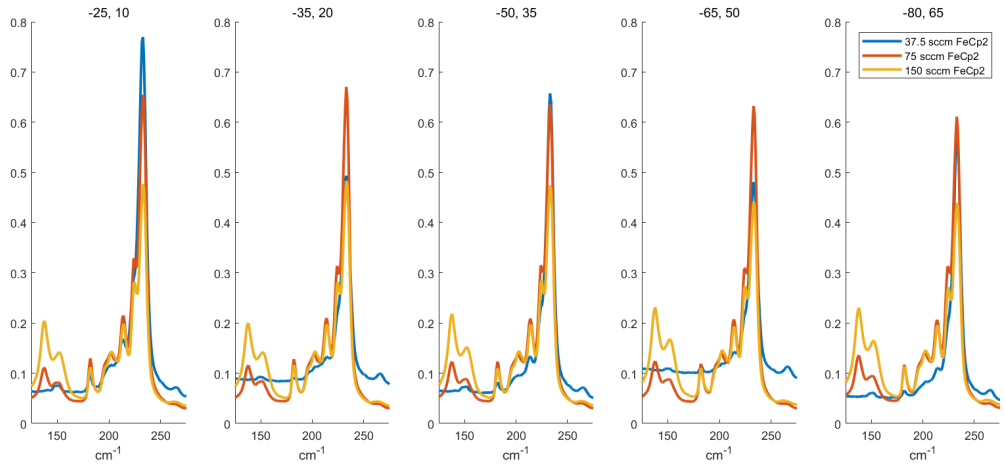

Figure 6.11: RBM portion of the Raman spectra of the three ferrocene flow rate cases overlaid at each injector position. Each spectra has been normalized to its respective G peak intensity. While all show a strong set of peaks in the 200–250 cm^{-1} range (~0.93–1.17 nm diameter), only the 75 and 150 sccm ferrocene cases show RBM peaks in the 125–175 cm^{-1} range, indicating larger CNTs with diameter ~1.35–1.98 nm. The intensity of these peaks is highest for the 150 sccm ferrocene case, indicating an upward shift in the diameter distribution of the CNTs as would be expected for a larger catalyst particle size distribution.

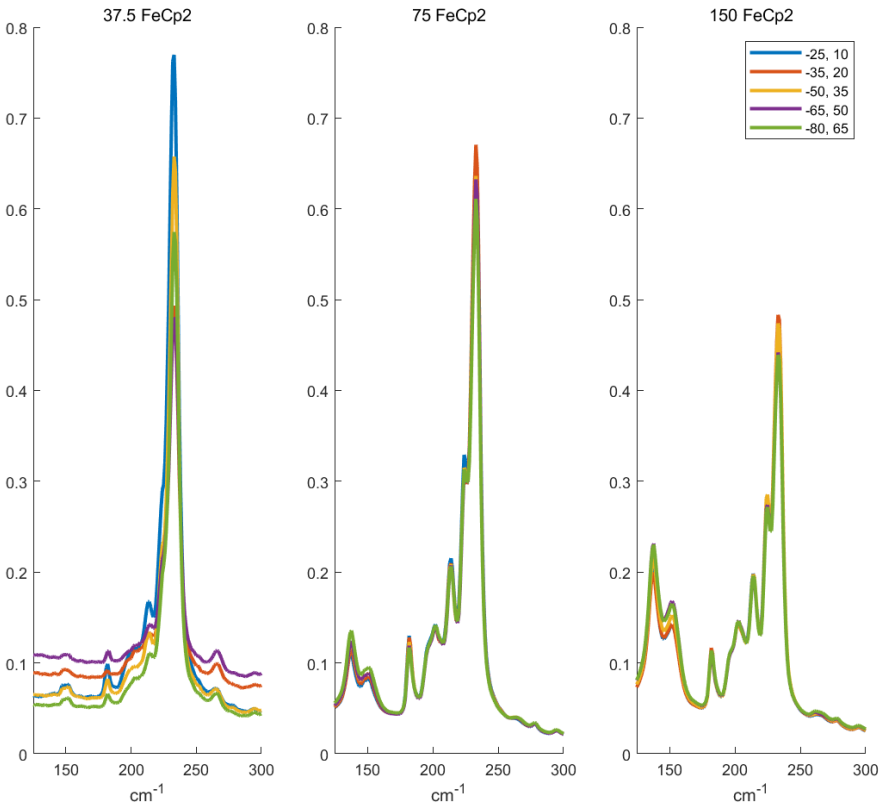

Figure 6.12: RBM portion of the Raman spectra of the five injector position cases overlaid for each ferrocene flow rate. Each spectra has been normalized to its respective G peak intensity. While it is expected that the mean catalyst particle size will increase with injector length, due to increased aggregation, the effect of this on the CNT diameter distribution, as indicated by Raman RBM intensities, is insignificant.

6.3.2 Flow rates and fields

Chapter 5 contains a pair of studies which use CFD modeling to understand the influence of gas flow rates and composition on aerosol formation within the microplasma housing and the transfer tube. In the context of (here), two conclusions are recalled. First, when a gas jet enters a low velocity coaxial stream within a circular channel, the relative density and velocity of the two streams will determine the flow field. If the velocity or density of the outer gas stream is too small relative to the gas jet, a toroidal eddy will form within the channel. This results in a skewed residence time distribution as some of the gas is trapped and recirculated in the eddy. Second, the low diffusivity of nanoparticles relative to gas molecules limits their mixing between the two streams. In the case of the microplasma jet and the transfer tube or injector, the aerosol jet will remain cohesive and concentrated even as the carrier gas diffuses into the surrounding gas. With this in mind, a series of CFD simulations and experiments were conducted to understand the flow field in the FC-CVD system inlet and the role of flow fields on CNT synthesis.

Flow within the injector

The analysis in Chapter 5, specifically Figure 5.9 show the potential for eddy formation within the injector. Both cases considered used an injector length of 100 mm, a total plasma flow of 900 sccm, and an injector flow of 2600 sccm. it was found that the use of a more dense injector flow, argon instead of helium, was about to suppress eddy formation. intuitively, increasing the flow rate of the injector gas will have the same effect. Alternatively, shortening the injector can reduce the required flow to prevent the formation of an eddy *within* the injector by simply ending the injector before the flow field has developed sufficiently.

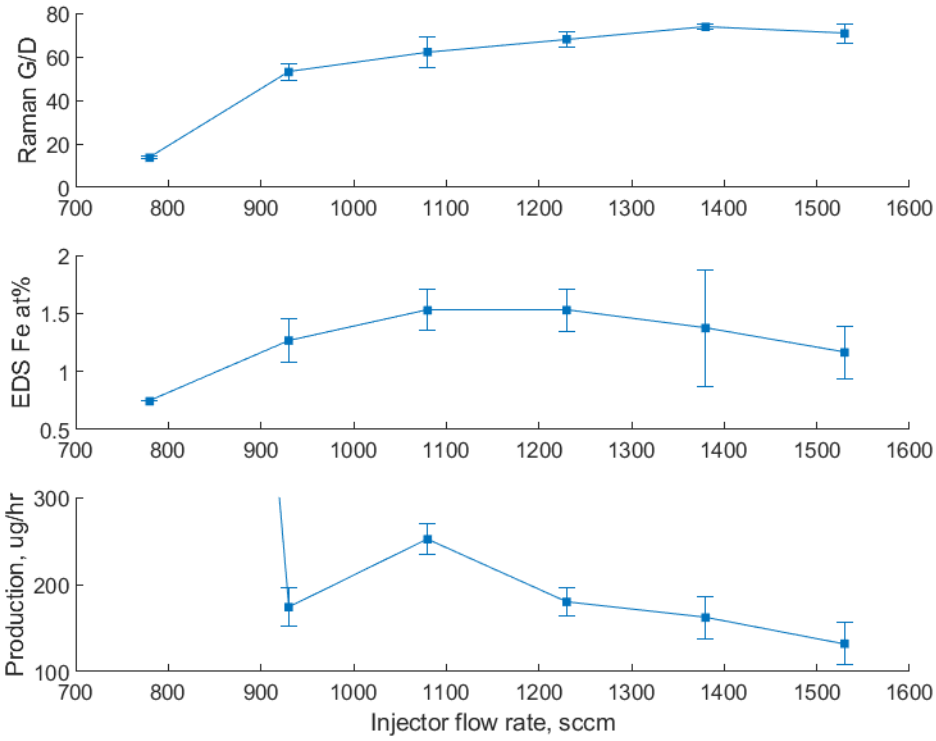

Figure 6.13: Characterization of Samples P369–373 and P375 showing the influence of injector flow rate of CNT production. Not shown, the 780 sccm case has a production rate of 2000 μg/hr.

However, if an eddy is formed it will necessarily be near the tip of the injector, and thus may allow the back-flow and recirculation of furnace gases within the injector. As Figure 5.9 shows, the flow of the aerosol jet in the center of the injector is not affected by the presence of an eddy within the injector, thus it is not apparent what, if any, effect an eddy at the injector tip may cause. The effect of injector flow rate with a short, 10 mm injector length was investigated to determine what flow structures develop and if any effect on CNT growth is ascertainable. Figure 6.13 shows characterization of Samples P369–373 and P375, conducted with a total plasma flow of 900 sccm and injector flow of 780–1530 sccm. The injector flow is 25% nitrogen and 75% hydrogen. The production rate for the 780 sccm case is 2000 μg/hr, out of scale for the plot. Strong trends in Raman G/D ratio and production rate, with small variations of Fe at% clearly indicate an increase in non-CNT solid carbon production at low injector flow rates. This trend is corroborated by the decreasing Fe at% from 1080 to 780 sccm. If these effects were attributable to a change in particle size distribution due to changing injector residence time, they would be expected to be more monotonic, rather than sharply changing at 930 and 780 sccm.

Instead, it is hypothesized that the increase in solid carbon formation is due to thermal decomposition of ethylene that is slowed down or trapped by the flow field near the injector tip. Figure 6.14 shows simulated velocity and ethylene molar concentration maps for the microplasma housing, injector, and furnace inlet corresponding to the conditions for Samples P369–373 and P375. Stagnant flow being to develop just inside the injector tip at 1080 sccm, with negative flow occurring at 930 sccm and even moreso at 780 sccm. Plots of ethylene molar concentration (equal to 0.017 in the incoming furnace flow) show the back diffusion of ethylene into the injector, exacerbated by the low or negative flow velocity at lower injector flow rates.

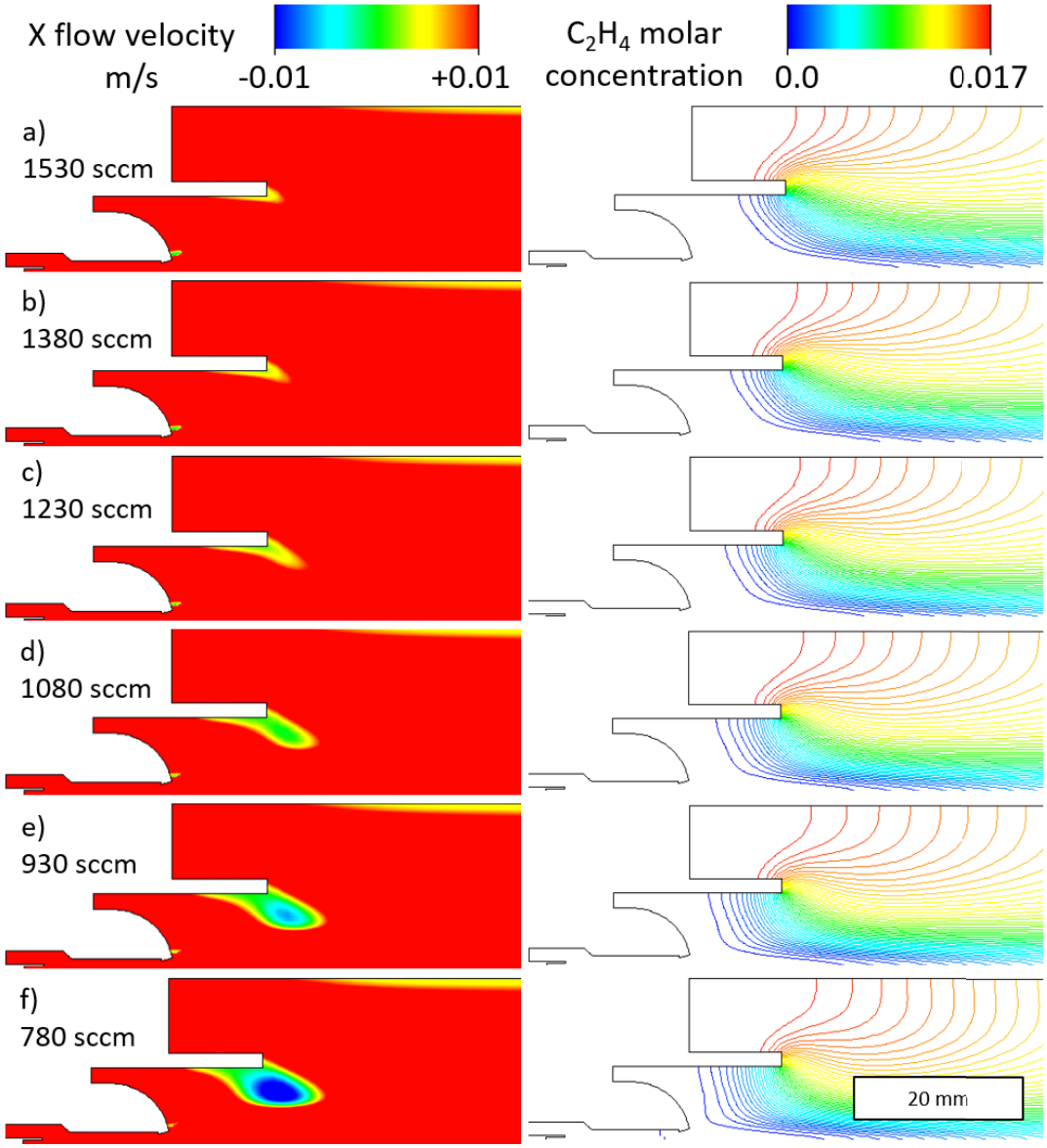

Figure 6.14: CFD simulations of the microplasma housing, injector, and furnace entry for injector flows of 780–1530 sccm, corresponding to Samples P369–373 and P375. X flow velocity is left to right, with negative value indicating back flow. Stagnant flow being to develop just inside the injector tip at 1080 sccm, with negative flow occurring at 930 sccm and even moreso at 780 sccm. Plots of ethylene molar concentration (equal to 0.017 in the incoming furnace flow) show the back diffusion of ethylene into the injector, exacerbated by the low or negative flow velocity at lower injector flow rates.

Zero-length injector

Having identified the formation of an eddy within the injector, and the back flow of ethylene within it, as the source of non-CNT carbon under those conditions, there appears to be a direct relationship between the injector flow rate and the product quality. To get around this limitation, the flow geometry must be changed such that eddy formation is discouraged regardless of the flow velocities. One way to do this is by taking the injector length trend to the extreme: an injector with zero length, i.e., placing the tip of the microplasma housing flush with the injector tip, will have no room for eddy formation within the injector.

In order to assess the viability of this approach, a relatively shallow injector position of -25 mm was selected, and a sweep of injector flow rates was explored for injector lengths of 0, 10, and 20 mm. It was previously determined that the microplasma reactor will operate normally at an absolute position of -25 mm, thus the microplasma operation at all three positions should be uniform, with any variability due to the flow fields.

Figure 6.15 shows characterization of product synthesized over a range of injector flow rate for injector length of 0, 10, and 20 mm. The results for 10 and 20 mm injector length are remarkable similar and exhibit the same trend with injector flow rate as observed in Figure 6.13. However, all flow rate cases with the 0 mm injector show poor or no CNT synthesis. At high injector flow rates, where the 10 and 20 mm cases produced CNTs, the production rate and Raman G/D indicate no CNT growth. At the lowest injector flow, 780 sccm, the higher production rate indicates increased non-CNT carbon production.

CFD simulations of the 0 mm injector length cases shown in Figure 6.16 confirm that the change in geometry prevents the formation of major eddies within the injector. Indeed, the flow field appears uniformly positive even at the lowest injector flow rate of

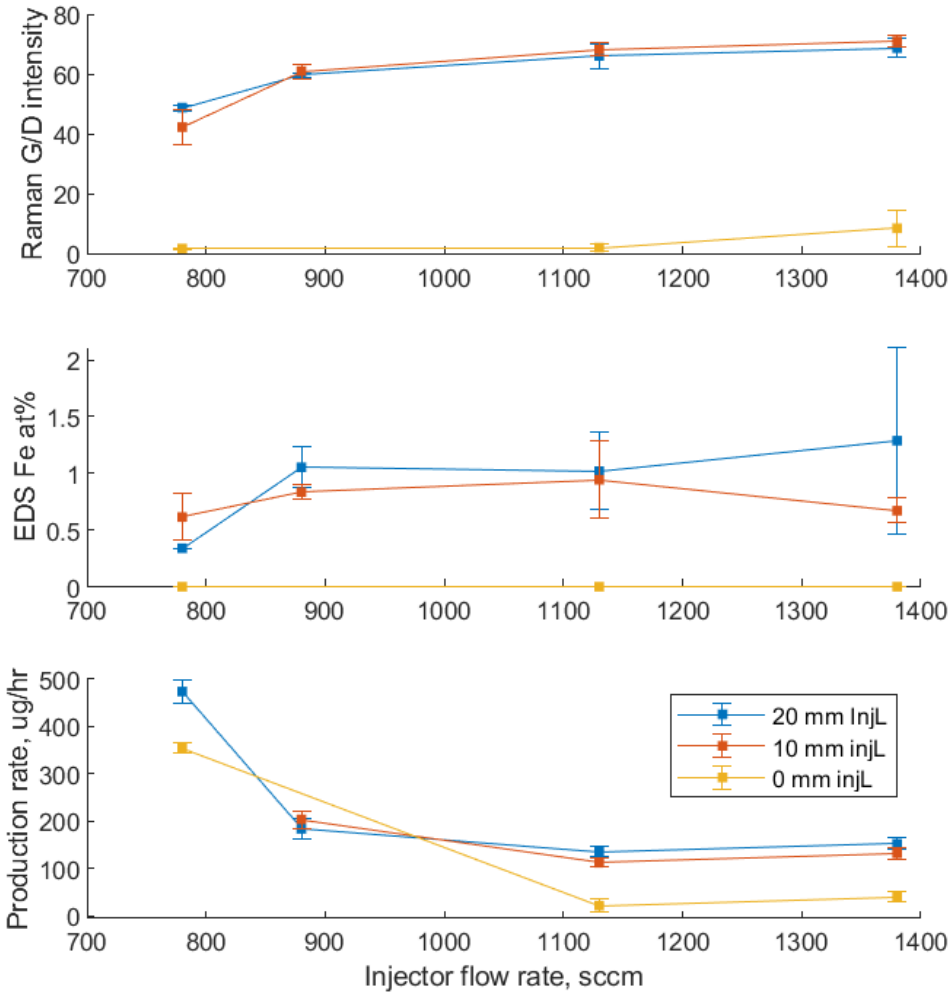

Figure 6.15: Characterization of Samples P399-410, parameter sweeps of injector flow rate at injector length of 0, 10, and 20 mm.

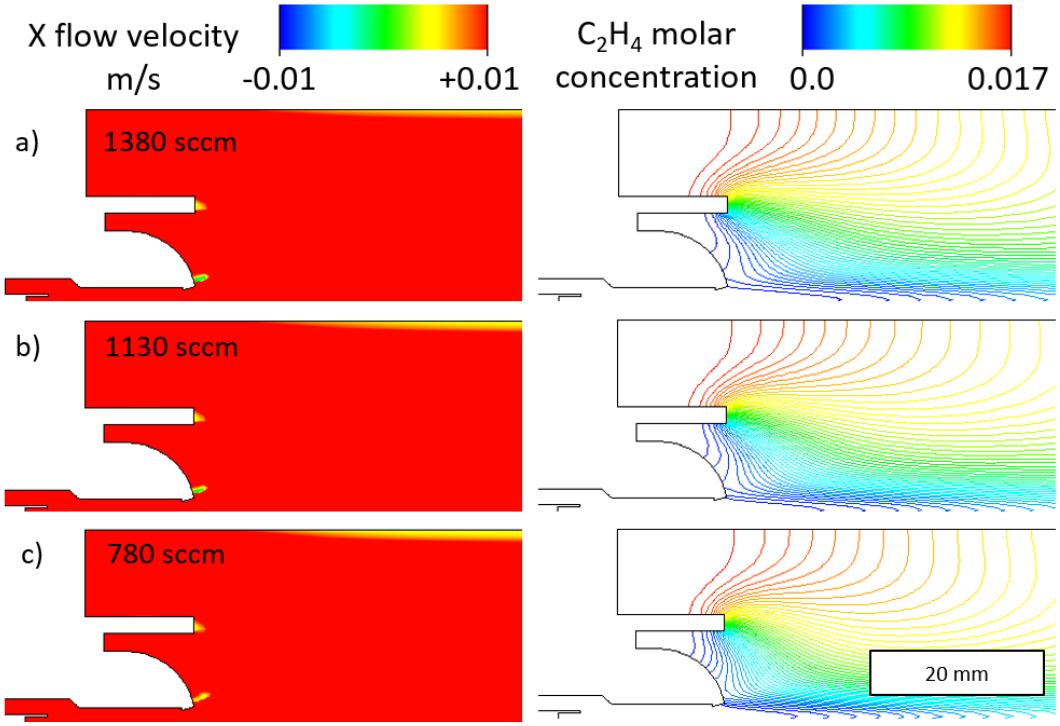

Figure 6.16: CFD simulations of the microplasma housing, injector, and furnace entry for injector flows of 780–1530 sccm, corresponding to Samples P369–373 and P375. X flow velocity is left to right, with negative value indicating back flow. Stagnant flow being to develop just inside the injector tip at 1080 sccm, with negative flow occurring at 930 sccm and even moreso at 780 sccm. Plots of ethylene molar concentration (equal to 0.017 in the incoming furnace flow) show the back diffusion of ethylene into the injector, exacerbated by the low or negative flow velocity at lower injector flow rates.

780 sccm. Thus, it appears that the high non-CNT carbon production at 780 sccm can not be attributed to ethylene decomposition in regions of slow or reversed flow.

Across all injector flow rates, the main distinction between the 0mm and 10 mm injector length cases can be seen in the ethylene concentration fields. At 0 mm injector length, the back diffusion of ethylene is sufficient to reach the microplasma housing. While the quartz housing itself is not reactive surface, the immediate availability of carbon to particles upon emerging from the microplasma housing may be the controlling factor. At 1130 and 1380 sccm the sample characterization is similar to that observed with low ferrocene input and a long injector in Section 6.3.1.

In both cases the catalyst particles are relatively small, either due to a short growth period in the 0 mm injector length case or due to a low aggregation rate in the low ferrocene concentration case, when they begin to mix with ethylene. These small particles or atomic clusters may still be catalytically active with respect to decomposing ethylene, but not of the right size to template CNT growth, resulting in the small production rate of disordered carbon observed. This mechanism does not fully explain the distinct result of the 780 sccm case, and a more detailed experimental study is warranted to better understand the abrupt onset of this non-CNT carbon production at low injector flow rate.

Furnace flow field

The same influence of eddy formation and its effect on the residence time distribution was investigated for the furnace tube. Analogous to the formation of an eddy within the injector if the injector flow is insufficient compared to the plasma flow, an eddy will form in the furnace tube if the furnace flow is insufficient compared to the total injector flow. The relationship between this eddy formation and the CNT product was investigated by setting a high injector flow rate, 2028 sccm, to ensure optimal flow out of the injector,

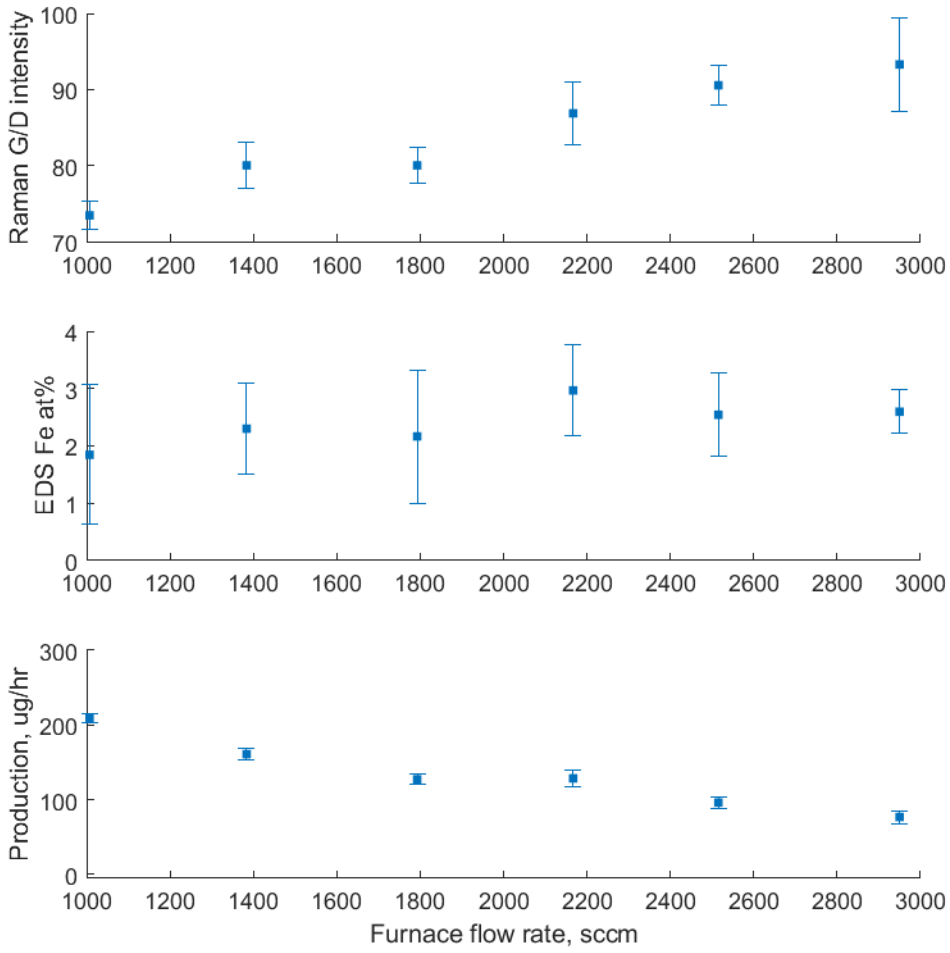

Figure 6.17: Characterization of Samples P414-419 showing the influence of furnace flow rate on CNT growth. A high injector flow, 2028 sccm, was used to ensure an optimal fow field at the injector outlet.

and then varying the furnace flow over 1007-2950 sccm. In all cases the flow rate of ethylene (in the furnace flow) was fixed at 50 sccm, and the bulk of the flow a 61:39 mix of argon and hydrogen. The total flow ranged from 3935 sccm for the 1007 sccm furnace flow case to 5878 sccm for the 2950 sccm furnace flow case.

Figure 6.17 shows a trend of decreasing Raman G/D ratio and increasing production rate with reduced furnace flow. These trends are attributed to the flow field in the furnace which transitions from uniformly positive at 2950 sccm furnace flow (Figure 6.17(a)) to having a large eddy at 1007 sccm furnace flow (Figure 6.17(c)). The gradual onset of the eddy and the continual nature of the CNT characterization trends indicate that the Raman G/D and production rate are influenced by the changing residence time distribution in general. In other words, the change in performance is due to a portion of the furnace flow remaining in the furnace for a significantly longer residence time than average, not whether that gas at some point had a negative x velocity. This increased residence time may allow for increased thermal decomposition of ethylene, producing non-CNT carbon which both increases the production rate and reduced the Raman G/D ratio by increasing the D peak intensity. The small change in the average residence time due to the change in total flow rate may also effect CNT growth. The characteristic velocity of the 1007 sccm furnace flow case (total flow of 3935 sccm) at 1000 °C is 0.3 m/s, while that of the 2950 sccm furnace flow case (total flow of 5878 sccm) is 0.43 m/s. For a heated length of 60 cm, this indicates a characteristic residence time of 2.0 to 1.4 s, and the increase in production rate at lower flow rate may also be a result of a longer time for CNT growth. Assuming this is proportional, it only accounts for ~60% of the increase in production rate.

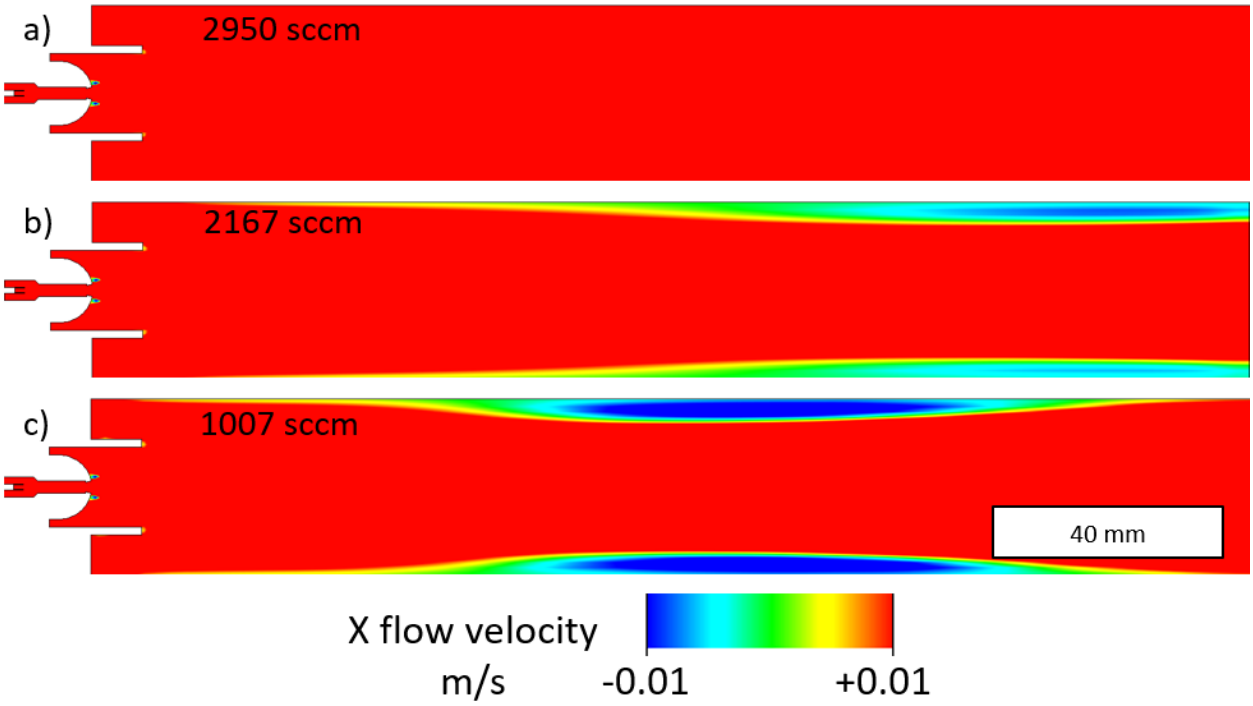

Figure 6.18: CFD simulations of the microplasma housing, injector, and furnace entry for furnace flows of 1007–29500 sccm. X flow velocity is left to right, with negative value indicating back flow.

Plasma flow rate

Having now understood the importance of matching the magnitude of the difference gas flows in order to control the flow field, the question of the plasma flow rate is investigated. A series of growth recipes (Cases 126–132 in Table 6.4.1) were developed based off of the high furnace flow recipe in Section 6.3.2 where no eddies are present in the injector or furnace. The total plasma flow (inner flow and sheath flow) was increased and then CFD was used to increase the injector and furnace flows until the no-eddy condition was re-established. In these experiments, the total plasma flow ranges from the typical 900 sccm up to 1800 sccm. The total flow ranges from 5125 to 7550 sccm, While the reduced furnace residence time at the higher flow rate conditions is expected to effect CNT growth, it is expected that the dominant impact results from changes to the catalyst size distribution due to changes in the plasma and injector residence time.

To qualitatively understand the effect of these flow rates on the catalyst size distribution, direct aerosol measurements were made using the SMPS and associated methodology described in Chapter 5. Because of limitations in the SMPS measurement system, an injector length of 70 mm is used, along with lower ferrocene flow rates of 15 and 30 sccm. Figure 6.19 shows the mean particle size and concentration for these experiments. When normalized to the total injector flow rate, the influence of plasma flow rate and ferrocene concentration collapse roughly onto the same curve, highlighting a trade-off between decreasing concentration while decreasing particle size. However, when considering the actual ferrocene concentration (ferrocene flow rate divided by the total plasma flow rate), it appears that increasing the total flow rate at a field ferrocene concentration can shift the curve to the left, maintaining concentration while reducing particle size. For example, the ferrocene concentration is the same for the case with 900 sccm total plasma and 15 sccm ferrocene and the case with 1800 sccm total plasma and 30

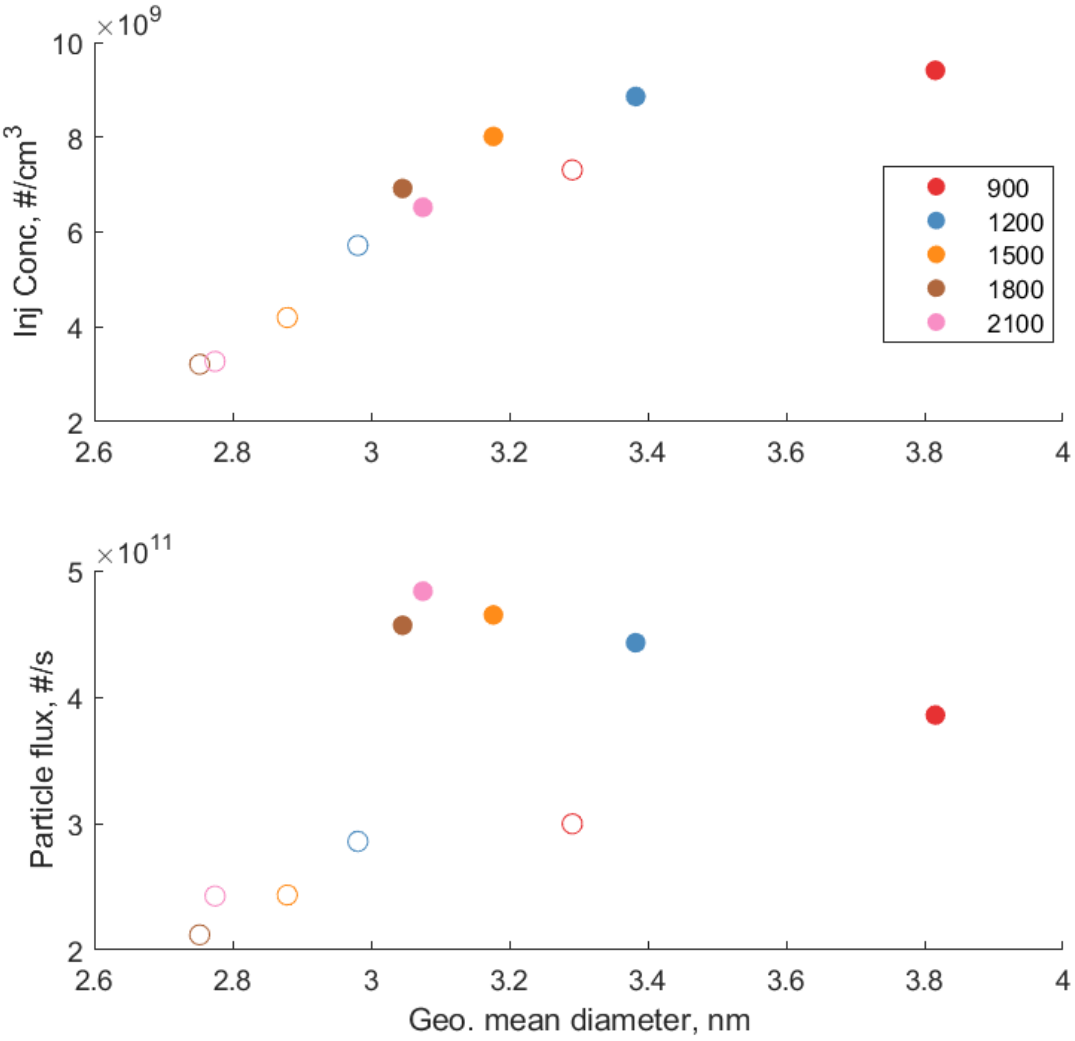

Figure 6.19: Direct aerosol mean diameter and concentration measurements for conditions analogous to the high plasma flow rate experiments.

sccm ferrocene (open red point and filled brown point, respectively, in Figure 6.19(a)). Both cases have a concentration of ~7×10^9 #/cm^3, yet the high flow case has mean diameter of 3.05 nm, compared to 3.29 nm for the low flow case. Given the ~1 nm diameter of CNTs produced in this system, it is likely that the smaller particles have greater CNT nucleation efficiency. When comparing the total particle production in Figure 6.19(b), two distinct trends are seem for the 15 and 30 sccm ferrocene cases. At 30 sccm ferrocene, the total particle flux at the end of the injector gradually increases with increasing plasma flow rate, as would be expected due to the reduced residence for aggregation. However, at 15 sccm ferrocene, the total particle flux decreases (along with particle diameter) with increasing plasma flow rate. A similar divergence of trends at high and low ferrocene concentrations was noted in Section 5.3.3 when the injector (transfer tube) length was changed. Both the total flow rate in this case, and the injector length in the previous case, control the residence time. See Section 5.3.3 for a discussion of potential mechanisms.

For CNT synthesis experiments at these plasma flow rates, a more typical 10 mm injector length is used. A baseline ferrocene flow rate of 150 sccm is used, as was done for some previous experiments with 900 sccm total plasma flow. At higher total plasma flow rates, one experiment was done at 150 sccm to maintain a constant ferrocene flux (but decreasing concentration in the plasma) and a second with proportionally higher ferrocene flow rate to maintain the concentration in the plasma. Figure 6.20 shows the characterization for these samples. Notably, the Raman G/D ratio is nearly constant across all conditions, ranging from 79 to 83. This uniformity further supports the conclusion in previous sections that the production of non-CNT carbon in eddies or stagnant flow regions is the primary factor effecting the Raman G/D ratio. This conclusion also implies that the source of the D band intensity is not defects within CNTs but carbon outside of them. The Fe at% is also relatively constant across flow

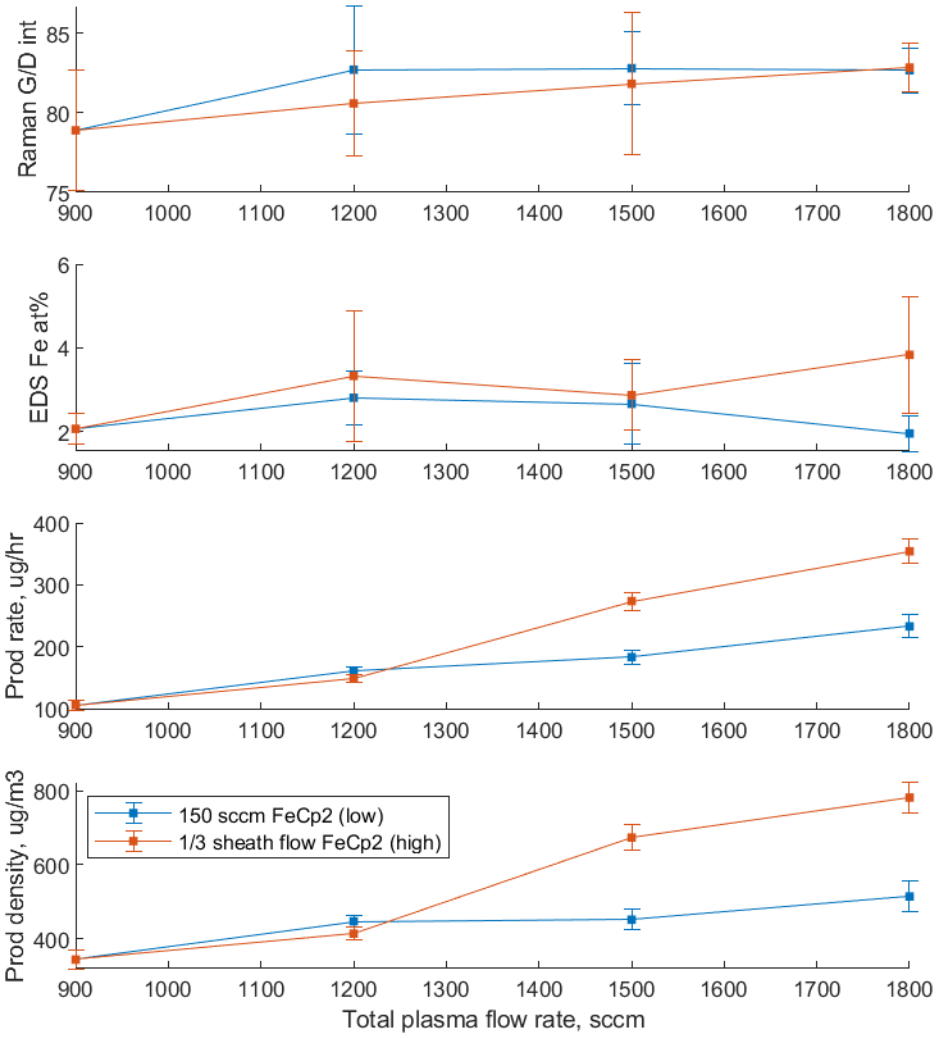

Figure 6.20: Characterization of Samples P420–426 showing growth results for the high plasma flow recipes. Injector and furnace flow rates increase in concert with the plasma flow rate to qualitatively maintain the flow field.

rates.

The production rate trend aligns with expectations based on the catalyst aerosol measurements, showing it is roughly proportional to the production of catalyst particles. The production rate doubles from 105 μg/hr in the 900 sccm total plasma flow case to 233 μg/hr at 1800 sccm total plasma flow with the same 150 sccm of ferrocene. The production rate more than triples to 354 μg/hr when the ferrocene flow is increased to maintain concentration. These gains remain when considering the product density, the production rate normalized to the total plasma flow rate: from 343 μg/m^3 to 514 and 781 μg/m^3, respectively.

Finally, Figure 6.21 shows the Raman spectra in the RBM window for each case, normalized by their respective G peak intensity. When the total plasma flow rate is increased with a constant 150 sccm ferrocene flow rate (Figure 6.21(a)) the intensity of large-diameter RBM peaks in the 125–175 cm^{-1} range decreases while the intensity of small diameter peaks in the 200–250 cm^{-1} range increased. This indicates a shift to smaller diameter CNTs. When the ferrocene flow rate is increased proportionally (150, 200, 250, 300 sccm for 900, 1200, 1500, 1800 sccm total plasma flows) there is some variation but no similar trend in the latter case. Both of these trends in CNT diameter mirror those seen for the mean particle diameter for the directly measured particles in the analogous experiment in Figure 6.19.

6.3.3 Moisture

The presence of oxygen or moisture in the CVD atmosphere has been shown to strongly effect CNT nucleation and growth [16, 17, 18]. First, substrate-based growth has shown that the oxidation state of the iron catalyst is important for CNT nucleation, with an important part of the substrate preparation being the reduction of the iron oxide thin

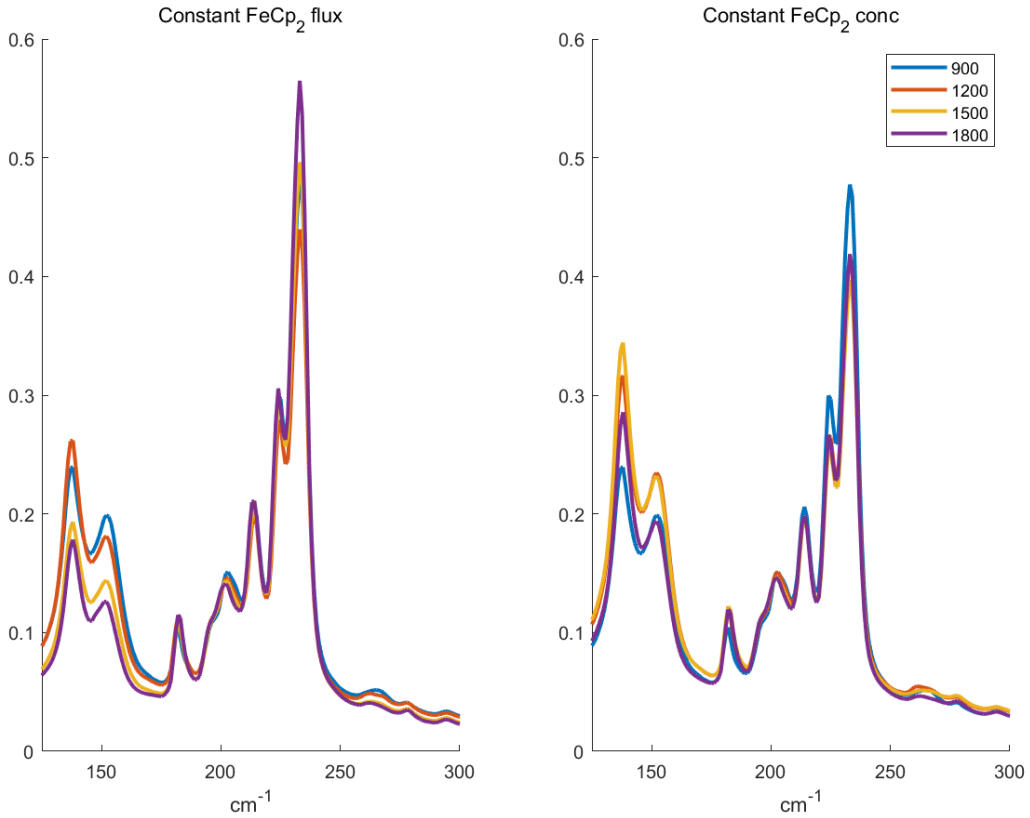

Figure 6.21: RBM portion of the Raman spectra for different total plasma flow rates. The left plot shows those with constant 150 sccm ferrocene flow rate. The right plot shows those with proportionally increasing ferrocene flow rate (150, 200, 250, 300 sccm for 900, 1200, 1500, 1800 sccm total plasma flows). In the former case, increasing the total plasma flow reduces the intensity of large-diameter RBM peaks in the 125–175 cm^{-1} range, while increasing the intensity of small diameter peaks in the 200–250 cm^{-1} range. There is some variation but no similar trend in the latter case.

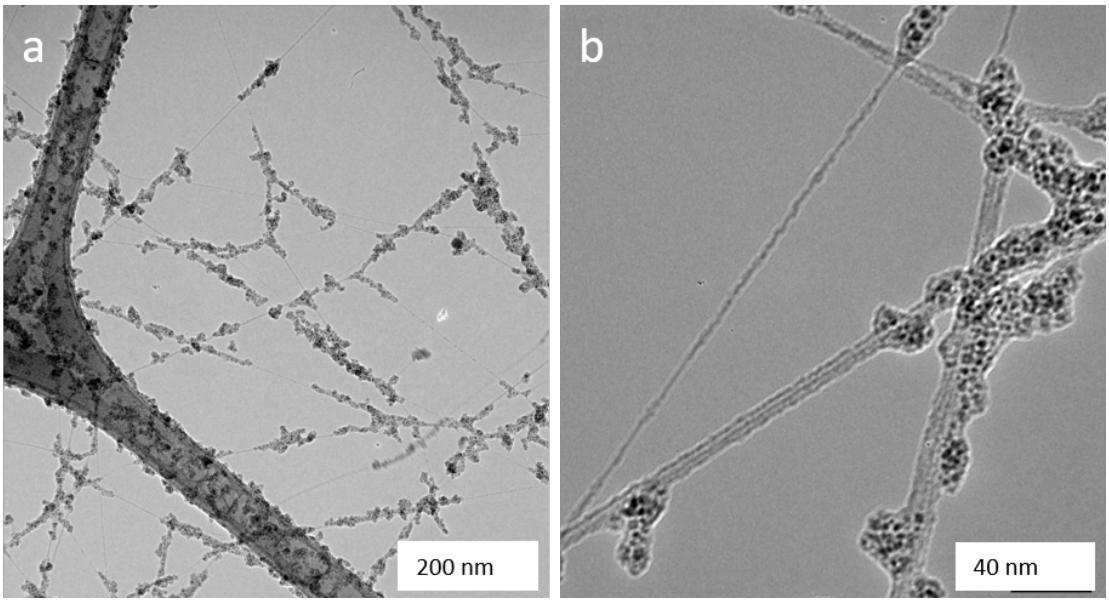

Figure 6.22: TEM images of sample P43 from March 2022 indicating small diameter SWCNTs as well as significant amorphous carbon and carbon-coated iron particles.

film during dewetting [16]. Thus, low moisture levels lead to increased CNT yields by contributing to a reducing environment. Second, higher levels of moisture, 100-500 ppmv, have been shown to be beneficial during substrate-based CNT growth due to the selective etching of amorphous carbon. This can increase the purity of the final product, and can prolong catalyst lifetime by preventing the formation of a carbon cap on the catalyst particle [19, 18, 16]. Unfortunately, relatively few studies of FC-CVD growth report moisture levels or investigate the influence of moisture directly. However, there have been numerous studies of oxygen-containing carbon precursors, primarily ethanol, which are reported to result in clean CNTs with little amorphous carbon due to the same oxygen etching mechanism [20, 21, 22].

Initial furnace moisture study

TEM analysis of samples circa March 2022 (P43) show significant number of iron particles which did not nucleate CNTs and instead are over coated in amorphous carbon

(Figure 6.22). Thus, it was hypothesized that increasing the moisture in the furnace might prevent the accumulation of this carbon and allow for a greater nucleation efficiency. A study was conducted to add moisture to the system via the furnace flow, thus also maintaining a reducing environment in the plasma and injector tube. Figure 6.23 shows Raman characterization for a set of 14 growths, P117-P130, at increasing moisture levels. The same gas recipe as for the early injector position experiment (Section 6.3.1) was used, with an injector position of -50 mm and furnace set point of 900 °C. The G/D ratio suggests that the optimal growth conditions are below ~200 ppmv. There is sufficient variability that it is not possible to discern if the addition of moisture below 200 ppmv results in any significant improvement. At higher moisture levels, the relatively constant D peak intensity suggests that the amount of amorphous carbon is relatively constant and unaffected by the etching mechanism that was predicted. Potentially, the short residence time of the FC-CVD reactor (~1–10 s) relative to substrate-based growth (~1–10 min) does not allow sufficient time for the reaction to progress.

Yet, the reduced G and RBM peak intensities indicate an adverse effect of increasing moisture on CNT growth. At minimum, these results indicate that the system's performance should be robust to small changes in the internal moisture level that result from variable humidity in the lab, which has been shown to significantly influence substrate-based growth in some cases [17].

Moisture study in all flows

An alternative explanation for the weak effect of furnace moisture is that carbon etching will only increase the CNT nucleation efficiency if it occurs within the CNT nucleation window. Further, that the etching effect of moisture is most effective if it is active at the time of carbon deposition when the carbon atom may be less well bonded to the particle, rather than once larger deposits have formed and potentially graphitized. It

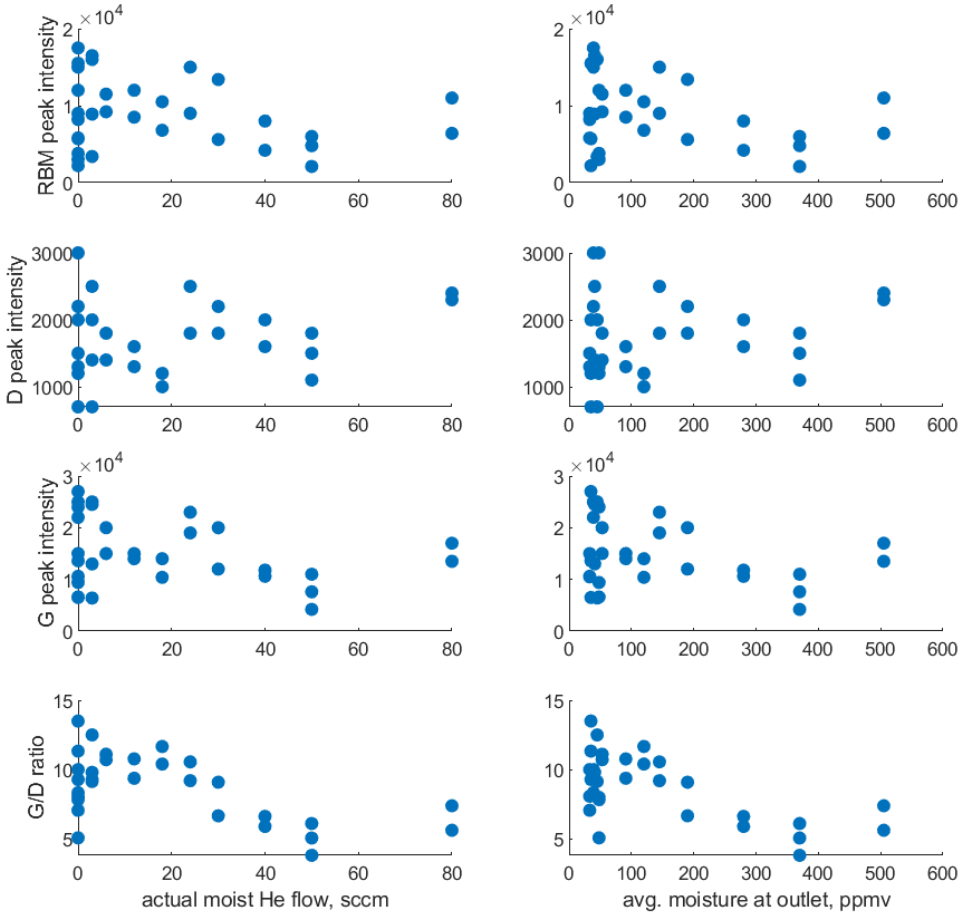

Figure 6.23: Characterization of samples P117-P130 showing the influence of moisture added to the furnace flow. Moisture is added by bubbling helium through water at 20 °C. In the left column the abscissa is the flow rate of moist helium in sccm. The right column abscissa is the measure moisture level at the system outlet.

is also possible that the source of the carbon on these inactive catalyst particles is not ethylene form the furnace flow, but carbon released from ferrocene in the microplasma reactor. Taking these factors into account, it stands to reason that the activity of the moisture may be higher if it is added early in the lifecycle of the catalyst particle. Thus, a second moisture study was conducted in June 2023 (P355-368 and P376-398) to explore the addition of moisture to all four gas flows. Full details of the growth conditions for these experiments can be found in Table 6.4.1. Figure 6.24 shows Raman G/D ratio, Fe at%, and production rate as a function of wet helium flow rate into the inner, sheath, injector, and furnace flows.

Once again, and borne out with additional characterization, the performance of the system is remarkably stable to changes in moisture level. For moisture additions below 200 ppmv there appears to be a small increase in G/D ratio when added to the injector and inner plasma flows, with no significant influence when added to the sheath or furnace flows. However, low amounts of moisture addition via the sheath flow do appear to increase the production rate, yet still within the range of baseline variability. Mechanistically, it is expected that moisture would have the greatest effect when added to the inner flow. The highest inner flow moisture level does have the lowest production rate and highest Fe at%, both indicating a decrease in CNT growth. This can be visually confirmed via SEM in Figure 6.25. While both cases show bright particles, likely including iron, decorating the CNTs, the baseline case shows a number of clean CNTs while in the high moisture case the CNTs are thoroughly coated.

The highest level of moisture addition in these experiments was limited by the flow rates available, and covers a range well beyond most successful CNT synthesis (when reported, typically less than 100 ppmv). Further, given the lack of clear trends at the higher moisture levels tested here, it appears unlikely that testing even higher moisture addition would yield a practical improvement. Those experiments may still provide

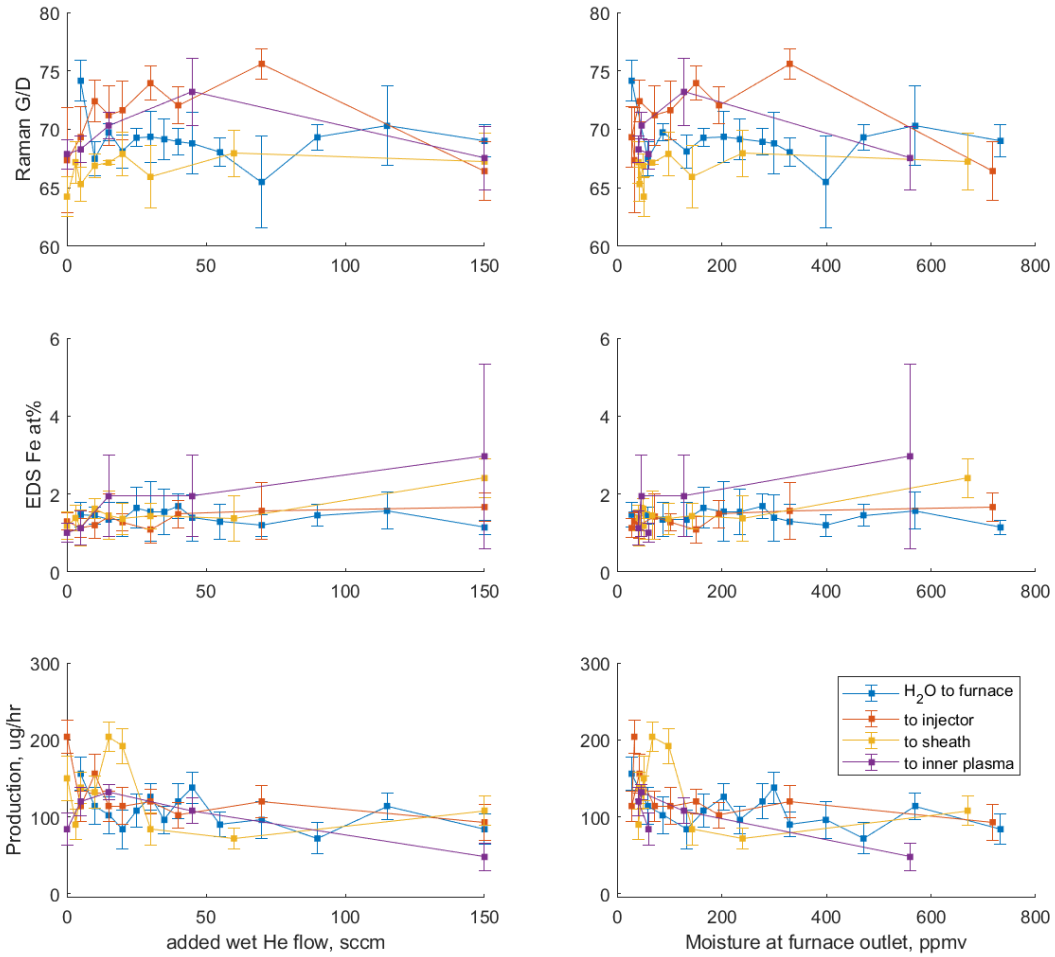

Figure 6.24: Characterization of samples P355-368 and P376-398 showing the influence of moisture added to all four gas flows. Moisture is added by bubbling helium through water at 20 °C. In the left column the abscissa is the flow rate of moist helium in sccm. The right column abscissa is the measure moisture level at the system outlet.

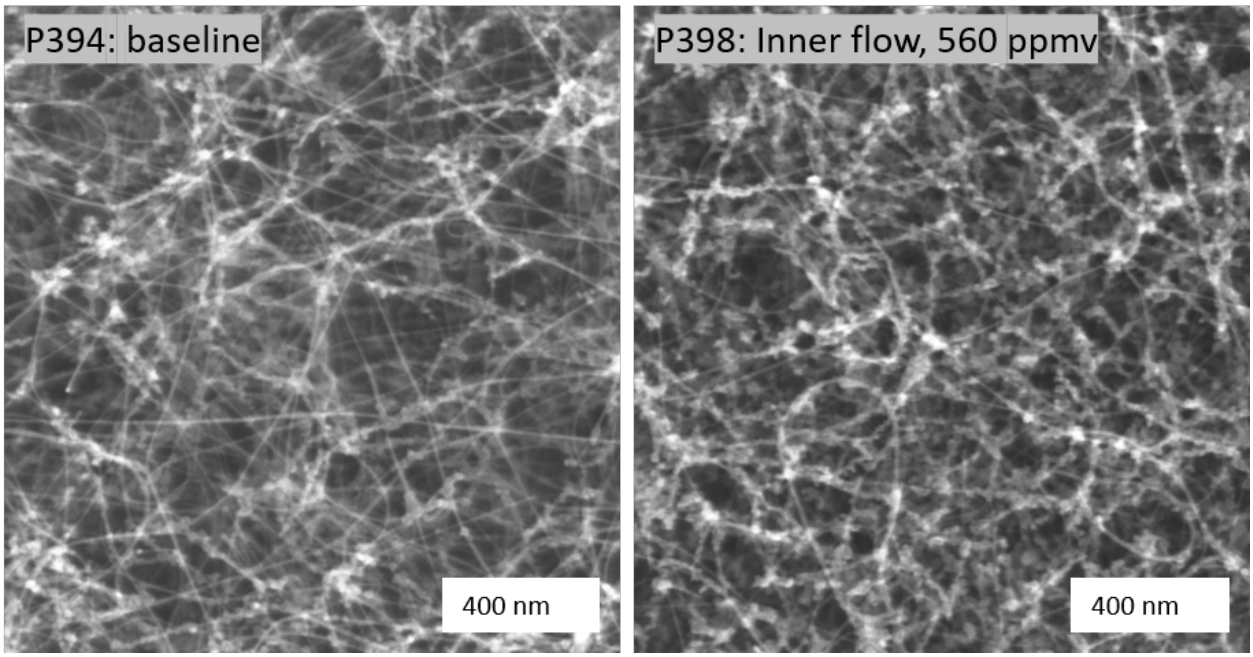

Figure 6.25: SEM images of sample P394, a baseline case with no moisture addition (average moisture level of 60 ppmv), and P398 with 150 sccm wet helium via the inner flow (average moisture level of 560 ppmv). P398 has a 50% lower mass production rate and is visibly more covered in inactive catalyst and non-CNT carbon.

insight into the interaction of moisture and catalyst particles in each part of the FC-CVD system. Rather, the weak influence found during these experiments is taken as evidence that the etching power of moisture in this system is low relative to the conditions driving particle overcoating. Part of this may be due to a weaker etching power in FC-CVD as compared to substrate-based growth due to the shorter residence time. The remainder must be due to conditions which more strongly drive the formation of non-CNT carbon on catalyst particles. Fundamentally, it is this latter point which must be better understood and addressed in order to increase CNT nucleation efficiency and increase yield.

6.3.4 Catalyst Composition

Initial carbon content

Having shown the ability to control the ratio of iron and carbon in the particles produced via the microplasma reactor in Section 5.3.4, here the effect of this composition on CNT synthesis is assessed. Two questions surround the use of these plasma parameters to influence the iron-carbon ratio of the initial particles. First, does the amount of carbon initially present in the particle influence CNT nucleation, or is it irrelevant considering the high availability of carbon once in the CVD furnace Second, if a benefit exists, does that outweigh any potentially negative effects of that plasma parameter on the particle size distribution or total particle concentration? The results in Section 5.3.4 suggest that using the high voltage polarity results in a trade-off between an aerosol with a smaller mean diameter but higher carbon content or an aerosol with larger mean diameter and lower carbon content. Additionally, using hydrogen in the inner or sheath flow presents a trade-off between a higher aerosol concentration but high carbon content or a lower aerosol concentration and lower carbon content.

Based on the results of the particle composition study, five recipes were developed to explore combinations of hydrogen addition in the inner flow, hydrogen addition in the sheath flow, and plasma high voltage polarity. In all cases hydrogen is added to the injector flow. Figure 6.26 shows characterization of CNT samples (P280–284) made at these conditions. These experiments were among the first conducted on the updated FC-CVD system in May 2023 and thus precede many of the process improvements detailed in this Chapter which explains the relatively poor characterization compared to other results presented here – The negative production rate for "No H_2, -HV" and "Inner H_2, +HV" indicate a negative change in mass between the initial and post-growth filters, potentially attributable to a small piece of filter material breaking off during handling,

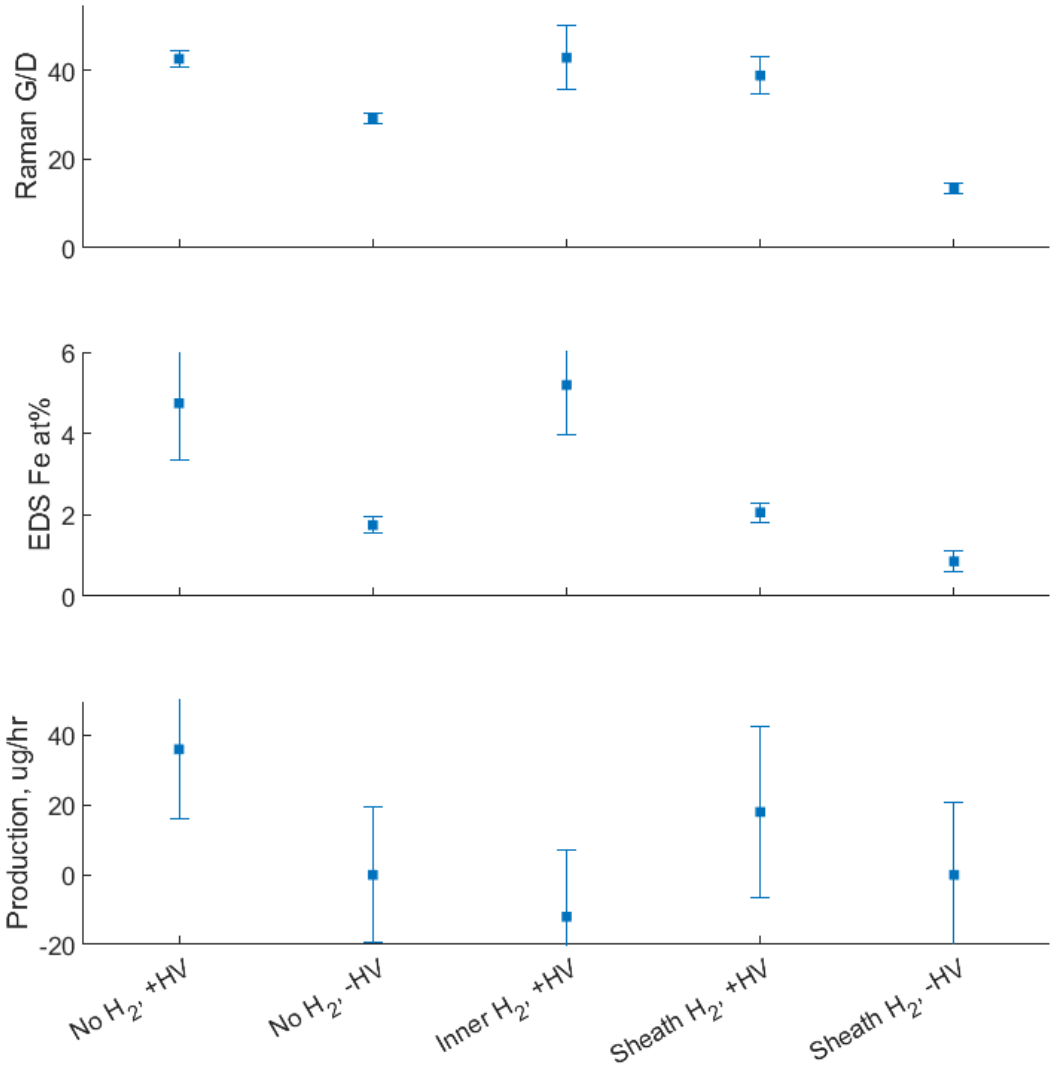

Figure 6.26: Characterization of samples P280-P284 synthesized with varying hydrogen flow to the plasma and high voltage polarity.

but should be interpreted as negligible production rates. Accounting for this, variations in production rate across the five cases are significant, with only the "No H_2, +HV" and "Sheath H_2, +HV" cases showing non-negligible production rates.

In Section 5.3.4 the iron mass fraction of particles in these two cases was found to be 0.47 and 0.56, respectively. The "No H_2, -HV" case was found to have a similar iron mass fraction as the "Sheath H_2, +HV" case at 0.59. The other two cases tested here did not correspond to cases in Section 5.3.4

The fact that two cases with relatively different iron mass fractions (0.59 was the highest, and 0.47 the second-lowest, reported in Section 5.3.4) have the highest production rates, while two cases with relatively similar iron mass fraction have relatively different production rates, indicates that the initial iron-carbon ratio of catalyst particles is not a primary control on CNT growth within this range. It thus appears more likely that the main effect on plasma high voltage polarity and hydrogen addition on CNT growth is through the effect of these parameters on the aerosol size distribution and concentration. Indeed, of these three cases where previous aerosol measurements were taken, their production rates correlate well to changes in the total aerosol concentration. It is also possible that the conditions within the injector contribute to reducing the particle iron content, as the addition of hydrogen to the transfer tube was found to have a slight effect in Section 5.3.4 (and may be stronger due to the elevated temperature). Thus, it may still be true that the carbon content of the catalyst particles is important for CNT nucleation, yet the iron-carbon ratio of particles at this point in the reactor may be somewhat decoupled from the iron-carbon ratio of particles at the microplasma reactor outlet.

6.3.5 Summary of CNT synthesis progress

The insights from these studies were applied throughout the process of designing and constructing the FC-CVD reactor and developing the gas flow rates and other operating conditions, resulting in a steady improvement of system performance over time. Figure 6.27 presents a historical view of all P series experiments, indicating those mentioned in previous sections of this chapter.

In many cases the development process has enabled concurrent improvements in multiple CNT metrics. yet, in some cases, changes to the system or operating condition trade off between metrics, and it is not obvious if these changes are improvements. One way to frame this would be to create a specific objective function to reduce these multiple metrics into a single quantity which can be minimized or maximized. However, given the range of uses for CNTs (and the disparate requirements for those uses), this approach seems limiting. Further, without a broader agreement on an objective function, different research or commercial groups are unable to unambiguously compare the capabilities of production processes. As the performance at only one or a few operating conditions is typically reported for research or commercial systems, it is natural for those reports to select data which reflects well on the process, based on some implicit multi-objective optimization. Alternatively, I propose the use of a Pareto front analysis to communicate the leading edge of the performance window across a wide range of operating conditions and thus CNT outputs. At its core, this highlights the severity of the trade-offs between different metrics.

Figure 6.28 shows the same summary data for all P series experiments arranged on several scatter plots, each comparing two metrics. The boundaries of these point clouds suggests the limits of performance for the historical and current iterations of this work. For example, the point cloud comparing Raman G/D ratio and production density re-

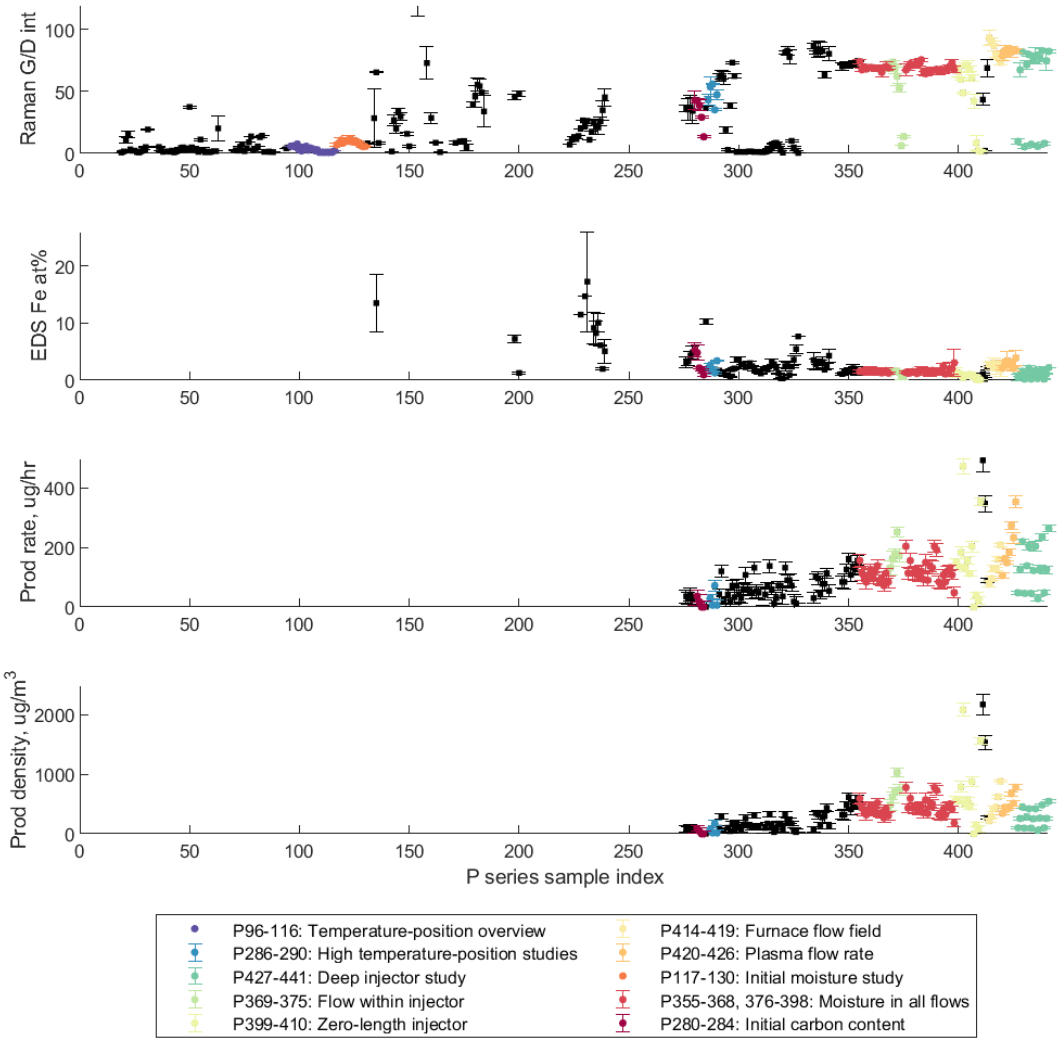

Figure 6.27: Overview of all P series experiments. Those experiments mentioned in earlier sections of Chapter 6 are indicated in color. Missing data points indicates an inability to characterize those samples, e.g., insufficient mass to measure a production rate.

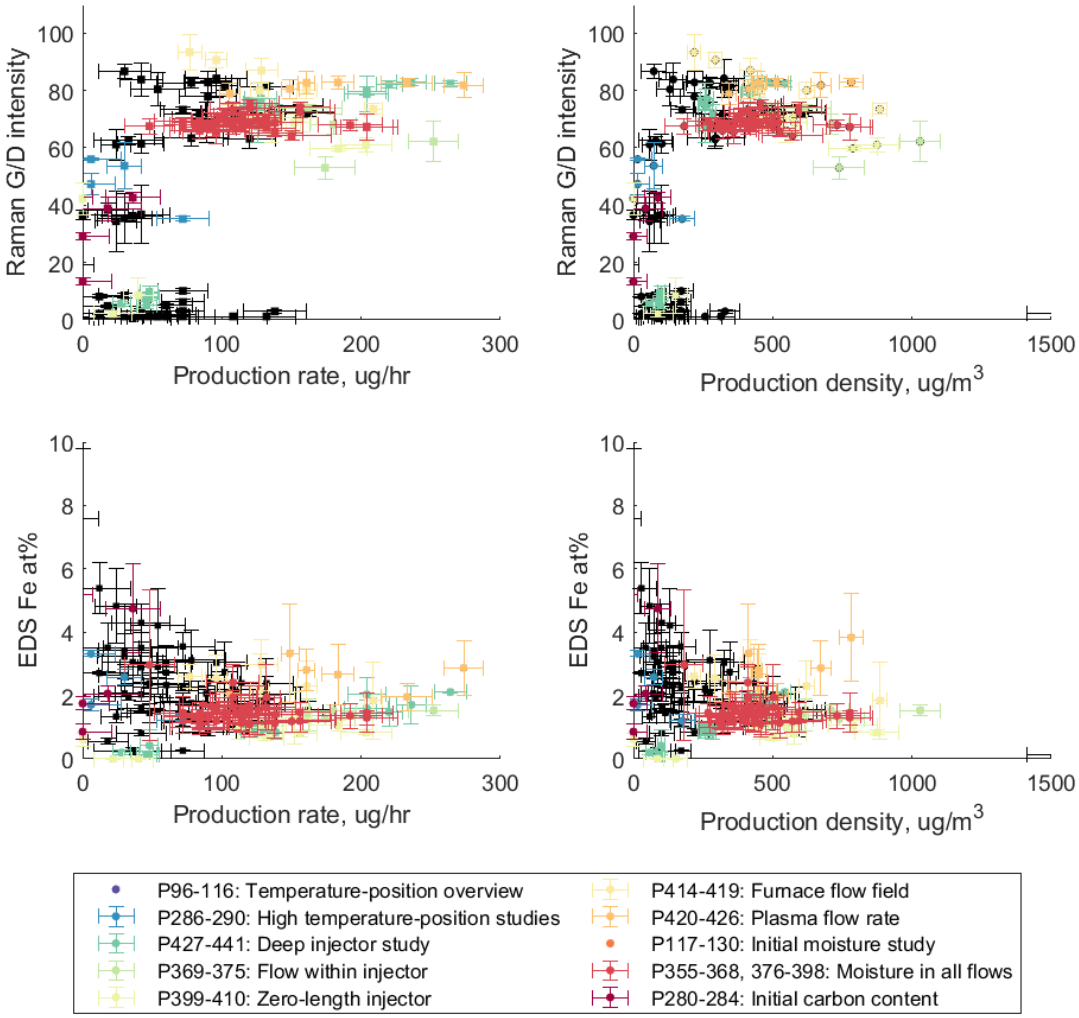

Figure 6.28: Multi-metric scatter plots for all P series experiments. Those experiments mentioned in earlier sections of Chapter 6 are indicated in color. Missing data points indicates an inability to characterize those samples, e.g., insufficient mass to measure a production rate. Tracing along the boundary of points defines the range of Pareto-optimal performance for those two metrics.

veals an inverse relationship in its upper-left boundary. This boundary traces out the range of Pareto-optimal for the system. Of the two quality metrics used here, Raman G/D ratio seems more insightful that the Fe at% data. In part, this may be due to the small range of Fe at% values relative to the accuracy of SEM-EDS at these concentrations. It also reflects the range of experimental conditions tested and the relationship between iron content and total production rate. Given that most conditioned used relatively similar ferrocene inputs, the total amount of iron is fixed, and thus the primary driver for the Fe at% is the amount of solid carbon produced - hence the well-defined Pareto front with an inverse relationship in both the production rate and production density plots.

6.4 Additional Information

6.4.1 Experimental conditions

Case name:	Sample name:	Notes:	plasma housing:	Injector IDxOD (mm)	Injector Length	Position	Proc. tube IDxOD (mm)	Plasma current (mA)	HV polarity	Inner flow (sccm)					Sheath flow (sccm)						Injector flow (sccm)					Furnace flow (sccm)							Total flow:	Furnace Setpoint	Filter Diameter
										He	He+FeCp2	H2	Other	Total:	He	He+FeCp2	N2	H2	Other:	Total:	He	H2	N2	Other:	Total:	He	H2	N2	Ar	C2H4	Other:	Total:			
Case0	**P239**	**best growth on 1/27/23 injector position sweep**	**#1**	**14x25**	**20 mm**	**-40 mm**	**35x39**	**1**	**+**	**580**	**0**	**20**		**600**	**100**	**50**	**150**	**0**	**300**	**0**	**2250**	**900**	**3150**	**0**	**1100**	**0**	**1800**	**50**	**2950**	**7000**	**900°C**	**9mm Dia**		
		20230509 growths																																
Case1	P276, P278, P279	Can't do 900 INJ N2 anymore, max 750. CFD says just dropping this is fine w/r/t eddies.	#1	14x25	20 mm	-40 mm	35x39	1	+	580	0	20		600	100	50	150	0	300	0	2250	750	3000	0	1100	0	1800	50	2950	6850	900°C	9mm Dia		
Case2	P277	real baseline, no H2 in plasma	#1	14x25	20 mm	-40 mm	35x39	1	+	600	0	0		600	100	50	150	0	300	0	2250	750	3000	0	1100	0	1800	50	2950	6850	900°C	9mm Dia		
Case3	P280	(20mm, yes H2 plasma, no h2 sheath, +HV)	#1	20x25	20 mm	-40 mm	35x39	1	+	580	0	20		600	100	50	150	0	300	0	2250	750	3000	0	1100	0	1800	50	2950	6850	900°C	9mm Dia		
Case4	P281, P285	(20mm, no H2 plasma, no h2 sheath, +HV)	#1	20x25	20 mm	-40 mm	35x39	1	+	600	0	0		600	100	50	150	0	300	0	2250	750	3000	0	1100	0	1800	50	2950	6850	900°C	9mm Dia		
Case5	P282	(20mm, no H2 plasma, yes h2 sheath, +HV)	#1	20x25	20 mm	-40 mm	35x39	1	+	600	0	0		600	79	50	150	21	300	0	2250	750	3000	0	1100	0	1800	50	2950	6850	900°C	9mm Dia		
Case6	P283	(20mm, no H2 plasma, no h2 sheath, -HV)	#1	20x25	20 mm	-40 mm	35x39	1	-	600	0	0		600	100	50	150	0	300	0	2250	750	3000	0	1100	0	1800	50	2950	6850	900°C	9mm Dia		
Case7	P284	(20mm, no H2 plasma, yes h2 sheath, -HV)	#1	20x25	20 mm	-40 mm	35x39	1	-	600	0	0		600	79	50	150	21	300	0	2250	750	3000	0	1100	0	1800	50	2950	6850	900°C	9mm Dia		
		Using Case5 as a basis, but exploring higher temp and geometry																																
Case8	*P286, P290*	(950*, -20mm)	#1	20x25	10 mm	-20 mm	35x39	1	+	600	0	0		600	79	50	150	21	300	0	2250	750	3000	0	1100	0	1800	50	2950	6850	950°C	9mm Dia		
Case9	*P287*	(950*, -30mm) plus higher current to stabilize	#1	20x25	10 mm	-30 mm	35x39	1.2	+	600	0	0		600	79	50	150	21	300	0	2250	750	3000	0	1100	0	1800	50	2950	6850	950°C	9mm Dia		
Case10	*P288*	(950*, -40mm) plus higher current to stabilize	#1	20x25	10 mm	-40 mm	35x39	1.2	+	600	0	0		600	79	50	150	21	300	0	2250	750	3000	0	1100	0	1800	50	2950	6850	950°C	9mm Dia		
Case11	*P289*	(950*, -50mm) plus higher current to stabilize	#1	20x25	10 mm	-50 mm	35x39	1.2	+	600	0	0		600	79	50	150	21	300	0	2250	750	3000	0	1100	0	1800	50	2950	6850	950°C	9mm Dia		
Case12	*P291, P297*	(1000*, -20mm)	#1	20x25	10 mm	-20 mm	35x39	1	+	600	0	0		600	79	50	150	21	300	0	2250	750	3000	0	1100	0	1800	50	2950	6850	1000°C	9mm Dia		
Case13	*P292*	(1000*, -30mm)	#1	20x25	10 mm	-30 mm	35x39	1	+	600	0	0		600	79	50	150	21	300	0	2250	750	3000	0	1100	0	1800	50	2950	6850	1000°C	9mm Dia		
Case14	*P293*	(1000*, -40mm)	#1	20x25	10 mm	-40 mm	35x39	1 to 1.2	+	600	0	0		600	79	50	150	21	300	0	2250	750	3000	0	1100	0	1800	50	2950	6850	1000°C	9mm Dia		
Case15	*P294*	(1000*, -50mm)	#1	20x25	10 mm	-50 mm	35x39	1.2	+	600	0	0		600	79	50	150	21	300	0	2250	750	3000	0	1100	0	1800	50	2950	6850	1000°C	9mm Dia		
Case16	*P295*	(1000*, -40mm, low C2H4)	#1	20x25	10 mm	-40 mm	35x39	1.2	+	600	0	0		600	79	50	150	21	300	0	2250	750	3000	0	1100	0	1800	10	2950	6850	1000°C	9mm Dia		
Case17	*P296*	(1000*, -40mm, low plasma flow, 300,550+50)	#1	20x25	10 mm	-40 mm	35x39	1.2	+	300	0	0		600	479	50	50	21	300	0	2250	750	3000	0	1100	0	1800	50	2950	6850	1000°C	9mm Dia		
Case18	P298	(1000*, -20mm, low plasma flow, 300,500+100)	#1	20x25	10 mm	-20 mm	35x39	1.2	+	300	0	0		600	429	50	100	21	300	0	2250	750	3000	0	1100	0	1800	50	2950	6850	1000°C	9mm Dia		
		5/14 C2H2 growths																																
Case19	P299	(600*, -10 mm)	#1	20x25	10 mm	-10 mm	35x39	1	+	600	0	0		600	79	50	150	21	300	0	2250	750	3000	0	1100	0	1800	200	1%C2H2	3100	7000	600°C	9mm Dia	
Case20	P300	(600*, -20 mm)	#1	20x25	10 mm	-20 mm	35x39	1	+	600	0	0		600	79	50	150	21	300	0	2250	750	3000	0	1100	0	1800	200	1%C2H2	3100	7000	600°C	9mm Dia	
Case21	P301	(600*, -30 mm)	#1	20x25	10 mm	-30 mm	35x39	1	+	600	0	0		600	79	50	150	21	300	0	2250	750	3000	0	1100	0	1800	200	1%C2H2	3100	7000	600°C	9mm Dia	
Case22	P302	(600*, -40 mm)	#1	20x25	10 mm	-40 mm	35x39	1	+	600	0	0		600	79	50	150	21	300	0	2250	750	3000	0	1100	0	1800	200	1%C2H2	3100	7000	600°C	9mm Dia	
Case23	P303	(600*, -50 mm)	#1	20x25	10 mm	-50 mm	35x39	1	+	600	0	0		600	79	50	150	21	300	0	2250	750	3000	0	1100	0	1800	200	1%C2H2	3100	7000	600°C	9mm Dia	
Case24	P304	(700*, -20 mm)	#1	20x25	10 mm	-20 mm	35x39	1	+	600	0	0		600	79	50	150	21	300	0	2250	750	3000	0	1100	0	1800	200	1%C2H2	3100	7000	700°C	9mm Dia	
Case25	P305	(700*, -30 mm)	#1	20x25	10 mm	-30 mm	35x39	1	+	600	0	0		600	79	50	150	21	300	0	2250	750	3000	0	1100	0	1800	200	1%C2H2	3100	7000	700°C	9mm Dia	
Case26	P306	(700*, -40 mm)	#1	20x25	10 mm	-40 mm	35x39	1	+	600	0	0		600	79	50	150	21	300	0	2250	750	3000	0	1100	0	1800	200	1%C2H2	3100	7000	700°C	9mm Dia	
Case27	P307, P312	(700*, -50 mm)	#1	20x25	10 mm	-50 mm	35x39	1	+	600	0	0		600	79	50	150	21	300	0	2250	750	3000	0	1100	0	1800	200	1%C2H2	3100	7000	700°C	9mm Dia	
Case28	P308	(700*, -60 mm)	#1	20x25	10 mm	-60 mm	35x39	1	+	600	0	0		600	79	50	150	21	300	0	2250	750	3000	0	1100	0	1800	200	1%C2H2	3100	7000	700°C	9mm Dia	
Case29	P309	(700*, -70 mm)	#1	20x25	10 mm	-70 mm	35x39	1	+	600	0	0		600	79	50	150	21	300	0	2250	750	3000	0	1100	0	1800	200	1%C2H2	3100	7000	700°C	9mm Dia	
Case30	P310	(700*, -80 mm)	#1	20x25	10 mm	-80 mm	35x39	1	+	600	0	0		600	79	50	150	21	300	0	2250	750	3000	0	1100	0	1800	200	1%C2H2	3100	7000	700°C	9mm Dia	
Case31	P311	(700*, -90 mm)	#1	20x25	10 mm	-90 mm	35x39	1	+	600	0	0		600	79	50	150	21	300	0	2250	750	3000	0	1100	0	1800	200	1%C2H2	3100	7000	700°C	9mm Dia	
Case32	P313	(700*, -50 mm)	#1	20x25	10 mm	-50 mm	35x39	1	+	300	0	0		600	479	50	50	21	300	0	2250	750	3000	0	1100	0	1800	200	1%C2H2	3100	7000	700°C	9mm Dia	
		5/17/23 Continue C2H2																																
Case33	P314	(800*, -30 mm)	#1	20x25	10 mm	-30 mm	35x39	1	+	600	0	0		600	79	50	150	21	300	0	2250	750	3000	0	1100	0	1800	200	1%C2H2	3100	7000	800°C	9mm Dia	
Case34	P315	(850*, -30 mm)	#1	20x25	10 mm	-30 mm	35x39	1	+	600	0	0		600	79	50	150	21	300	0	2250	750	3000	0	1100	0	1800	200	1%C2H2	3100	7000	850°C	9mm Dia	
Case35	P316	(900*, -30 mm)	#1	20x25	10 mm	-30 mm	35x39	1	+	600	0	0		600	79	50	150	21	300	0	2250	750	3000	0	1100	0	1800	200	1%C2H2	3100	7000	900°C	9mm Dia	
Case36	P317	(950*, -30 mm)	#1	20x25	10 mm	-30 mm	35x39	1	+	600	0	0		600	79	50	150	21	300	0	2250	750	3000	0	1100	0	1800	200	1%C2H2	3100	7000	950°C	9mm Dia	

Case name:	Sample name:	Notes:	plasma housing:	Injector IDxOD (mm)	Injector Length	Position	Proc. tube IDxOD (mm)	Plasma current (mA)	HV polarity	He	He+FeCp2	H2	Other	Total:	He	He+FeCp2	N2	H2	Other:	Total:	He	H2	N2	Other:	Total:	He	H2	N2	Ar	C2H4	Other:	Total:	Total flow:	Furnace Setpoint	Filter Diameter
Case37	P318	(1000*, -30 mm)	#1	20x25	10 mm	-30 mm	35x39	1	+	600	0	0		600	79	50	150	21		300	0	2250	750		3000	0	1100	0	1800	200	1%C2H2	3100	7000	1000°C	9mm Dia
Case38	P319	(1050*, -30 mm)	#1	20x25	10 mm	-30 mm	35x39	1	+	600	0	0		600	79	50	150	21		300	0	2250	750		3000	0	1100	0	1800	200	1%C2H2	3100	7000	1050°C	9mm Dia
Case39	P320	(1100*, -30 mm)	#1	20x25	10 mm	-30 mm	35x39	1	+	600	0	0		600	79	50	150	21		300	0	2250	750		3000	0	1100	0	1800	200	1%C2H2	3100	7000	1100°C	9mm Dia
		5/17/23 Higher FeCp2 with C2H4																																
Case40	P321	(1000*, -30 mm, high FeCp2)	#1	20x25	10 mm	-30 mm	35x39	1	+	600	0	0		600	34	95	150	21		300	0	2250	750		3000	0	1100	0	1800	50		2950	6850	1000°C	9mm Dia
Case41	P322	(1050*, -30 mm, high FeCp2)	#1	20x25	10 mm	-30 mm	35x39	1	+	600	0	0		600	34	95	150	21		300	0	2250	750		3000	0	1100	0	1800	50		2950	6850	1050°C	9mm Dia
Case42	P323	(1100*, -30 mm, high FeCp2)	#1	20x25	10 mm	-30 mm	35x39	1	+	600	0	0		600	34	95	150	21		300	0	2250	750		3000	0	1100	0	1800	50		2950	6850	1100°C	9mm Dia
		5/25/23 low C2H2																																
Case43	P325	(950°C, -30 mm, 80 c2h2, 50 FeCp2)	#1	20x25	10 mm	-30 mm	35x39	1	+	600	0	0		600	79	50	150	21		300	0	2250	750		3000	0	1100	0	1800	80	1%C2H2	2980	6880	950°C	9mm Dia
Case44	P326	(950°C, -30 mm, 34 c2h2, 50 FeCp2)	#1	20x25	10 mm	-30 mm	35x39	1	+	600	0	0		600	79	50	150	21		300	0	2250	750		3000	0	1100	0	1800	34	1%C2H2	2934	6834	950°C	9mm Dia
Case45	P327	(950°C, -30 mm, 14 c2h2, 50 FeCp2)	#1	20x25	10 mm	-30 mm	35x39	1	+	600	0	0		600	79	50	150	21		300	0	2250	750		3000	0	1100	0	1800	14	1%C2H2	2914	6814	950°C	9mm Dia
		5/25/23 CH4 growths																																
Case46	P328	(900°C, -30 mm, 15 sccm CH4)	#1	20x25	10 mm	-30 mm	35x39	1	+	600	0	0		600	79	50	150	21		300	0	2250	750		3000	0	1100	0	1800	15 sccm	CH4	2915	6815	900°C	9mm Dia
Case47	P329	(900°C, -30 mm, 50 sccm CH4)	#1	20x25	10 mm	-30 mm	35x39	1	+	600	0	0		600	79	50	150	21		300	0	2250	750		3000	0	1100	0	1800	50 sccm	CH4	2950	6850	900°C	9mm Dia
Case48	P330	(1000°C, -10 mm, 15 sccm CH4)	#1	20x25	10 mm	-10 mm	35x39	1.2	+	600	0	0		600	79	50	150	21		300	0	2250	750		3000	0	1100	0	1800	15 sccm	CH4	2915	6815	1000°C	9mm Dia
Case49	P331	(1000°C, -30 mm, 15 sccm CH4)	#1	20x25	10 mm	-30 mm	35x39	1.2	+	600	0	0		600	79	50	150	21		300	0	2250	750		3000	0	1100	0	1800	15 sccm	CH4	2915	6815	1000°C	9mm Dia
Case50	P332	(1000°C, -10 mm, 50 sccm CH4)	#1	20x25	10 mm	-10 mm	35x39	1.5	+	600	0	0		600	79	50	150	21		300	0	2250	750		3000	0	1100	0	1800	50 sccm	CH4	2950	6850	1000°C	9mm Dia
Case51	P333	(1000°C, -30 mm, 50 sccm CH4)	#1	20x25	10 mm	-30 mm	35x39	1.5	+	600	0	0		600	79	50	150	21		300	0	2250	750		3000	0	1100	0	1800	50 sccm	CH4	2950	6850	1000°C	9mm Dia
		5/31/23 C2H4 growths; varying flow rates																																
Case52/H1	P334, P341	(high plasma, high inj+furn)*case 12 but higher FeCp2 and plasma current	#1	20x25	10 mm	-20 mm	35x39	1.5->2	+	600	0	0		600	34	95	150	21		300	0	2250	750		3000	0	1100	0	1800	50		2950	6850	1000°C	9mm Dia
Case53/H2	P335	(high plasma, med inj+furn)	#1	20x25	10 mm	-20 mm	35x39	2	+	600	0	0		600	34	95	150	21		300	0	1440	480		1920	0	778	0	1272	50		2100	4920	1000°C	9mm Dia
Case54/H3	P336	(med plasma, med inj+furn)	#1	20x25	10 mm	-20 mm	35x39	2	+	450	0	0		450	234	95	100	21		450	0	1440	480		1920	0	778	0	1272	50		2100	4920	1000°C	9mm Dia
Case55/H4	P337	(low plasma, med inj+furn)	#1	20x25	10 mm	-20 mm	35x39	2	+	300	0	0		300	434	95	50	21		600	0	1440	480		1920	0	778	0	1272	50		2100	4920	1000°C	9mm Dia
Case56/H5	P338	(low plasma, low inj+furn - C2H4 limit)	#1	20x25	10 mm	-20 mm	35x39	2	+	300	0	0		300	434	95	50	21		600	0	1440	480		1920	0	710	0	1160	50		1920	4740	1000°C	9mm Dia
Case57/H6	P339	(low plasma, v low inj+furn - eddy limit)	#1	20x25	10 mm	-20 mm	35x39	2	+	300	0	0		300	434	95	50	21		600	0	1035	345		1380	0	778	0	1272	50		2100	4380	1000°C	9mm Dia
Case58	P340	(low plasma high n2, v low inj+furn - eddy limit)	#1	20x25	10 mm	-20 mm	35x39	2	+	300	0	0		300	334	95	150	21		600	0	1035	345		1380	0	778	0	1272	50		2100	4380	1000°C	9mm Dia
		6/08/23 Ru cases																**RuCp2:**																
Case59	P347, P348, P354	(med plasma, v low else, 100 Fe)	#1	16x19	10 mm	-20 mm	35x39	1.5	+	450				450	180	100	150	20	0	450	0	1035	345		1380	0	778		1272	50		2100	4380	1000°C	9mm Dia
Case60	P349	(med plasma, v low else, 99Fe+1Ru)	#1	16x19	10 mm	-20 mm	35x39	1.5	+	450				450	164	99	150	20	17	450	0	1035	345		1380	0	778		1272	50		2100	4380	1000°C	9mm Dia
Case61	P350	(med plasma, v low else, 98.5Fe+1.5Ru)	#1	16x19	10 mm	-20 mm	35x39	1.5	+	450				450	156.5	98.5	150	20	25	450	0	1035	345		1380	0	778		1272	50		2100	4380	1000°C	9mm Dia
Case62	P351	(med plasma, v low else, 97.5Fe+2.5Ru)	#1	16x19	10 mm	-20 mm	35x39	1.5	+	450				450	140.5	97.5	150	20	42	450	0	1035	345		1380	0	778		1272	50		2100	4380	1000°C	9mm Dia
Case63	P352	(med plasma, v low else, 95Fe+5Ru)	#1	16x19	10 mm	-20 mm	35x39	1.5	+	450				450	101	95	150	20	84	450	0	1035	345		1380	0	778		1272	50		2100	4380	1000°C	9mm Dia
Case64	P353	(med plasma, v low else, 89Fe+11Ru)	#1	16x19	10 mm	-20 mm	35x39	1.5	+	450				450	0* (mi	89	150	20	186	445	0	1035	345		1380	0	778		1272	50		2100	4375	1000°C	9mm Dia
		6/08/23 moisture cases																												**H2O bubbler**				
Case65	P355	(med plasma, v low else, 5 H2O)	#1	16x19	10 mm	-20 mm	35x39	1.5	+	450				450	180	100	150	20	0	450	0	1035	345		1380	0	778		1272	50	5	2105	4385	1000°C	9mm Dia
Case66	P356	(med plasma, v low else, 10 H2O)	#1	16x19	10 mm	-20 mm	35x39	1.5	+	450				450	180	100	150	20	0	450	0	1035	345		1380	0	778		1272	50	10	2110	4390	1000°C	9mm Dia

Case name:	Sample name:	Notes:	plasma housing:	Injector IDxOD (mm)	Injector Length	Position	Proc. tube IDxOD (mm)	Plasma current (mA)	HV polarity	He	He+FeCp2	H2	Other	Total:	He	He+FeCp2	N2	H2	Other:	Total:	He	H2	N2	Other:	Total:	He	H2	N2	Ar	C2H4	Other:	Total:	Total flow:	Furnace Setpoint	Filter Diameter
Case67	P357	(med plasma, v low else, 15 H2O)	#1	16x19	10 mm	-20 mm	35x39	1.5	+	450				450	180	100	150	20	0	450	0	1035	345		1380	0	778		1272	50	15	2115	4395	1000°C	9mm Dia
Case68	P358	(med plasma, v low else, 20 H2O)	#1	16x19	10 mm	-20 mm	35x39	1.5	+	450				450	180	100	150	20	0	450	0	1035	345		1380	0	778		1272	50	20	2120	4400	1000°C	9mm Dia
Case69	P359	(med plasma, v low else, 25 H2O)	#1	16x19	10 mm	-20 mm	35x39	1.5	+	450				450	180	100	150	20	0	450	0	1035	345		1380	0	778		1272	50	25	2125	4405	1000°C	9mm Dia
Case70	P360	(med plasma, v low else, 30 H2O)	#1	16x19	10 mm	-20 mm	35x39	1.5	+	450				450	180	100	150	20	0	450	0	1035	345		1380	0	778		1272	50	30	2130	4410	1000°C	9mm Dia
Case71	P361	(med plasma, v low else, 35 H2O)	#1	16x19	10 mm	-20 mm	35x39	1.5	+	450				450	180	100	150	20	0	450	0	1035	345		1380	0	778		1272	50	35	2135	4415	1000°C	9mm Dia
Case72	P362	(med plasma, v low else, 40 H2O)	#1	16x19	10 mm	-20 mm	35x39	1.5	+	450				450	180	100	150	20	0	450	0	1035	345		1380	0	778		1272	50	40	2140	4420	1000°C	9mm Dia
Case73	P363	(med plasma, v low else, 45 H2O)	#1	16x19	10 mm	-20 mm	35x39	1.5	+	450				450	180	100	150	20	0	450	0	1035	345		1380	0	778		1272	50	45	2145	4425	1000°C	9mm Dia
Case74	P364	(med plasma, v low else, 55 H2O)	#1	16x19	10 mm	-20 mm	35x39	1.5	+	450				450	180	100	150	20	0	450	0	1035	345		1380	0	778		1272	50	55	2155	4435	1000°C	9mm Dia
Case75	P365	(med plasma, v low else, 70 H2O)	#1	16x19	10 mm	-20 mm	35x39	1.5	+	450				450	180	100	150	20	0	450	0	1035	345		1380	0	778		1272	50	70	2170	4450	1000°C	9mm Dia
Case76	P366	(med plasma, v low else, 90 H2O)	#1	16x19	10 mm	-20 mm	35x39	1.5	+	450				450	180	100	150	20	0	450	0	1035	345		1380	0	778		1272	50	90	2190	4470	1000°C	9mm Dia
Case77	P367	(med plasma, v low else, 115 H2O)	#1	16x19	10 mm	-20 mm	35x39	1.5	+	450				450	180	100	150	20	0	450	0	1035	345		1380	0	778		1272	50	115	2215	4495	1000°C	9mm Dia
Case78	P368	(med plasma, v low else, 150 H2O)	#1	16x19	10 mm	-20 mm	35x39	1.5	+	450				450	180	100	150	20	0	450	0	1035	345		1380	0	778		1272	50	150	2250	4530	1000°C	9mm Dia
		6/17/23 Inj Flow Sweep																																
Case79	P369	(1530 inj, 2100 furn)	#1	16x19	10 mm	-20 mm	35x39	1.5	+	450				450	180	100	150	20	0	450	0	1147	383		1530	0	778		1272	50		2100	4530	1000°C	11mm Dia
Case80	P370, P376, P385, P394	(1380 inj, 2100 furn) Case59 baseline but bigger filter	#1	16x19	10 mm	-20 mm	35x39	1.5	+	450				450	180	100	150	20	0	450	0	1035	345		1380	0	778		1272	50		2100	4380	1000°C	11mm Dia
Case81	P371	(1230 inj, 2100 furn)	#1	16x19	10 mm	-20 mm	35x39	1.5	+	450				450	180	100	150	20	0	450	0	922	308		1230	0	778		1272	50		2100	4230	1000°C	11mm Dia
Case82	P372	(1080 inj, 2100 furn)	#1	16x19	10 mm	-20 mm	35x39	1.5	+	450				450	180	100	150	20	0	450	0	810	270		1080	0	778		1272	50		2100	4080	1000°C	11mm Dia
Case83	P373	(930 inj, 2100 furn)	#1	16x19	10 mm	-20 mm	35x39	1.5	+	450				450	180	100	150	20	0	450	0	697	233		930	0	778		1272	50		2100	3930	1000°C	11mm Dia
Case84	P374, P375	(780 inj, 2100 furn)	#1	16x19	10 mm	-20 mm	35x39	1.5	+	450				450	180	100	150	20	0	450	0	585	195		780	0	778		1272	50		2100	3780	1000°C	11mm Dia
		6/17/23 Inj Moisture Sweep																						**H2O:**										
Case85	P377	(5 H2O to Inj, else Case80)	#1	16x19	10 mm	-20 mm	35x39	1.5	+	450				450	180	100	150	20	0	450	0	1030	345	5	1380	0	778		1272	50		2100	4380	1000°C	11mm Dia
Case86	P378	(10 H2O to Inj, else Case80)	#1	16x19	10 mm	-20 mm	35x39	1.5	+	450				450	180	100	150	20	0	450	0	1025	345	10	1380	0	778		1272	50		2100	4380	1000°C	11mm Dia
Case87	P379	(15 H2O to Inj, else Case80)	#1	16x19	10 mm	-20 mm	35x39	1.5	+	450				450	180	100	150	20	0	450	0	1020	345	15	1380	0	778		1272	50		2100	4380	1000°C	11mm Dia
Case88	P380	(20 H2O to Inj, else Case80)	#1	16x19	10 mm	-20 mm	35x39	1.5	+	450				450	180	100	150	20	0	450	0	1015	345	20	1380	0	778		1272	50		2100	4380	1000°C	11mm Dia
Case89	P381	(30 H2O to Inj, else Case80)	#1	16x19	10 mm	-20 mm	35x39	1.5	+	450				450	180	100	150	20	0	450	0	1005	345	30	1380	0	778		1272	50		2100	4380	1000°C	11mm Dia
Case90	P382	(40 H2O to Inj, else Case80)	#1	16x19	10 mm	-20 mm	35x39	1.5	+	450				450	180	100	150	20	0	450	0	995	345	40	1380	0	778		1272	50		2100	4380	1000°C	11mm Dia
Case91	P383	(70 H2O to Inj, else Case80)	#1	16x19	10 mm	-20 mm	35x39	1.5	+	450				450	180	100	150	20	0	450	0	965	345	70	1380	0	778		1272	50		2100	4380	1000°C	11mm Dia
Case92	P384	(150 H2O to Inj, else Case80)	#1	16x19	10 mm	-20 mm	35x39	1.5	+	450				450	180	100	150	20	0	450	0	885	345	150	1380	0	778		1272	50		2100	4380	1000°C	11mm Dia
		6/17/23 Sheath moisture sweep																	**H2O:**															
Case93	P386	(3.1 H2O to Sheath, else Case80)	#1	16x19	10 mm	-20 mm	35x39	1.5	+	450				450	177	100	150	20	3.1	450.1	0	1035	345	0	1380	0	778		1272	50		2100	4380.1	1000°C	11mm Dia
Case94	P387	(5 H2O to Sheath, else Case80)	#1	16x19	10 mm	-20 mm	35x39	1.5	+	450				450	175	100	150	20	5	450	0	1035	345	0	1380	0	778		1272	50		2100	4380	1000°C	11mm Dia
Case95	P388	(10 H2O to Sheath, else Case80)	#1	16x19	10 mm	-20 mm	35x39	1.5	+	450				450	170	100	150	20	10	450	0	1035	345	0	1380	0	778		1272	50		2100	4380	1000°C	11mm Dia
Case96	P389	(15 H2O to Sheath, else Case80)	#1	16x19	10 mm	-20 mm	35x39	1.5	+	450				450	165	100	150	20	15	450	0	1035	345	0	1380	0	778		1272	50		2100	4380	1000°C	11mm Dia
Case97	P390	(20 H2O to Sheath, else Case80)	#1	16x19	10 mm	-20 mm	35x39	1.5	+	450				450	160	100	150	20	20	450	0	1035	345	0	1380	0	778		1272	50		2100	4380	1000°C	11mm Dia
Case98	P391	(30 H2O to Sheath, else Case80)	#1	16x19	10 mm	-20 mm	35x39	1.5	+	450				450	150	100	150	20	30	450	0	1035	345	0	1380	0	778		1272	50		2100	4380	1000°C	11mm Dia
Case99	P392	(60 H2O to Sheath, else Case80)	#1	16x19	10 mm	-20 mm	35x39	1.5	+	450				450	120	100	150	20	60	450	0	1035	345	0	1380	0	778		1272	50		2100	4380	1000°C	11mm Dia
Case100	P393	(150 H2O to Sheath, else Case80)	#1	16x19	10 mm	-20 mm	35x39	1.5	+	450				450	30	100	150	20	150	450	0	1035	345	0	1380	0	778		1272	50		2100	4380	1000°C	11mm Dia
		6/17/23: Inner flow moisture sweep											**H2O:**																					
Case101	P395	(5 H2O to Plasma, else Case80)	#1	16x19	10 mm	-20 mm	35x39	1.5	+	445			5	450	180	100	150	20		450	0	1035	345		1380	0	778		1272	50		2100	4380	1000°C	11mm Dia

Case name:	Sample name:	Notes:	plasma housing:	Injector IDxOD (mm)	Injector Length	Position	Proc. tube IDxOD (mm)	Plasma current (mA)	HV polarity	He	He+FeCp2	H2	Other	Total:	He	He+FeCp2	N2	H2	Other:	Total:	He	H2	N2	Other:	Total:	He	H2	N2	Ar	C2H4	Other:	Total:	Total flow:	Furnace Setpoint	Filter Diameter
Case102	P396	(15 H2O to Plasma, else Case80)	#1	16x19	10 mm	-20 mm	35x39	1.5	+	435			15	450	180	100	150	20		450	0	1035	345		1380	0	778	1272	50		2100	4380	1000°C	11mm Dia
Case103	P397	(45 H2O to Plasma, else Case80)	#1	16x19	10 mm	-20 mm	35x39	1.5	+	405			45	450	180	100	150	20		450	0	1035	345		1380	0	778	1272	50		2100	4380	1000°C	11mm Dia
Case104	P398	(150 H2O to Plasma, else Case80)	#1	16x19	10 mm	-20 mm	35x39	1.5	+	300			150	450	180	100	150	20		450	0	1035	345		1380	0	778	1272	50		2100	4380	1000°C	11mm Dia
		6/22/23: 20mm InjL inj flow sweep - fresh mesh and plasma housing																																
Case105	P399	(1380 inj, 2100 furn, 20mm injL, -25mm inj pos)	#2	16x19	20 mm	-25 mm	35x39	1.5	+	450				450	180	100	150	20		450		1035	345		1380		778	1272	50		2100	4380	1000°C	11mm Dia
Case106	P400	(1130 inj, 2100 furn, 20mm injL, -25mm inj pos)	#2	16x19	20 mm	-25 mm	35x39	1.5	+	450				450	180	100	150	20		450		847	283		1130		778	1272	50		2100	4130	1000°C	11mm Dia
Case107	P401	(880 inj, 2100 furn, 20mm injL, -25mm inj pos)	#2	16x19	20 mm	-25 mm	35x39	1.5	+	450				450	180	100	150	20		450		660	220		880		778	1272	50		2100	3880	1000°C	11mm Dia
Case108	P402	(780 inj, 2100 furn, 20mm injL, -25mm inj pos)	#2	16x19	20 mm	-25 mm	35x39	1.5	+	450				450	180	100	150	20		450		585	195		780		778	1272	50		2100	3780	1000°C	11mm Dia
Case109	P403	(1380 inj, 2100 furn, 10mm injL, -25mm inj pos)	#2	16x19	10 mm	-25 mm	35x39	1.5	+	450				450	180	100	150	20		450		1035	345		1380		778	1272	50		2100	4380	1000°C	11mm Dia
Case110	P404	(1380 inj, 2100 furn, 10mm injL, -25mm inj pos, high plasma)	#2	16x19	10 mm	-25 mm	35x39	1.5	+	450				450	330	100	150	20		600		1035	345		1380		778	1272	50		2100	4530	1000°C	11mm Dia
Case111	P405	(1130 inj, 2100 furn, 10mm injL, -25mm inj pos)	#2	16x19	20 mm	-25 mm	35x39	1.5	+	450				450	180	100	150	20		450		847	283		1130		778	1272	50		2100	4130	1000°C	11mm Dia
Case112	P406	(880 inj, 2100 furn, 10mm injL, -25mm inj pos)	#2	16x19	20 mm	-25 mm	35x39	1.5	+	450				450	180	100	150	20		450		660	220		880		778	1272	50		2100	3880	1000°C	11mm Dia
Case113	P407	(780 inj, 2100 furn, 10mm injL, -25mm inj pos)	#2	16x19	20 mm	-25 mm	35x39	1.5	+	450				450	180	100	150	20		450		585	195		780		778	1272	50		2100	3780	1000°C	11mm Dia
																			Ru:														
Case114	P408	(1380 inj, 2100 furn, 0mm injL, -25mm inj pos)	#2	16x19	10 mm	-25 mm	35x39	1.5	+	450				450	180	100	150	20		450		1035	345		1380		778	1272	50		2100	4380	1000°C	11mm Dia
Case115	P409	(1130 inj, 2100 furn, 10mm injL, -25mm inj pos)	#2	16x19	20 mm	-25 mm	35x39	1.5	+	450				450	180	100	150	20		450		847	283		1130		778	1272	50		2100	4130	1000°C	11mm Dia
Case116	P410	(780 inj, 2100 furn, 10mm injL, -25mm inj pos)	#2	16x19	20 mm	-25 mm	35x39	1.5	+	450				450	180	100	150	20		450		585	195		780		778	1272	50		2100	3780	1000°C	11mm Dia
Case117	P411	(780 inj, 2100 furn, 10mm injL, -5mm inj pos)	#2	16x19	20 mm	-25 mm	35x39	1.5	+	450				450	180	100	150	20		450		585	195		780		778	1272	50		2100	3780	1000°C	11mm Dia
Case118	P412	(780 inj, 2100 furn, 10mm injL, -25mm inj pos + 5% Ru)	#2	16x19	20 mm	-25 mm	35x39	1.5	+	450				450	101	95	150	20	84	450		585	195		780		778	1272	50		2100	3780	1000°C	11mm Dia
		7/04/23: Furnace flow rate sweep																						**Ar:**										
Case119	P413	(K2, 2950 furn)	#2	16x19	10 mm	-25 mm	35x39	2	+	450				450	130	150	150	20		450		1170		390	1560		1100	1800	50		2950	5410	1000°C	16 mm Dia
Case120	P414	(K2 + 30% inj, 2950 furn)	#2	16x19	10 mm	-25 mm	35x39	2	+	450				450	130	150	150	20		450		1521		507	2028		1100	1800	50		2950	5878	1000°C	16 mm Dia
Case121	P415	(K2 + 30% inj, 2515 furn (935 H2, 1530 Ar))	#2	16x19	10 mm	-25 mm	35x39	2	+	450				450	130	150	150	20		450		1521		507	2028		935	1530	50		2515	5443	1000°C	16 mm Dia
Case122	P416	(K2 + 30% inj, 2167 furn (803 H2, 1314 Ar))	#2	16x19	10 mm	-25 mm	35x39	2	+	450				450	130	150	150	20		450		1521		507	2028		803	1314	50		2167	5095	1000°C	16 mm Dia
Case123	P417	(K2 + 30% inj, 1793 furn (661 H2, 1082 Ar))	#2	16x19	10 mm	-25 mm	35x39	2	+	450				450	130	150	150	20		450		1521		507	2028		661	1082	50		1793	4721	1000°C	16 mm Dia
Case124	P418	(K2 + 30% inj, 1384 furn (506 H2, 828 Ar))	#2	16x19	10 mm	-25 mm	35x39	2	+	450				450	130	150	150	20		450		1521		507	2028		506	828	50		1384	4312	1000°C	16 mm Dia
Case125	P419	(K2 + 30% inj, 1007 furn (363 H2, 594 Ar))	#2	16x19	10 mm	-25 mm	35x39	2	+	450				450	130	150	150	20		450		1521		507	2028		363	594	50		1007	3935	1000°C	16 mm Dia
		7/06/23: K series plasma flow rates																						**Ar:**										
Case126	P420	(K2b, 900, 2100, 2125)	#2	16x19	10 mm	-25 mm	35x39	2	+	450				450	130	150	150	20		450		1575		525	2100		785	1290	50		2125	5125	1000°C	16 mm Dia
Case127	P421	(K3b, 1200, 2400, 2400)	#2	16x19	10 mm	-25 mm	35x39	2	+	600				600	230	150	200	20		600		1800		600	2400		890	1460	50		2400	6000	1000°C	16 mm Dia
Case128	P422	(K3b high Fe, 1200, 2400, 2400)	#2	16x19	10 mm	-25 mm	35x39	2	+	600				600	180	200	200	20		600		1800		600	2400		890	1460	50		2400	6000	1000°C	16 mm Dia
Case129	P423	(K4b, 1500, 2600, 2675)	#2	16x19	10 mm	-25 mm	35x39	2	+	750				750	330	150	250	20		750		1950		650	2600		995	1630	50		2675	6775	1000°C	16 mm Dia
Case130	P424	(K4b high Fe, 1500, 2600, 2675)	#2	16x19	10 mm	-25 mm	35x39	2	+	750				750	230	250	250	20		750		1950		650	2600		995	1630	50		2675	6775	1000°C	16 mm Dia
Case131	P425	(K5b, 1800, 2800, 2950)	#2	16x19	10 mm	-25 mm	35x39	2	+	900				900	430	150	300	20		900		2100		700	2800		1100	1800	50		2950	7550	1000°C	16 mm Dia

Case name:	Sample name:	Notes:	plasma housing:	Injector IDxOD (mm)	Injector Length	Position	Proc. tube IDxOD (mm)	Plasma current (mA)	HV polarity	He	He+FeCp2	H2	Other	Total:	He	He+FeCp2	N2	H2	Other:	Total:	He	H2	N2	Other:	Total:	He	H2	N2	Ar	C2H4	Other:	Total:	Total flow:	Furnace Setpoint	Filter Diameter
Case132	P426	(K5b high Fe, 1800, 2800, 2950)	#2	16x19	10 mm	-25 mm	35x39	2	+	900				900	280	300	300	20		900		2100		700	2800		1100		1800	50		2950	7550	1000°C	16 mm Dia
		7/13/23: deep injector																						**Ar:**										
Case133	P427	(K5long, 10, -25, 37.5 fe)	#2	16x19	10 mm	-25 mm	35x39	1.5	+	900				900	542.5	37.5	300	20		900		2150		1050	3200		1100		1950	50		3100	8100	1000°C	16 mm Dia
Case134	P428	(K5long, 10, -25, 75 fe)	#2	16x19	10 mm	-25 mm	35x39	1.5	+	900				900	505	75	300	20		900		2150		1050	3200		1100		1950	50		3100	8100	1000°C	16 mm Dia
Case135	P429	(K5long, 10, -25, 150 fe)	#2	16x19	10 mm	-25 mm	35x39	1.5	+	900				900	430	150	300	20		900		2150		1050	3200		1100		1950	50		3100	8100	1000°C	16 mm Dia
Case136	P430	(K5long, 20, -35, 37.5 fe)	#2	16x19	20 mm	-35 mm	35x39	1.5	+	900				900	542.5	37.5	300	20		900		2150		1050	3200		1100		1950	50		3100	8100	1000°C	16 mm Dia
Case137	P431	(K5long, 20, -35, 75 fe)	#2	16x19	20 mm	-35 mm	35x39	1.5	+	900				900	505	75	300	20		900		2150		1050	3200		1100		1950	50		3100	8100	1000°C	16 mm Dia
Case138	P432	(K5long, 20, -35, 150 fe)	#2	16x19	20 mm	-35 mm	35x39	1.5	+	900				900	430	150	300	20		900		2150		1050	3200		1100		1950	50		3100	8100	1000°C	16 mm Dia
Case139	P433	(K5long, 35, -50, 37.5 fe)	#2	16x19	35 mm	-50 mm	35x39	1.5	+	900				900	542.5	37.5	300	20		900		2150		1050	3200		1100		1950	50		3100	8100	1000°C	16 mm Dia
Case140	P434	(K5long, 35, -50, 75 fe)	#2	16x19	35 mm	-50 mm	35x39	1.5	+	900				900	505	75	300	20		900		2150		1050	3200		1100		1950	50		3100	8100	1000°C	16 mm Dia
Case141	P435	(K5long, 35, -50, 150 fe)	#2	16x19	35 mm	-50 mm	35x39	1.5	+	900				900	430	150	300	20		900		2150		1050	3200		1100		1950	50		3100	8100	1000°C	16 mm Dia
Case142	P436	(K5long, 50, -65, 37.5 fe)	#2	16x19	50 mm	-65 mm	35x39	1.5	+	900				900	542.5	37.5	300	20		900		2150		1050	3200		1100		1950	50		3100	8100	1000°C	16 mm Dia
Case143	P437	(K5long, 50, -65, 75 fe)	#2	16x19	50 mm	-65 mm	35x39	1.5	+	900				900	505	75	300	20		900		2150		1050	3200		1100		1950	50		3100	8100	1000°C	16 mm Dia
Case144	P438	(K5long, 50, -65, 150 fe)	#2	16x19	50 mm	-65 mm	35x39	1.5	+	900				900	430	150	300	20		900		2150		1050	3200		1100		1950	50		3100	8100	1000°C	16 mm Dia
Case145	P439	(K5long, 65, -80, 37.5 fe)	#2	16x19	65 mm	-80 mm	35x39	1.5	+	900				900	542.5	37.5	300	20		900		2150		1050	3200		1100		1950	50		3100	8100	1000°C	16 mm Dia
Case146	P440	(K5long, 65, -80, 75 fe)	#2	16x19	65 mm	-80 mm	35x39	1.5	+	900				900	505	75	300	20		900		2150		1050	3200		1100		1950	50		3100	8100	1000°C	16 mm Dia
Case147	P441	(K5long, 65, -80, 150 fe)	#2	16x19	65 mm	-80 mm	35x39	1.5	+	900				900	430	150	300	20		900		2150		1050	3200		1100		1950	50		3100	8100	1000°C	16 mm Dia
		Plasma housing 1: 19TW capillary tube, 2 mm electrode gap, quartz plasma housing has 1.98 mm tip orifice. "mesh holder" portion is 10.3 mm long with 3 mm ID and aluminum.																																	
		Plasma housing 2: Identical except 2.15 mm orifice in quartz plasma housing, "mesh holder" is stainless steel.																																	

References

[1] William James Sawyer. “Toward improved manufacturing of carbon nanotubes by microplasma synthesis of catalyst nanoparticles”. Massachusetts Institute of Technology, 2020.

[2] Derek Albert Long. “Raman spectroscopy”. In: *New York* 1 (1977).

[3] MS Dresselhaus, G Dresselhaus, and R Saito. “Physics of carbon nanotubes”. In: *Carbon* 33.7 (1995), pp. 883–891.

[4] Mildred S Dresselhaus et al. “Raman spectroscopy of carbon nanotubes”. In: *Physics reports* 409.2 (2005), pp. 47–99.

[5] Li Zhang et al. “Excitation, temperature, and structural dependence of second-order raman modes in single-wall carbon nanotubes”. In: *The Journal of Physical Chemistry C* 113.37 (2009), pp. 16432–16438.

[6] Mildred S Dresselhaus et al. “Perspectives on carbon nanotubes and graphene Raman spectroscopy”. In: *Nano letters* 10.3 (2010), pp. 751–758.

[7] Ying Tian et al. “Validity of measuring metallic and semiconducting single-walled carbon nanotube fractions by quantitative Raman spectroscopy”. In: *Analytical chemistry* 90.4 (2018), pp. 2517–2525.

[8] Attarad Ali et al. “Synthesis, characterization, applications, and challenges of iron oxide nanoparticles”. In: *Nanotechnology, Science and Applications* (2016), pp. 49–67.

[9] John Konopka. “Options for quantitative analysis of light elements by SEM/EDS”. In: *Thermo Fisher Scientific;* Technical Note 52523 (2013).

[10] Taras Kolodiazhnyi and Martin Pumera. “Towards an ultrasensitive method for the determination of metal impurities in carbon nanotubes”. In: *Small* 4.9 (2008), pp. 1476–1484.

[11] Desirée L Plata et al. “Multiple alkynes react with ethylene to enhance carbon nanotube synthesis, suggesting a polymerization-like formation mechanism”. In: *Acs Nano* 4.12 (2010), pp. 7185–7192.

[12] Lee Weller et al. “Mapping the parameter space for direct-spun carbon nanotube aerogels”. In: *Carbon* 146 (2019), pp. 789–812.

[13] Sung-Hyun Lee et al. “Deep-injection floating-catalyst chemical vapor deposition to continuously synthesize carbon nanotubes with high aspect ratio and high crystallinity”. In: *Carbon* 173 (2021), pp. 901–909.

[14] Anna Moisala et al. “Single-walled carbon nanotube synthesis using ferrocene and iron pentacarbonyl in a laminar flow reactor”. In: *Chemical Engineering Science* 61.13 (2006), pp. 4393–4402.

[15] Takeshi Saito et al. “Selective diameter control of single-walled carbon nanotubes in the gas-phase synthesis”. In: *Journal of nanoscience and nanotechnology* 8.11 (2008), pp. 6153–6157.

[16] Jinjing Li et al. “Highly consistent atmospheric pressure synthesis of carbon nanotube forests by mitigation of moisture transients”. In: *The Journal of Physical Chemistry C* 120.20 (2016), pp. 11277–11287.

[17] C Ryan Oliver et al. “Statistical analysis of variation in laboratory growth of carbon nanotube forests and recommendations for improved consistency”. In: *ACS nano* 7.4 (2013), pp. 3565–3580.

[18] Gilbert D Nessim et al. “Synthesis of tall carpets of vertically aligned carbon nanotubes by in situ generation of water vapor through preheating of added oxygen”. In: *Carbon* 50.11 (2012), pp. 4002–4009.

[19] Placidus B Amama et al. “Role of water in super growth of single-walled carbon nanotube carpets”. In: *Nano letters* 9.1 (2009), pp. 44–49.

[20] Albert G Nasibulin et al. “Carbon nanotube synthesis from alcohols by a novel aerosol method”. In: *Journal of Nanoparticle Research* 8.3-4 (2006), pp. 465–475.

[21] Shigeo Maruyama et al. “Low-temperature synthesis of high-purity single-walled carbon nanotubes from alcohol”. In: *Chemical physics letters* 360.3-4 (2002), pp. 229–234.

[22] Ya-Li Li et al. “Synthesis of high purity single-walled carbon nanotubes from ethanol by catalytic gas flow CVD reactions”. In: *Nanotechnology* 18.22 (2007), p. 225604.

7. Summary and outlook

7.1 Summary of Contributions

In summary, this thesis describes the design, construction, and implementation of a lab-scale system that achieves end-to-end control of catalyst generation and aerosol CNT growth for the purpose of understanding these processes and assessing potential scalability. This enabled a better understanding of aerosol nanoparticle formation, CNT nucleation, and growth dynamics in the aerosol phase.

First, a novel atmospheric pressure DC microplasma reactor was developed and used to study the synthesis of iron-carbon nanoparticles from ferrocene vapor. This device is capable of producing high concentration ($> 10^9$ #/cm^3) sub-3 nm iron particles with narrow size distribution ($\sigma_g < 1.3$) during stable operation for multiple hours. This represents an order of magnitude increase in concentration over the concentration-diameter Pareto front of previously reported systems. This performance is explained using a charge-mediated formation mechanism and the uniquely short ~ 10 μs plasma residence time of the system. The addition of N_2 to the sheath flow is used to focus the plasma by producing a spatial gradient of dielectric strength in the gas within the reactor. Ensuing that the plasma discharge is centered in the reactor appears to enable nearly complete dissociation of the $Fe(Cp)_2$ precursor as evidenced by Y_{Fe} up to 0.93.

Second, a FC-CVD system is built and integrated with the microplasma reactor

and used to explore CNT synthesis on iron-carbon catalyst aerosols. Controlling temperature, gas chemistry, and flow conditions at which the catalyst aerosol and carbon precursor streams mix is shown to be critical for enabling CNT nucleation, controlling CNT diameter, and limiting iron and amorphous carbon impurities. In particular, the use of an injector if found to be critical for delaying the mixing of the catalyst aerosol and carbon precursor until sufficiently deep in the furnace for conditions to support CNT nucleation. A large experimental data set is also used to reveal the range of Pareto-optimal performance for the FC-CVD system when considering multiple competing objectives such as the Raman G/D ratio and production density. This highlights the magnitude of trade-offs between performance objectives for various operating parameters, most clearly shown in the experimental evaluation of the injector and furnace flow rates.

7.2 Outlook

At the outset, the intent of this thesis was to make progress on two questions. First, what are the practical limitations for high quality CNT synthesis today, and can we push the performance envelope using new techniques or savvy machine design? Second, what are the fundamental limitations of this process? Both in the narrow sense of the synthesis process – how far can the envelope be pushed? – but also with respect to the utility and cost of these materials to society.

The first question is only important in the context of the second; it is the hope that these materials will have a positive impact on the world that motivates this work. Yet, when an experimental system is so early in the development process, so far from ideal that a few months of work or a lucky hypothesis can increase the performance by an order of magnitude, it is futile and impertinent to extrapolate out costs and life cycle impacts. Even at the scale of the largest commercial reactors, 10 tons/year for OcSiAl's

single-wall CNTs, is too small to prognosticate from. So, we have a lot of work to do.

And yet, a few paths are becoming clear for aerosol CNT synthesis. As the analysis in Chapter 3 shows, aerosol dynamics present a limit for the concentration of CNTs, and thus the cost and impact of the process with respect to the needed gas flows. If not fundamental limits, then fundamental points of diminishing returns, and most current FC-CVD systems are well below this production density for single-wall CNTs.

Hitting this limit will require the ability to generate catalyst particles at concentrations of 10^{11} to 10^{12} #/cm^3, a CNT nucleation efficiency of 0.1 to 1, and growth rates of the order 500 um/s.

In this thesis, we have pushed the limit of aerosol concentration up from of order 10^9 to 10^{10}, and done so with high conversion efficiency of relatively small precursor concentrations. Importantly, this is the concentration *as measured* in an experimental set-up that realistically mimics the flow path and aggregation residence time that would be experienced when integrated into a FC-CVD system. Another order of magnitude increase is likely attainable through the continued development of microplasma reactors: increasing precursor concentration, tuning ion concentration to influence aggregation, and hardware design to enable better system integration.

Achieving high CNT nucleation efficiency may be more challenging, in part due to the difficulty of studying this in the aerosol phase, but there is no reason why it should not be possible: A sustained effort to study CNT nucleation on substrates has lead to deep understanding of how CNT nucleation can be enabled through control of particle formation, composition, and size, attaining efficiency of up to 0.9 [1, 2, 3]. While the nucleation efficiency (or iron-to-carbon yield) achieved in this work is well below these achievements, or that attained in other FC-CVD systems, that is attributed to limited opportunity for CVD condition tuning. As CNT nucleation is a process that involves only a single catalyst particle and the local environment, there should be no

influence of aerosol concentration, and it should be possible to combine the high catalyst concentration achieved here with high nucleation efficiency.

Finally, the need for a high growth rate is already apparent in the trend towards higher temperatures for FC-CVD synthesis. At the upper range of temperatures currently used, 1200-1300 °C, there are unique considerations involving the temperature, flow conditions and residence times, catalyst material, and carbon precursor. Evaporation of catalyst metals and the thermal decomposition of carbon precursors must be understood and properly handled. This may require the use of low vapor pressure metals or alloys, more stable carbon precursors, and the ability to more sharply define thermal and compositional gradients than in a typical flow-through CVD furnace. The use of a microplasma reactor with multiple metal precursors may uniquely enable rapid experimentation and high-temperature catalyst discovery.

Taken as a whole, the contributions of this thesis and the anticipated future work outlined above will result in new CNT production systems which overcome the current practical limitations, and an expanded body of knowledge upon which we will be better positioned to evaluate the fundamental limits and opportunity of high quality single-wall CNTs.

References

[1] Rahul Rao et al. “Maximization of carbon nanotube yield by solid carbon-assisted dewetting of iron catalyst films”. In: *Carbon* 165 (2020), pp. 251–258.

[2] Nicholas T Dee et al. “Carbon-assisted catalyst pretreatment enables straightforward synthesis of high-density carbon nanotube forests”. In: *Carbon* (2019).

[3] Nicholas Thomas Dee. “In situ monitoring and control of carbon nanotube synthesis”. PhD thesis. Massachusetts Institute of Technology, 2020.